Black Carbon and the Regional Climate of California

Report to the
California Air Resources Board
Contract 08-323

Prepared by:

V. Ramanathan
Principal Investigator

Dr. R. Bahadur[1]
Dr. V. Ramanathan[1]
Dr. P. S. Praveen[1]
Dr. K. A. Prather[2]
Dr. A. Cazorla[2]
Dr. T. Kirchstetter[3]
Dr. O. L. Hadley[3]
Dr. R. Leung[4]
Dr. C. Zhao[4]

[1]Scripps Institution of Oceanography
University of California at San Diego

[2]Department of Chemistry and Biochemistry
University of California at San Diego

[3]Lawrence Berkeley National Lab.

[4]Pacific Northwest National Lab.

April 15, 2013

DISCLAIMER

This report was prepared by the University of California, San Diego (Contractor), in association with Lawrence Berkeley National Laboratories and Pacific Northwest National Laboratories (Sub-Contractors) as an account of work sponsored by the California Air Resources Board (CARB), under contract # 08-323. The statements and conclusions in this report are those of the contractor, and not necessarily of CARB. The mention of any commercial products, their use in conjunction with material reported here, or their source is not to be construed as an actual or implied endorsement of such products.

ACKNOWLEDGEMENTS

We thank Dr. Nehzat Motallebi for project management, support, and guidance over the duration of this contract.

We thank Dr. D. Chand, Dr. B. Schmid, and Dr. H. H. Jonsson for providing measurements collected during the CalNex and CalWater field campaigns used to validate aerosol sources.

We gratefully acknowledge Dr. Ron Cohen (UC Berkeley), Dr. Surabi Menon (LBL), and Dr. Yan Feng (Argonne National Labs.) for their scientific input and additional guidance for the project.

We would also like to thank Dr. Lynn M. Russell (UCSD) for heading the associated CARB funded work constraining the indirect effect of black carbon on clouds in California.

We acknowledge the National Energy Research Scientific Computing Center (NERSC), which is supported by the U.S. Department of Energy Office of Science under Contract No. DE-AC02-05CH11231, and the PNNL Institutional Computing, for providing computing resources for the regional model simulations performed by PNNL

We would like to acknowledge the hard work and contribution of several graduate students and post graduate researchers including Yangyang Xu (UCSD), Liliana Nunez (UCSD), and Dev Milstein (LBL) who contributed in part to this work.

The work described in this report was primarily accomplished by post-graduate researchers Dr. Ranjit Bahadur (UCSD), Dr. P. S. Praveen (UCSD), Dr. Alberto Cazorla (UCSD), Dr. Odelle Hadley (LBL), Dr. Chun Zhao (PNNL), and Project PIs Prof. V. Ramanathan (UCSD), Prof. K. Prather (UCSD), Prof. T. Kirchstetter (LBL), and Dr. R. Leung (PNNL).

TABLE OF CONTENTS

LIST OF TABLES

LIST OF FIGURES

Figure 3.6 Annual cycles of BC concentrations by decade in California and New Jersey between 1960 and 2000.

Figure 3.7 Annual cycles of carbon monoxide emissions measured in several cities and modeled by Glen et al. (1996).

Figure 3.8 Weekly cycle of BC concentration by decade in California and New Jersey from 1960-2000.

Figure 3.9 Weekly cycle of BC concentration by decade in California air basins.

Figure 3.10 Distillate fuel oil consumption in California by sector, illustrating the portion of transportation distillate that is taxable (i.e., on-road) diesel.

Figure 3.11 Consumption of fossil fuel and biomass fuels in California. Note that energy consumption is plotted on a logarithmic scale.

Figure 3.12 Residual fuel oil consumption in California by sector.

Figure 4.1 Annual means of measured Black Carbon and BC fossil fuel emissions in California from 1985 to 2008 for the entire state, and by region in Southern (South of 35 N), Northern (North of 38 N), and Central California; and Annual means of measured Sulfate, Nitrate, and OC from IMPROVE network.

Figure 4.2 20-year average BC Concentration, rate of change of BC concentration, and rate of change of BC/non-BC aerosols from the IMPROVE network in California with measuring stations are indicated.

Figure 4.3 (Location of IMPROVE sampling stations in continuous operation from 1988-2007 in California, with annual means of measured BC, and average annual rate of change in mean BC concentration for IMPROVE sites with greater than 75% coverage in each time period.

Figure 4.4 Time series of measured BC/non-BC Aerosol ratio from the IMPROVE network in California and derived co-Single Scattering Albedo for visible light calculated using fixed absorption cross sections of 10.1 x 10^{-6} m^2 mg^{-1} and 7.5 x10^{-6} m^2 mg^{-1}.

Figure 4.5 Monthly averaged SSA calculated from measurements and retrieved from the AERONET network in California from 1988-2010.

Figure 4.6 Annual mean measurements from the South Lake Tahoe (SOLA) station in California for (a) OC and EC absolute concentrations and (b) EC/OC and K/EC ratios.

Figure 4.7 Annual mean measurements of EC from the IMPROVE and EPA-STN networks in California that represents non-urban and urban measurements respectively.

Figure 5.1 Normalized frequency distributions for the Scattering Angstrom Exponent (440-675 nm), Absorption Angstrom Exponent (440-675 nm), Absorption Angstrom Exponent (675-870 nm), and AAE2/AAE1 ratio measured at DU, BB, UF, and NF AERONET sites.

Figure 5.2 Scatter plots of AAE1 and EAE1 calculated from AERONET measurements at (a) DU, (b) BB, (c) UF, (d) NF, and (e) CA sites.

Figure 5.3 Mean value of AAE1 determined by averaging the frequency distribution for selected AERONET sites.

Figure 5.4 Normalized frequency distribution of the OC absorption Angstrom exponent determined from BB, CA, NF, and UF sites between 440 and 675 nm.

Figure 5.5 Calculated SSA value at 675 nm for EC, OC, and Dust using AERONET stations segregated into source regions.

Figure 5.6 The calculated AAE1 for the total aerosol as a function of AOD at 440 nm and 675 nm, and the measured SSA at 440 nm and 675 nm from selected AERONET site.

Figure 5.7 Calculated AAE1 for the total aerosol as a function of AOD at 440 nm, and measured SSA at 440 nm from selected AERONET sites.

Figure 5.8 Species resolved AOD, AAOD, and emissions in California for EC, OC, and dust. Also illustrated is the wavelength dependent relative absorption of OC and EC.

Figure 5.9 Fraction of AAOD in CA attributed to dust, OC, and EC at 440 nm as a function of AAE and EAE/SAE

Figure 5.10 Comparison of AAOD from CA sites directly measured from AERONET and reconstructed from equation 5.4 at 440 nm, 675 nm, and 870 nm

Figure 6.1 Division of the Absorption Ångström Exponent vs. Scattering Ångström Exponent space, the Ångström matrix, overlapped with the AERONET measurements from stations with a dominant species (fossil fuel, biomass burning or dust).

Figure 6.2 Location of flight paths of the aircraft campaigns and the AERONET stations used for relating absorbing aerosols to emission sources.

Figure 6.3 Estimated contribution to light absorption derived from AERONET stations in California separated by region and season: (Northern vs. Southern California and winter/spring vs. summer/autumn).

Figure 6.4 Representative ATOFMS spectra for different aerosol sources including primary fossil fuel, secondary fossil fuel, primary biomass burning, secondary biomass burning, and dust.

Figure 6.5 Overall chemical composition detected with the ATOFMS in the three aircraft campaigns conducted in California: CalNex, CARES, and CalWater.

Figure 6.6 Absorption Ångström Exponent vs. Scattering Ångström Exponent scatter plot of in situ aircraft measurements in California; the color code represents the dominant aerosol source detected with the ATOFMS for each measurement. Also shown is a frequency histogram of the Absorption Ångström Exponent for each aerosol source.

Figure 7.1 Estimated contributions of black and organic carbon to the spectral attenuation of a residential wood smoke particulate matter sample.

Figure 7.2 Histograms of absorption Ångström exponents computed over the 360 to 700 nm spectral range.

Figure 7.3. Fraction of solar radiation absorbed by organic carbon rather than black carbon in residential wood smoke particulate matter.

Figure 8.1 Operational AERONET sites in California and neighboring states, indicating availability of valid quality assured measurements.

Figure 8.2 Average MISR satellite retrievals of the total AOD, total AAOD, EC AOD, and EC AAOD for the months of June-August in the California domain.

Figure 8.3 Seasonally averaged values of the SSA from GOCART and AERONET at 440 nm, 670 nm, and 870 nm. The wavelength dependence of all available SSA measurements is also illustrated.

Figure 8.4 Relative contributions to the AAOD (550 nm) from dust and carbonaceous aerosols calculated using MISR AOD and SSA_AERONET, MISR AOD and SSA_GOCART, and GOCART simulations

Figure 8.5 Relative contributions to the AAOD (550 nm) from EC and OC calculated using MISR AOD and SSA_AERONET, MISR AOD and SSA_GOCART, and GOCART simulations

Figure 8.6 Comparison of simulated AOD and AAOD for carbonaceous aerosols from the GOCART and WRF models with the observationally constrained approach followed in this study.

Figure 8.7 Seasonally and spatially resolved vertical profiles of aerosols in California constructed from CALIPSO satellite retrievals. Aerosol extinction is directly correlated to aerosol mass loading.

Figure 8.8 Atmospheric heating due to carbonaceous aerosols (EC+OC) in California calculated using observationally constrained data, GOCART simulations, and WRF simulations.

Figure 8.9 Radiative forcing at the (a) Top-of-Atmosphere (TOA), (b) in the Atmosphere (atm), and (c) at the surface (sfc) attributable to dust and carbonaceous aerosols in California determined using observationally constrained aerosol properties.

Figure 8.10 Top of the Atmosphere forcing for EC and Carbonaceous aerosols determined in the bounding cases using SSA_AERONET and SSA_GOCART in California.

Figure 8.11 Change in the radiative forcing due to carbonaceous aerosols as a consequence of a 50% reduction in EC aerosol loading in California between 1980-2000.

Figure 9.1 Location of sites in the CIMIS network in California that provide solar flux data in the decades between 1980-2010.

Figure 9.2 Monthly averages of surface solar flux in California obtained from the CIMIS network. A large summer-winter variability is observed.

Figure 9.3 Diurnal variations in surface flux measured at the Davis station in (a) June and (b) December. Large deviations from the upper envelope indicate the influence of clouds.

Figure 9.4 Histogram of surface flux measurements at the (a-b) Davis and (c-d) Riverside stations in (a,c) June and (b,d) December. The second (higher) mode represents clear-sky flux.

Figure 9.5 Trends in the clear-sky daytime surface flux measured by the CIMIS network for (a,c) summer months and (b,d) winter months, in (a-b) Northern and (c-d) Southern California.

Figure 9.6 Time-space average diurnal-seasonal average summer time-series for Southern California for all-sky (a) and clear-sky fluxes (b).

Figure 9.7 Time series of measured (a) AOD and (b) AAOD at 675 nm from the AERONET network in California. Bars represent the standard deviation of the daily variability in the annual mean values.

Figure 12.1 Seasonal mean mass concentrations of speciated $PM_{2.5}$ such as EC, OM, dust, sulfate, nitrate, ammonium, sea salt, and unspeciated $PM_{2.5}$ from IMPROVE and EPA measurements and the corresponding WRF-Chem simulations over California in 2005. The right-bottom panel shows the results from WRF-Chem sensitivity simulation with anthropogenic EC emissions doubled.

Figure 12.2 Spatial distributions of seasonal mean 550 nm AOD and AAOD from the WRF-Chem simulations with anthropogenic EC emissions doubled over California in 2005. The numbers represent the four AERONET sites: 1-Trinidad Head; 2-Fresno; 3-UCSB; 4-Tonopah Airport.

Figure 12.3 Seasonal variations of total 550 nm AOD and AAOD and their contributions from sulfate, OM, EC, dust, and other species from the WRF-Chem simulations with anthropogenic EC emission doubled. Other species include nitrate, ammonium, sea salt, and unspeciated $PM_{2.5}$.

Figure 12.4 Spatial distributions of seasonal mean aerosol direct radiative forcing at the top of atmosphere (TOA), in the atmosphere (ATM), and at the surface (BOT) from the WRF-Chem simulations with anthropogenic EC emissions doubled over California in 2005. At TOA and BOT, positive value represents downward radiation; in ATM, positive value represents warming.

Figure 12.5 Seasonal variations of aerosol direct radiative forcing and its contributions from sulfate, OM, EC, dust, and other species at the TOA, in the atmosphere, and at the surface from the WRF-Chem simulations with anthropogenic EC emission doubled.

Figure 12.6 WRF surface temperature compared to CIMAS measurements for summer and winter seasons.

Figure 12.7 WRF precipitation compared to CIMAS measurements for summer and winter seasons.

Figure 12.8 Comparison of WRF-Chem-predicted surface concentrations of EC with measured EC concentrations from IMPROVE and EPA networks for summer and winter.

Figure 12.9 Comparison of WRF-Chem-predicted surface concentrations of PM2.5 with measured PM2.5 concentrations from IMPROVE and EPA networks for summer and winter.

Figure 12.10 Modeled SW surface flux vs. the off-line, calculated SW surface flux.

Figure 12.11 Contribution of BC to total atmospheric heating due to aerosol absorption as a function of altitude.

Figure 13.1 Changes in all-sky net solar radiation at the surface (in W m^{-2}) comparing simulations for the 2000s (2xEC) to the 1960s (10xEC).

Figure 13.2 Left: Changes in diabatic heating comparing the simulation for the 2000s with the 1960s (in K/day). Right: Similar to the left but for changes in atmospheric temperature (^{o}C).

Figure 13.3 Changes in 2-meter surface temperature comparing the 2000s to the 1960s in ^{o}C.

Figure 13.4 Comparison of observed (solid) and simulated (dashed) temperature profiles averaged over three sounding locations in CA (OAK, VGB, NKX) for four seasons for 2005.

Figure 13.5 (a) Percent reduction in BC concentration as a result of cutting BC emissions in half, and (b) the associated change in atmospheric heating as a function of altitude.

Figure 13.6 The change in cloud optical thickness in (a) Summer and (b) Winter as a result of reducing baseline BC emissions by half.

LIST OF ACRONYMS

ARCTAS	Arctic Research of the Composition of the Troposphere from Aircraft and Satellites
A-ATOFMS	Aircraft ATOFMS
ATOFMS	Aerosol Time of Flight Mass Spectrometry
AAE	Absorption Angstrom Exponent
AAOD	Absorption Aerosol Optical Depth
AERONET	Aerosol Robotic Network
AOD	Aerosol Optical Depth
AQMD	Air Quality Management District
Atm	Atmospheric Heating
ATN	Light Attenuation
BB	Biomass Burning sites
BC	Black Carbon
BrC	Brown Carbon (Absorbing Fraction of OC)
CARB	California Air Resources Board
CARES	Carbonaceous Aerosols and Radiative Effects Study
CERES	Clouds and the Earths Radiative Energy System
CFORS	Chemical Weather Forecast System
CIMIS	California Irrigation Management Information System
COH	Coefficient of Haze
DPF	Diesel Particulate Filter
DU	Dust dominated AERONET sites
EAE	Extinction Angstrom Exponent
EC	Elemental Carbon
EGA	Evolved Gas Analysis
EI_BU	Emission Inventory based, Bottom-Up approach
EPA-STN	Environmental Protection Agency-Speciated Trends Network
GCM	General Circulation Model
GOCART	Goddard Chemistry, Aerosol, Radiation, and Transport model
GWP	Global Warming Potential
IMPROVE	Interagency Monitoring of Protected Visual Environments
LBL	Lawrence Berkeley Laboratories
MACR	Monte Carlo Cloud Radiation model
MISR	Multi-angle Imaging Spectro Radiometer
MODIS	Moderate Resolution Imaging Spectroradiometer

NCA	Northern California
NF	Non-Urban Fossil fuel dominated sites
OC	Organic Carbon
OC_TD	Observationally Constrained, Top-Down approach
OM	Organic Matter
PM	Particulate Matter
PNNL	Pacific Northwest National Laboratories
PST	Pacific Standard Time
SAE	Scattering Angstrom Exponent
SCA	Southern California
SeaWIFS	Sea Viewing Wide Field of View Sensor
Sfc	Surface Forcing
SSA	Single Scattering Albedo
TOA	Top Of Atmosphere
UF	Urban Fossil fuel dominated sites
VOC	Volatile Organic Compounds
WRF-Chem	Weather Research and Forecasting model with Chemistry

ABSTRACT

This report provides an assessment of the impact of black carbon on the regional radiative forcing and climate trends of California. The present regional integrated assessment is the first such attempt to estimate the radiative forcing of BC for one region (California in this case), both from a bottom-up approach (starting with emission inventory as input to aerosol-transport models) and a top-down approach (adopting satellite data in conjunction with ground based column averaged aerosol optical properties). This approach enabled us to uncover three unanticipated major findings: i) The first finding concerns the large decadal trends in BC concentrations largely in response to policies enacted to decrease PM emissions from diesel combustion. ii) The second is the discovery of the large effects of brown carbon (a form of organic carbon aerosols) on radiative forcing. iii) The third is the large discrepancy between the top-down and the bottom-up approach of estimating radiative forcing and ways to close the gap.

Observed multi-decadal BC trends: The trends in BC concentrations were determined from assimilation of mass-based measurements (from the IMPROVE network that typically samples remote areas), and from analysis of the large set of available COH (Coefficient of Haze) measurements (which typically sample urban areas). The more reliable IMPROVE data showed that the annual average BC concentrations in California have decreased by about 50% from 0.46 μg m^{-3} in 1989 to 0.24 μg m^{-3} in 2008. The COH data revealed that BC concentrations in California decreased markedly from about 3.9 μg m^{-3} in 1966 to 2.3 μg m^{-3} in 1980 to 1.1 μg m^{-3} in 2000, agreeing with the trends reported from the IMPROVE data sets. Trends in other co-emitted aerosols such as OC, sulfates were much smaller or statistically insignificant. BC trends are related to an order of magnitude reduction in diesel PM emissions since the first smoke reduction standards were introduced in the 1970s. Other determining factors likely include BC emissions reduction from other sources in the transport sector, the cleanup of BC emissions in the industrial sector, and decreasing wood and waste burning since 1990. *Observations of large negative trends in BC and the lack of corresponding negative trends in co-emitted OC and sulfate aerosols gives compelling observational evidence for the model based hypothesis (e.g, Jacobson, 2010; Bond et al, 2013) that mitigation of diesel BC would mitigate global warming.*

Importance of Brown Carbon for Solar absorption: Analysis of the spectral dependence of solar absorption, measured in-situ as well as over the column, indicates an enhanced absorption at shorter (<500 nm) wavelengths that deviates from the expected behavior of BC. This enhanced absorption is attributed to organic, “brown”, carbon. The solar absorption due to brown carbon is found to contribute as much as 40% of the BC forcing in the near-UV (<440 nm) wavelengths. Field measurements in several independent campaigns using aethalometers for absorption, and the ATOFMS for detailed chemical analysis find that brown carbon is primarily related to residential wood burning. However,

a new class of particles related to secondary organics, i. e., aged large organic particles, is also found to contribute to solar absorption, thus raising the possibility that fossil fuels also contribute – via their contribution to secondary organic particles – to brown carbon absorption. *We find that the direct warming effect of brown carbon, ignored in most models, offsets about 60% to 90% of the direct cooling effects of other organic carbon aerosols.*

Direct Radiative Forcing Over California: We determine the radiative forcing using a top-down approach developed by the PI's (VR) group that relies on NASA's ground based AERONET data and assimilated satellite measurements (MISR) of aerosol optical properties. This observationally constrained top-down (OC_TD) estimate includes solar absorption by brown carbon while the emission inventory based bottom-up (EI_BU) estimates included in this study do not account for brown carbon. The uncertainty in the OC_TD forcing is about ±40%. For the annual mean, the current top-of-atmosphere (TOA) forcing of BC+OC varies from about 0.2 Wm^{-2} over Northern California (NCA) to as large as 1.9 Wm^{-2} over Southern California (SCA). The implication is, in the 1980s when BC concentrations were higher by about 100%, the TOA forcing for BC+OC could have been as large as 0.4 to 3.8 Wm^{-2}. *Overall we conclude that the large negative trend in BC radiative forcing and the lack of corresponding negative trends in OC, confirms the assessment of some other studies [Bond et al., 2013; Jacobson, 2010a] that diesel related BC emission reduction would lead to global cooling.*

Regional Climate Effects: The regional climate changes associated with the observed reduction in BC concentrations were estimated with a regional climate model. *The declining trends in BC (by a factor of five to approximate the 1960s) cause a reduction in the TOA direct radiative forcing everywhere and the cooling effect ranges from -0.5 to -3.5 Wm^{-2}, consistent with the OC_TD estimates, with larger effects during summer than winter.* In response to this change, the lower atmosphere is found to cool everywhere, accompanied by a smaller warming near the surface, which is not statistically significant in any season. Overall, the local climate effects are small.

Primary Finding: Mitigation of Global Warming

Reductions in emissions of BC, mostly from diesel engines, since the 1980s have led to a measurable mitigation of anthropogenic global warming, equivalent to the mitigation of 21 million metric tons of CO_2 emissions annually. This climate benefit may date back to at least the 1960s, and is currently ongoing.

Because of the long lifetime of CO_2 (one century or longer) compared with the much shorter lifetime of BC (about one week), mitigation of CO_2 is critical for limiting long term (>50 years) global warming, while mitigation of BC is critical for limiting warming projected for the coming decades.

EXECUTIVE SUMMARY

OVERALL FINDING

BC emission reductions since the 1980s, attributed in large part to diesel engine emissions mitigation, are equivalent to *reducing CO_2 emissions by 21 million metric tons annually. This is approximately equal to 5 % of the total direct CO_2 annual emissions of 393 million metric tons.*

As on-road diesel is very low in sulfur in developed regions and lowering elsewhere, and since compared to other major BC sources, diesel PM has more BC and less OC, it follows that controlling diesel BC would have a cooling effect. The control of BC from diesel therefore is an effective means of mitigating near-term global climate change. This observationally based conclusion is consistent with recent modeling studies [e.g. Jacobson, 2010; *Bond et al.*, 2013], which suggested that reduction of BC from diesel sources would lead to global cooling. However, we would like to caution that, without simultaneous reduction of CO_2 emissions, it will not be possible to limit future warming to below 2^0C as required by the Copenhagen accord.

Background

Black Carbon (BC): Soot contains black carbon and organic carbon aerosols, which absorb and scatter solar radiation and thus impacts the climate system from local to regional and global scales. The component of soot that absorbs solar radiation is usually referred to as black carbon (BC) or elemental carbon (EC). The two terms, BC and EC, are used interchangeably and we follow the same practice in this report. BC or EC is simply a functional definition that depends on the measurement technique. In principle, the relatively strong light absorption properties of BC can be used to infer BC from an optical measurement and knowledge of the mass specific absorption of BC. In thermal methods, the filter media used for sample collection is heated and the thermally evolved carbon in the specified temperature plateau and analysis atmosphere defines the concentration of EC and organic carbon (OC).

Brown Carbon (BrC): Organic carbon is normally assumed to be a pure scattering aerosol. However, recent experimental studies have demonstrated that a fraction of OC also absorbs sunlight with their absorption increasing dramatically towards shorter wavelengths (<500 nm wavelengths). The absorbing part of OC referred to as brown carbon. In this report, the term OC includes BrC.

Radiative Forcing: The net effect of absorption and scattering of solar radiation by, BC and OC, is to alter the solar radiation absorbed by the surface and the atmosphere, which is the fundamental driver of the global climate system. The

change in the radiative heating of the climate system is referred to as the 'Radiative Forcing" [see the primer on radiative forcing later in the summary]. The change in the forcing due to scattering and absorption of solar radiation is referred to as 'Direct Forcing". But the addition of BC and OC aerosols as well as the alteration of solar heating by BC and OC alters the cloud fraction and cloud properties, which in turn alters the radiative forcing since clouds are the largest modulators of solar radiation. These cloud induced radiative forcings are referred to as indirect and semi-direct forcings [see the primer]. These changes to the solar radiative forcing [units of W m^{-2}] are the primary metric used to assess the importance of BC and OC on climate.

Motivation [BC is the second Largest Contributor to Global Warming]: Black carbon (BC), the main light-absorbing component of soot is the principal absorber of visible solar radiation in the atmosphere. *Jacobson, [2001]* and *Ramanathan and Carmichael* [2008] concluded that BC is the second largest contributor to global warming, next to CO_2. For present day BC, due to both natural and anthropogenic sources, Ramanathan and Carmichael estimated a direct forcing of 0.9 Wm^{-2} [0.45 to 1.35 Wm^{-2}] compared to 1.6 W m^{-2} for CO_2 [*Forster et al.*, 2007] - this conclusion was debated because most estimates of forcing from models were a factor of two to three lower. A major landmark study of the BC forcing problem was published this year [*Bond et al.*, 2013] by a group of researchers that included many modeling groups, and their estimate of 0.88 Wm^{-2} for the BC direct forcing (due to all BC sources) is nearly identical to Ramanathan and Carmichael's estimate of 0.9 W m^{-2}. Because of its short life times of few weeks, BC is concentrated close to the sources and hence a regional evaluation is critical for a better understanding of the global effects. Furthermore, California has witnessed major decreases in its BC concentrations and we need to understand the impact of these regional trends in climate.

The unique integrated approach

We have developed a balanced approach between observations, data analyses, and modeling studies, allowing us to uniquely constrain the estimates provided in this study using measurements conducted by ground based network, aircraft and satellite instruments. The study consisted of four primary components (i) analysis of available measurements, and documentation of multi-decadal BC trends constrained by field measurements, (ii) estimation of the direct aerosol forcing due to black and brown carbon using integrated observations as well as models, (iii) Source apportionment based upon chemical mixing state, and (iv) estimating the climate impact of BC emissions under various mitigation scenarios. The full climate impact of BC on the regional climate of California is evaluated by using regional climate models in a series of numerical experiments with varying BC emissions to determine changes in the surface temperature and hydrology. The regional climate models used to evaluate the climatic impacts of BC are also used in step (ii) to estimate the BC forcing, so their uncertainty can be assessed by comparing their estimated BC forcing with the observation based estimates. Statewide temporal and spatial resolved BC concentrations have been derived

by analyzing the coefficient of haze [COH] (directly correlated to the BC) recorded at 100 locations throughout California (data available from CARB). A key component of this work involves determining the actual single particle mixing state of soot particles in California. These measurements allow us to proceed without making major assumptions regarding the size, mixing state, and optical properties of ambient soot particles that have resulted in tremendously large uncertainties in prior studies.

Principal Findings

I. *BC concentration results*

We examine the temporal and the spatial trends in the concentrations of black carbon (BC) using filter based mass measurements recorded by the IMPROVE monitoring network, and optical measurements reconstructed from the available Coefficient of Haze (COH) records in California.

1. *Annual average BC concentrations measured at California IMPROVE sites have decreased by about 50% from 0.46 µg m^{-3} in 1989 to 0.24 µg m^{-3} in 2008 compared to a corresponding reductions in diesel BC emissions (also about 50%) from a peak of 0.013 Tg Yr^{-1} in 1990 to 0.006 Tg Yr^{-1} by 2008 (Figure 2(a)).*

2. *A larger set of COH measurements is also used to determine BC concentrations and reveals that these trends are uniform across the state and persistent in several major air basins (Figure 2(b))*.

The consistency between the IMPROVE and COH trends is important since the COH data are largely from urban sites whereas IMPROVE is from remote sites.

3. *A corresponding trend in co-pollutants such as nitrates, sulfates, and organic carbon is not observed (Figure 2(a)).*

This finding is crucial, since the co-pollutants are largely cooling aerosols, through their direct and indirect effects on clouds. Since they are not showing negative trends, it implies that the decrease in BC will most likely lead to a global cooling effect from California's BC reductions.

4. *As no similar trends are observed in other chemical source tracers (such as K, for biomass burning), we therefore attribute the observed BC trends primarily to the emission reduction from transport-related PM emissions, primarily from diesel.*

A detailed analysis of technology based emission inventories and fuel use in California indicates that although the total consumption in diesel fuel has increased, the emissions of BC from diesel fuel combustion have decreased

significantly. The reduction in emissions is due to a number of factors, including the introduction of low sulfur fuel, tighter emission standards, cleaner burning engines, and other improvements in technology mandated by statewide regulations. California therefore appears as a success story in mitigating the anthropogenic impact on climate. While, decreasing trends in BC have been noted in other states (of US), we are unable to comment on their climate mitigation efficacy since data on other co-pollutants have not been analyzed in published literature.

5. *Our conclusion that the reduction in diesel emissions is the primary cause of the observed BC reduction is also substantiated by a significant decrease in the ratio of BC to non-BC aerosols.*

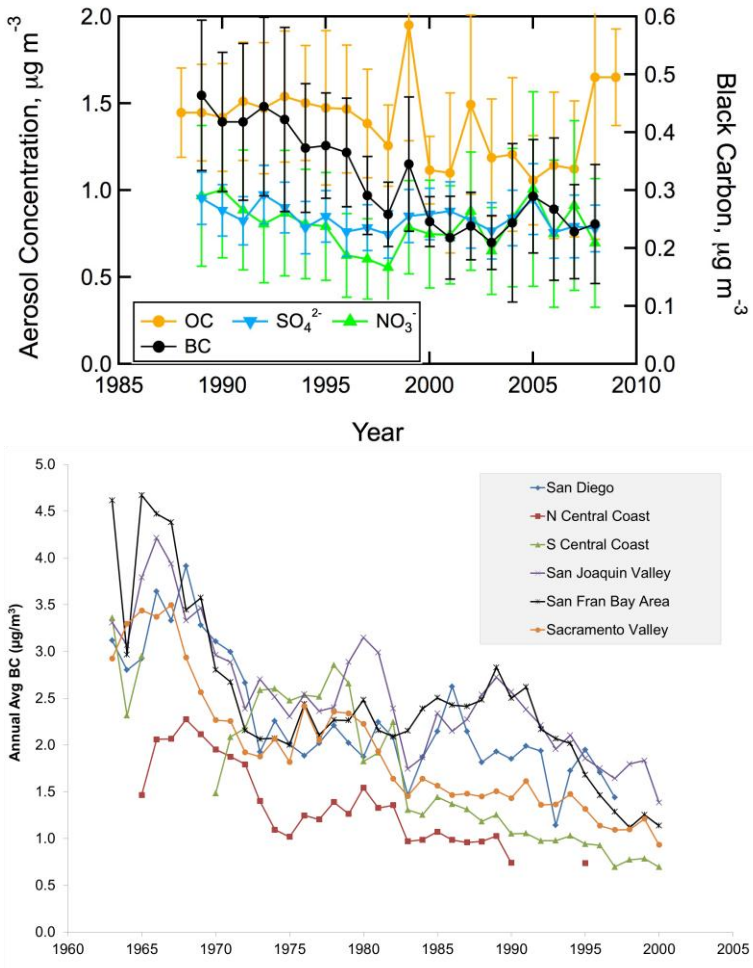

Figure 0.1 (a) Statewide trends in concentrations of common aerosol species from the IMPROVE network, and (b) historical BC concentrations resolved by air basin. A clear reduction in BC is observed.

II. *Role of brown carbon absorption*

We have developed an observationally based analytical method for rigorously partitioning measured aerosol absorption optical depths (AAOD) and single scattering albedo (SSA) among EC and BrC using multi wavelength measurements of total (EC, OC and Dust) absorption.

1. *We have quantified column-integrated absorption in multiple wavelengths by brown carbon from observations for the first time.*

The new method we developed separates dust, BC and BrC absorption from spectral solar observations. It can now be applied to other regions of the world.

2. *Organic carbon (OC) is shown to absorb strongly at visible to UV wavelengths, an effect typically not represented in climate models. The BrC absorption at 440 nm is about 40% of the EC, while at 675 nm it is less than 10% of EC (Figure 2).*

We find an enhanced absorption due to BrC in the summer months, and in South California (related to forest fires and secondary OC). The contribution of BrC to the total aerosol absorption is largest over northern and central California.

3. *BrC emissions are likely both from biomass burning (forest fires and residential wood burning) as previously thought, and also from large aged particles indicating that secondary organics may also be absorbing.*

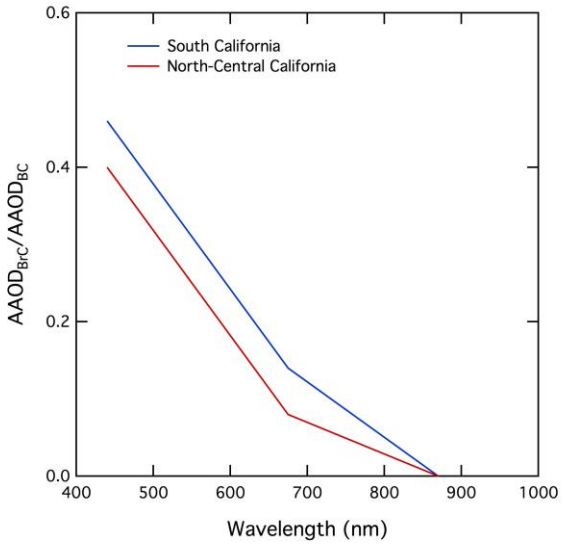

Figure 0.2 Wavelength dependent relative Absorption Aerosol Optical Depths (AAODs) for BC and BrC determined from ground-based estimates of the SSA and AOD in California.

III. *Source attribution and speciation*

1. *Major differences exist in the PM sources in northern and southern California. In-situ measurements of optical properties and chemical mixing state reveal fossil fuel sources contribute the most strongly in southern California, whereas biomass burning and biogenic sources dominate in northern California. This has been shown in other recent studies as well (Cahill et al. 2012).*

2. *Using optical properties for estimating aerosol speciation using satellites or networks such as AERONET has the potential to provide extensive input into global climate and air pollution studies. This study demonstrates that the interpretation of the AERONET results is strengthened by complementary measurements of aerosol sources.*

Speciation of dust, BC and BrC are well classified by optical data, but the separation between fossil fuel and biomass burning sources has limitations because of their overlapping optical properties.

3. *Despite these limitations, detailed comparison reveals the significance of aerosol absorption due to secondary organic aerosol (OC) which is currently underestimated in climate models, in addition to black carbon. Brown carbon and secondary sources impact many absorption events, indicating these processes must be given consideration when developing future climate mitigation policies.*

IV. Radiative forcing results: Present day values

Radiative Forcing: A Primer

Direct Radiative Forcing: BC and OC increase the amount of solar radiation absorbed by the atmosphere, by intercepting the direct incoming solar radiation and also by intercepting the solar radiation reflected by the surface, the atmosphere and the clouds. The interception of solar radiation also leads to a decrease in solar radiation absorbed at the surface (dimming). The alteration of the solar absorption of the surface and the atmosphere by BC and OC is referred to as *direct radiative forcing*. The net effect is the sum of the atmospheric heating and the surface dimming and is referred to as the top-of-the atmosphere (TOA) forcing. The TOA forcing is the most relevant quantity for assessing the significance of California's BC policy actions for mitigating global warming. However, for assessing the impacts on California's regional climate, we have to examine the impact of EC and OC on atmospheric solar heating (atmospheric forcing) and surface solar dimming (surface forcing).

Indirect and semi-direct Radiative Forcing: BC and OC also influence cloud formation. They nucleate cloud drops that increase the number of cloud drops and also increase cloud fraction, both of which enhance the cloudy-sky albedo and lead to cooling. This is the indirect effect of BC and OC. On the other hand, the solar heating of the atmosphere by BC and BrC leads to burn-off of clouds. In addition, inclusion of BC in cloud drops also enhances solar absorption by the drops. This cloud-inclusion effect also enhances cloud burn-off. The burn-off in turn decreases the cloudy-sky albedo and thus provides an offset to the cooling effect of the indirect effect.

The annual average direct radiative forcing associated with BC+OC from the observationally constrained Top-Down (OC_TD) approach, initialized with two assimilated data sets is summarized in Table 0.1. The total aerosol optical depth (AOD) is retrieved from the MISR satellite whereas the single scattering albedo (SSA) is based upon observations from the AERONET network, and from the GOCART climate model. The two different values of SSA allow us to estimate the upper and lower limits for the BC and BrC (details in Chapter 9). However, our baseline estimate is that given by the version of OC_TD with SSA from AERONET. Table 0.1 also shows simulated forcing by the emission-inventory based bottom up (EI_BU) WRF-Chem models. PNNL and LBL refer to the two modeling groups participating in our study.

1. *Direct Radiative Forcing by BC+OC is positive everywhere in California. It ranges from 0.2 Wm^{-2} in northern California to 0.88 Wm^{-2} over S. California.*

2. *The annual average BC+OC direct forcing for California estimated using the WRF-Chem regional climate model (with the published emission inventory) is 0.16 W m^{-2}, compared to 0.51 W m^{-2} (±40%) from the observationally constrained estimate. Thus, even regional models with region specific emissions; severely underestimate the BC+OC warming effects by a factor of three.*

The WRF-Chem model also underestimates surface BC concentrations by a factor of two. We show the forcing with BC emissions increased by a factor of 2 (4^{th} column) that reduce this discrepancy, but the model forcing of 0.29 W m^{-2} is still much lower than the OC_TD approach. Some of the remaining discrepancy can be further explained due to the neglect of BrC absorption in the regional models.

3. *The underestimation (by a factor of three) is consistent with Bond et al. [2013]'s conclusion that models underestimate absorption by BC by a factor of three on a global mean basis.*

4. *The BrC absorption has a major impact on the direct forcing due to OC aerosols. Without BrC absorption, models estimate direct forcing due to OC to be between -0.30 and -0.15 W m^{-2} depending on the location and region, whereas inclusion of BrC brings the net cooling down to between 0.00 and -0.10 W m^{-2}. Thus models that neglect BrC severely overestimate the OC cooling effects.*

Table 0.2 presents a comparison in the atmospheric heating rates from the observationally constrained calculations, and the WRF-Chem regional model operating in two independent configurations. All three calculations produce similar trends in the magnitude of the forcing. This agreement obtained from three independent calculations indicates the robustness and significance of the results.

5. *The atmospheric heating, or energy added to the atmosphere, is a factor of four to eight larger than the TOA forcing (Table 0.2).*

Carbonaceous aerosols are found to be warming in all regions and seasons with a magnitude ranging between 0.5 and 3.5 W m^{-2}. The greatest warming is observed in Southern California (which typically has a higher anthropogenic aerosol concentration and lower cloud cover), and also in the summer (possibly due to a higher net solar flux).

	Observationally Constrained Top-Down (OC_TD)		Emission Inventory Based Bottom-Up (EI_BU)	
	SSA from AERONET	SSA from GOCART	WRF_PNNL (1*BC)	WRF_PNNL (2*BC)
TOA forcing				
North	0.20	0.28	0.09	0.16
Central	0.44	0.48	0.17	0.32
South	0.88	1.92	0.21	0.40
State	0.51	0.89	0.16	0.29
Atmospheric heating, W m^{-2}				
North	1.73	1.79	0.60	0.82
Central	2.40	2.78	0.86	1.25
South	2.44	4.05	0.96	1.41
State	2.19	2.87	0.81	1.16
Surface forcing, W m^{-2}				
North	-1.54	-1.47	-0.51	-0.65
Central	-1.94	-2.38	-0.68	-0.92
South	-1.62	-2.47	-0.75	-1.01
State	-1.70	-2.11	-0.65	-0.86

Table 0.1 Annual average radiative forcing attributed to BC+OC at the top of the atmosphere, atmospheric heating, and at the surface determined using the observationally constrained MACR model and the WRF-Chem climate model simulations based on emission inventories.

V. Surface brightening:

Radiative calculations also estimate that the 50% decrease in BC concentration from the 1980s to current levels should have led to an increase in the surface solar radiation (surface brightening) between 1.5-3.5 W.m^{-2}.

We looked for this brightening effect in a network of surface solar radiometers operated by California's CIMIS network since 1982. The inter-annual variability was much larger than the detected trend in solar flux measurements and when this is considered with the limited data duration of the measurements (about 25 years), we are led to the deduction that the detected trends during the 1980s to 1990s are not statistically significant to verify the predicted brightening trends due to decreasing BC concentrations.

VI. Implication to mitigation of global warming

1. *Our findings thus far suggest that policies enacted by California to reduce diesel emissions should have led to a measurable mitigation of the global warming associated with anthropogenic aerosols, equivalent to the elimination of 21 million metric tons of CO_2 annually.*

This conclusion is derived from the following observations and model simulations:

2. *The observed decrease in surface-BC by a factor of 2 from 1989 to 2008 and by a factor of 3.5 from 1960s to 2008.*

3. *This decrease was not accompanied by a comparable decrease in OC or other cooling aerosols such as sulfates.*

4. *As a result the decrease of BC was accompanied by a decrease in ratio of BC to Non-BC aerosols, which implies the warming aerosols decreased more in relation to cooling aerosols.*

5. *The observed BC decreases were largely attributed to the decrease in diesel emissions of BC.*

6. *Targeted emission controls adopted by the State of California are shown to be effective in reducing BC concentrations, by a factor of at least 2 dating back to the 1980s, and by as much as a factor of 3.5 dating back to the 1960s. At the regional level this decrease is associated with a TOA cooling of between 0.5 and 1.5 W m^{-2}.*

7. *The indirect and semi-direct forcing changes due to the observed decrease in BC is expected to be much smaller than the direct forcing changes given above, due to the following two reasons: The negative indirect forcing is large*

mainly for OC and we did not observed statistically significant changes in OC concentrations (as expected for diesel related BC changes); As estimated by UNEP(2011) and Bond et al (2013), the sum of the indirect effect and the semi-direct effect is nearly zero for BC.

The above finding, while it is the most important scientific aspect of our results, needs to be validated by doing similar analyses for other states of US that have experienced strong reductions in BC.

In order to estimate the global warming mitigation from this diesel related BC forcing decrease, we need to account for not only the direct radiative forcing due to BC but also the following: Brown Carbon absorption; indirect effects of BC and OC; cloud-inclusion effects of BC and BrC; semi-direct effects of BC and BrC. We are aware of only one such modeling study by *Jacobson* [2010] that has explicitly estimated the global warming potential of fossil fuel BC. Furthermore, Jacobson's direct forcing estimate is consistent with our OC_TD estimates. As a result, we rely on Jacobson's 100 Year-GWP, which for fossil BC is 3000 (using his lower range).

8. We estimate that reduction of BC emissions primarily from diesel engines from 1989 to 2008 has mitigated global warming equivalent to reducing annual CO_2 emissions by 21 million metric tons/year. This corresponds to about 5% of California's 2009 CO_2 direct emissions of 393 metric tons.

VII. Validation and Improvement of regional climate model treatment of BC forcing

Our goal is to use Emission Inventory based bottom-up (EI_BU) regional models to understand the regional climate effects of BC mitigation measures. However, we must validate these models first. In this study, we use the WRF-Chem model in a variety of numerical experiments to estimate the seasonal scale changes in radiative forcing. Two configurations of the WRF-Chem model were used, the standard version 3.2.1, and one that includes more updated cloud microphysical and radiative transfer parameterizations [*Zhao et al.*, 2012].

1. *A comparison between the simulated BC concentration and measurements at over 30 sites in California revealed that WRF-Chem under-predicted BC by nearly a factor of two, which indicates that the emission inventory developed in the ARCTAS-CA campaign, may be under representing BC.*

The climate impact of BC was evaluated by changing the emissions by factors of 10x, 5x, and 2x. The 2x case approximates the conditions for the present day emissions; the 5x and the 10x cases approximate the emissions during the 1980s and the 1960s respectively.

2. *The simulated seasonal and regional variation in BC forcing is consistent with the patterns in OC_TD and furthermore, in agreement with OC_TD, the TOA forcing is positive everywhere. However, the direct forcing of (BC+OC) even with the 2x simulations is about 60% smaller than the OC_TD values.*

Table 0.2 compares the atmospheric heating calculated using both the observationally constrained and climate model approaches. Two sets of observationally constrained calculations were performed – in the first, OC was treated as a scattering species, and in the second, some of the OC was allowed to absorb light as well as the BC.

3. *The comparison indicates that about a third of this difference between the models and the observationally constrained approach is due to the fact that the models ignore BrC. With respect to the other 2/3, we must point out that the observational estimates have an uncertainty of ±40%.*

		Observationally Constrained BC Only	Observationally Constrained BC+OC	WRF-CHEM calculation using 2xBC emission: PNNL	WRF-CHEM calculation using 2xBC emission: LBL
Annual Average	North	1.36	1.54	0.82	0.99
	Central	2.10	2.26	1.25	1.31
	South	2.24	2.34	1.41	1.49
Spring Average	North	1.71	1.97	0.74	0.95
	Central	2.77	2.85	1.12	1.30
	South	2.41	2.43	1.37	1.55
Summer Average	North	1.95	2.21	1.35	1.85
	Central	3.17	3.49	2.04	2.14
	South	3.70	3.94	2.23	2.33
Fall Average	North	1.03	1.12	0.72	0.98
	Central	1.37	1.55	1.11	1.33
	South	1.95	2.09	1.25	1.48
Winter Average	North	0.75	0.85	0.45	0.45
	Central	1.08	1.15	0.70	0.64
	South	0.91	0.91	0.77	0.80

Table 0.2 Comparison of Atmospheric Heating Rates in Wm^{-2} in California attributed to carbonaceous aerosols, calculated using both an observationally constrained aerosol approach (for AOD and AAOD), and from the WRF-Chem model using a 2x scaled up BC emission inventory.

VIII. Regional climate impact results

To determine the climate impacts of BC, we performed two simulations, each covering 5 years for the 2005 - 2009 meteorological conditions. In one simulation, we used 2xBC to represent the conditions of the 2000s, and in the

other simulation, we used 10xBC to represent the conditions of the 1960s (with BC reduced by a factor of five to approximate the historical COH records). Following this decreasing trend, we expect the top of the atmosphere (TOA) to cool.

1. *Overall, comparing the 2000s to the 1960s we find that the TOA radiative forcing decreases by up to 3 W m^{-2} (Figure 4) with larger and statistically significant changes at 90% confidence level in the summer and fall and over the Central Valley and southern CA.*

The diabatic heating in the atmosphere is reduced by up to 0.06 K/day, and maximizes in the summer and at about 2 km above the surface. Reduction in BC leads to brightening at the surface as expected.

2. *Corresponding to the enhanced surface solar radiation, skin temperature increases while the TOA radiative cooling leads to a cooling of atmospheric temperatures, but the average temperature changes are small (<0.1 C) and are not statistically significant due to the large inter-annual variability.*

Winds at 10m generally become weaker over CA but stronger off shore in southern CA. Finally, changes in surface hydrology are small because the BC effects are generally small during winter, and BC is mostly concentrated in the Central Valley and southern CA, so its effects are negligible in the Sierra Nevada, which is where hydrology is most critical.

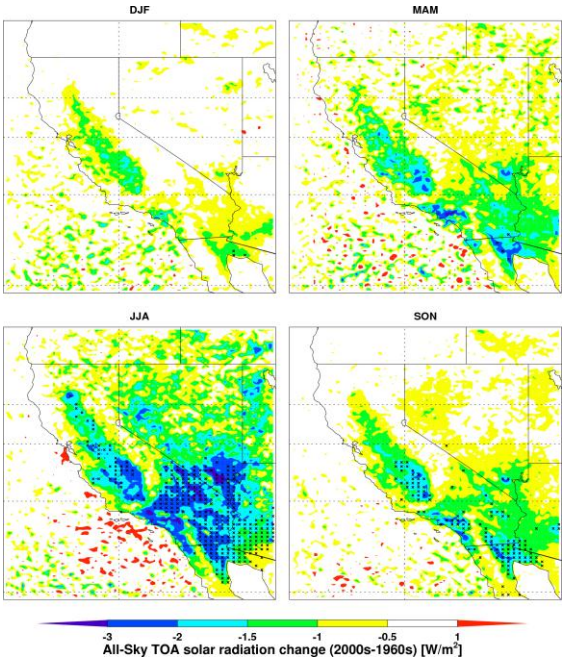

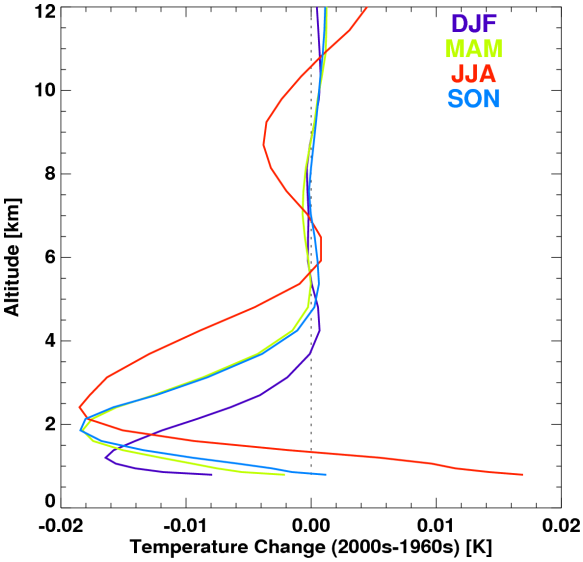

Figure 0.3 Changes in TOA solar radiation in the last 40 years attributed to BC decrease. Changes that are statistically significant at the 90% confidence level are stippled. The simulated atmospheric cooling and surface warming (only in summer) are shown on the right panel (not significant at the 90% level).

1. *Based on an assessment of regional climate models, the observed reduction of BC concentrations from the 1960s to 2000s produce a cooling of the lower atmosphere. This cooling of the atmosphere has been accompanied by an average decrease in surface temperatures; however, the small decrease (0.01 K) is not significant compared to the inter-annual variability.*

However, the larger scale and remote influence due to BC reduction over CA cannot be assessed in the regional modeling framework, which could also potentially affect the regional results over CA. In addition, the WRF-Chem model does not account for solar absorption by brown carbon. These uncertainties should be addressed in future studies.

Recommended future work

A more comprehensive understanding of the climate impacts of California's BC (+OC) mitigation on global and regional climate (including impacts on California's snow packs) processes requires further work along the following lines:

I. Global climate mitigation

1. *We need to estimate the magnitude and uncertainty associated with the regional indirect and semi-direct effects through the OC_TD approach to better constrain the models.*

While the scope of this work was limited to determining the impact of BC, we discovered that BrC is also a significant absorber of radiation, particularly at short wavelengths and may serve as an extra warming agent due to its typically higher concentrations. The BrC is particularly important for California since our data reveals that open biomass burning is a large source for BrC. This opens up a whole new avenue of research as unlike BC, the sources, chemistry, and optical properties of BrC are less well understood. In particular we need to understand the following physic-chemical-optical properties of BrC:

2. What is the relative role of primary aerosols from biomass burning and diesel sources to BrC?

3. What is the relative role of secondary organics from biomass burning and diesel sources to BrC?

4. What are the intrinsic properties of BrC such as: size distribution, the single scattering albedo, and the angstrom exponent of absorption coefficient and scattering coefficient of BrC?

5. How does BrC within cloud drops and as interstitial aerosols in clouds enhance radiative forcing?

We recommend extensive future work, including field studies, laboratory studies, and data assimilation and modeling studies to better understand BrC. Further, current climate models do not consider BrC absorption and treat OC as a cooling agent – while there still exists an uncertainty in the final sign of the net OC forcing we assert that climate models are overestimating its cooling impact.

In this report we presented several mitigation scenarios for BC that represent current and historical records of BC concentrations in California that are shown to be consistent with the control of diesel emissions. The mitigation scenarios considered in this study were constructed based on trends in California's aerosol concentrations. Although regional emissions are most important considering the short lifetime of BC, we did not consider variations in long-range transport (such as from Asia) in this study. Future studies should attempt to distinguish between transported and locally emitted BC.

II. Regional climate change

1. *Continuation of EC/BC monitoring networks. The major findings of this study were made possible by the excellent networks of surface BC and column averaged aerosol optical properties. Unlike the long-lived greenhouse gases, documenting the impacts of mitigating short lived climate warmers such as BC requires continuation of such local and regional networks.*

In the course of this study, we also discovered large uncertainties in existing data sets and resources that are currently used by climate scientists, such as in the solar flux measurements (Chapter 9) and the BC emission inventory (Chapter 11).

2. *We recommend a more complete analysis of these resources and possible studies to implement better quality control, and to reduce the associated uncertainty.*

3. *Reducing uncertainty in regional model forcing: As documented here the OC_TD and EI_BU estimates of the forcing differ by a factor of almost two. Model treatment of EC and BrC emission inventory, optical effects, long range transport of BC from outside California, and vertical profiles of BC in models and simulation of clouds have to be validated first to bring the two approaches closer*

For example, an earlier study by us [*Hadley et al.*, 2007] revealed that about 75% of BC above 2 km over California during spring time is transported from Eastern Asia.

4. *A more detailed assessment of regional affects: The current study does not allow for the interaction with the larger scale circulation. Imbedding the WRF-Chem in a global model is required to simulate the potential changes in large-scale circulation due to BC reductions in CA.*

5. *The model does not account for solar absorption of OC, so the climate influence may be underestimated. In addition, it has been shown in an earlier study [Hadley and Kirchstetter, 2012] that snowfall deposits about 90% of the BC emissions to the snow packs of California, contributing to their melting.*
6. *Lastly, model biases and uncertainties in the model formulations and parameterizations, particularly related to clouds and aerosol-cloud interactions, should be addressed in the future to provide more robust simulations of BC climate effects.*

III. Health Impact Studies

We recommend that our climate benefits studies of BC reductions be followed with a study that estimates the health benefits of the observed reductions in BC in rural and urban areas of California.

1.0 INTRODUCTION

1.1 Motivation

Black Carbon, or BC, is a major component of ambient aerosols, and is generally related to combustion sources such as automobile exhaust and biomass burning [*Andreae and Merlet*, 2001]; yet the effects of BC remain a wildcard in assessing the impacts of aerosols on climate change. BC is ubiquitous as recent studies show that 10% to 80% of the submicron particle number size distribution measured in Mexico City were primarily black carbon or contained black carbon [*Moffet et al.*, 2008]. BC's light absorbing and myriad chemical properties enhance its contribution to visibility degradation, change in the earth's radiation budget, and health risks from air pollution. Recent research has also shown that BC contributes to the accelerated melting of snow and ice in the poles and mountain glaciers through the reduction in snow albedo [*Hansen and Nazarenko*, 2004]. Studies show that BC in Arctic snow increases the absorption of shortwave radiation by 5-10% compared to soot-free snow [*Clarke and Noone*, 1985]. The heating of the atmospheric boundary layer also compounds this increase in the sensible heat at the surface. At the meso-scale, *Ramanathan et al.* [2007] showed that the atmospheric heating related to BC is of the same magnitude as greenhouse gases over the Himalayas and regional scales as large as the Indian subcontinent. Atmospheric BC also reduces regional rainfall and changes the spatial distribution of precipitation [*Chung et al.*, 2005; *Menon et al.*, 2002]. Furthermore, BC contributes to sea ice and glacier melting [*Flanner et al.*, 2011; *Menon et al.*, 2010; *Ramanathan et al.*, 2007; *Shindell and Faluvegi*, 2010] further impacting regional climate. BC aerosol particles have an atmospheric lifetime of the order of one week [*Ogren and Charlson*, 1983; *Stier et al.*, 2007] and are not well mixed in the atmosphere but are instead geographically and temporally correlated to emission sources. Reducing BC emissions therefore has been proposed as a control strategy to offset short-term climate changes [*Jacobson*, 2002]. BC particles also impact climate in a series of feedbacks through their interaction with clouds and temperature [*Jacobson*, 2002; *Koch and Del Genio*, 2010]. BC particles internally mixed with or coated by hygroscopic species serve as efficient cloud condensation nuclei (CCN) for both warm and mixed-phase clouds [*Andreae and Rosenfeld*, 2008; *Chen et al.*, 2010; *Dusek et al.*, 2006; *Koehler et al.*, 2009; *Lammel and Novakov*, 1995]. Perturbations to the BC concentration can therefore change the cloud droplet number (CDN) concentration and droplet size [*Roberts et al.*, 2003], which in turn influence both the cloud optical properties and cloud lifetime. These two so-called aerosol indirect effects are thought to have a net cooling effect on the atmosphere [*Lohmann and Feichter*, 2005]. Competing semi-direct effects are found to decrease the cloud cover by stabilizing the atmosphere through BC

warming [*Hansen et al.*, 1997] and to increase absorption by the cloud, helping to burn it off [*Jacobson*, 2006]. In contrast to the direct aerosol effect, the net climate forcing due to these cloud feedbacks and semi-direct effects are highly uncertain [*Forster et al.*, 2007]. A recent international assessment by UNEP & WMO [*Shindell et al.*, 2012b] has estimated that the two effects nearly offset each other leaving the direct forcing as the dominant effect.

California's regional climate may especially be sensitive to these radiative effects of BC. Summer water supplies in California rely predominantly on run-off from mountain snow packs located within the state as well as from the Rocky Mountains via the Colorado River. Agriculture, which represents a large fraction of California's economy, suffers drastically during water shortages. The potential impact of aerosols including BC on precipitation and freshwater availability has received increasing attention in California [*Jacobson*, 2007; *Lynn et al.*, 2007]. Furthermore, a warmer atmosphere over already dry regions, combined with less mountain runoff during the summer months, leads to optimal conditions for wildfires. A recent study has tied an observed increase in frequency and duration of wildfires in Western United States to warmer temperatures, earlier snowmelt, and drier summers [*Westerling et al.*, 2006]. On the other hand, increases in wildfires serve only to further enhance the concentration of light absorbing carbon particles and additional climate impacts on California.

Due to its short atmospheric lifetime, BC is not well mixed globally and reductions in BC emissions are a low hanging fruit for slowing down global warming in the coming decades. However, unlike ozone or carbon dioxide for which strict chemical definitions and measurement standards are clear, black carbon is chemically ambiguous and operationally defined. While this shortcoming in no way minimizes the importance of black carbon for climate and air quality, it does mean that monitoring and mitigating it will be subject to a series of technical and legal challenges. To address these environmental issues and reduce the warming commitment, the California Air Resource Board (CARB) has adopted the nation's most sweeping global warming plan, outlining for the first time how individuals and businesses will have to meet a landmark 2006 law that made the state of California a leader on curbing the emissions of greenhouse gases. This report details the results of a two-year effort combining observational and modeling studies that provides insights on the role of BC aerosols in California weather and climate, and help remove impedance to policy-making decisions.

1.2 Prior work

Compared to greenhouse gases, aerosol concentrations have much greater spatial and temporal variation because they reside in the atmosphere for much shorter times. Consequently, frequent measurements at numerous sites are needed to reliably track trends in aerosol concentrations and evaluate the changing impact of aerosols on climate over time. There are, however, few extensive records of aerosol concentrations in existence. One of the longest BC records is from coefficient of haze (COH) measurements in California. COH

levels recorded at 100 sites throughout California have been archived by the California Air Resources Board (CARB). We previously analyzed a fraction of this data set to derive ambient BC concentrations in the San Francisco Bay Area over the 37-year period from 1967 to 2003 (Figure 1.1).

With respect to elemental carbon (EC) and black carbon terminology, estimates of BC and EC are made with a variety of instrumentation and measurement techniques. In principle, the relatively strong light absorption properties of BC can be used to infer BC from an optical measurement and knowledge of the mass specific absorption of BC. In thermal methods, the filter media used for sample collection is heated and the thermally evolved carbon in the specified temperature plateau and analysis atmosphere defines the concentration of EC and organic carbon (OC). Light-absorbing carbon or BC is often equated with EC. However, there are subtle differences given that each term represents a functional definition that is dependent on the chemical and physical properties measured to determine each class of carbonaceous PM. Like modern measurements of BC made with the aethalometer, COH values are a measure of light attenuation by particles, and available data indicate that COH values are proportional to BC concentrations [*Allen et al.*, 1999; *Kirchstetter et al.*, 2008]. Our analysis, which addressed the relative importance of BC sources in the Bay Area and provided a temporally resolved record of BC concentrations, demonstrates the value of long-term records of aerosol measurements.

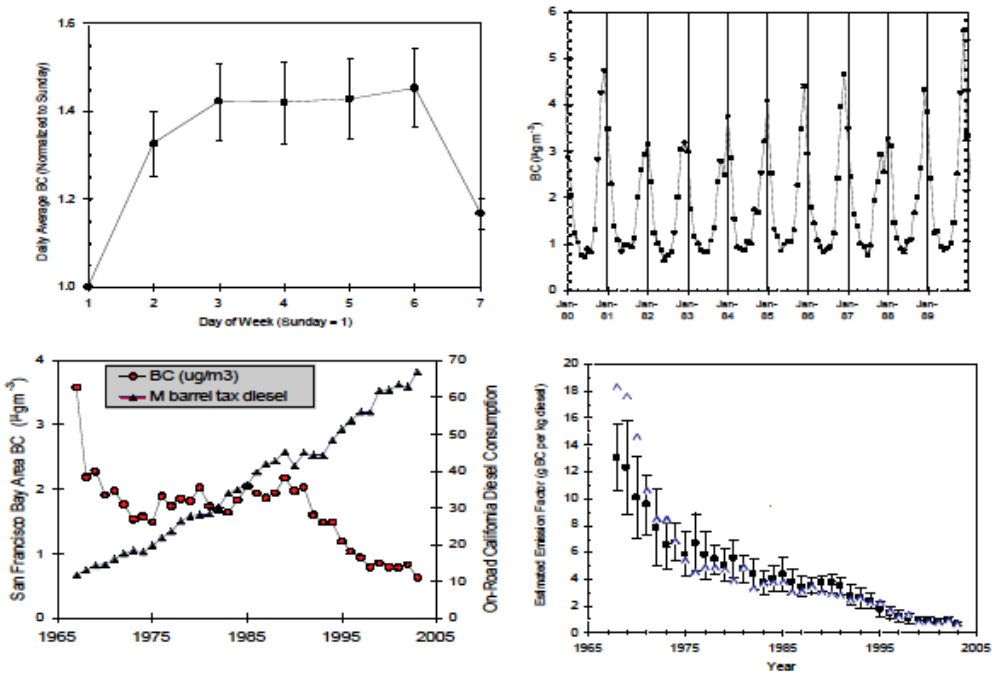

Figure 1.1 Trends in San Francisco Bay Area BC Concentration [Kirchstetter et al, 2008] resolved by (a) day of week, (b) season, (c) year, and (d) estimated diesel emission factors.

Reduced BC concentrations on weekends relative to weekdays are consistent with reduced diesel traffic on weekends, and peak concentrations in winter are consistent with reduced dispersion (mixing height and wind speed) and possibly wood burning in winter (Figs 1a,b). BC concentrations have decreased markedly since 1990 despite continued increase in diesel fuel consumption, consistent with an order of magnitude decrease in on-road diesel vehicle BC emission factors during the past 35+ years (Figs 1c,d). Additionally, preliminary analysis of annual average BC concentrations in three air basins in California are coincident with an observed statewide surface temperature increase [*Novakov et al.*, 2008], suggesting that a reduction in aerosol concentrations may have contributed to the observed surface temperature increase.

Long range trans-Pacific transport of BC to the west coast of North America during April 2004 has been estimated to be approximately 25 – 32 Gigagrams, of which roughly 75% originated in Asia [*Hadley et al.*, 2007]. Most of this transport (>78%) was located above 2km, where the westerlies are strongest. Using the CFORS (Chemical weather FORecast System) chemical transport model, the contribution of Asian BC to total BC over California below 2 km was predicted at 20 to 30%. The model, however, tended to drastically over predict BC in the boundary layer, and therefore the actual contribution at low elevations is likely smaller. In a subsequent study (in preparation), using elemental markers for Asian transport and comparing to observed BC, the estimate of Asian contribution to BC in California's mountain elevations in the spring was lowered to 25 to 30%. At other seasons the contribution is much smaller as spring marks the peak in observed trans-Pacific transport [*Liu et al.*, 2003].

Combining satellite aerosol data, surface network of aerosol remote sensing instruments and field observations together with chemical transport and radiative transfer models the global mean BC direct radiative forcing for the 2001 to 2003 period is estimated to be 0.9 W m^{-2} at the top of the atmosphere (TOA), with about ±50% uncertainty [*Chung et al.*, 2005]. This estimate is consistent with and slightly in the high end of the latest IPCC assessment for BC radiative forcing [*Forster et al.*, 2007], 0.45±0.25 W m^{-2}. This is likely due to the adoption of aerosol absorption retrieved from the worldwide surface network of solar spectral radiometers (AERONET), which tend to be a factor of two or more larger than the GCM-simulated values [*Sato et al.*, 2003; *Schuster et al.*, 2005]. In the California region, the annual mean BC-induced surface dimming (reduction in the surface solar radiation) is estimated at about -3 W m^{-2} to -12 W m^{-2} according to the global model study, which is large enough to mask the greenhouse warming at the surface, whereas the increase of solar heating in the atmosphere is about 2 W m^{-2} to 6 W m^{-2} and thus can augment the greenhouse warming at high altitudes [*Ramanathan and Carmichael*, 2008].

Finally, Figure 1.2 illustrates seasonal and geographical variations in the assimilated absorbing aerosol optical depth (mainly due to BC), including both long-range transported and local emissions [*Ramanathan et al.*, 2007]. The largest aerosol absorption occurs during the dry season from Sep to Oct, which

also overlaps with the intensive irrigation activities, accompanied with significant land-use changes. Maximum absorbing AOD values reach to ~0.06 in the S. California, Los Angeles area, implying the dominance of local BC emissions. In winter, the anthropogenic AOD reaches its minimum value as increasing precipitation washes out aerosols. From April to June, the long-range transported pollution plumes from E. Asia contribute to the build-up of absorbing aerosols on the west coast of California. In spring and summer (April through August), a heavy anthropogenic pollution plume (both BC and non-BC aerosols) with AOD of 0.4 originates from Central America near Mexico city; although the majority of this plume moves northeastward due to the persistent subtropical Californian high pressure system, some of the pollution may cross into South California by the small- to meso- scale processes.

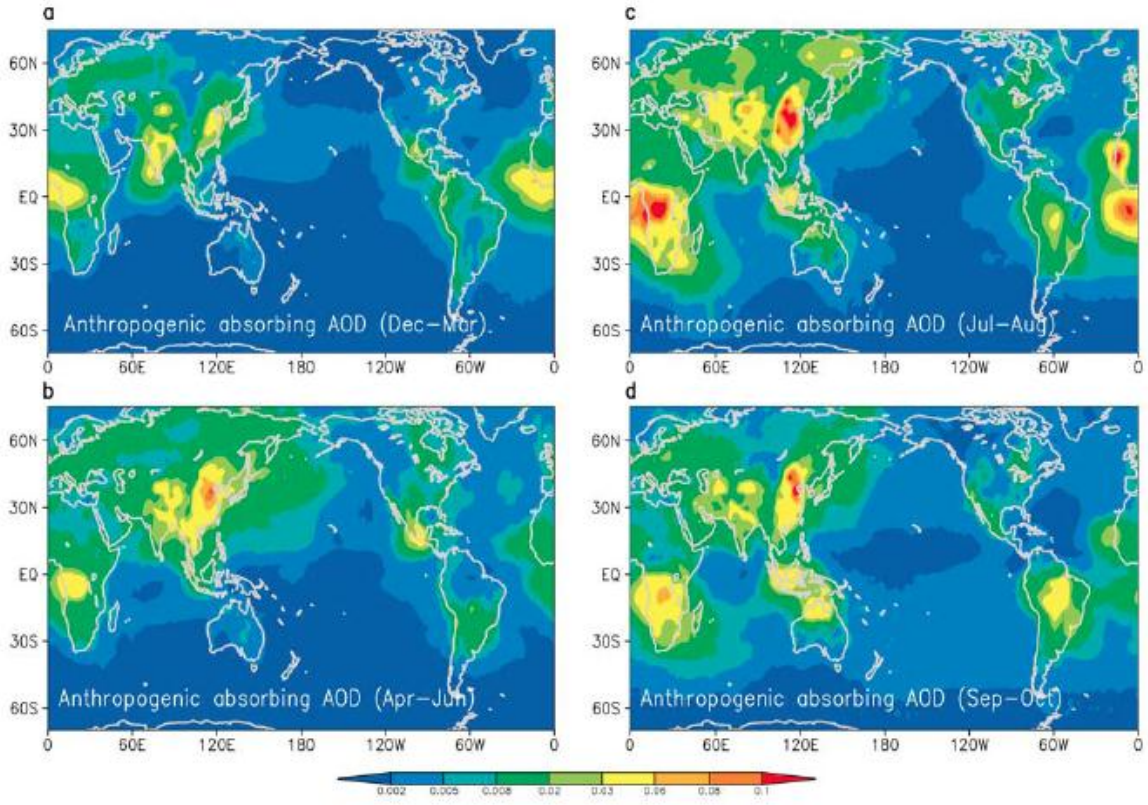

Figure 1.2 Trans-oceanic and trans-continental BC aerosols represented by assimilated anthropogenic aerosol optical depth resolved by season [Chung et al, 2005].

1.3 Research objectives

The primary objective of this research study is to assess the impact of BC on California's climate by developing a balanced approach between observations, data analyses, and modeling studies. The tasks included in this study fall under

two broad categories: observational estimates and regional modeling studies. By fully utilizing a vast wealth of existing data and measurements, in this study we aim to fully characterize the long term and spatial trends in aerosols in California, with a specific focus on absorbing carbonaceous aerosols, namely Black and Brown Carbon. In addition, a limited set of field measurements are used to relate BC aerosols to their sources, and impact on visibility. The climate impact is quantified by determining the total (direct) radiative forcing that can be ascribed to BC aerosols using both a column-integrated Monte Carlo model that is initialized with the integrated observations, and with validated climate models. Finally, impacts on surface temperature, hydrology, and precipitation are assessed by performing a series of experiments with regional climate models varying the BC emissions by factors of 10, 5, and 2. The changes in emissions are not arbitrary, but rather based upon observed trends in BC concentrations between 1960 and 2010.

1.4 Structure of report

The overall research objective of this work was accomplished by the completion of several specific tasks that are discussed in detail in the following chapters. The tasks themselves can be divided into four categories, which in turn organize this report into four unofficial sections.

Section 1: Data assimilation of existing measurements

Task 1: Long-term variations in BC concentration based upon analysis of COH data. Results from this task are described in Chapters 2 and 3.

Task 2: Multi-platform data analysis for BC and other aerosol properties. Results from this task are described in Chapters 4 and 5.

Section 2: Limited field measurements

Task 3: Preliminary source-apportionment of aerosols and black and brown carbon. Results from this task are described in Chapters 6 and 7.

Section 3: Calculating BC radiative forcing

Task 4: Radiative forcing attributed to BC based on observed aerosol properties. Results from this task are described in Chapter 8.

Task 5: Validation of surface brightening/dimming using flux measurements. Results from this task are described in Chapter 9.

Section 4: Climate impacts due to BC and BC mitigation

Task 6: Validation of the regional WRF-Chem model and its emission inventory with assimilated measurements, and calculation of aerosol forcing from

the integration of observations with the WRF-Chem model. Results from this task are described in Chapters 10 and 11.

Task 7: Regional climate impact of BC aerosols. Results from this task are described in Chapter 12

Work conducted as part of this study and associated central conclusions has been published in a number of peer- reviewed journals, specifically –

R. Bahadur, P. S. Praveen, Y. Xu, and V. Ramanathan (2012), Solar absorption by elemental and brown carbon determined from spectral observations.
Proceedings of the National Academy of Sciences, *109*(43), 17366-17371.

R. Bahadur, L. M. Russell, M. Z. Jacobson, K. Prather, A. Nenes, P. Adams, and J. H. Seinfeld (2012), Importance of composition and hygroscopicity of BC particles to the effect of BC mitigation on cloud properties: Application to California conditions.
*Journal of Geophysical Research-Atmospheres, 117.*doi:10.1029/2011JD017265

T. W. Kirchstetter and T. L. Thatcher (2012), Contribution of organic carbon to wood smoke particulate matter absorption of solar radiation.
Atmospheric Chemistry and Physics, 12(14), 6067-6072.

R. Bahadur, Y. Feng, L. M. Russell, and V. Ramanathan (2011), Response to comments on “Impact of California’s air pollution laws on black carbon and their implications for direct radiative forcing”,
Atmospheric Environment, *45*(24), 4119-4121.

R. Bahadur, Y. Feng, L. M. Russell, and V. Ramanathan (2011), Impact of California's air pollution laws on black carbon and their implications for direct radiative forcing.
Atmospheric Environment, *45*(5), 1162-1167.

C. Zhao, L. R. Leung, R. Easter, J. Hand, and J. Avise (2013), Characterization of speciated aerosol forcing over California.
Journal of Geophysical Research-Atmospheres (In Press).

In addition, we are in the process of preparing an additional set of manuscripts shortly to be submitted for review, specifically –

O. L. Hadley, L. Valin, D. Milstein, S. Menon, and T. W. Kirchstetter (2013), Regional climate response to reduced black carbon emissions in California.
In preparation.

Y. Xu, R. Bahadur, C. Zhao, R. L. Leung, and V. Ramanathan (2013), Estimating radiative forcing of carbonaceous aerosols over California based on satellite and ground observations.

In Preparation.

A. Cazorla, R. Bahadur, D. Chand, B. Schmid, H. H. Jonsson, V. Ramanathan, and K. Prather (2013), Relating aerosol absorption due to black carbon, brown carbon, and dust to emission sources determined from in-situ measurements.
In Preparation.

C. Zhao, L. R. Leung, R. Bahadur, and V. Ramanathan (2013), A regional modeling study of the climatic effects of black carbon in California.
In preparation.

2.0 Coefficient of haze as a black carbon proxy

2.1 Introduction

This chapter describes an experiment to determine the relationship between coefficient of haze (COH) and black carbon (BC). COH serves as a measure of reduced visibility caused by pollution and was one of the first measures of particulate matter air pollution adopted by regulatory agencies. Introduced in the early 1950s [*Hemeon et al.*, 1953], COH monitors were in operation at numerous locations in the United States from the mid-1960s to the early 2000s. As other metrics of particulate matter air pollution became popular, COH instruments were retired. Very few COH monitors are in operation today. In California, for example, COH monitors were in operation the majority of the year at more than fifty locations in 1980. That number dropped to fifteen in 2003. At the time of the preparation of this report, only one COH is still in operation in the state.

2.2 Operational principles

COH has been compared to more contemporary measures of atmospheric particulate matter, including total suspended particles, coarse and fine particle mass concentration, and elemental carbon [*Wolff et al.*, 1983]. The COH measurement, however, is most similar to that of the aethalometer [*Hansen et al.*, 1984], a widely used instrument for measuring the concentration of airborne black carbon (BC). Both instruments draw air through a white filter and periodically record the transmission of light through the filter, which decreases as particles are collected on the filter. COH and BC are computed based on measured transmission, T, with equations 2.1 and 2.2, respectively.

$$\frac{\mathrm{COH}}{1000\mathrm{ft}} = \log(1/\mathrm{T})\,\frac{\mathrm{A_{COH}}}{\mathrm{Q_{COH}}\Delta\mathrm{t}} \qquad (2.1)$$

$$\mathrm{BC}(\mu\mathrm{g\ m^{-3}}) = \frac{1}{\sigma}\ln(1/\mathrm{T})\,\frac{\mathrm{A_{aeth}}}{\mathrm{Q_{aeth}}\Delta t} \qquad (2.2)$$

In both equations, A is the area of filter used to collect particles (m^2), Q is the volumetric air sampling rate ($m^3\ s^{-1}$), and Δt is the time (s) between measurements. In equation 2.2, σ is an attenuation coefficient ($m^2\ g^{-1}$) that relates particle light attenuation to BC mass. Whereas BC is reported in units of mass concentration, COH values express aerosol concentrations in terms of COH per 1000 linear feet (305 m) of sampled air, where the COH unit was defined as the amount of aerosol that produced an optical density of 0.01.

Given the similarity in measurement methods and equations 2.1 and 2.2, it is reasonable to expect that archived records of COH concentrations could be used for reconstructing past concentrations of BC. There are some distinctions between the two measurement methods that are worth noting, however, as they could complicate the relationship between COH and BC concentrations. Specifically, the optics and filter media of the COH and BC instruments differ.

Regarding optics, the COH monitor uses an incandescent lamp to illuminate the sample and a photocell to measure the intensity of transmitted light. The contemporary aethalometer uses a discrete light emitting diode centered at 880 nm in wavelength to illuminate the sample and a photodiode to measure the intensity of transmitted light. The incandescent lamp emits radiation over a much broader range of wavelengths than the discrete light emitting diode, but the peak intensity of the incandescent lamp is in the near-infrared close to 880 nm [*Kirchstetter et al.*, 2003]. Regarding filter media, the COH monitor collects particles on a white paper filter (Whatman No. 4 paper tape), whereas the aethalometer collects particles on a quartz fiber filter (Pallflex type Q250F). It has been well established that the collection of particles in a highly reflective filter amplifies the response of the aethalometer to particle light absorption but mutes the response to particle light scattering [*Arnott et al.*, 2005; *Hansen et al.*, 1984]. The extent to which the same is true of the COH instrument has not been evaluated.

Side-by-side measurements of ambient COH and BC would provide the most direct basis for developing a relationship to convert COH to BC concentrations, but such data are scarce. Previously, [*Kirchstetter et al.*, 2008a] concluded that COH and BC were approximately proportional based on a limited amount of data and recommended that additional measurements were needed to determine the relationship between COH and BC with greater confidence. To that end, we reinstated two COH monitors and deployed them with aethalometers.

2.3 Restoration and laboratory evaluation of COH Instruments

Several retired COH monitors were acquired from the San Francisco Bay Area and Lake County Air Quality Management Districts (AQMDs) and the California Air Resources Board, and their historic operation was discussed with various personnel. Two COH monitors were restored to good working condition with original lamps, photocells, and filter paper. Each unit was upgraded with a mass flow controller (Figure 2.1) and connected to a computer for data acquisition and instrument control.

Prior to field deployment, the two field-bound COH instruments were operated in the laboratory to examine their performance and any bias. For that evaluation, the instruments sampled soot generated with a methane-air flame [*Kirchstetter and Novakov*, 2007]. The results are presented in Figure 2.2, which illustrates good agreement between COH concentrations measured with the two

instruments. COH concentrations were linearly correlated with a slope near one, an intercept of zero, and correlation coefficient $R^2 = 0.96$.

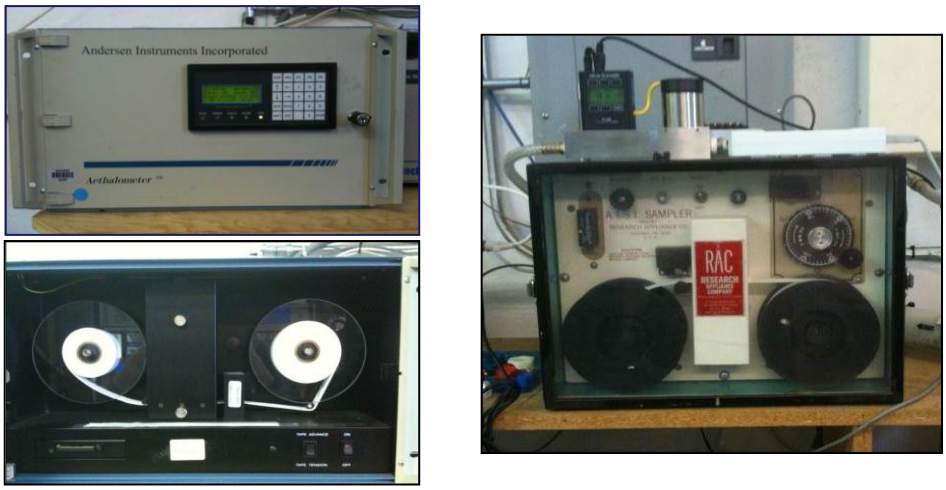

Figure 2.1 Front panel (top left) and inside front panel (bottom left) of aethalometer and refurbished COH instrument (right) as sited for this study in Vallejo, California. The refurbished COH instrument was equipped with a mass flow controller and data acquisition hardware (shown atop the instrument).

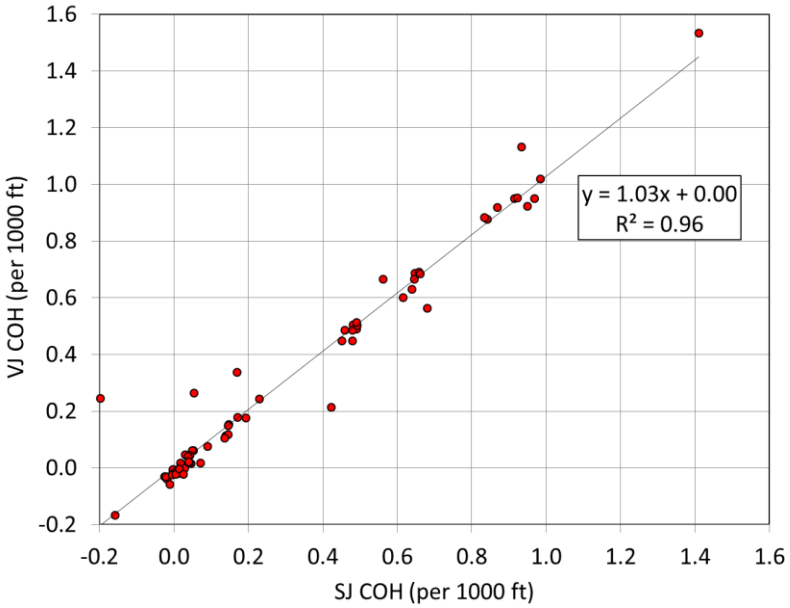

Figure 2.2. Laboratory comparison of two-hour average COH concentrations measured with the two field-bound refurbished monitors when subjected to soot from a methane-air flame.

The laboratory evaluation also demonstrated that the COH measurement technique, like the analogous BC measurement technique, is subject to a sampling artifact. Specifically, as the filter that collects particles becomes increasingly darkened, reported concentrations of COH erroneously decrease. In the lab, where the generation of soot sampled can be controlled, this effect is quite noticeable. As shown in Figure 2.3, over a period of several hours, when the concentration of soot in air was gradually decreasing, measured COH exhibits a pattern of markedly decreasing values followed by a sudden jump in value. This pattern corresponds to the collection of soot for a period of time and then an advance of the instrument's particle-laden filter to a pristine position. This so-called filter loading effect has been well documented for the aethalometer and it is most significant when the sampled particles have a low single scattering albedo, i.e., are mostly light absorbing [*Arnott et al.*, 2005; *Coen et al.*, 2010; *Kirchstetter and Novakov*, 2007].

In the lab experiments depicted in Figure 2.3, the particles were only black carbon soot and the particle concentration was an order of magnitude higher than it is in polluted ambient air. Thus, the magnitude of the effect in Figure 2.3 quite likely exaggerates the magnitude of the effect under conditions of sampling ambient air. Nonetheless, the recognition that both the COH instrument and the aethalometer exhibit this filter loading effect suggests that the correlation between COH and BC would be strongest when concentrations are averaged over time periods that are equal to or longer than the time between advances of the collection filter. As illustrated in Figure 2.3, COH concentrations averaged over full sampling cycles agree well with the measured trend in soot particle concentration because the filter loading effect is "averaged out."

2.4 Collocated field measurements of BC and COH

To evaluate the relationship between BC and COH concentrations, aethalometers and COH instruments were collocated at two stations in the Bay Area AQMD's regional air monitoring network— one in Vallejo and the other in San Jose. Vallejo is the largest city in Solano County with a population of 116,000 according to the 2010 census. The monitoring station is located in a mixed commercial and residential neighborhood one mile east of downtown and 0.5 miles west of Interstate 80. San Jose is the largest city in Santa Clara County and the largest city in the San Francisco Bay Area, with a population of 946,000 according to the 2010 census. The air monitoring station is located in the center of northern Santa Clara Valley, in a commercial and residential part of downtown San Jose. This area is completely encircled by major freeways, and has a large airport just to the northwest. The aethalometer and COH instrument were operated from March 2010 thru April 2011 (14 months) at the San Jose station and from March 2010 thru March 2012 (25 months) at the Vallejo station. The Bay Area AQMD provided the aethalometers. One had recently been serviced and was active in their air monitoring network. The other, which was inactive, was serviced by its manufacture at the commencement of this study.

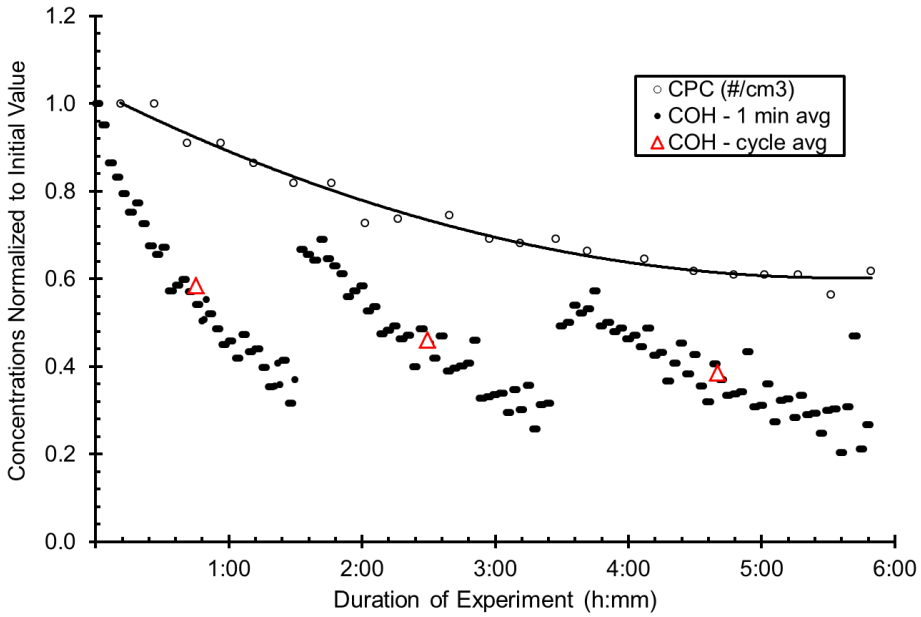

Figure 2.3 Time series of COH and particle number concentrations measured with a condensation particle counter (CPC) during a laboratory evaluation of COH instrument performance. Both monitors sampled soot generated with a methane-air flame.

Discussions with AQMD staff indicated that standard operation of the COH monitor did not call for a particle size selective inlet or conductive sampling tubing. Consistent with their historic operation, in this study, the COH monitors were installed with 0.25 inch Teflon tubing without an inlet cyclone and operated at an airflow rate of 6.25 L min^{-1}. Consistent with contemporary sampling practice, the aethalometers were installed with electrically conductive tubing (0.375 inch aluminum in San Jose and 0.625 inch stainless steel in Vallejo) and an inlet cyclone (BGI, model SCC1.829). They were operated at an airflow rate of 5 L min^{-1}, where the cyclone provided a 2.5 µm diameter cutpoint with a very low pressure drop.

Drawing from a reserve of filter wound onto a spool (see Figure 2.1), the aethalometer and COH instrument automatically advance to a pristine filter after a period of sample collection. The COH monitors were initially programmed to filter advance once every two hours, which is how they were typically operated when in wide use. However, it was quickly apparent that filter loadings after two hours were very light. To increase the amount of particulate matter collected on the COH filter and thereby increase the measurement sensitivity, the COH instruments were reprogrammed to filter advance once every six hours. With each advance, a six-hour average COH concentration was recorded. In effect, the longer sampling period mimicked a historic two-hour sampling interval at a

COH concentration three times higher than the contemporary COH concentration. The aethalometer filter was programmed to advance when measured attenuation reached the factory default value of 75, which occurred about four times every five days.

2.5 Relationship between COH and BC

Figure 2.4 illustrates the relationship between daily and monthly average concentrations of BC and COH at both the Vallejo and San Jose sampling locations. At both sites, lowest concentrations were measured in May, June, and July, and highest concentrations were measured in December and January. The relationship between COH and BC is essentially the same at both locations and whether daily or monthly averages are considered. A linear regression of the combined data from both sampling locations provides an equation for converting measured COH concentrations to BC concentrations: BC ($\mu g\ m^{-3}$) = 6.7COH + 0.1. The high value of the correlation coefficient ($R^2 > 0.9$) indicates that COH is a good proxy for BC. The intercept of the linear regression equation is small compared to past BC concentrations – annual average BC concentration ranged between 1 and 4 over most of the >35 year COH record for California and was considerably higher in other states (see Figure 3.6). This indicates that historical BC and COH concentrations are approximately proportional.

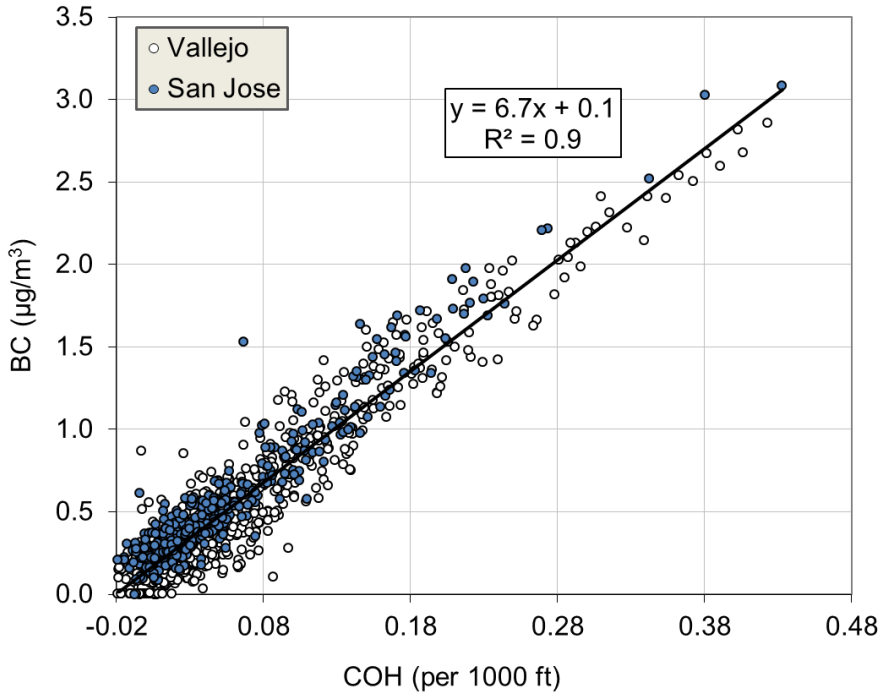

Figure 2.4 Scatter plot of daily average BC and COH concentrations measured in San Jose (March 2010 thru April 2011) and Vallejo (March 2010 thru March 2012).

2.6 Conclusions

Allen et al., [1999] presented data collected during summer 1992 in Philadelphia, Pennsylvania, which indicated that BC (µg m^{-3}) = 5.7•COH – 0.3. A composite study [*Kirchstetter et al.*, 2008a] evaluated that data together with data collected in Fresno, California and suggested using a factor of 5.4 to convert COH to BC. The conversion factor based on our sampling in Vallejo and San Jose for 25 and 14 months, respectively, is about 24% larger. [*Wolff et al.*, 1983] presented data collected during summer 1981 in Detroit, Michigan, which indicated that concentrations of elemental carbon (EC) and COH were well correlated: EC (µg m^{-3}) = 8.9•COH – 0.6. The study of Allen et al. also indicated that BC concentrations were about 75% of EC concentrations. Multiplying the equation of Wolff et al. by 0.75 indicates that BC ~ 6.7•COH, which is the same relation derived from the measurements in our current study. However, we do not place too much stock in this agreement because many studies show wide, aerosol-dependent variation in the relationship between EC and BC (e.g., [*Jeong et al.*, 2004] and references therein). Rather, we conclude that the collective evidence indicates that COH is a reasonable measure of BC and that past BC concentrations can reasonably be inferred from an analysis of the archived records of COH concentration.

3.0 Trends in urban BC concentration, 1960-2000

3.1 Introduction

This chapter describes an analysis of trends in BC concentrations over the period from the early 1960s to the early 2000s. BC concentrations were inferred from COH data based on the relationship between COH and BC described in the previous chapter. The focus of this work is primarily on BC trends in California but data from other states are included in the analysis for context and comparison.

3.2 Data sources

Records of ambient COH concentrations were acquired from the California Air Resources Board (CARB), the New Jersey Department of Environmental Protection (NJDEP), and the Environmental Protection Agency's Air Quality System. The EPA's data set included COH concentrations for many states, but the temporal and spatial coverage was very limited in most cases. Included in this analysis are states with COH records covering ten or more years (Figure 3.1): California, New Jersey, Virginia, Pennsylvania, Colorado, Ohio, Illinois, New York, and Missouri. The most spatially and temporally comprehensive data sets are available for California and New Jersey. The CARB and EPA data sets contained COH records for California for overlapping periods, which provided an opportunity for comparison.

The locations of COH monitors and Interagency Monitoring of Protected Visual Environments (IMPROVE) sites operated in California are shown in Figure 3.2. COH monitors were located predominantly in urban areas at low altitude at monitoring stations maintained by state AQMDs. Most IMPROVE sites are rural in location. As indicated in the figure, EC concentrations are measured at IMPROVE sites. Trends in EC concentrations at IMPROVE sites are further discussed in Chapter 4. The location and number of COH monitors operating in California varied over time. From the mid-1970s to 2000, thirty or more COH monitors were in operation at least six months in any given year, according to the records obtained for this study (Figure 3.2). The number of COH monitors in operation dropped quickly after 2000 to just one in a rural location in 2005.

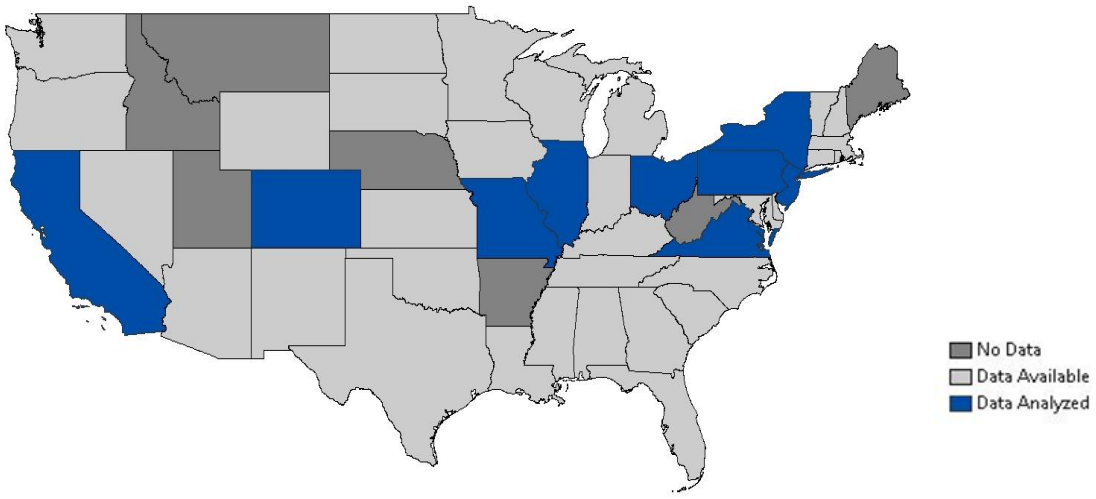

Figure 3.1 A map of the U.S. indicating the states for which at least some COH records exist, and the nine states (in blue) for which we have determined annual BC trends.

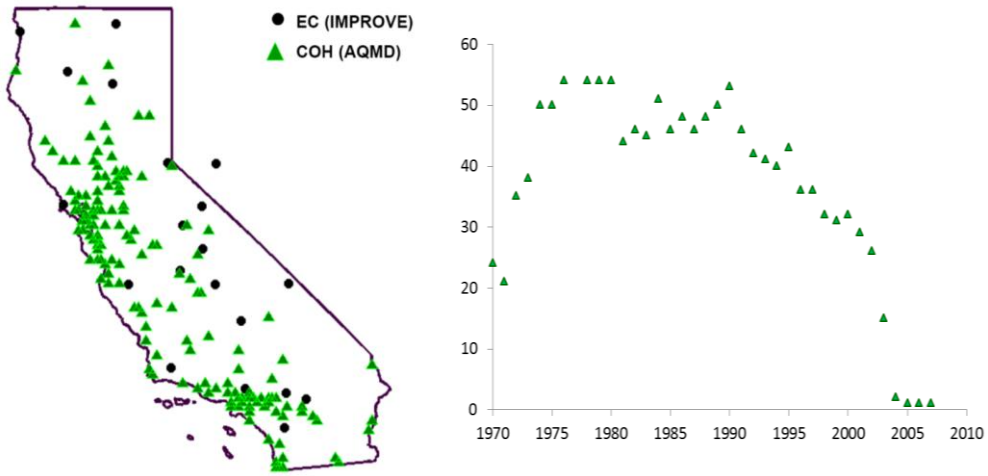

Figure 3.2 (Left) Map of California showing where COH and EC were measured: IMPROVE sites operating between 2001 and 2005, and COH sites from 1980 to 2007. (Right) Graph showing the number of COH monitors in operation in California at least six months in any given year over the period 1970 to 2007.

3.3 Black carbon trends

Statewide average BC concentrations in California were computed separately using the data available from CARB and the EPA. Using the CARB data, air-basin average BC concentrations were computed from which statewide average values were calculated. Using the EPA dataset, statewide average values were determined as the average of BC concentrations measured at all sites across the state. The EPA data set was missing a considerable amount of data contained in the CARB data set. Data recorded by the South Coast AQMD were notably missing from both sources, which prevented the evaluation of BC trends for the Los Angeles-San Bernardino region. Statewide average BC concentrations for other states were computed as the average of concentrations measured at all sites across each state.

Annual, monthly, and daily average BC concentrations were calculated. Statewide annual average BC concentrations in California are shown over a 45+ year period in Figure 3.3. BC concentrations in California decreased markedly from about 3.9 μg m^{-3} in 1966 to 2.3 μg m^{-3} in 1980 to 1.1 μg m^{-3} in 2000. Where the EPA and CARB datasets overlap, agreement is very good. The observed decrease of approximately 50% in the time period between 1980 and 2000 is consistent with that reported by [*Bahadur et al.*, 2011] and may possibly be related to emissions control on diesel engines. The more recent values shown in Figure 3.3 (i.e., those after 2000) may not be truly indicative of statewide concentrations because of the small number of monitors operation. However, the continued downward trend is consistent with EC concentrations measured throughout the San Francisco Bay Area [*BAAQMD*, 2012].

Annual average BC concentrations in averaged over several California air basins are shown in Figure 3.4. These show considerable variation but generally follow the decreasing statewide average trend. Lowest BC concentrations are in the North Central Coast air basin. As noted above, COH data were not available for the Los Angeles-San Bernardino region. [*Cass et al.*, 1984] reported an average EC concentration of 5 μg m^{-3} in the Los Angeles from 1958 to 1981. Assuming the EC concentrations are a reasonable estimate of BC concentrations, the report of Cass et al. indicates that BC concentrations were considerably higher in the Los Angeles area than in the rest of California, at least until 1980. Thus, the statewide average BC concentrations shown in Figure 3.3 are likely biased low due to the exclusion of data from the Los Angeles region.

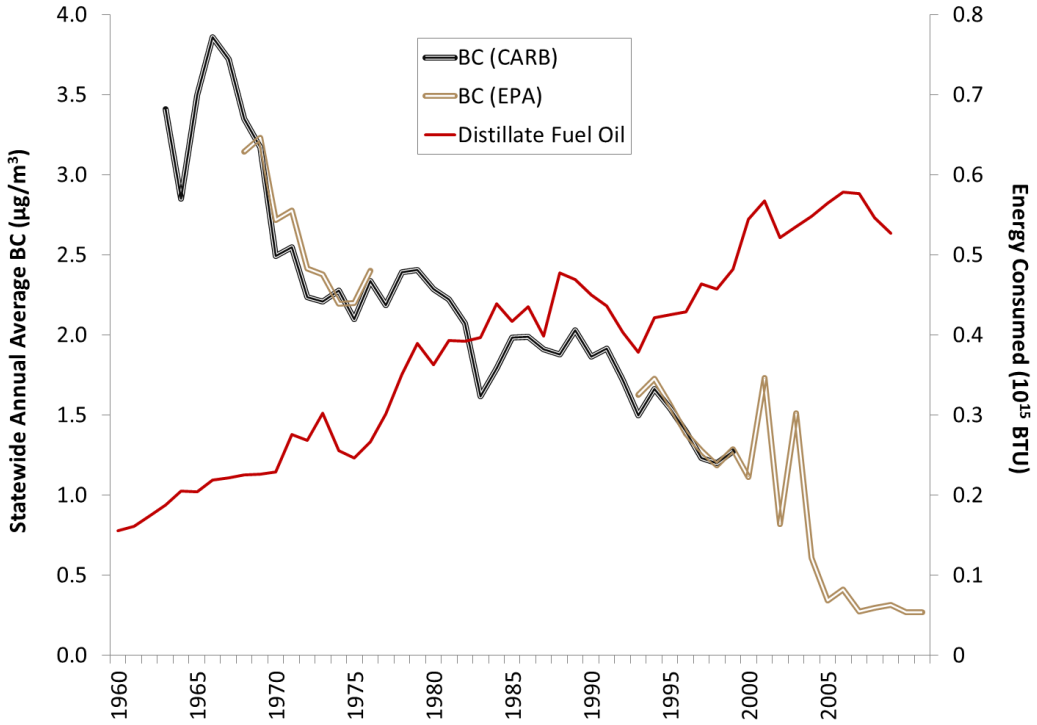

Figure 3.3 Statewide average BC concentrations based on COH data sets obtained from CARB and EPA and distillate fuel oil (i.e., diesel fuel) consumption, a source of BC, in California since 1960.

The trends in statewide annual average BC concentrations in California and other states are compared in Figure 3.5. During a period of markedly decreasing BC concentrations from the mid-1960s to 1980, concentrations were generally bound at the high end by those measured in New Jersey and at the low end by those measured in California. Thus, compared to the distinct reduction in BC concentrations in California, the decreases in the other states was even more marked as shown in Figure 3.5. Since 1980, the decline in BC concentrations in New Jersey and California has been more gradual, with New Jersey concentrations having apparently plateaued at a level that is twice the statewide average level in California.

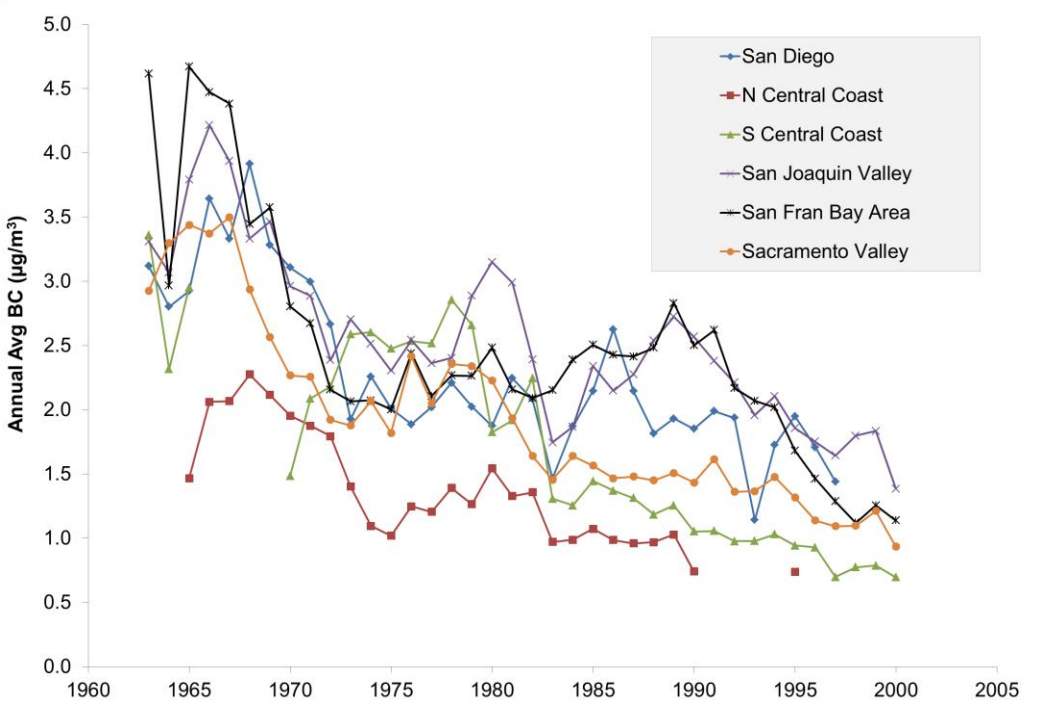

Figure 3.4 Average BC concentrations in California reconstructed from COH records resolved by air basin.

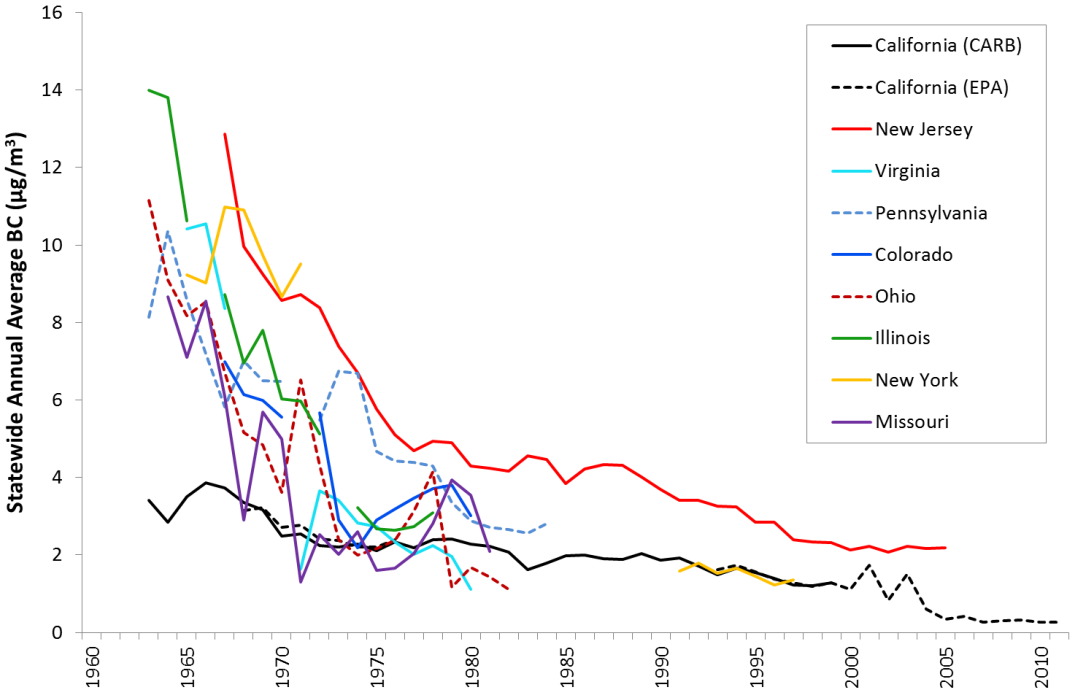

Figure 3.5 Statewide average BC concentrations in nine states in the U.S. with available COH records.

3.4 Seasonal patterns in BC

Monthly statewide average BC concentrations were computed on a decadal basis to examine how seasonal trends evolved over time (Figure 3.6). A strong annual cycle is apparent, with wintertime maxima and summertime minima. This seasonality continued over time in California, similar to the seasonal trend in the San Francisco Bay Area and in Los Angeles reported by [*Kirchstetter et al.*, 2008a] and [*Cass et al.*, 1984], respectively. In contrast, the seasonal cycle evident in BC concentrations in New Jersey in the 1970s and 1980s was not evident in the 1990s and early 2000s.

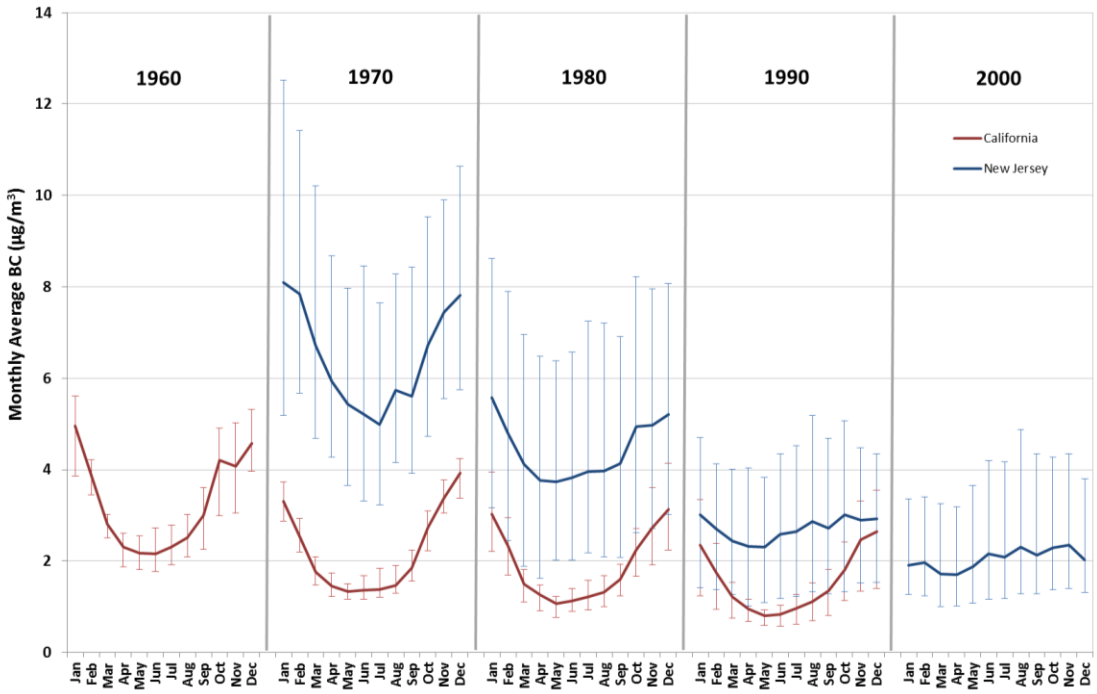

Figure 3.6 Annual cycles of BC concentrations by decade in California and New Jersey between 1960 and 2000.

To aid in the interpretation of these BC trends, concentrations of carbon monoxide (CO) – another primary air pollutant – are shown in Figure 3.7 for several cities. These data are an excerpt from the study of [*Glen et al.*, 1996] and show excellent agreement between CO concentrations that were measured and modeled. In modeling CO concentrations, Glen et al. treated CO emissions as constant throughout the year. Variability in modeled CO was introduced only by variability in wind speed and atmospheric mixing height (i.e., pollutant dispersion). The fact that modeled and measured concentrations are in good agreement suggests that the modeled dispersion of CO is accurate. These data

illustrate that wintertime maxima and summertime minima in CO concentrations in San Francisco are due to the seasonal cycle of pollutant dispersion, with lower wind speed and mixing height in the winter. Conversely, the lack of a seasonal cycle in CO concentrations in several east coast cities is due to the lack of a seasonal cycle in pollutant dispersion.

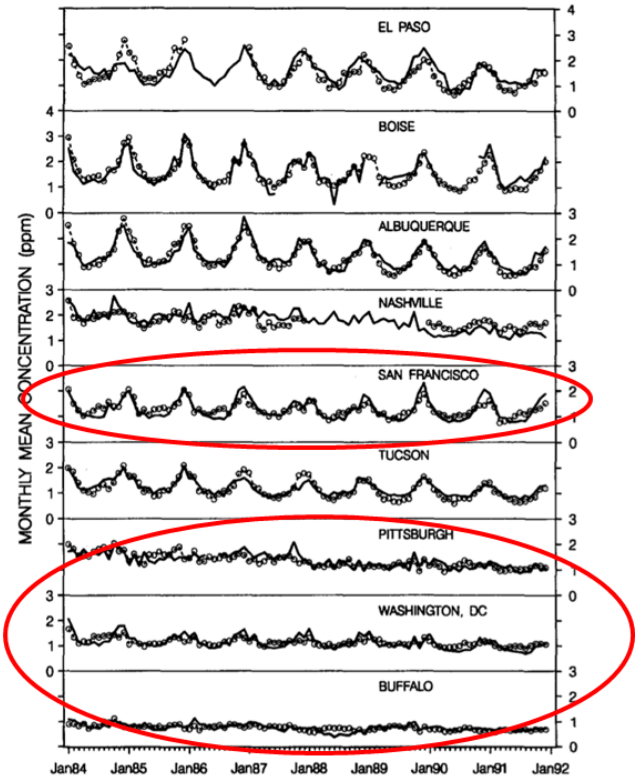

Figure 3.7 Annual cycles of carbon monoxide emissions measured in several cities and modeled by Glen et al. (1996).

Given the results of Glen et al., we infer that the persistent annual cycle in BC concentrations in California is due to meteorological conditions that have not changed over the time scale indicated in Figure 3.6. As noted above, most of the COH monitors were located in urban settings at low altitude. In the winter, these regions are characterized by a low boundary layer and stagnant air, which promotes the buildup in pollutant concentrations. Residential wood burning that peaks in the wintertime [*Fairley*, 2006] could also contribute to this winter-time maxima. However wood burning emits an order of magnitude more OC than BC, and the analysis of [*Schauer and Cass*, 2000] suggests that, at most, 20% of wintertime ambient BC concentrations in Fresno, California are from residential wood burning. Regarding the trends in New Jersey, we infer that the absence of an annual cycle in BC concentrations in the 1990s and 2000s is due to the

absence of an annual cycle in the region's meteorological influence on pollutant dispersion. This is consistent with the results of Glen et al. for other east coast cities. Assuming broad meteorological patterns have not changed in New Jersey, the annual cycle in BC concentrations in the 1970s and 1980s was likely due to increased wintertime BC emissions, which have since been controlled.

3.5 Weekly patterns in BC

Daily statewide average BC concentrations, normalized to concentrations on Sundays, are shown in Figure 3.8 for California and New Jersey. The same is shown for individual air basins in California in Figure 3.9. A weekly cycle is clearly evident, with the lowest BC concentrations on Sunday and second lowest on Saturday. Diesel truck activity, but not the activity of gasoline fueled vehicles, follows a similar weekly pattern, with activity on Sundays equal to 25% of the weekday average in California [*Dreher and Harley*, 1998]. In a given region, the weekly cycle in BC concentration becomes more pronounced as BC concentrations decrease: in recent decades rather than earlier decades (Figures 3.8 and 3.9) and in summer rather than winter (not shown).

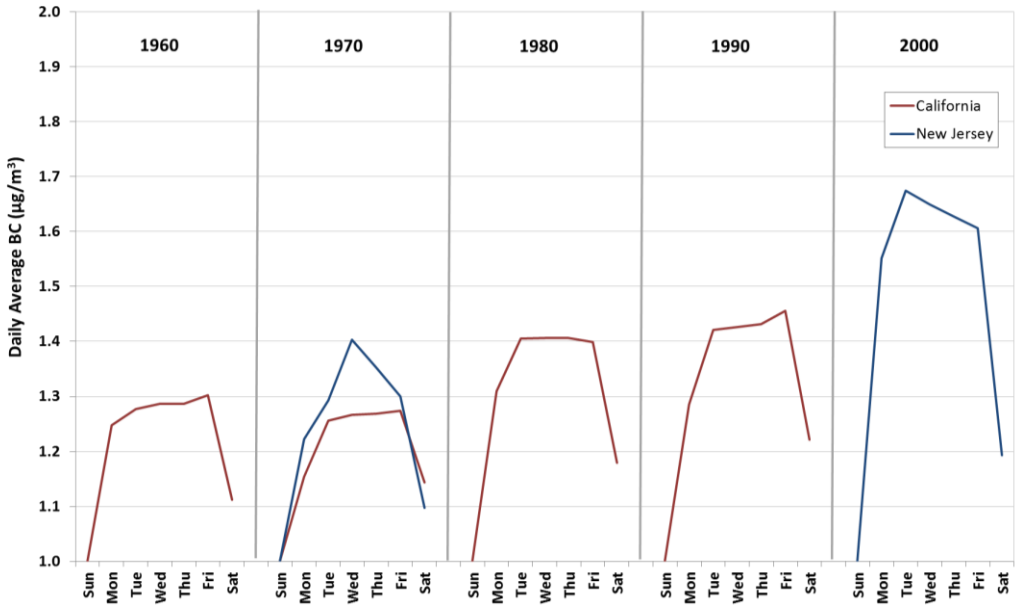

Figure 3.8 Weekly cycle of BC concentration by decade in California and New Jersey from 1960-2000.

Figure 3.9 illustrates that the weekly cycle in BC concentrations is weakest in the North Central Coast where BC concentrations are lowest (Figure 3.4). Likewise, the weekly cycle in BC concentrations tends to be strongest in the San Francisco Bay Area, San Joaquin Valley, and San Diego where BC are generally the highest. A plausible explanation is that diesel vehicle activity is lowest in the North Central Coast resulting in the lowest BC concentrations and the weakest weekly cycle in BC.

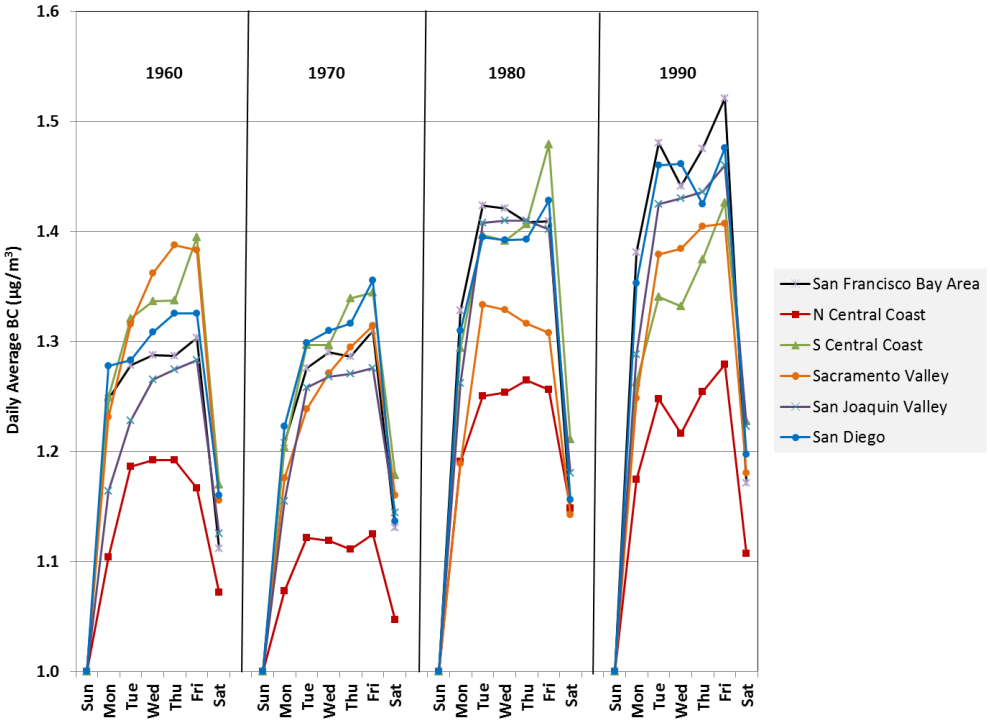

Figure 3.9 Weekly cycle of BC concentration by decade in California air basins.

3.6 Energy consumption trends

Energy consumption data were downloaded from the U.S. Energy Information Administration [*EIA*, 2012]. Over the period 1960 to 2000, total energy consumption in California increased from 3.5 to 8.0 quads (10^{15} BTU) and fossil fuel consumption roughly doubled from 3 to 6 quads. The consumption of distillate fuel oil, which includes on-road diesel fuel and is a primary BC-producing fuel, is shown together with the long-term statewide average BC trend in Figure 3.3. As shown, concurrent with the factor of 4 decrease in BC concentrations, distillate fuel oil consumption increased by about a factor of 5 (from 0.1 to 0.5 quads). Since 1960, the majority of distillate fuel oil has been increasingly consumed in the transportation sector, and since 1970, the majority of transportation distillate has been consumed by on-road diesel vehicles (Figure 3.10).

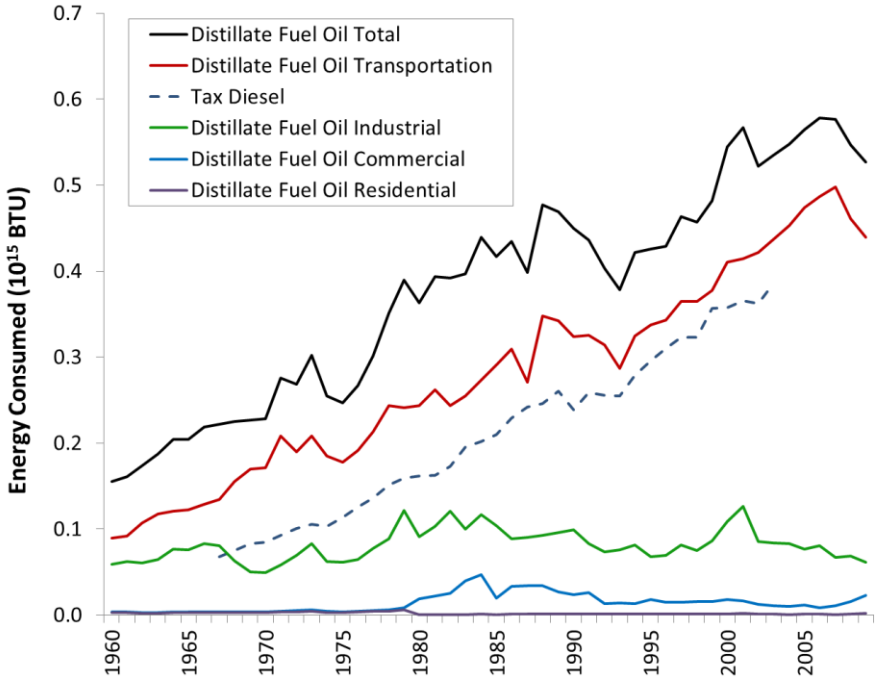

Figure 3.10 Distillate fuel oil consumption in California by sector, illustrating the portion of transportation distillate that is taxable (i.e., on-road) diesel.

Given that diesel truck activity has persistently influenced BC concentrations in California (Figures 3.8 and 3.9), one might expect that the increasing use of diesel fuel would result in increasing BC concentrations. Yet BC concentrations in California have declined. The apparent paradox must be due to the fact that the mass of BC emitted by on-road diesel trucks per kilogram of diesel consumed has decreased more than diesel fuel consumption has increased. Evidence to support this notion is presented by [*Yan et al.*, 2011], [*Kirchstetter et al.*, 2008a], and [*Lloyd and Cackette*, 2001], who reported that fuel normalized emissions of PM and BC from on-road heavy-duty trucks have decreased by about an order of magnitude since the first smoke reduction standards were introduced in 1970. Since 1970, on-road diesel fuel consumption has increased by a factor of 4. Therefore, despite their increasing fuel consumption, on-road diesel truck emissions of BC have likely decreased by about a factor of 2 over the period of study.

Even more pronounced than the weekday/weekend difference in the activity of on-road diesels, survey data from southern California show > 90% reduction in construction activity (i.e. off-road diesel consumption) on weekends [*Coe et al.*, 2003]. This activity pattern likely contributes to the weekly BC cycle shown in Figure 9. Only recently, however, have steps been taken to reduce particulate matter emissions from new off-road engines [*Dieselnet*, 2012]. As a result, this vehicle class may not have contributed much to the decline in BC concentrations over the several decades illustrated in Figure 3.3.

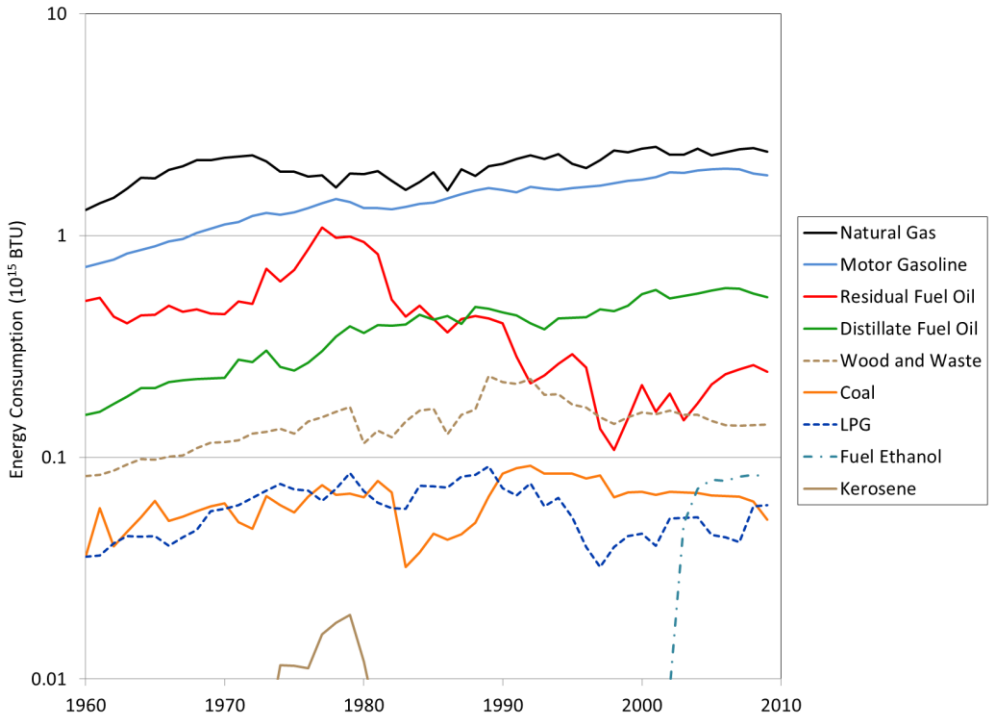

Figure 3.11 Consumption of fossil fuel and biomass fuels in California. Note that energy consumption is plotted on a logarithmic scale.

As shown in Figure 3.11, fuels other than diesel supply most of California's energy needs. Thus, it is likely that factors in addition to the cleanup of the diesel truck fleet have contributed to the decrease in BC concentration. Natural gas and gasoline account for most of the energy consumption in California, followed by residual and distillate fuel oils, wood and waste, coal, and liquefied petroleum gas (Figure 3.11). Ethanol for transportation shows up in the early 2000s but is minor compared to gasoline and diesel (distillate). BC emissions from natural gas are thought to be negligible [*Bond et al.*, 2004]. While fuel normalized BC emissions from gasoline vehicles are approximately 30 times smaller than those from heavy diesel trucks [*Ban-Weiss et al.*, 2008; *Kirchstetter et al.*, 1999], roughly six times more gasoline than diesel fuel is consumed in California. Thus it is reasonable to expect that gasoline vehicles emit on the order of 20% of the amount of BC emitted by on-road diesel trucks. Since BC emissions from light-duty vehicles are decreasing over time, their cleanup has likely contributed to decreasing BC concentrations in California. In addition, decreasing wood and waste burning since 1990 and the cleanup of BC emissions by the industrial sector which has consumed a rather constant amount of distillate fuel oil over the study period (Figure 3.10), have likely contributed to decreasing BC concentrations in California.

This consumption history of residual fuel oil is very different than that of other fuels, which either steadily increased (gasoline, diesel fuel) or remained very small and approximately constant (coal and liquefied petroleum gas). The consumption history of residual fuel oil (which includes bunker fuel oil) increased substantially from 0.4 quads in 1970 to a historic maximum of 1.1 quads in 1977 (Figure 3.12). This sharp rise was followed by an equally sharp decline to 0.4 quads in 1983 and then a more gradual decrease to about 0.2 quads in 2000. The peak in residual fuel oil was driven primarily by increased use in the electric utility sector and to a lesser extent by increased use for ships in the transportation sector (Figure 3.12).

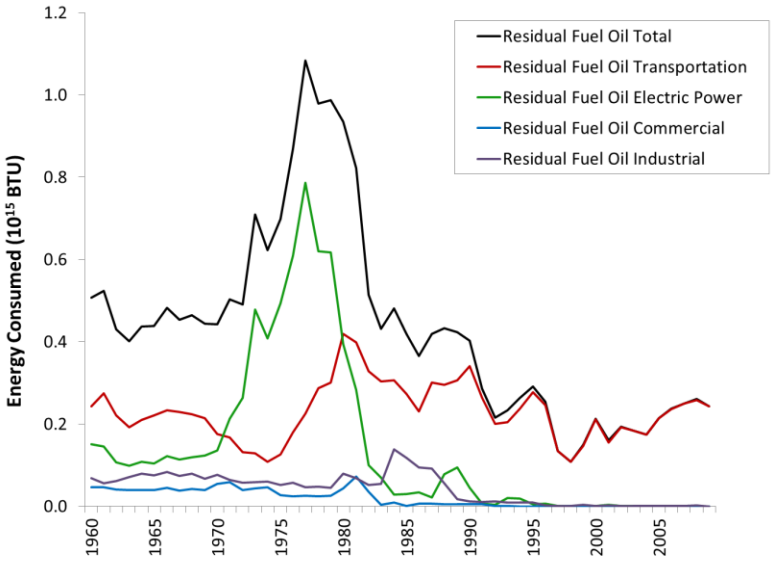

Figure 3.12 Residual fuel oil consumption in California by sector.

The peak in residual fuel oil consumption in the mid-1970s was coincident with a change in the trajectory of BC concentrations from markedly decreasing to approximately constant (Figure 3.3). The subsequent sharp decline in residual fuel oil starting in 1980 coincides with the resumption in decreasing BC concentrations. This is an indication that residual fuel oil combustion may have influenced BC concentrations in California. Unlike BC emissions from electric utilities that are generally considered to be negligible [*Bond et al.*, 2004], BC emissions per kg of residual fuel oil combustion in ships are likely higher than that from diesel fuel combustion in trucks. Thus, it may be that the rise in transportation residual fuel oil contributed to the plateau in BC concentrations in the mid-1970s.

3.7 Conclusions

Historical records of COH have been used to construct statewide trends in ambient BC concentrations in California. Overall, BC concentrations in California

decreased markedly from about 3.9 μg m^{-3} in 1966 to 2.3 μg m^{-3} in 1980 to 1.1 μg m^{-3} in 2000, agreeing with the trends reported by [*Bahadur et al.*, 2011]. A persistent winter-time maxima in BC concentration is observed in the state, which is related to meteorological conditions. An analysis of weekly patterns suggests that the transportation sector is the primary driving force for BC concentrations. Despite an increase in diesel fuel consumption from 1960-2000, a simultaneous decrease in emission factors due to cleaner technology may have resulted in the observed decrease in BC. Further, the steady decrease in transportation related consumption of residual fuel oil from the early 1980s to 2000, and the coincident elimination of residual fuel oil in the industrial sector (Figure 3.12) in favor of cleaner burning natural gas, likely have contributed to the steady decrease in BC concentrations in California.

4.0 Trends in non-urban BC concentration, 1980-2000

4.1 Introduction

Given the large uncertainty in model estimates of BC emissions from various sources, their atmospheric concentrations and their optical properties [*Forster et al.*, 2007] it would be highly advantageous to have empirical data to validate model predictions. The IMPROVE monitoring network provides a record of elemental carbon (EC) measured using thermal optical reflectance techniques [*Chow et al.*, 2001; *Chow et al.*, 2004] , that is typically used as a surrogate for BC. Since the optically-based definition of BC includes EC and a small fraction of organic carbon (OC), this corresponds to an atmospheric lower bound. In addition to EC, the network also provides measurements of organic carbon (OC), sulfate, and nitrate in the fine aerosol (<2.5 μm) phase from 22 operational sites in California from 1988-2008, allowing us to establish spatially resolved trends of BC and non-BC aerosols California and their radiative properties.

The IMPROVE protocol has been applied consistently on the measurements in this study, making the observed trends reliable. The IMPROVE protocol has been shown to compare well with other evolved gas and optical measurements, although different ambient compositions (with different contributions of diesel and wood burning contributions, as well as interference from dust) could result in greater discrepancies as discussed by [*Chow et al.*, 2005] in a recent review. For example, adsorption of volatile species and dust minerals associated can lead to discrepancies in the corrections for charring that have been shown to cause both positive and negative biases in EC measurements [*Countess*, 1990; *Schmid et al.*, 2001; *Turpin et al.*, 1990; *Watson et al.*, 2009].

In addition to the filter-based measurements, aerosol scattering coefficients at the surface and column measurements of the aerosol single scattering albedo are also available in California. These unique data sets enable us to ask the following questions: What was the impact of diesel emission control on BC concentrations in the atmosphere? And how did it alter the radiative properties of aerosols? And lastly, what was the impact on the direct radiative forcing of the atmosphere?

4.2 BC aerosol and diesel emissions

Black carbon (BC) is a substantial component of carbonaceous aerosols produced from fossil fuel combustion and to a lesser extent, biomass burning [*Andreae and Merlet*, 2001]. Studies in regions dominated by fossil fuel combustion [*Allen et al.*, 1999; *Liousse et al.*, 1993] have found strong correlations between EGA EC and aethalometer BC, indicating that EC from diesel emissions are likely to be well represented by the IMPROVE

measurements [*Turpin et al.*, 2000]. To investigate correspondence between trends in measured EC and diesel fuel emissions in California, we incorporate two independent emission inventories in this study. An estimate of fossil fuel emissions – attributed to diesel and gasoline – is available from [*Ito and Penner*, 2005], and the California Air Resource Board [*CARB*, 2008] maintains an almanac of total particulate emissions and source related emission factors that can be used to estimate diesel fuel BC in California.

4.3 Temporal trends in BC concentration

Figure 4.1(a) illustrates the annual averages for BC in California for the twenty-year period between 1989 and 2008. The annual mean concentrations show a steady decline within this time period (from 0.46 μg m^{-3} in 1988 to 0.24 μg m^{-3} in 2008), with annual variability expressed as a standard deviation (1σ adjusted for multiple sites) approximately 40% of the mean value. The major portion of the decline in BC concentration appears to occur between 1989 and 1998 (from 0.46 to 0.26 μg m^{-3}) with a slower decrease between 1999 and 2008. The spikes in BC concentration in 1999 and 2008 correspond to major California forest fire years. The rate of decline in BC concentration agrees well with the decline in both total fossil fuel emissions [*Ito and Penner*, 2005] and diesel vehicle emissions [*CARB*, 2008] which show emissions peaked between 1985 and 1990 and declined thereafter. This correspondence in trend between reduced diesel emissions and BC concentrations is consistent with, and reinforces the conclusions of *Novakov et al.*, [2008b] who report a reduced emission factor for diesel fuels between 1960 and 2000.

Figure 4.1(b) compares the statewide annual mean BC with the mean calculated in three geographic zones – South California (South of 35N) which contains the Los Angeles-Long Beach-Santa Ana metropolitan areas, Central California (between 35 and 38N) which contains the San Joaquin bay area and most of the central valley, and North California (North of 38N). While the background BC concentrations (as measured by the IMPROVE network) are higher in the more populous Southern and Central zones, a similar decline is observed in all three regions indicating that the observed decline in BC is uniform statewide, and not dominated by a few stations.

The measured sulfate, nitrate, and OC (Figure 4.1(c)) show no statistically significant trend in concentration between 1989 and 2008, with the approximately 10% change in annual mean values being significantly smaller than the standard deviation in annual measurements. These contrasting trends suggest that the reduction in diesel fuel aerosol emissions is likely to be the dominant contributing factor to the reduction in BC concentration – particularly in the time frame following the introduction of PM emission standards for heavy duty engines. These results further reinforce our conclusion that the IMPROVE data constitute an ideal set of ambient measurements for evaluating the climate impact of mitigating BC via diesel emission control.

Table 4.1 summarizes annual means and rate of change in BC concentration, BC/sulfate ratio, and BC/non-BC aerosol ratio. A faster drop in BC concentration is observed for the winter and spring months (Nov-Apr), compared to the summer and fall months (May-Oct) that correspond to the wildfire season in California. This seasonal variation is consistent with a greater reduction in anthropogenic emissions compared to forest fire emissions and trans-Pacific transport. The ratios also show a steady reduction from 1989 to 2008 for all seasons, indicating that the decline in BC has outpaced the decline in total aerosol concentration. The BC/sulfate ratio decreased at approximately double the rate (-6% compared to -3%) of BC/non-BC aerosol ratio, further supporting our conclusion that reduction in emissions from low sulfate fuels (such as diesel) and the proliferation of cleaner emission vehicles are primarily responsible for the reduction in BC aerosols.

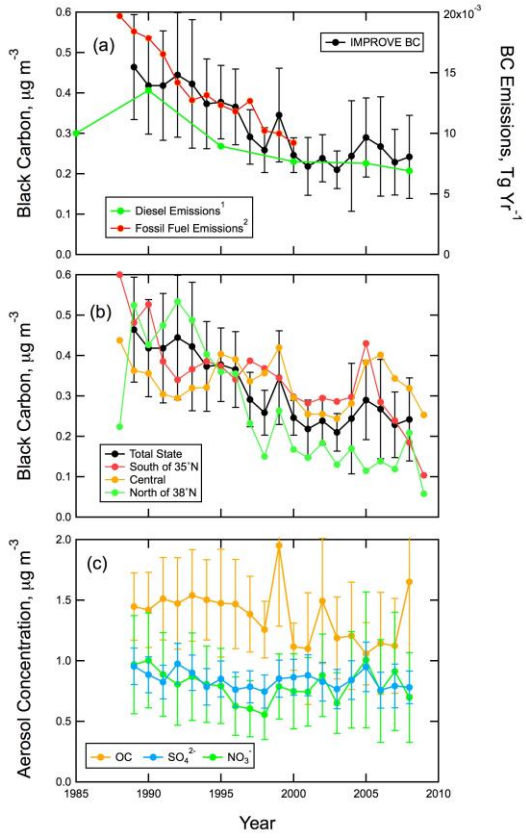

Figure 4.1 (a) Annual means of measured Black Carbon (left axis) and BC fossil fuel emissions (right axis) in California from 1985 to 2008. Error bars correspond to standard deviation between measurements at each station. Dashed lines indicate a linear fit. Aerosol measurements from the IMPROVE network, emission inventories from (1) CARB, (2) [*Ito and Penner*, 2005] (b) Annual means of BC measured in Southern (South of 35 N), Northern (North of 38 N),

and Central California (c) Annual means of measured Sulfate, Nitrate, and OC from IMPROVE network.

	Mean value		% Rate of change				
	1989	2008	Annual	Spring (Feb-Apr)	Summer (May-Jul)	Fall (Aug-Oct)	Winter (Nov-Jan)
BC, μg m^{-3}	0.46±0.13	0.24±0.10	**-4.8**±0.5	-5.9±0.2	-3.6±0.2	-4.3±0.5	-6.6±0.4
BC/Sulfate	0.39±0.11	0.36±0.12	**-6.1**±0.4	-7.8±0.5	-4.6±0.3	-4.6±0.6	-7.6±0.8
BC/non-BC	0.14±0.01	0.07±0.01	**-3.0**±0.3	-3.3±0.3	-3.5±0.2	-3.5±0.4	-3.1±0.2

Table 4.1 Annual mean and standard deviations of measured BC concentration and BC/non-BC Aerosol ratios in California. Rates of change are calculated based on a linear fit for annual mean values between 1989 and 2008.

4.4 Spatial trends in BC concentration

The twenty year average BC concentration measured at the IMPROVE sites is illustrated in Figure 4.2(a). A low background concentration between 0.1 and 0.2 μg m^{-3} is observed over the majority of the state, with significantly higher concentrations (up to 0.7 μg m^{-3}) in the central valley and the south coast air basin, indicating that anthropogenic emissions are the principal source of BC in the state. Figures 4.2(b) and 4.2(c) illustrate the rate of change in BC concentration and BC/non-BC aerosol (represented here by sulfate, nitrate, and OC) respectively, which are negative over the entire state indicating that anthropogenic aerosols generated by BC emissions have been declining in California between 1989 and 2008.

Although the IMPROVE network has been in continuous operation since 1987, coverage across the component stations has not been temporally uniform. Any significant biasing of the statewide trend introduced due to IMPROVE sites coming online or going offline over the study period can be understood by examining the non-aggregated trends at the 6 sites with complete coverage between 1988 and 2007. These sites are illustrated in Figure 4.3(a) and span the entire geographic extent of California, providing a reasonable sampling cross-section. Figure 4.3(b) illustrates the trends in annual means for measured BC at each of these stations. Similar to the statewide trend, we see a high inter-annual variability, which still gives rise to a total decrease at the decadal time scale. In fact, the decrease between 1988 and 2007 at each of the sites is found to be comparable to the observed 50% statewide decrease, for example 0.22 to 0.13 μg m^{-3} (-40%) at LAVO, 0.14 to 0.07 μg m^{-3} (-50%) at PORE, and 0.45 to 0.20 μg m^{-3} (-55%) at PINN.

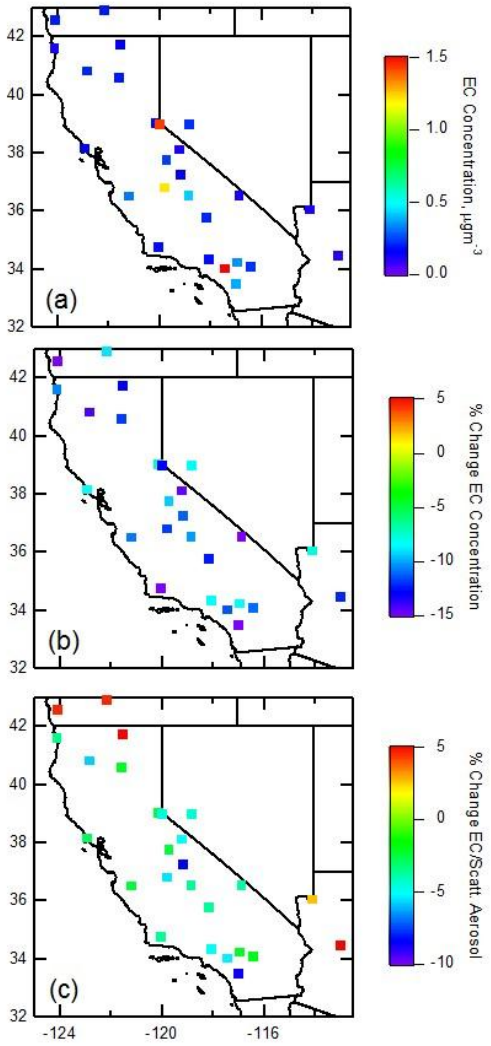

Figure 4.2 (a) 20-year average BC Concentration from IMPROVE network in California expressed in µg m^{-3} (b) Average rate of change of BC Concentration, % (c) Average rate of change of BC/non-BC aerosol ratio. Locations of the measuring stations are indicated.

Since these 6 sites establish a reliable baseline and confirm our overall statewide trend from Figure 4.1, we expand our analysis to include all sites with measurements spanning at least 75% of three time periods between 1988-1997, 1998-2007, and 1988-2007. With the exception of South Lake Tahoe (SOLA) these sites are all located in remote areas. To contrast these measurements to urban trends, we also include results from BC measurements collected at three locations in the Bay Area [*Novakov et al.*, 2008a; b]. Figure 4.3(c) shows the change in BC as a function of average BC concentrations and Figure 4.3(d) shows the change as a function of latitude. At each of these sites we find an average annual decrease between 40 and 70% from 1988-1997 and between 15 and 40% from 1998-2007, which correspond to a total decrease between 40-60%

at each of these sites matching up well with the statewide average of 50%. We do not find any correlation with either the total BC concentration or latitude, indicating that the downward trend is fairly uniform across the state, in both rural and urban areas and is unlikely to be biased by a few outliers.

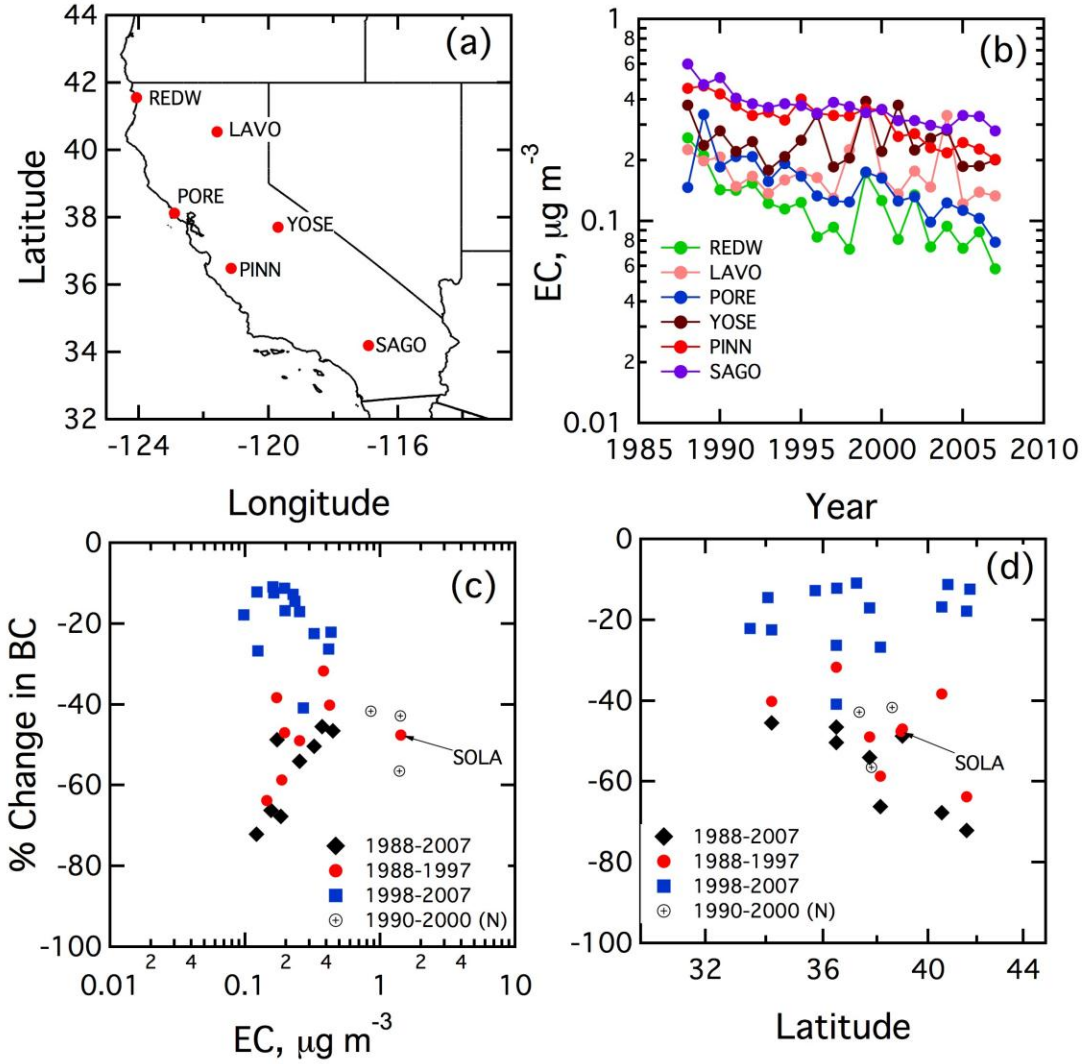

Figure 4.3 (a) Location of IMPROVE sampling stations in continuous operation from 1988-2007 in California, (b) Annual means of measured BC at each site in continuous operation (c,d) Average annual rate of change in mean BC concentration for IMPROVE sites with greater than 75% coverage in each time period. Urban measurements from South Lake Tahoe (SOLA, labelled) and the Bay Area (designated N) [*Novakov et al.*, 2008a] included for comparison.

4.5 Changes in aerosol radiative properties

Figure 4.4 illustrates the approximately 50% reduction in ratio of BC (an absorbing aerosol) to the total sulfate, nitrate, and OC (primarily scattering

aerosols), from 0.14 (1989) to 0.07 (2008). We can infer an aerosol absorption coefficient (k) from the BC concentrations using a conversion factor of 7.5×10^{-6} as recommended by Bond and Bergstrom [2006] or 10.1×10^{-6} m^2 mg^{-1} recommended under the IMPROVE protocol [*Horvath*, 1993]. The k can then be combined with nephelometer measurements [*Malm and Gebhart*, 1996; *Malm and Pitchford*, 1997] of the aerosol scattering coefficient (s) from the IMPROVE network to obtain the single scattering albedo (SSA) defined as: s/(s+k). A more useful quantity for tracking the forcing impact of absorbing aerosols is the co-single scattering albedo Ae = (1-SSA), which is the quantity shown in Fig. 4.3. Ae peaked at 0.13 in 1989 and decreased by about 40% to 0.08 in 2004 (the last year for which data were available). Values less than 0.05 will typically lead to net negative forcing while values greater than about 0.15 lead to net warming, and for values in between 0.05 and 0.15, the sign and magnitude will depend on the surface albedo, cloud fraction, vertical profile and latitude and season. The observed scattering coefficient changed very little with time therefore trends in Ae closely resemble the trend in BC. The negligible trend in s is consistent with corresponding small trends in SO4 and NO3 (which dominate scattering) shown in Fig. 4.1(c), thus demonstrating the over all consistency of the various data sets used in this study for establishing the impact of diesel emission reductions. In summary, the rate of decline in BC concentrations has outpaced the decline in non-BC aerosols (primarily sulfate), resulting in a reduced warming, or equivalently cooling, potential of aerosols in California.

4.6 Implications for direct radiative forcing

In order to use the surface data for exploring implications for radiative forcing, we need to examine the link between surface SSA and column SSA, which is discussed next. Figure 4.5 illustrates the monthly average SSA over California between 1988 and 2010 from both the IMPROVE measurements at the surface and the AERONET network [*Holben et al.*, 1998; *Holben et al.*, 2001] data (available from 3 stations in California between 2005 and 2010) which estimates the column averaged SSA. Though the increase in calculated surface SSA is expected as a consequence of decreasing BC concentrations, the trend is consistent with the more recently available column AERONET observations. It is important to note that these two quantities are not directly equivalent, as the near-surface SSA will be largely driven by regional emissions, while the column-integrated SSA will also be impacted by vertical stratification in the mixing state of aerosols, and long-range transport. The correspondence in trends illustrated in Figure 4.5 however indicates that the column SSA values, which drive the radiative forcing are primarily dominated by regional emissions.

The impact on direct radiative forcing due to the changes in aerosol loadings is estimated with a Monte Carlo radiative transfer model [*Kim and Ramanathan*, 2008]. The calculated aerosol optical depth (AOD) decreased about 19% from 0.27 in 1989 to 0.22 in 2008. The modeled Ae decreased from 0.116 to 0.077, comparing well with the observed trend (Fig. 3). In the forcing estimates, we used 0.23 and 0.18 for AODs in 1989 and 2008 to match the regional mean

MODIS/Terra AOD retrieval[*Platnick et al.*, 2003] (0.18) in 2008 over California, but retained the AOD decrease based on the IMPROVE values.

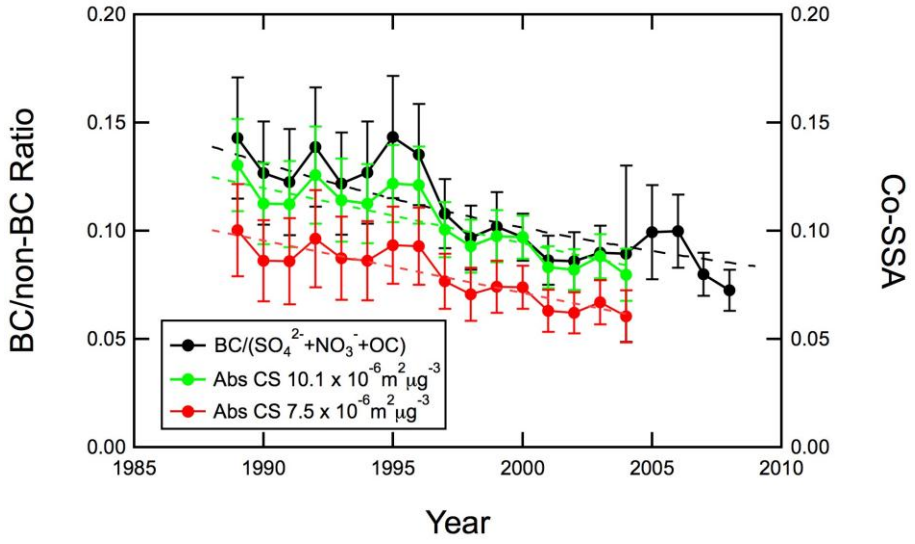

Figure 4.4 Time series of measured BC/non-BC Aerosol ratio from the IMPROVE network in California (left axis) and derived co-Single Scattering Albedo for visible light (right axis). Co-SSA is calculated using 10.1 x 10^{-6} m^2 mg^{-1} [*Horvath*, 1993] and 7.5 x10^{-6} m^2 mg^{-1} [*Bond and Bergstrom*, 2006] for BC absorption cross section.

The cooling effect of aerosols at the top-of-the Atmosphere (TOA) changed by -1.4 W m^{-2} between 1989 and 2008, with the absorption in the atmosphere decreasing by 6.5 W m^{-2} and incoming solar radiation reaching the surface increasing by 5.1 W m^{-2}. The uncertainty in the estimated changes in TOA forcing arises from the model-input values for AOD and the vertically integrated SSA. The estimated uncertainty in forcing is about 8% (surface), 14% (atmosphere) and 28% (TOA) due to the differences between the calculated and satellite-based AOD. With respect to SSA, the observationally based SSA (Fig. 4) is only for the near-surface air, which we assumed to hold for other levels in the atmosphere. We don't have observational data for the vertical variation in SSA, which prevents us from making an objective estimate for the uncertainty. Our guess is that it should be at least ± 50%. The estimated large cooling effect of the reduction in diesel related BC aerosols is consistent with recent model predictions [*Jacobson*, 2010c].

The surface brightening of 5.1 W m^{-2} (±60%), caused by reduction in diesel based BC is about 3% of the net surface solar radiation (190 W m^{-2}), is large enough to be detectable. Such large increases in surface solar radiation as a

result of aerosol (BC in our case) reductions is consistent with an observed clear-sky brightening of 5.0 W m^{-2} observed over the United States between 1997 and 2006 [*Long et al.*, 2009]. This does not necessarily imply that reduction in BC should have contributed to surface warming over California, since the decrease in atmospheric solar absorption (6.5 W m^{-2}) is much larger, leading to a TOA negative forcing and mitigation of human impact on global warming. The magnitude of the surface brightening and atmospheric decrease in solar heating are sufficiently large to have had an impact on regional heat and water budget. Black carbon reduction should also have led to alteration of clouds by deceasing cloud nuclei and cloud albedo (warming effect; see [*Chen et al.*, 2010; *Jacobson*, 2010c]) and increased cloud fraction (cooling effect; see [*Ackerman et al.*, 2000]). The net effect of BC interactions with clouds is estimated to be warming [*Jacobson*, 2010c], but this requires further study and the California data reported here should offer an excellent opportunity to validate published hypotheses for BC-Cloud interactions.

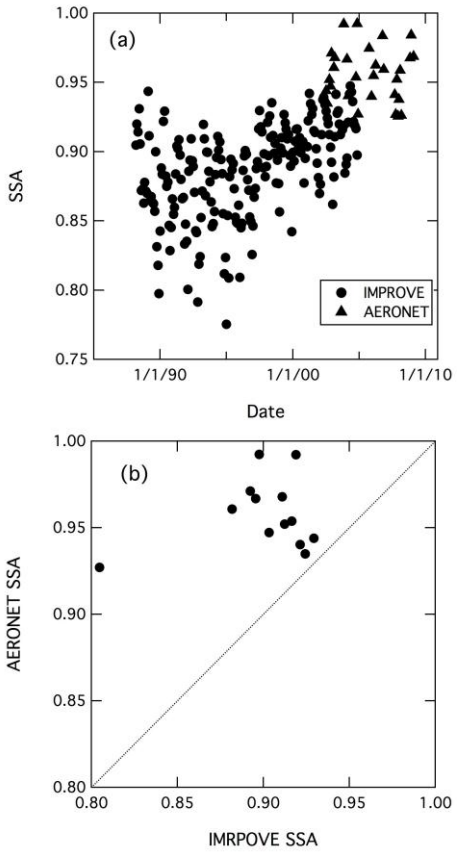

Figure 4.5 (a) Monthly averaged SSA calculated from measurements and retrieved from the AERONET network in California from 1988-2010 (b) Comparison of SSA monthly averages from IMPROVE and AERONET between 2007 and 2008. The 1:1 line is drawn for clarity.

4.7 Impact of diesel emissions control policies

California has been a national and global leader in implementing aggressive laws to reduce particulate emissions. Such laws led to the introduction of Diesel Particulate Filters (DPFs) in non-road machines since 1980, and in automobiles since 1996. The first state-wide regulation on diesel engine emissions was introduced in 1987 with the first California Heavy Truck rule capping particulate emissions at 0.60 g/BHP Hour, and progressively tighter standards have been subsequently implemented. While no jurisdiction has made DPFs mandatory, the increasingly stringent emissions regulations mean that eventually all on-road diesel engines will be fitted with them – for instance, the American 2007 heavy truck engine emissions regulations cannot be met without filters. The "Risk Reduction Plan to Reduce Particulate Matter Emissions from Diesel-Fueled Engines and Vehicles" adopted by the California Air Resource Board (CARB) established further goals to reduce diesel emissions in California by 75% in 2010 and 85% in 2020. To support the diesel risk reduction plan CARB has introduced regulations including (but not limited to) the control equipment verification program (2007), public transit bus rules (2000), transport refrigeration unit regulation (2003), and proposed future idling regulations, details of which may be obtained under the California Code of Regulations Section 13 [*CCR*, 2010]. These regulations have a mandatory character (in California) but allow a flexibility of approach which can be met by a variety of approaches including retrofitting engines with emission controls systems (such as DPFs and oxidation catalysts), replacement of existing engines with newer technology engines, and restrictions placed on the operation of existing equipment. Significantly, the reduction - 0.007 Tg Yr^{-1} in diesel emissions and 0.008 Tg Yr^{-1} in total BC emissions[*CARB*, 2008] – between 1990 and 2008 - is comparable, indicating the total decrease in BC is almost entirely attributable to diesel emission standards.

4.8 The Role of urban sites and South Lake Tahoe

While reduction in dispersed diesel emissions appear to be the primary driving force behind reduced BC concentrations, the inclusion of urban sites could potentially bias trend analyses due to their higher absolute concentrations. Such a concern would be legitimate had we focused on long-lived greenhouse gas trends, but urban locations are just as important as rural locations in obtaining statewide BC trends. Rather, our analyses would have been more representative had there been more IMPROVE locations in urban sites. This is a rather moot issue, since the trends we see in individual stations are not strongly dependent on either the absolute concentrations or on the geographical location (see Figure 4.3). In fact, the trends in urban stations are similar to those in rural sites.

Observed BC reduction at the South Lake Tahoe urban site can also be attributed to mitigation of residential wood smoke emissions following the retrofit program of 1993. The sharp decrease in both organic carbon (OC) and BC starting in 1993 illustrated in Figure 4.6(a) is consistent with this conclusion, but may not provide a complete picture, as aerosol concentrations at a site cannot be

interpreted solely from local emission sources. In fact, long-range transport of pollutants has been well established in the literature [*Hadley et al.*, 2007; *VanCuren et al.*, 2005; *VanCuren and Cahill*, 2006]. Further, aerosol phase potassium and a lower EC/OC ratio (compared to fossil fuel emissions) are widely accepted tracers of wood smoke and biomass burning aerosols [*Cachier et al.*, 1989; *Echalar et al.*, 1995; *Novakov et al.*, 2000]. If BC reduction were to be attributed solely to wood smoke, we also then also expect to see an increase in the EC/OC ratio and a decrease in the K/EC ratio. Figure 4.6(b) reveals, however, just the opposite. It shows that EC/OC ratio decreased while the K/EC ratio increased over the same time period in South Lake Tahoe. The observed trends then raise the interesting possibility that though the total BC emissions attributable to residential wood burning have decreased, the contribution to BC from diesel sources may have decreased at a faster rate. This indicates that even at the South Lake Tahoe site, BC mitigation from diesel sources is a significant factor.

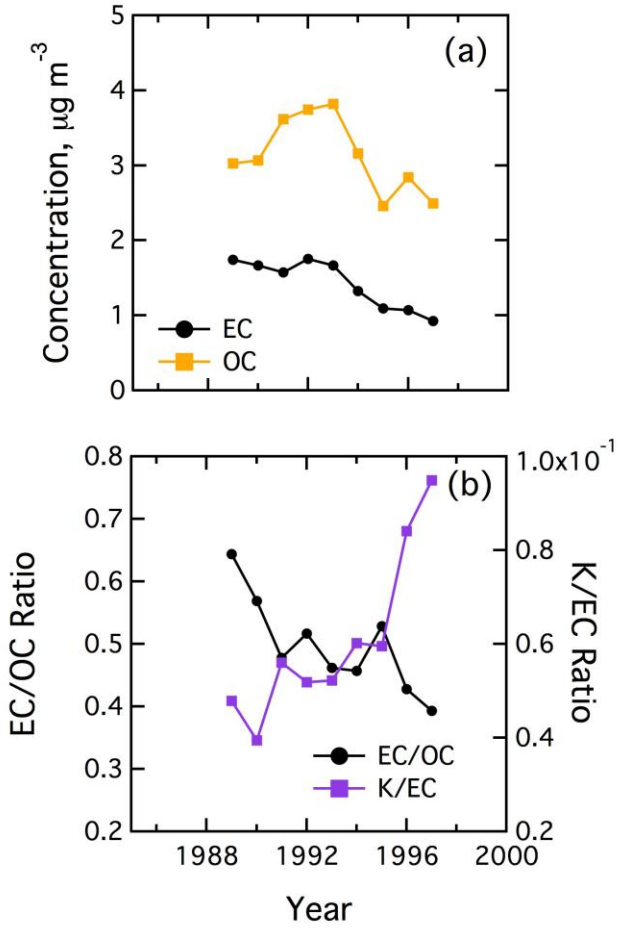

Figure 4.6 Annual mean measurements from the South Lake Tahoe (SOLA) station in California for (a) OC and EC absolute concentrations and (b) EC/OC and K/EC ratios.

4.9 EPA speciated trends network

The IMPROVE network typically represents non-urban and background aerosol concentrations as it's monitoring stations are located by design in state and national parks, and other remote locations. A parallel monitoring network maintained by the EPA, called the speciated trends network (STN) has been in operation since 2000 and follows a similar filter based protocol to measure fine mode aerosols in urban centers. At present, there are 9 sites operating in California as a part of the STN. Figure 4.7 compares trends in the EC annual mean measured by the two networks.

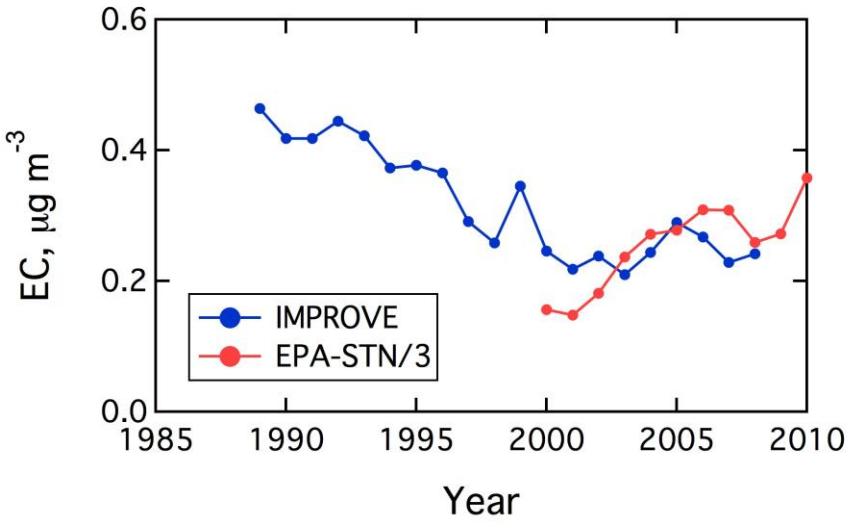

Figure 4.7 Annual mean measurements of EC from the IMPROVE and EPA-STN networks in California that represents non-urban and urban measurements respectively. The higher urban concentrations measured by the EPA-STN network are scaled down by a factor of three to enable a direct visual comparison between the two networks.

We find the trend in the short period covered by the STN (10 years) parallels the fluctuations in the means observed in IMPROVE concentrations for the same time period, with a higher magnitude reflecting its urban locations. The coverage however is inadequate and fails to capture the long term decreases in EC concentration that occurred starting in the 1960s (Chapter 2) and were measured by the IMPROVE network. Due to these concerns, we remain confident that the trends indicated by the more reliable IMPROVE and COH based networks that also have a larger spatial and temporal coverage, reflect the true nature of BC concentration in California.

4.10 Conclusions

The availability of aerosol phase measurements of BC from the IMPROVE monitoring network, in conjunction with California's air pollution laws for BC

reduction, provide a comprehensive picture of atmospheric BC trends over California. The data indicate that the annual mean BC concentration has decreased by 50% from 0.46 μg m^{-3} in 1989 to 0.24 μg m^{-3} in 2008, and followed a parallel trend in the reduction of fossil fuel (primarily diesel) BC emissions (also about 50%). The correlation between BC decline and diesel emission decline is further supported by the relatively constant concentrations of sulfate, nitrate, and OC aerosols over the same time period. The use of multi-site aerosol phase measurements allows us to constrain changes in the SSA compared to retrievals from AERONET, and construct vertical concentration profiles within the boundary layer. These measurements provide an invaluable resource for determining the climate impact of BC, and in conjunction with emission inventories provide a direct link between regulatory control policies and the long-term impact of anthropogenic emissions. Our model calculation indicates that the decrease in BC in California has lead to a cooling of 1.4 W m^{-2} (±60%). The regulation of diesel fuel emissions in California therefore has proven to be a viable control strategy for climate change in addition to mitigating adverse human health effects.

5.0 Solar absorption by black carbon and brown carbon

5.1 Introduction

As mentioned in Chapter 4, black carbon (BC) emitted from combustion sources such as automobile exhaust is commonly considered to be equivalent to elemental carbon (EC), and the organic fraction of carbonaceous aerosols (OC) is considered to only scatter light, and is therefore found to have a cooling impact on the climate [*Koch et al.*, 2007; *Myhre et al.*, 2008]. It is important to realize not only does BC from all emission sources contain both elemental and organic fractions [*Chow et al.*, 2009], but non-soot OC, particularly that emitted from biomass burning processes has a significant absorbing component at short wavelengths that may be comparable to the EC absorption [*Andreae and Gelencser*, 2006; *Hoffer et al.*, 2006; *Jacobson*, 1999; *Kirchstetter et al.*, 2004; *Magi et al.*, 2009]. Consequently, OC that is weakly absorbing in the visible and near-UV spectrum may also contribute to the warming potential of aerosols. In addition to their differing spectral dependence, the wide range of optical properties reported for EC, OC, and mineral dust in the literature [*Alfaro et al.*, 2004; *Bergstrom et al.*, 2007; *Bond and Bergstrom*, 2006; *Clarke et al.*, 2004; *Fialho et al.*, 2006] leads to uncertainties in estimating the absorption attributable to these species. While the attribution of ambient aerosol absorption to EC may be a reasonable approximation in areas dominated by fresh soot emissions, it may lead to misleading estimates of the aerosol forcing when other light absorbing particles are present.

In more complex environments, a separation of the total absorption into different chemical species is therefore essential, both for constraining the large uncertainties in current aerosol forcing estimates [*Forster et al.*, 2007] and for informing any emissions based control policy. Recent studies reporting the fractions of EC, OC, and mineral dust absorption follow one of three general approaches. First - measured optical and size distribution properties of the aerosol are related to spatial emission patterns to determine the dominant absorbing species [*Dubovik et al.*, 2002; *Eck et al.*, 1999; *Rizzo et al.*, 2011; *Russell et al.*, 2010]; second – detailed aerosol transport and chemistry models are used in conjunction with assumed optical properties to estimate absorption which is validated against measurements [*Arola et al.*, 2011; *Chin et al.*, 2009; *Dey et al.*, 2006; *Koven and Fung*, 2006; *Park and Chang*, 2007; *Sato et al.*, 2003]; and third – closure studies are performed to relate collocated chemically resolved measurements of aerosol mass with optical measurements [*Sandradewi et al.*, 2008; *Yang et al.*, 2009]. A recent study by Chung et al. [*Chung et al.*, 2012b] exploited the wavelength dependence of the absorption aerosol optical depths (AAOD) of BC, BrC and dust aerosols to resolve their relative contribution to the observed absorption optical depths, but used published values for the wavelength dependence of AAOD for OC (brown carbon) and assumed the

single scattering albedo (SSA) for EC and OC instead of self-consistently determining these critical properties from observations. This study uses the formalism of Chung et al. without invoking the assumptions noted above. Specifically, the present approach offers the following major improvements: – (1) By solving for BC and BrC simultaneously we eliminate the need for assumption of CA (carbonaceous aerosol) properties that depend on source specific compositions, (2) The OC AAE is determined empirically by exploiting measurements at the longer wavelengths of 870 and 1020 nm, (3) We consider scattering optical depths to better constrain the phase space based on size, and finally (4) We also offer empirical estimates of the SSA. The proposed empirical scheme only requires a single set of aerosol optical measurements, allowing for spatial and temporal coverage on a nearly global scale. We provide a robust set of constraints that will allow climate modelers to improve the estimation of the BrC aerosol forcing.

5.2 Partitioning AAOD

The total aerosol optical depth (AOD) represents the total light extinction due to scattering and absorption by an aerosol and is related to the absorption aerosol optical depth (AAOD) through the single scattering albedo (SSA) as

$$AAOD(\lambda)=(1-SSA(\lambda)) \times AOD(\lambda). \quad (5.1)$$

The AOD and AAOD are extensive properties that depend on the total aerosol concentration, while the SSA (the fraction of total aerosol extinction due to scattering) is an intensive property that depends only on the aerosol composition; however the value of all three depends on the wavelength of the incident light. The spectral dependence of the AOD and AAOD is related to reference values with an exponential dependence

$$AOD(\lambda)=AOD_{ref}(\lambda/\lambda ref)^{-EAE}$$

$$AAOD(\lambda)=AAOD_{ref}(\lambda/\lambda ref)^{-AAE} \quad . \quad (5.2)$$

In the classical formulation, the extinction Angstrom exponent (EAE) and absorption Angstrom exponent (AAE) are thought to be constants, however recent studies have shown them to depend on the wavelength, particle size, and particle composition [*Flowers et al.*, 2010; *Gyawali et al.*, 2009; *Moosmuller et al.*, 2011]. Since the total AAOD is an extensive property, the contributions due to EC, OC, and dust are additive such that

$$AAOD(\lambda)=AAOD_{EC}(\lambda)+AAOD_{OC}(\lambda)+AAOD_{dust}(\lambda). \quad (5.3)$$

Equations 5.2 and 5.3 can be combined to generate a set of independent equations that comprise our primary formulation.

$$AAOD(\lambda i)=AAOD_{ref,EC}(\lambda i/\lambda ref)^{-AAEEC,i}+AAOD_{ref,OC}(\lambda i/\lambda ref)^{-AAEOC,i} +AAOD_{ref,dust}(\lambda i/\lambda ref)^{-AAEdust,I} \quad (5.4)$$

If the AAOD is known at at least three wavelengths (i.e. i=1,2,3), the set of three equations 5.4 can be solved for the three unknown reference AAOD values corresponding to EC, OC, and dust, which can then in turn be used to partition the AAOD at any wavelength. The complete set of AAE values parameterize these equations and constrain the phase space in which physically relevant solutions exist. There are only two inherent assumptions in this formulation – first, the AAE values for the component absorbing species EC, OC, and dust are intrinsic properties that are not dependent on the mixing state; and second that the measured AAOD value represents a well mixed sample of these species.

The full implementation of this method requires knowledge of the AAE values to partition the AAOD and the SSA values in order to determine the AOD. In theory a number of pathways can be employed to determine these parameters, but as stated in the introduction, in this work we rely only on empirical values derived from optical measurements of ambient aerosols. Finally, since the absorption and scattering components of extinction can be related to aerosol chemistry and size respectively [*Horvath and Noll*, 1969], we use the Scattering Angstrom Exponent (SAE) in place of the EAE for the remainder of this work.

5.3 Aerosol Robotic Network (AERONET)

The ground based AERONET (Aerosol Robotic Network), a globally distributed network of automated sun and sky radiometers [*Holben et al.*, 2001] provides long-term, continuous, and readily available measurements of aerosol optical properties that are an ideal resource for this study. In addition to multi-band retrievals of AOD between 340 and 1020 nm from direct sun measurements, the inversion algorithm provides SSA (and corresponding AAOD) estimates from sky radiance measurements at 440, 675, 870, and 1020 nm [*Dubovik and King*, 2000]. Several AERONET sites are dominated by emissions corresponding to a single absorbing aerosol [*Russell et al.*, 2010]. To parameterize Equation 5.4 with AAE values for EC, we use fossil fuel dominated sites separated into urban and non-urban regions. Similarly, we use biomass burning dominated sites to parameterize OC/BrC, and dust dominated sites for dust. Table 5.1 provides the details of the sites selected for this analysis. We use the daily average quality assured data (designated as Version 2 Level 2.0). Although this limits the total number of valid SSA (and corresponding AAOD) retrievals, there are however sufficient data for the results to be statistically significant.

Since the primary focus of this work is partitioning absorption in the visible and near-UV spectrum, we select the three shortest AERONET wavelengths for the remainder of our analysis. We designate the angstrom exponents for AOD and AAOD between 440 and 675 nm as SAE1 and AAE1, and similarly the angstrom exponents between 675 and 870 nm as SAE2 and AAE2 respectively.

Group	Dominant Emission Source	Sites	Valid SSA retrievals	Reference
DU	Dust	Tamanrasset, Solar Village, Hamim, Eilat	1312	[*Kim et al.*, 2011]
BB	Biomass Burning	Abracos Hill, Alta Floresta, Belterra, Campo Grande, Petrolina, Rio Branco, Mongu, Skukuza	1452	[*Hoelzemann et al.*, 2009; *Magi et al.*, 2009]
UF	Urban Sites, Fossil Fuel combustion	Billerica, CCNY, Fresno, GSFC, Halifax, MD Science Center, Hamburg, IFT Leipzig, ISDGM, Mainz, Palaiseau, Rome, Hong Kong, Karachi, New Delhi, Taipei CWB, Kanpur	2105	[*Xia et al.*, 2008]
NF	Non-Urban Sites, Fossil Fuel and mixed sources	Appledore Island, Bondville, Sioux Falls, Walker Branch, CART Oklahoma, Hyttiala, Tenerife, Toravere, Villefranche, Dongsha Island, Gandhi College, Pantnagar, Xanthi	1385	[*Xia et al.*, 2008]
CA	Mixed	Fresno, La Jolla, MISR-JPL, Monterey, Moss Landing, San Nicholas, Table Mountain, Trinidad Head, UCLA, UCSB	342	

Table 5.1 AERONET sites used to obtain AOD and AAOD measurements.

5.4 Constraining the AAE and SAE

Since dust and carbonaceous aerosols have distinct sources and differing chemical and physical properties [*Russell et al.*, 2010], the determination of dust absorption characteristics is the first logical step in our analysis. However, ambient dust is often mixed with anthropogenic and biogenic pollution even at desert sites (and conversely, combustion dominated sites show influence of dust) [*Eck et al.*, 2010] and the entire DU data set cannot be used to determine properties for pure dust. Compared to combustion aerosols that are predominantly in the fine (submicron) mode close to sources, dust particles are dominated by coarse (supermicron) mode particles that have a weak spectral dependence for the total extinction [*Kim et al.*, 2011]. At the same time, dust particles absorb more strongly at shorter wavelengths, so we can establish thresholds in the AAE1 and SAE1 for identifying dust-dominated (and dust-free) measurements [*Russell et al.*, 2010]. Figure 5.1(a) shows the normalized probability distribution of the SAE1 determined from the AERONET data summarized in Table 5.1. We find a clear separation between the DU and BB/Urban and Non-Urban sites FF measurements. A threshold value of 0.5 in the SAE1 results in a good separation, with 76 % of DU measurements satisfying the

condition EAE1<0.5, compared to only 1% of BB/FF measurements. Figure S1(b) shows a larger overlap when only the AAE1 is considered, with 72 % of DU measurements and 17 % of BB/FF measurements satisfying the condition AAE1>1.5. The AAE2 overlap for all data sets (Figure 5.1(c)), and there is appears to be a separation when the AAE2/AAE1 ratio is considered (Figure 5.1(d)). Due to the existing overlaps in any one of these frequency distributions, we employ a dual threshold to rigorously identify dust dominated measurements - SAE1<0.5 AND (AAE1>1.5 OR AAE2/AAE1<0.4). This condition is satisfied by 66% of the DU points and less than 0.5% of BB/FF points. We calculate the angstrom exponents for pure dust by averaging these measurements and find AAE1 = 2.20±0.50 and AAE2 = 1.15±0.40.

We follow a similar procedure for establishing threshold values for identifying dust-free (alternatively, carbon dominated) measurements. We select the conditions SAE1>1.2 OR AAE2/AAE1>0.8 that are satisfied by 97% of all BB/FF measurements and 18% of the DU measurements. The mean values for AAE1 calculated from dust-free measurements for absorption due to total carbon are 1.06 (FF), 1.14 (NF), and 1.28 (BB), agreeing well with the value of 1.0 typically reported for black carbon [*Bond and Bergstrom*, 2006]. It is important to note two subtle yet important conclusions based on these values. Firstly, the similarity in magnitude across varied geographical regions and emission sources supports the hypothesis that the absorption Angstrom exponent is an inherent intrinsic property. Secondly, the differences can be attributed to different relative amounts of elemental and organic carbon [*Levin et al.*, 2010], with biomass burning aerosols containing a larger organic fraction, and therefore having a larger absorption Angstrom exponent than fossil fuel aerosols.

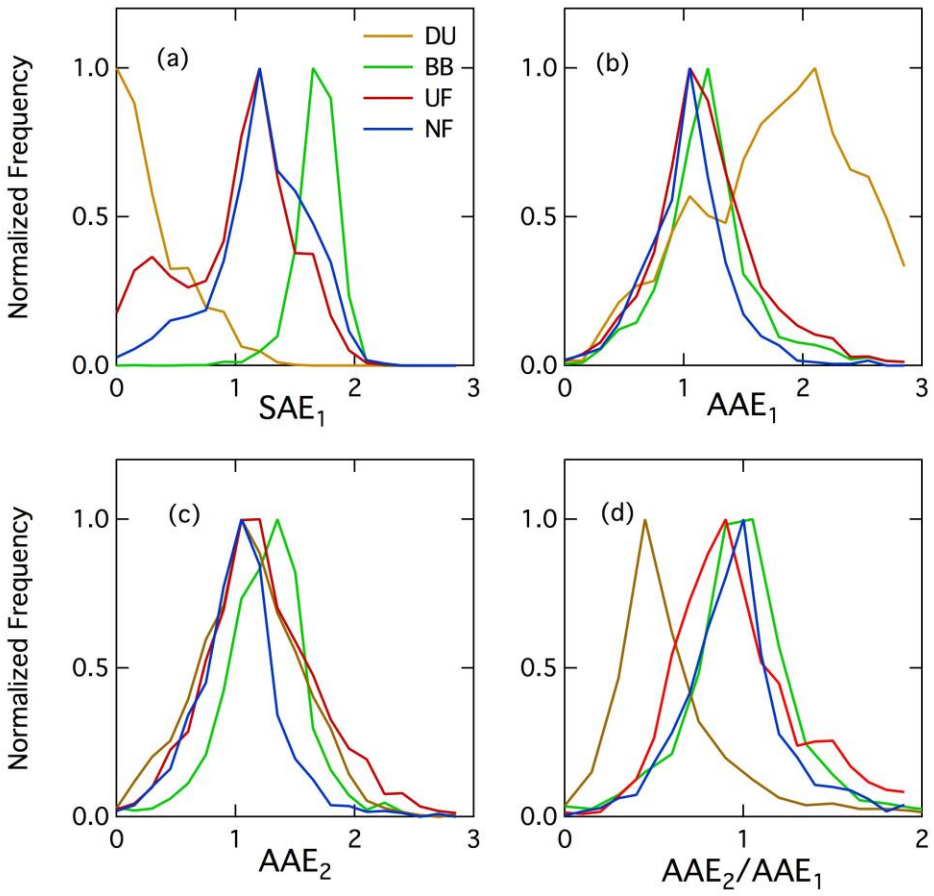

Figure 5.1 Normalized frequency distributions for the (a) Scattering Angstrom Exponent (440-675 nm), (b) Absorption Angstrom Exponent (440-675 nm), (c) Absorption Angstrom Exponent (675-870 nm), and (d) AAE2/AAE1 ratio measured at DU (brown), BB (green), UF (red), and NF (blue) AERONET sites listed in Table 5.1.

Figure 5.2 illustrates the relationship between AAE1 and SAE1 for all AERONET measurements included in this study. While the separation between dust-dominated and dust-free measurements based on the threshold values is clear, all fossil fuel and biomass burning measurements occupy a continuous region of the phase space and the separation of pure EC and pure OC contributions requires additional analysis. Since EC has a weaker spectral dependence than OC, we can posit that the lower end of the AAE1 values reflects absorption due to EC.

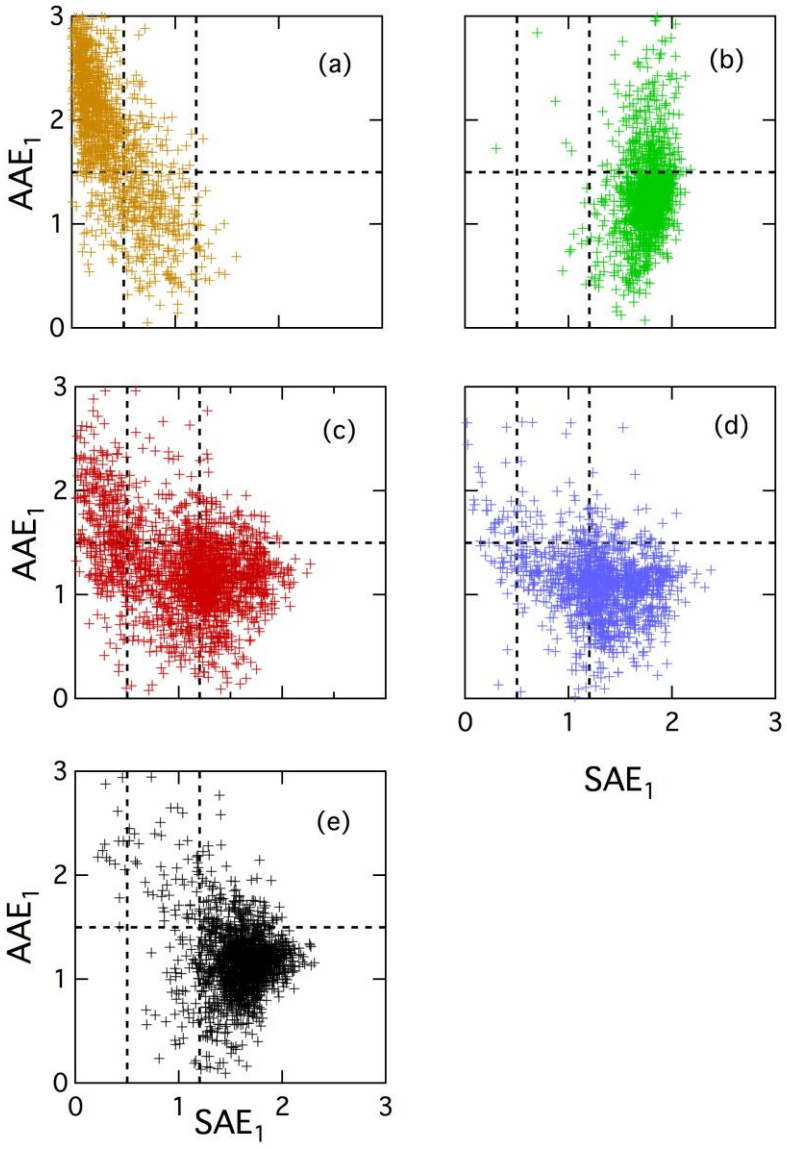

Figure 5.2 Scatter plots of AAE1 and EAE1 calculated from AERONET measurements at (a) DU, (b) BB, (c) UF, (d) NF, and (e) CA sites. Dashed lines illustrate the threshold values of SAE1=0.5, SAE1=1.2, and AAE1=1.5 used to separate dust dominated and dust free regimes.

Figure 5.3 illustrates the mean values of AAE1 calculated by averaging different fractions of the total frequency distribution at the different AERONET sites. We find that the mean AAE1 value asymptotically converges to 0.55±0.24 representing the average low-end baseline for the absorption Angstrom exponent. We relate this value to pure EC, again noting that varying amounts co-occurring OC raise this value in ambient measurements. A similar analysis gives

us a value of AAE2 = 0.83±0.40 for EC. These values are found to be independent of the location, source, and total aerosol concentration [*Bahadur et al.*, 2012a] and therefore can be considered robust representations of pure EC. Since both OC and dust have a stronger spectral dependence than EC, any observed values of AAE lower than these mean values correspond to BC dominated aerosols, leading to our third constraint, If AAE1<0.55 AND AAE2<0.83, AAOD=$AAOD_{EC}$.

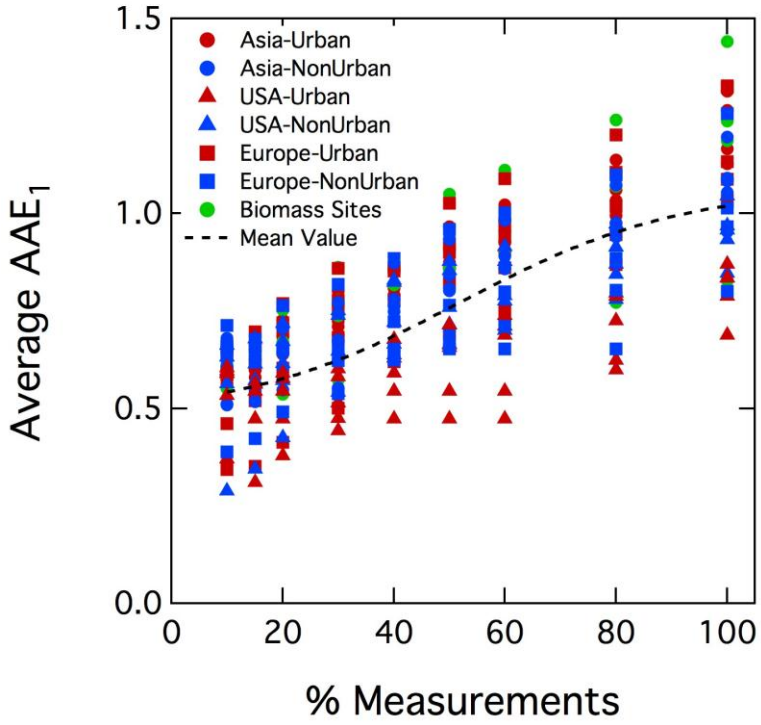

Figure 5.3 Mean value of AAE1 determined by averaging the frequency distribution for AERONET sites in Table 5.1. The dashed line shows a fit to the mean value.

The calculation of OC absorption Angstrom exponents requires one additional assumption. Since OC absorbs primarily in the UV and at shorter visible (lambda<700 nm) wavelengths [*Kirchstetter et al.*, 2004; *Laskin et al.*, 2010], we modify equation 5.4 such that

$$AAOD_{OC}(870) = 0. \quad (5.5)$$

In dust free regions the total AAOD at 870 nm is entirely due to EC, and the EC AAOD at 675 and 440 nm are calculated using equation 5.2. Finally, equation 5.3 is used to calculate the OC AAOD at these two wavelengths, and the value of AAE1 for OC can be determined (since we assume OC does not absorb at 870 nm, the AAE2 is undefined). The frequency distribution of OC AAE1 determined

in this fashion is illustrated in Figure 5.4, and is found to have a narrow distribution centered around 4.5 for all sites, further supporting our hypotheses that the absorption Angstrom exponent is an intrinsic property. The mean value is found to be 4.55±2.01.

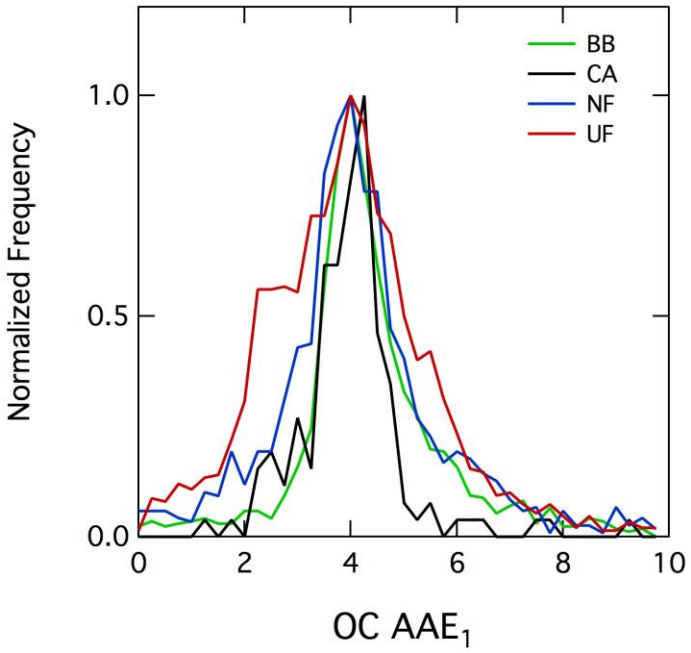

Figure 5.4 Normalized frequency distribution of the OC absorption Angstrom exponent determined from BB, CA, NF, and UF sites between 440 and 675 nm.

Table 5.2 summarizes the values of absorption Angstrom exponents determined in this work, and compares them with the ranges of values reported in the literature, both based on measurements, and determined from models using an assumed refractive index. The AAE values for dust and total carbon lie within the ranges reported in the literature, and typically agree will with the central values. The AAE values for EC determined in this study are lower than literature values, and the values for OC lie toward the upper end reported in the literature. This indicates that EC and OC (treated as pure chemical species in this study) are typically co-mingled in combustion studies, even close to the source. Recent modeling studies have examined the effect of internal mixing between EC/OC on the AAE using a Mie-scattering algorithm in conjunction with a core-shell assumption [*Chung et al.*, 2012a; *Gyawali et al.*, 2009]. OC coatings (representing internal mixing) are found to change the AAE for BC from 0.7 (no particles coated) to 0.1 (all particles coated), with this range being consistent with the value of 0.55±0.24 calculated in this work. One final caveat needs to be considered in our approach – any absorption by fine mode dust (high AAE, high SAE) would be masked by absorption due to OC. Figure 5.2(a) illustrates however that less than 1% of observations in regions with significant dust

absorption lie in this phase space, consistent with most mineral dust being found in the coarse mode [*Kim et al.*, 2011], similarly less than 10% of points in the other regions fall in the coarse dust-region. We therefore do not expect significant errors due to fine dust absorption.

	This Work		Literature, measured		Literature, modeled	
Species	AAE1	AAE2	AAE	Ref.	AAE	Ref.
Dust	2.20±0.50	1.15±0.50	1.0-4.0	[*Coen et al.*, 2004; *Fialho et al.*, 2006; *Russell et al.*, 2010; *Weinzierl et al.*, 2011]		
Total Carbon	1.17±0.40	1.23±0.40	1.0-1.3	[*Bergstrom et al.*, 2007; *Russell et al.*, 2010; *Schnaiter et al.*, 2003; *Virkkula et al.*, 2005]	1.0-1.7	[*Gyawali et al.*, 2009]
BC/EC/Soot	0.55±0.24	0.85±0.40	0.8-1.1	[*Levin et al.*, 2010; *Sandradewi et al.*, 2008]	1.00	[*Gyawali et al.*, 2009]
OC	4.55±2.01	-	1.8-7.0	[*Bergstrom et al.*, 2007; *Clarke et al.*, 2007; *Kirchstetter et al.*, 2004; *Levin et al.*, 2010; *Russell et al.*, 2010; *Sandradewi et al.*, 2008; *Schnaiter et al.*, 2005; *Schnaiter et al.*, 2006]	3.0-6.0	[*Arola et al.*, 2011; *Sun et al.*, 2007a]

Table 5.2 Absorption Angstrom exponents for dust, total carbon, BC, and OC determined in this study and the ranges reported in the literature.

5.5 Single Scattering Albedo

While the total AAOD can be attributed to BC, OC, and dust using equation 5.4, a similar partitioning of the AOD is not possible due to the variable contribution of purely scattering aerosols. Instead, using an ensemble of measurements we try

to locate the limiting case via extrapolation where the influence of scattering aerosols is negligible, and the SSA may be therefore be attributed to the absorbing species only. In order to determine this limit mathematically, we first need to establish a linear relationship between the SSA and AOD. In a mixture of an absorbing aerosol A and non-absorbing aerosol N, the scattering optical depth, SAOD, and the absorption optical depth, AAOD, can be written as:

$$SAOD = SAOD_A + SAOD_N \quad (5.5)$$

$$AAOD = AAOD_A + AAOD_N \quad (5.6)$$

Furthermore, since SSA= SAOD/(SAOD+AAOD), we can rewrite the above equations as:

$$(SSA)AOD = (SSAA)AOD_A + (SSA_N)AOD_N \quad (5.5\text{-a})$$

$$(1-SSA)AOD=(1-SSA_A)AOD_A+(1-SSA_N)AOD_N. \quad (5.6\text{-a})$$

Realizing that SSAN=1, the ratio of the two equations yields

$$SSA/(1-SSA) = SSAA/(1-SSAA) +k(AOD-AODA)/AODA \quad (5.7)$$

Where k=1/(1-SSAA) and the limit of AOD=AODA represents the point where the aerosol consists entirely of a single absorbing species (the limit of interest). The advantage of formulating the AOD as a difference in this manner is that this 0 limit allows us to mathematically isolate the contributions from a single absorbing species (such as EC, or BrC) whereas all absorbing species co-exist to a certain degree even in emissions dominated by a single species. The pure component SSA can be calculated by applying equation 5.7 to sets of observations likely to be dominated by a single absorbing species to minimize deviation from the limit of AOD-AODA=0 – i.e. BC SSA is determined from the fossil fuel burning stations in Table S1, OC SSA is determined from the biomass burning stations, and Dust SSA is determined from the dust dominated stations. As written, Equation 5.7 cannot be directly solved since it contains two unknowns – SSAA and AODA, with SSA and AOD comprising the ensemble of observations. Instead, we determine SSAA recursively using a least-squares regression with an assumed value of SSAA applied to Eq. 5.7, treating observed SSA/(1-SSA) as the y (dependent) variable and (AOD-AODA)/AODA as the x (independent) variable. For a given set of observations, values of SSA and AAODA (based on our partition scheme) are known – we then assume a (initial) value of SSAA from the literature (Table 5.3) allowing us to calculate AODA and (recursively) determine the y-intercept (corresponding to the limit of absorption by a single species), and recalculate a new value of SSAA that is then treated as the new "assumed' value and the process is repeated. When the assumed and calculated SSA values agree within a tolerance of 10%, we consider the solution to have converged.

	SSA, this work			SSA, measured		SSA, GOCART	
	440 nm	675 nm	870 nm	550 nm	Ref.	550 nm	Ref.
BC	0.480	0.428	0.386	0.15-0.30	[*Bond and Bergstrom*, 2006; *Koylu and Faeth*, 1994; *Magi et al.*, 2009; *Schnaiter et al.*, 2003]	0.20-0.50	[*Chin et al.*, 2009]
OC	0.772	0.801	1.000	0.85-0.95	[*Bergstrom et al.*, 2007; *Magi et al.*, 2009; *Russell et al.*, 2010]	0.90-1.00	[*Chin et al.*, 2009]
Dust	0.870	0.901	0.941	0.90-0.95	[*Bergstrom et al.*, 2007; *Russell et al.*, 2010; *Wolff et al.*, 2009]	0.60-0.90	[*Chin et al.*, 2009]

Table 5.3 Wavelength dependent Single Scattering Albedo determined in this work compared with literature values.

Figure 5.5 illustrates the SSA (at 675 nm) calculated for EC, OC, and dust using AERONET sites grouped by region. We find similar values among the different regions, indicating that similar to the AAE, the SSA appears to be an intrinsic chemical property largely independent of the emission source and region. The corresponding wavelength dependence is summarized in Table 5.3, which also shows the range of corresponding measured values, and those currently used in the Goddard Chemistry, Aerosol, Radiation and Transport (GOCART) model.

The SSA is calculated at sites where each absorbing species is expected to be dominant, for example BC SSA is determined only from fossil fuel dominated sites. In summary, the derived SSA for dust and OC are consistent with the range of values reported in the literature [*Bahadur et al.*, 2012a] and both become more absorbing at shorter wavelengths. The spectral dependence of EC SSA on the other hand is weak and within the error at each bar at each wavelength, therefore we use the value at 870 nm (with no OC and minimal dust absorption) for EC. We find a higher SSA for EC (0.38) than that typically reported by measurements (0.15-0.30). The published estimates are for aerosol particles generated in the laboratory, or calculated in models (GOCART) while our SSA is based on ambient observations that are likely to reflect

atmospherically processed EC that may have contamination from internally and/or externally mixed organics. This mixing will tend to enhance the aerosol SSA therefore our SSA values should be considered as an upper limit. Our analysis constrains the EC SSA at 440 nm to values between 0.15 and 0.48, with and average value of 0.38. It should be noted, the derived SSA does not influence the absorption estimates since AAODs were derived independent of the SSAs.

5.6 Concentration Independence of intrinsic properties

A limitation of the AERONET data set used to tune the equations in this work is that SSA retrievals are valid only when the AOD (440nm)>0.4, i.e. high pollution events. This raises the possibility that the intrinsic properties we calculate – the AAE and SSA may be biased and not universal for the dust, EC, and OC.

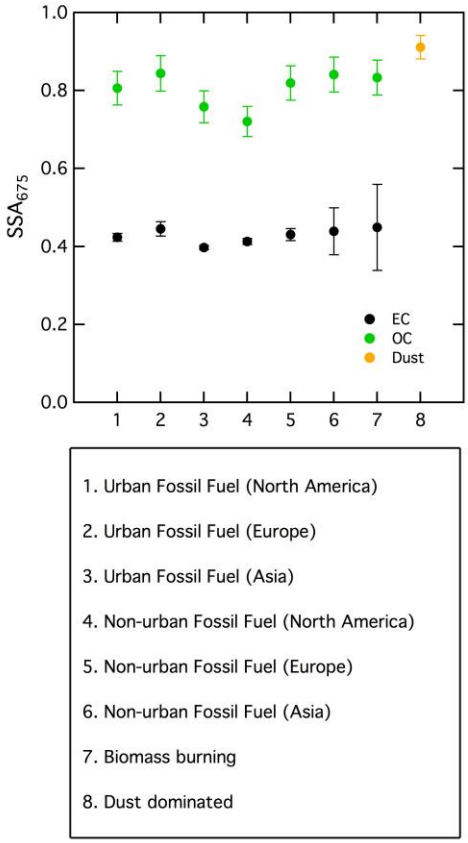

Figure 5.5 Calculated SSA value at 675 nm for EC, OC, and Dust using AERONET stations segregated into source regions as described in Table 5.1.

Figures 5.6(a) and 5.6(b) illustrate the measured SSA and calculated AAE1 as a function of the measured AOD for the AERONET sites listed in Table 5.1. We

find that the AAE is independent of the measured AOD and that the Biomass sites have the largest AAE – consistent with a higher absorbing OC fraction at these sites, while the North American Urban sites have the lowest AAE – again consistent with a larger EC fraction.

Similarly, the scatter plots in Figures 5.6(c) and 5.6(d) show the independence of SSA relative to the AOD, though all measurements with SSA correspond to high pollution events, i.e. AOD>0.4. We find that SSA at 675 is generally higher than SSA at 440 nm – this is consistent with aerosols becoming less absorbing at longer wavelengths – i.e. loss of absorption due to OC and dust. These scatter plots suggests that there is no bias in the AERONET for the SSA and AAE measurements.

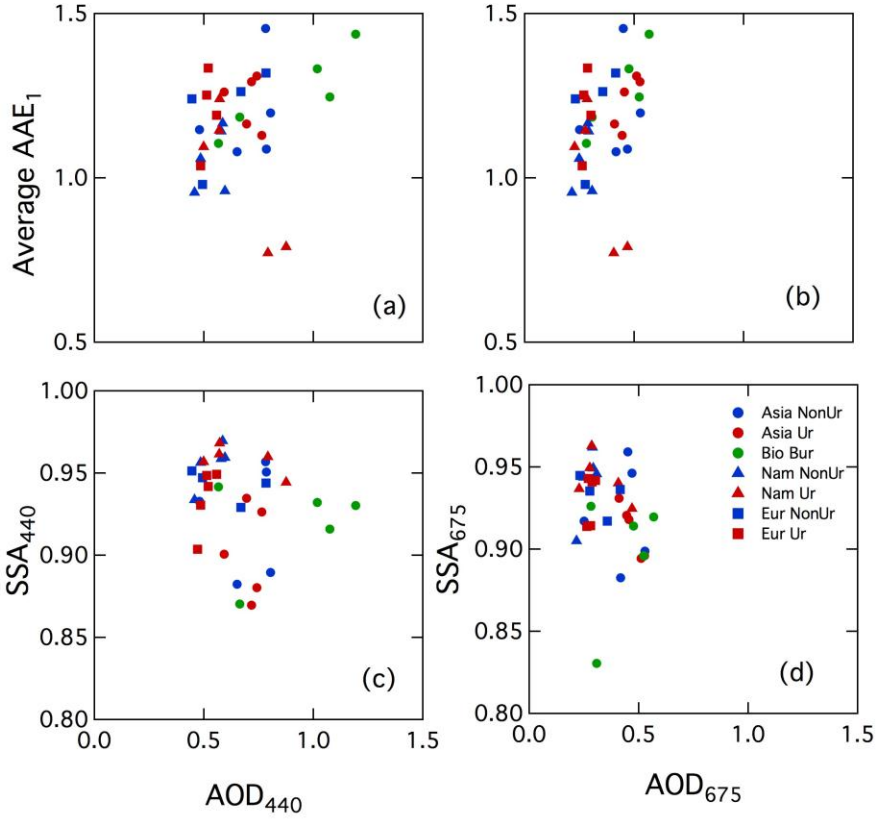

Figure 5.6 The calculated AAE1 for the total aerosol as a function of AOD at (a) 440 nm and (b) 675 nm, and the measured SSA at (c) 440 nm and (b) 675 nm from AERONET sites listed in Table 5.1.

In addition to regional averages, we have also examined the dependence of AAE and SSA on the AOD at individual AERONET sites to isolate any bias. Again, we find that these properties are independent of the total aerosol depth (Figure 5.7), and are likely a function only of the mixing state of the aerosols.

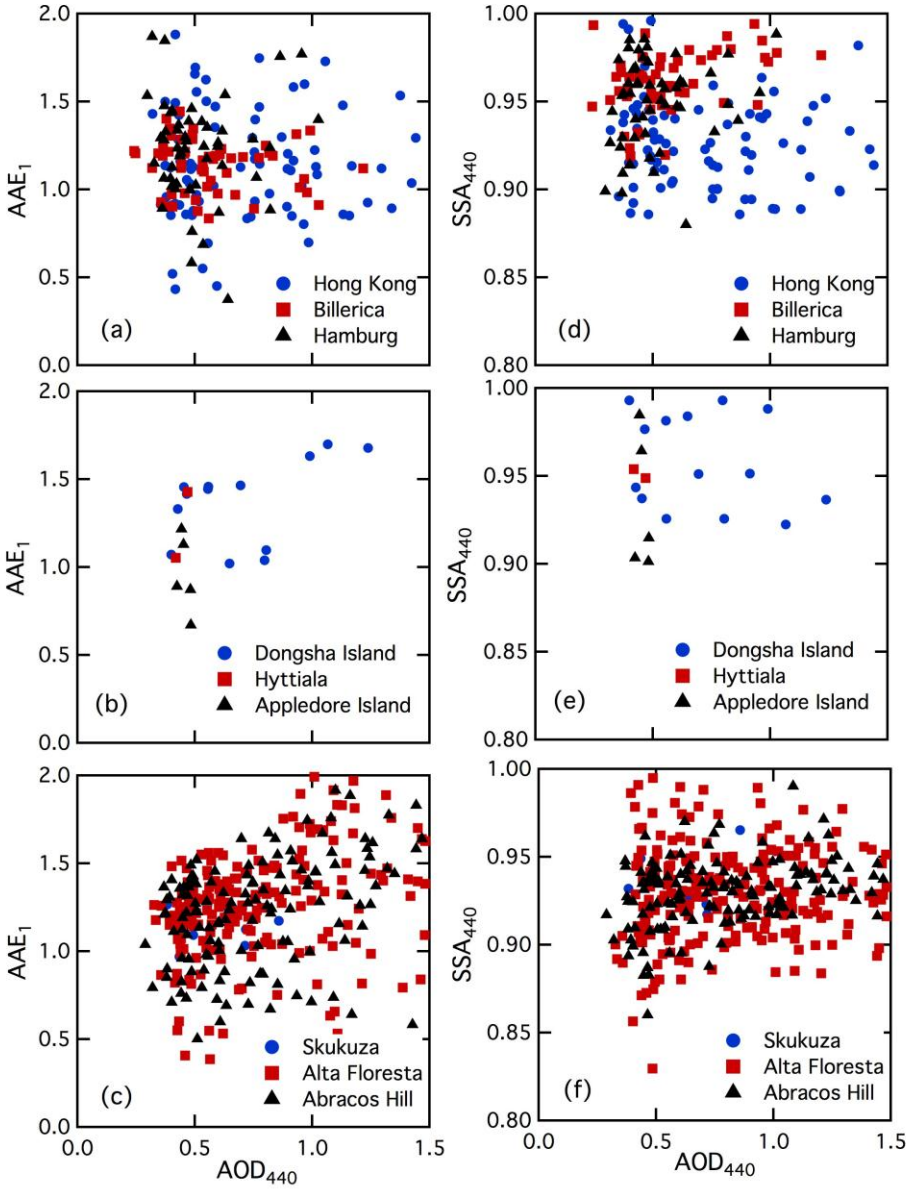

Figure 5.7 (a-c) Calculated AAE1 for the total aerosol as a function of AOD at 440 nm, and (d-f) Measured SSA at 440 nm from selected AERONET sites listed in Table 5.1.

5.7 Brown carbon absorption in California

With the complete set of AAE and SSA values, equation 5.4 with its associated constraints for dust-dominated, dust-free, and EC-dominated regimes can be

applied to any set of multi wavelength absorption measurements. Here we apply this method to California, which provides as ideal test case due to varied aerosol emissions sources, and readily available aerosol measurements and emission inventories. Although the CA AERONET dataset with valid SSA measurements is of insufficient size to construct a complete climatology, we can assess the seasonal and regional trends in aerosol properties and compare them to GOCART model [*Chin et al.*, 2009] predictions and regional emission estimates [*CARB*, 2008]. Currently, the composite set of AERONET measurements with valid SSA retrievals covers the ten-year period between 1998 and 2009. We define North-Central California to be one region (North of 35N), and South California to be the other, such that both contain 5 operational AERONET sites, and the year is divided into two seasons – winter-spring from December to May, and summer-fall from June to November. Table 5.4 summarizes the trends in AOD and AAOD for the absorbing species based on the CA measurements and the GOCART model. Since SSA retrievals are valid only when the total AOD > 0.4 [*Dubovik and King*, 2000], comparing the absolute values results in a significant bias. We therefore report the AOD and AAOD fractions normalized by the total.

In the seasonal comparison, we find that dust contributes a higher fraction of the AAOD in the winter-spring months (19% in North California and 72% in South California) compared to the summer-fall months (7% in North California and 3% in South California). Although the South winter value may be anomalously high due to a few outliers, this general trend is consistent with trans-Pacific transport of dust seen in California in the winter months [*Hadley et al.*, 2007]. We find a much higher absorption attributed to OC in the summer-fall months (27% in the North and 39% in the South) compared to the winter-spring months (15% in the North and 9% in the South) which is consistent with the California wildfires associated with these months [*Westerling et al.*, 2006]. The BC makes up between 57 and 60 % of the AAOD in all cases, indicating that there are no seasonal or regional trends in California fossil fuel emissions. Regionally, dust comprises a higher fraction of the AAOD in North California (consistent with transport events) and OC comprises a higher fraction in the South. The regional pattern may be an indication of absorption due to secondary organics that are typically present in high concentrations in the urban areas of South California. We find good agreement in the OC fraction between our observationally constrained method and the GOCART predictions, with calculated values between 15-39% at 440 nm and 3-11% at 675 nm bracketing the modeled fraction of 11 % at 550 nm. We find a lower contribution and higher variability in the dust (7- 72%) compared to GOCART, which attributes between 38-51% of AAOD to dust. One possible explanation for this difference is that the AERONET sites are primarily located along the coast and may not be sampling dust lofted from exposed lakebeds in inland California and the desert regions of Nevada and Arizona. Finally, we find that the three absorbing species comprise between 16 and 52% of the total AOD, which is typically lower (except the anomalously high South California winter value) than the 27-32 % predicted by GOCART indicating that the aerosol represented by AERONET measurements is more scattering.

This difference can again be explained by the influence of the coastal sites that typically have a larger fraction of optical extinction due to purely scattering sea salt and sulfate particles.

The total AOD and AAOD (at 675 nm) for dust, EC, and OC are illustrated in Figure 5.8 (a) and (b) respectively – while these are based on high pollution events, they still agree with the regional trends in emissions illustrated in Figure 5.8 (c), indicating that our method provides a reasonable partitioning between the three species. Finally, Figure 5.8 (d) provides a unique wavelength dependent perspective on the relative contribution of OC absorption – while it is negligible at long wavelengths, it comprises up to 50% of the EC absorption at short wavelengths, indicating that the treatment of OC as being absorbing is critical for successful estimations of aerosol forcing. This result is consistent with measurements conducted in the Los Angeles basin that attributed between 25 and 30% of UV light absorption to organic carbon species, and between 50 and 62% to black carbon particulates [*Jacobson*, 1999].

AAOD											
		n	This Work 440 nm			GOCART 550 nm			This Work 675 nm		
			Dust	OC	BC	Dust	OC	BC	Dust	OC	BC
North & Central California (>35 N)	Dec-May	77	0.19	0.15	0.66	0.51	0.11	0.38	0.12	0.03	0.84
	Jun-Nov	150	0.07	0.27	0.65	0.46	0.11	0.43	0.05	0.07	0.88
South California (<35 N)	Dec-May	35	0.72	0.09	0.18	0.50	0.10	0.40	0.64	0.03	0.33
	Jun-Nov	66	0.03	0.39	0.57	0.38	0.11	0.52	0.02	0.11	0.87
AOD											
			This Work 440 nm			GOCART 550 nm			This Work 675 nm		
			Dust	OC	BC	Dust	OC	BC	Dust	OC	BC
North & Central California (>35 N)	Dec-May	26	0.11	0.05	0.08	0.25	0.05	0.02	0.04	0.01	0.06
	Jun-Nov	87	0.05	0.11	0.10	0.23	0.05	0.02	0.02	0.01	0.09
South California (<35 N)	Dec-May	35	0.52	0.03	0.03	0.25	0.05	0.02	0.36	0.01	0.05
	Jun-Nov	66	0.01	0.14	0.07	0.19	0.05	0.03	0.01	0.03	0.12

Table 5.4 Dust, OC, and BC fraction of the total AAOD and AOD as determined from AERONET (this work) and the GOCART model in California

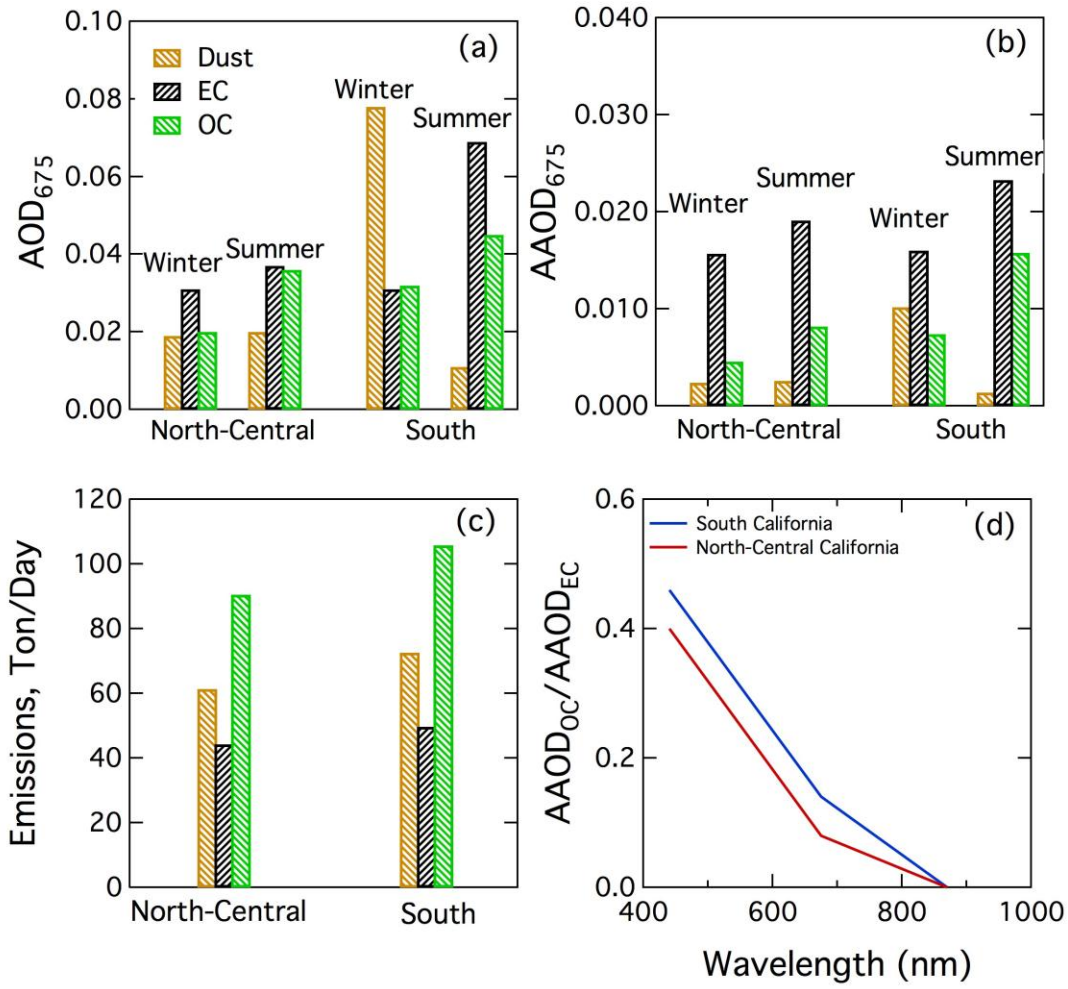

Figure 5.8 Species resolved (a) AOD, (b) AAOD, and (c) emissions in California for EC, OC, and dust. (d) Wavelength dependent relative absorption of OC and EC.

Figure 5.9 illustrates the relative contribution of the dust, OC, and EC to the AAOD at 440 nm in California. We find that dust is the weakest absorber in California, but also has the highest variability, with a mean AAOD of 0.005±0.018. OM comprises the next highest fraction, with a mean AAOD of 0.009±0.014, and EC has an average AAOD of 0.018±0.012. The average contribution to the total AAOD is 15% (dust), 28% (OC), and 56 % (EC). Finally, only measurements with a high AAE/low EAE have significant dust absorption, correspondingly measurements with high AAE/high EAE have significant OC absorption, with BC absorption being predominant at low AAE values. These trends are consistent with those expected for dust, biomass burning, and fossil fuel aerosols respectively [*Russell et al.*, 2010].

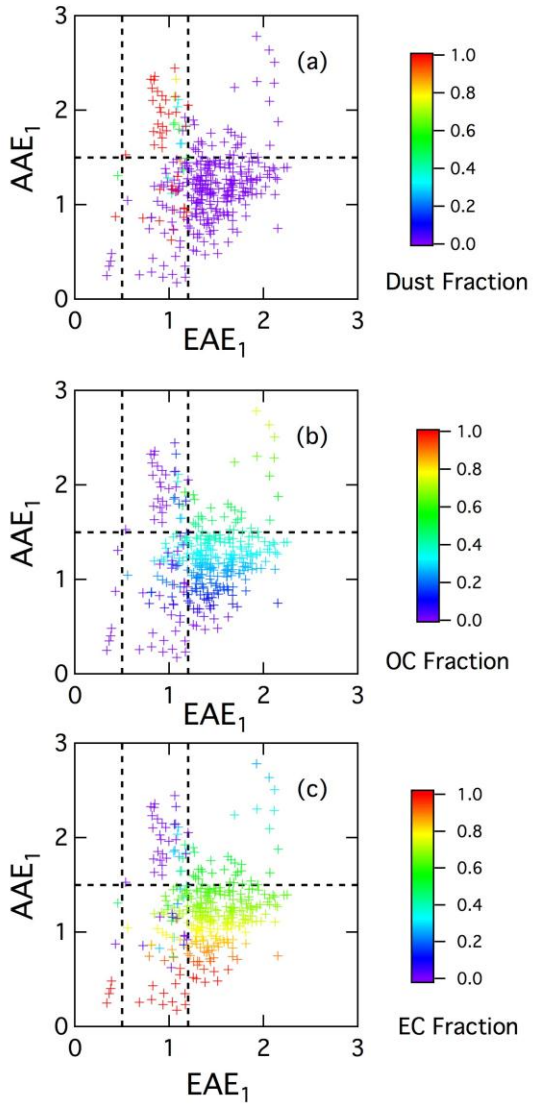

Figure 5.9 Fraction of AAOD in CA attributed to (a) dust, (b) OC, and (c) EC at 440 nm as a function of AAE and EAE/SAE

5.8 Sensitivity to AAE

Due to the exponential nature of Equation 5.4, it is possible that the choice of AAE for the three absorbing species may have a significant impact on the AAOD partition. Using the California AERONET data as a comparative case study, we recalculate the AAOD for dust, OC (BrC), and BC using the extreme values of AAE reported in Table 5.2 to determine the sensitivity of the partitioning method to the parameterization. The results are summarized in Table 5.5 at 440 nm. For the various cases, we still find that BC is the primary absorber, (except when we select the low extreme value for both the BC and OC AAE), contributing about

45% of the total AAOD, with dust and OC making up the remainder. The partitioning for dust is most stable, with dust AAOD varying between 0.005 and 0.011, and the highest variability is found in OC absorption, with the AAOD varying between 0.000 (negligible) and 0.014. This result is consistent with the SAE-AAE phase space we have defined, since dust absorption is clearly separated, while OC/BC partitioning is less defined.

California AAOD at 440 nm			
Perturbation	Dust	OC	BC
Base Conditions (AAE values listed in Table 0.1)	0.009	0.007	0.017
BC AAE1 = 0.79, AAE2 = 1.25	0.008	0.005	0.020
BC AAE1 = 0.31, AAE2 = 0.45	0.008	0.009	0.016
OC AAE1 = 6.56	0.005	0.000	0.028
OC AAE1 = 2.54	0.007	0.012	0.014
BC AAE1 = 0.79, OC AAE1 = 6.56	0.011	0.003	0.019
BC AAE1 = 0.31, OC AAE1 = 2.54	0.007	0.014	0.012
Dust AAE1 = 1.70, AAE2 = 0.65	0.006	0.009	0.018
Dust AAE1 = 2.70, AAE2 = 1.65	0.011	0.005	0.017

Table 5.5 Sensitivity of AAOD partitioning to choice of AAE for the California case study.

5.9 Estimation of error

Figure 5.10 illustrates the AAOD reconstructed from equation 5.4 compared to the AERONET measured value using 675 nm as the reference wavelength. The discrepancy in values corresponds to the error introduced by the partitioning method. We find that at 440 nm the AAOD is overestimated by 0.5% on average, and at 870 nm the AAOD is underestimated by 4.0%. Negative values of AAOD for at least one of the species is predicted for 27 out of the 342 measurements (7%) – these values are excluded from determining ensemble averages. These relatively small values of error indicate that the method based upon a set of global measurements is fairly robust and applicable even at the regional scale.

Overall, we find that the partitioning scheme reproduces between 95 and 100% of the measured AAOD at all wavelengths and produces non-physical results for approximately 8% of all measurements. However, we contend that these uncertainties are not unreasonably large, and the method reproduces seasonal and regional trends that are consistent with observed emission patterns.

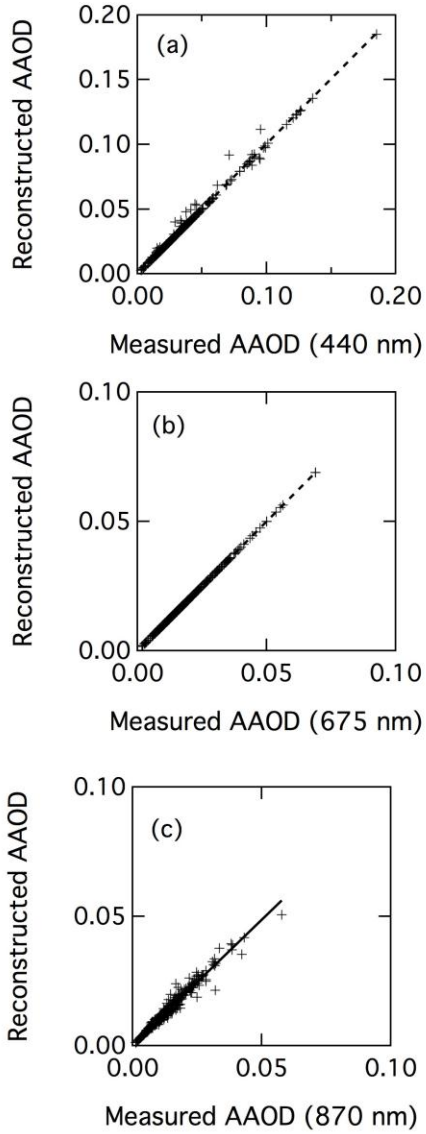

Figure 5.10 Comparison of AAOD from CA sites directly measured from AERONET and reconstructed from equation 5.4 at (a) 440 nm, (b) 675 nm, and (c) 870 nm

5.10 Conclusions

We have proposed an empirical method for determining the fraction of aerosol absorption attributable to dust, OC, and EC that exploits the differences in wavelength dependence for the principal absorbing species. We have self-consistently determined the AAE and SSA values associated with these species based on a large global ensemble of AERONET measurements dominated by

specific emission types. The parameter values are based entirely on observations and therefore do not require the assumption of aerosol chemical and physical properties such as refractive index, mixing state, or size distributions. These values are found to be consistent with those reported in the literature and in use in current aerosol models, in particular the AAE value for total carbon close to the theoretical value of 1.0. The method has been applied to California as a test case, where we find an enhanced absorption due to dust in the winter months, and due to OC in the summer months. We find that OC on average contributes 28% to the total absorption at the shortest wavelength (440 nm), providing a good first order estimate for the so-called brown carbon absorption that is presently poorly quantified.

We conclude by commenting on the general applicability of this method. Although we recommend values for the model parameters based upon a global data set, the equations can be fine tuned to any region by following the procedures outlined here for determining the SSA and AAE values. Since the only required input for the equation is a multi band measurement of the total absorption depth, the AERONET results reported here can be extended to the large ensembles of available diverse laboratory, ground based, and remote satellite measurements. Finally, the analyses indicate the existence of significant BrC absorption that has been largely overlooked in climate models.

6.0 Sources for BC and BrC aerosol particles

6.1 Introduction

As shown in Chapter 5, the absorbing properties of atmospheric aerosol particles are strongly dependent on the composition and mixing state of the particles [*Bond and Bergstrom*, 2006; *Schnaiter et al.*, 2006]. A separation of the total aerosol absorption into different chemical species that may be further related to emission sources is therefore essential, both for constraining the large uncertainties in current aerosol forcing estimates [*Forster et al.*, 2007] and for informing any emissions based control policy. This chapter presents a detailed study of the chemical composition and size distribution of aerosol particles, and how they relate to the optical properties, which in turn are essential to evaluate their impact on the climate.

Russell et al., [2010] highlighted that many recent studies have shown the persistent connections between aerosol sources and composition, and the wavelength dependence of absorption. Previous experimental studies have classified aerosol types from either chemical measurements [*Fisher et al.*, 2010; *Kaplan and Gordon*, 1994; *Schauer*, 2003] that were related to source terms, or optical properties measured on ground stations [*Dubovik et al.*, 2002; *Eck et al.*, 1999; *Fialho et al.*, 2006; *Meloni et al.*, 2006] and from satellites [*Barnaba and Gobbi*, 2004; *Higurashi and Nakajima*, 2002; *Jeong et al.*, 2005; *Kaufman et al.*, 2005]. In this study, we concentrate instead on a unique approach following simultaneous in-situ optical properties and single particle chemical composition measured during three aircraft field campaigns in California. The measurements are combined in order to validate the methodology for the estimation of aerosol composition using spectral optical properties described in Chapter 5. In addition, this approach is extended and applied to a long-term remote sensing optical measurements database, i.e. AERONET, using data from California ground stations and separating between northern and southern California and by seasons (winter/spring and summer/autumn).

6.2 Spectral properties and composition

As described in Chapters 5 and 7, the spectral dependency of the absorption coefficient, AAE, can be related with the source of absorbing aerosol. Black carbon typically follows a λ^{-1} spectral dependency, yielding an AAE close to 1, while organic carbon in biomass smoke aerosols and mineral dust contributed to light absorption in the ultraviolet and blue spectral regions yielding an AAE greater than 1. On the other hand, the spectral dependency of the scattering coefficient, the SAE, depends primarily on the dominant size mode of the particles, typically ranging from 4 to 0 where larger numbers associate with small

particles, i.e. fine mode, and smaller numbers suggest the dominance of large particles, i.e. coarse mode [*Bergstrom et al.*, 2007].

Thus, in a very intuitive way, the AAE vs. SAE space partitions into regions that correlate to combinations of smaller and bigger particles and, particles that follow the λ^{-1} trend for absorption, and those with enhancement on the shorter wavelengths absorption. The principal advantage of this dual size-chemistry related partitioning is that in the ideal case it separates the three aerosol absorbing species – BC, OC, and mineral dust. First, measurements representing dust separate along the SAE axis, as dust is primarily found in the coarse mode as compared to carbonaceous aerosols that are primarily in the fine and ultra-fine mode close to emission sources. Second, BC is an efficient absorber at all wavelengths compared to OC which absorbs strongly only at short wavelengths, separating these species along the AAE axis. In addition to these ideal cases we can relate the remainder of the phase space to aerosols with different predicted combinations of SAE (representing size) and AAE (representing chemistry), and their mixtures. The generalized AAE/SAE phase space (illustrated in Figure 6.1) relies on the optical properties of aerosols, but lacks a correlation to measured particle chemistry. A comparison with in-site chemical measurements, as presented in this work, therefore is an invaluable aid in relating measured ambient aerosols as quantified by their size and chemistry to their optical properties.

AERONET station	Lat (°) N	Lon (°) W	Region	Aerosol source
Billerica, USA	42.5	71.3	Coastal Urban	Fossil Fuel
CCNY, USA	40.8	74.0	Coastal Urban	Fossil Fuel
Dayton, USA	39.8	84.1	Inland Urban	Fossil Fuel
Fresno, USA	36.8	119.8	Central Valley, CA	Fossil Fuel
GSFC, USA	39.0	76.8	Inland Urban	Fossil Fuel
Halifax, Canada	44.6	63.6	Coastal Urban	Fossil Fuel
Hamburg, Germany	53.6	-10.0	Inland Urban	Fossil Fuel
Hong Kong	22.2	-114.3	Coastal Urban	Fossil Fuel
IFT Leipzig, Germany	51.4	-12.4	Inland Urban	Fossil Fuel
Mainz, Germany	50.0	-8.3	Inland Urban	Fossil Fuel
Maryland Sci. Cen., USA	39.3	76.6	Inland Urban	Fossil Fuel
New Delhi, India	28.6	-77.2	Inland Urban	Fossil Fuel
Palaiseau, France	48.7	-2.2	Inland Urban	Fossil Fuel
Philadelphia, USA	40.0	75.0	Inland Urban	Fossil Fuel
Rome Tor Vergata, Italy	41.8	-12.7	Inland Urban	Fossil Fuel
Sandy Hook, USA	40.5	74.0	Coastal non-Urban	Fossil Fuel
UCLA, USA	34.1	118.5	Coastal Urban, CA	Fossil Fuel
Abracos Hill, Brazil	10.8	62.4	Inland Forest	Biomass Burning
Alta Floresta, Brazil	-9.9	56.1	Inland Forest	Biomass Burning
Belterra, Brazil	-2.7	55.0	Inland Forest	Biomass Burning
Campo Grande, Brazil	-20.5	54.6	Inland Urban	Biomass Burning
CELAP-BA, Argentina	-34.6	58.5	Inland non-Urban	Biomass Burning
Cordoba CETT, Argentina	-31.5	64.5	Inland Urban	Biomass Burning
CUIABA Miranda, Brazil	-15.7	56.0	Inland Forest	Biomass Burning
Mongu, Zambia	-15.3	-23.2	Inland non-Urban	Biomass Burning
Petrolina SONDA, Brazil	-9.4	40.5	Inland Urban	Biomass Burning
Rio Branco, Brazil	-10.0	67.9	Inland Forest	Biomass Burning

Skukuza Aeroport, S Africa	-25.0	-31.6	Inland non-Urban	Biomass Burning
Eilat, Israel	29.5	-34.9	Coastal Desert	Dust
Hamim, UAE	23.0	-54.3	Coastal Desert	Dust
Solar Village, Saudi Arabia	24.9	-46.4	Inland Desert	Dust
Tamanrasset INM, Algeria	22.8	-5.5	Inland Desert	Dust
Tamanrasset TMP, Algeria	22.8	-5.5	Inland Desert	Dust

Table 6.1 List of the AERONET stations around the world with dominant species used for the creation of the Ångström matrix.

Figure 6.1 illustrates the division of the Ångström matrix with labels for the aerosol types based on the optical properties, and it shows data from the 33 AERONET stations color-coded by dominant type. Table 6.1 lists the stations and its location and dominant aerosol species. Measurements from the dust dominant region fall mainly into the dust dominant region ("upper left quadrant"), however some measurements fall into the phase space representing polluted dust, mixed aerosols, or the coarse coated type. On the other hand, for ambient measurements, there is a larger overlap between fossil fuel and biomass-burning related sources since all combustion produces both EC and OC, and there are no pure EC or OC ambient measurements. The methodology described in Chapter 5 provides an effective mathematical scheme for attributing aerosol absorption between EC, OC, and dust, but does not provide insights into their emission sources in complex mixed environments.

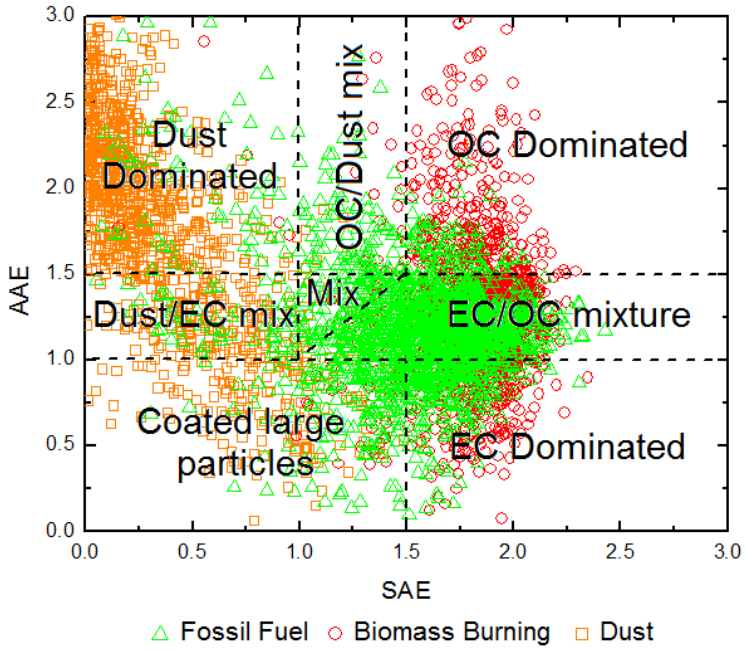

Figure 6.1 Division of the Absorption Ångström Exponent vs. Scattering Ångström Exponent space, the Ångström matrix, overlapped with the AERONET

measurements from stations with a dominant species (fossil fuel, biomass burning or dust).

To gain a better understanding of how the optical properties of aerosols relate to emissions, we use California as an initial test case, where the Ångström matrix can be compared to a large wealth of field data. We use measurements from a total of ten operational AERONET stations in California to obtain the spectral and optical properties of the aerosols. The stations are divided by region, into Northern California for the stations with latitude above 36°N and Southern California for the stations below 36°N. Data are also divided by seasons grouping winter and spring in one season and summer and autumn in another season. Table 6.2 presents the name, location and available period of time in years for the 10 continuously operational California AERONET stations (also illustrated on in Figure 6.2). By exploiting the optical properties in the AAE/SAE phase space, we obtain an estimate for the relative contribution of absorbing aerosols in California.

AERONET station	Latitude (°) N	Longitude (°) W	Data Availability
Fresno	36.782	119.773	2002-2011
La Jolla	32.870	117.250	1994-2011
MISR-JPL	34.119	118.174	1996-2009
Monterey	36.593	121.855	1998-2011
Moss Landing	36.793	121.788	2004-2006
San Nicolas	33.257	119.487	1997-2007
Table Mountain	34.380	117.680	1998-2011
Trinidad Head	41.054	124.151	2005-2011
UCLA	34.070	118.450	2000-2009
UCSB	34.415	119.845	1994-2011

Table 6.2. Location and period of data availability of operational AERONET stations in California.

Figure 6.3 shows the relative contribution of absorbing species determined in this fashion, resolved by geographic regions and seasons in pie charts. Panel a) shows the contribution for Northern California during winter/spring, panel b) shows the contribution for Northern California during summer/autumn, panels c) and d) show the contributions for Southern California during winter/spring and summer/autumn, respectively. At first glance, both seasons in northern California show similar aerosol contribution and they are dominated by a mixture of EC and OC aerosol that contribute over 40% of all measurements. The difference lies on the coated large particles and mix types. For southern California, the summer/autumn season is dominated by a mixture or EC and OC aerosol (almost 40%) and OC and OC mixed with dust type. The winter/spring season is dominated by dust (over 45%) and coated large particles (almost 30%). It should be noted that this large contribution from dust resulted possibly from a misclassification of HULIS like substances that contain carbonaceous material and are large in size (discussed further in Section 6.6).

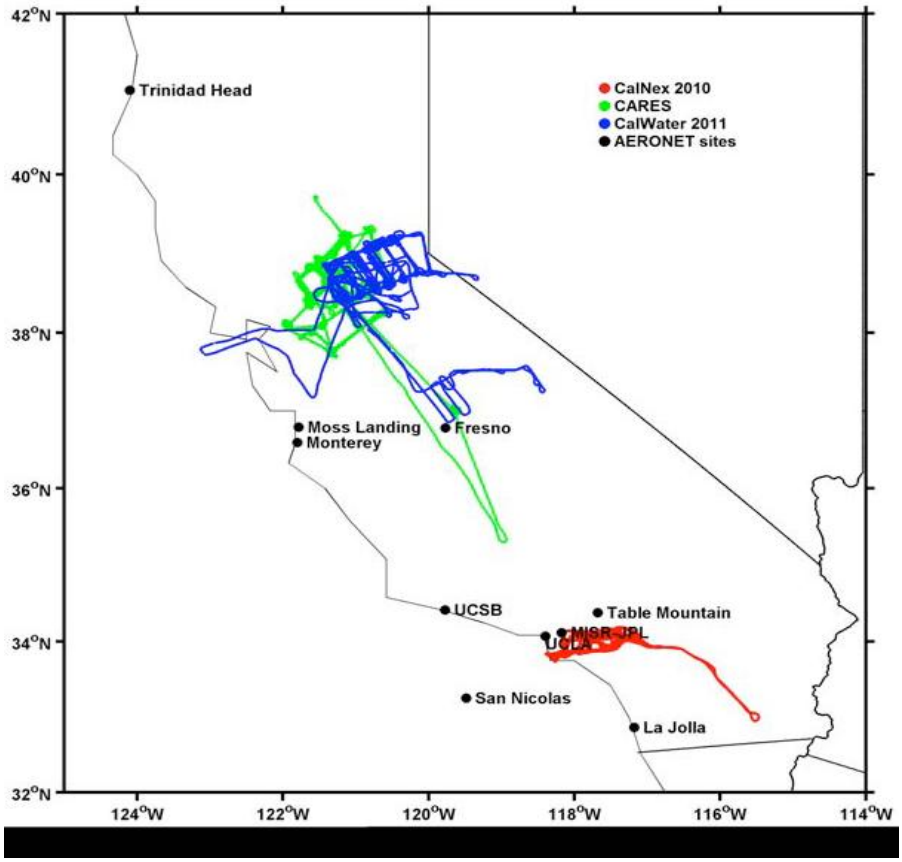

Figure 6.2 Location of flight paths of the aircraft campaigns and the AERONET stations used for relating absorbing aerosols to emission sources.

6.3 In-situ aircraft measurements

Using the in situ optical properties and chemical composition measured during the three aircraft field campaigns, we can establish a link between the optical properties, in this case the AAE and the SAE, and the measured chemical composition of the aerosol particles.

Campaign Name	Location	Dates	Absorption Coefficient	Scattering Coefficient	Chemical composition
CalNex 2010	Los Angeles basin	May 2010	PSAP	PCASP size distribution	ATOFMS
CARES	Sacramento area and central valley	June 2010	PSAP	Nephelometer	ATOFMS
CalWater2011	Sacramento area and central valley	February – March 2011	PSAP	Nephelometer	ATOFMS

Table 6.3 Name and location of the aircraft field campaigns and optical properties measured used in this work.

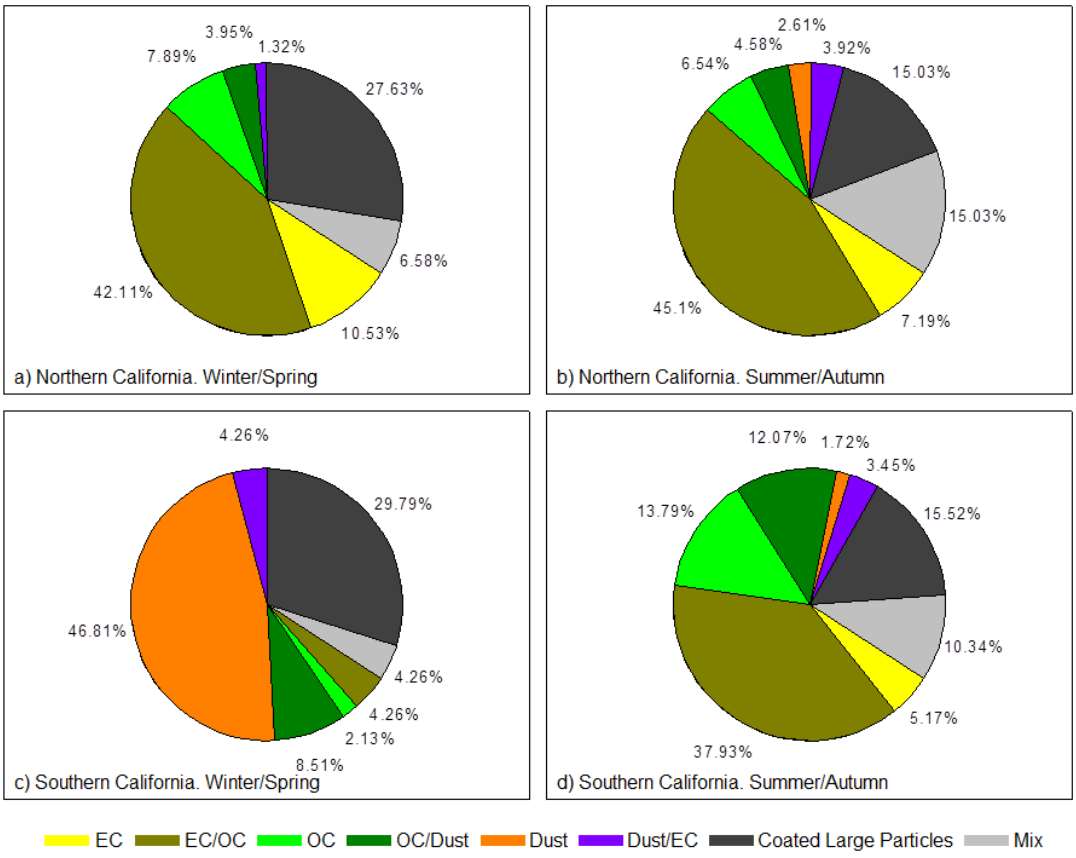

Figure 6.3 estimated contributions to light absorption derived from AERONET stations in California separated by region and season: a) Northern California – winter/spring, b) Northern California – summer/autumn, c) Southern California – winter/spring, and d) Southern California – summer/autumn.

In-situ data were measured during three aircraft field campaigns performed in California. CalNex 2010 was a joint field study coordinated by the California Air Resources Board (CARB), the National Oceanic and Atmospheric Administration (NOAA) and the California Energy Commission (CEC), with a primary goal to study the atmospheric processes over California and the eastern Pacific coastal region. Measurements used in this work were taken on the Center for Interdisciplinary Remotely-Piloted Aircraft Studies (CIRPAS) Twin Otter, flying mainly in the Los Angeles basin during May 2010. CARES (Carbonaceous Aerosols and Radiative Effects Study), was a field study funded but the US Department of Energy (DOE) Atmospheric Radiation Measurement (ARM) program, and was designed to increase scientific knowledge about evolution of black carbon and secondary organic aerosols from both urban/manmade and

biogenic sources. Data used from this campaign were measured onboard the DOE Gulfstream–1 (G–1), based in Sacramento during June 2010. CalWater 2011 field campaign, funded by CEC, was designed to better assess the effects aerosols have on precipitation in the Sierra Nevada during the winter season. Data used in this work were collected onboard the DOE G–1, based in Sacramento, between February and March 2011. Table 6.3 summarizes the name and location of the field campaigns, and the optical properties measured onboard used in this work. The different aircrafts carried instrumentation for the retrieval of the optical properties of aerosols, i.e. absorption and scattering coefficients. Figure 6.2 shows the flight paths for the three campaigns.

The Absorption coefficient, σ_a was derived using a Particle Soot Absorption Photometer (PSAP) at 462, 523 and 648 nm. The Scattering coefficient, σ_s, was measured using a nephelometer at 450, 550 and 700 nm during CARES and CalWater and derived from a PCASP size distribution applying Mie theory (using a refractive index of 1.5) during CalNex. PSAP data were corrected based on [*Bond et al.*, 2009] and [*Ogren*, 2010] and nephelometer data were corrected based on [*Anderson and Ogren*, 1998]. AAE and SAE were calculated applying Eq. (1) and (2) respectively using σ_a instead of the column integrated value (A-AOD) and σ_s instead of the S-AOD. Wavelengths used as λ_1 and λ_2 were 462 and 648 nm for the PSAP and 450 and 700 for the nephelometer, since those are closer to the AERONET wavelength used in section 2.1.

6.4 Aerosol time of flight mass spectrometry

Measurements of the chemical composition of individual particles during the three aircraft campaigns were performed using the aircraft aerosol time-of-flight mass spectrometer (A-ATOFMS) [*Pratt et al.*, 2009]. The A-ATOFMS measures, in real time, the size and chemical composition of individual particles ranging in size from 70 to 2500 nm. Following a ^{210}Po neutralizer and pressure controlled inlet [*Bahreini et al.*, 2003], particles are focused in an aerodynamic lens system. The particles are optically detected by two 532 nm lasers spaced 6.0 cm apart, providing particle velocity and, ultimately, vacuum aerodynamic diameter (d_{va}). Finally, species are desorbed and ionized using 266 nm radiation from a Q-switched Nd:YAG laser operating at ~0.4–0.6 mJ. Positive and negative ion mass spectra resulting from individual particles are measured in a dual-polarity time-of-flight mass spectrometer.

Spectra are grouped into chemically similar clusters using the ART2-a algorithm [*Song et al.*, 1999]. The initial clusters are then manually grouped in a small set of clusters based on the identification of the mass spectral peaks that correspond to the most probable ions for a given mass-to-charge ratio (m/z) based on previous lab and field studies. These clusters are then related to a source of absorbing aerosols as follows: primary fossil fuel, secondary fossil fuel, primary biomass burning, secondary biomass burning and dust, excluding other non-absorbing sources. Figure 6.4 shows a representative mass/charge spectrum for each aerosol source determined from ATOFMS studies.

Briefly, primary fossil fuel particles are characterized by the presence of carbon cluster ion peaks: C_n^+ and C_n^-, representative of the elemental carbon (EC), and spectra that also contain weak m/z 27($C_2H_3^+$), 37(C_3H^+) and 39($C_3H_3^+$). Secondary fossil fuel particles contain m/z 27($C_2H_3^+$/CHN^+), 37(C_3H^+), 39($C_3H_3^+$) and 43($C_2H_3O^+$) in the positive spectra and mainly nitrate and sulfate ion peaks in the negative ion mass spectra: m/z -62(NO_3^-) and -97(HSO_4^-) respectively [*Moffet et al.*, 2008]. Biomass burning particles are characterized by an intense potassium peak m/z 39(K^+) with less intense carbonaceous markers (e.g. m/z 12(C+), 27($C_2H_3^+$), 36(C_3^+), 37(C_3H^+) [*Silva et al.*, 1999]. The difference between primary and secondary biomass burning is established by looking at the negative spectra that presents carbon clusters in the case of primary biomass burning or mainly nitrate/sulfates in the case of secondary biomass burning. Finally, dust is characterized by inorganic ion peaks e.g. m/z 27(Al^+), 39(K^+), and/or 40(Ca^+), and the presence of silicates: -60(SiO_2^-) and -76(SiO_3^-) [*Silva and Prather*, 2000].

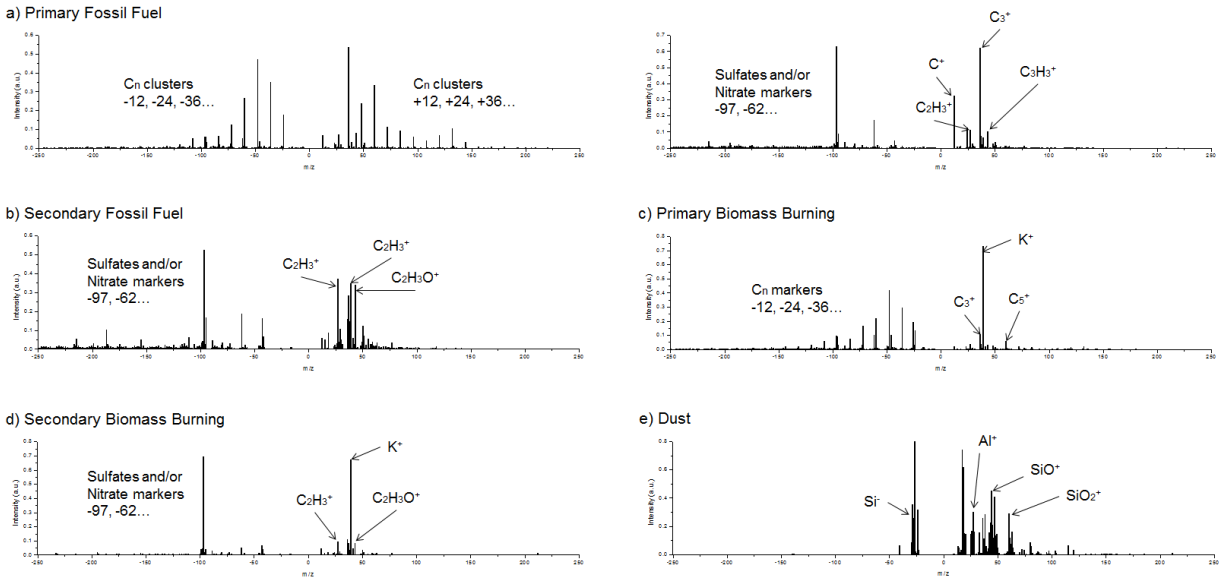

Figure 6.4 Representative ATOFMS spectra for different aerosol sources a) Primary fossil fuel, b) Secondary fossil fuel, c) Primary biomass burning, d) Secondary biomass burning, and e) dust.

A summary of the overall chemical composition detected during the three aircraft campaigns considered here is shown in Figure 6.5. Each pie chart represents the number fraction of absorbing sources detected during CalNex on the left panel, CARES in the middle, and CalWater on the right panel. Also each campaign, because of their relative location and dates, can be associated with a region and season. Therefore, CalNex corresponds with southern California during the summer, CARES is northern California also during the summer, and CalWater is

northern California during the winter. Both seasons in northern California present similar sources with a contribution dominated by secondary fossil fuel aerosol and biomass burning. Also, more dust is detected during the winter. In southern California, the contribution from primary fossil fuel (35%) and secondary fossil fuel (47%) dominates.

6.5 Comparison of ATOFMS and spectral classification

In order to validate the Ångström matrix we matched the spectral optical properties and the chemical composition measured during the flights. For each flight, we calculated the 5-minute average of the AAE and SAE. On the other hand, for the same 5-minute periods, we calculated the fraction of the different chemical sources detected with the A-ATOFMS. We considered periods with a dominant species. The criteria for dominant species is that 75% of the particles detected by the A-ATOFMS are from one species.

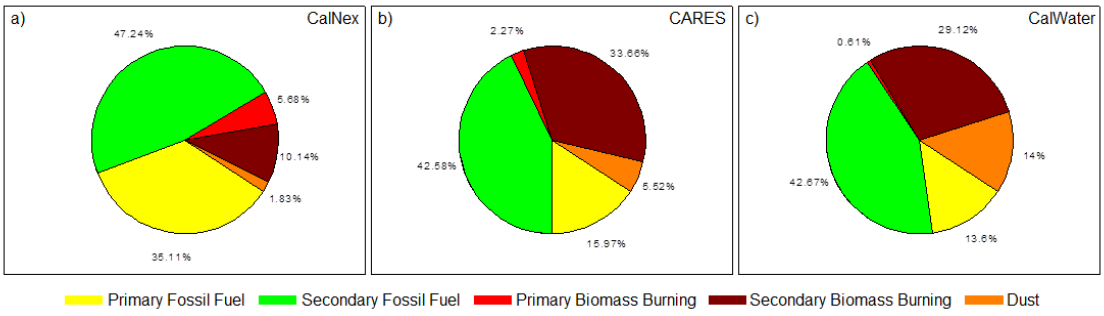

Figure 6.5 Overall chemical composition detected with the ATOFMS in the three aircraft campaigns: a) CalNex, b) CARES, and c) CalWater.

Thus, we screen the data using the 5-minute average values that correspond with a dominant species. The AAE and SAE values that match the dominant species criteria are represented, in Figure 6.6, on an AAE vs. SAE scatter plot with color representing the dominant species. Panels a), b) and c) correspond to each different field campaign (CalNex, CARES and CALWATER respectively). AAE is smaller on average during CalNex than during CARES, consistent with the type of dominant aerosol detected, mainly primary fossil fuel during CalNex, i.e. black carbon, in contrast with the secondary fossil fuel particles that dominate during CARES. The number of samples from the CalWater campaign is small, as the flights focused on clouds and not many data samples were acquired from outside of clouds. SAE shows less variability during CARES than during CalNex,

but we need to take into account that the range of particles sizes entering the inlet of the aircrafts has limitations.

Since the AAE is related to the chemistry, panel d) in Figure 6.6 shows a frequency histogram of the AAE associated to the aerosol sources showing that primary fossil fuel particles have a mean value of AAE = 1.1±0.6, which is close to the expected 1 for black carbon. Secondary fossil fuel particles can be associated with an AAE = 1.5±0.3 and biomass burning to AAE = 1.8±0.4.

		Ångström Matrix							
		EC dom.	**EC/OC mix**	**OC dom.**	**OC/Dust mix**	**Dust dom.**	**Dust/EC mix**	**Coated**	**Mix**
ATOFMS	**Prim. Fossil Fuel**	1.20	27.71	31.33	21.69	1.20	0	10.84	6.02
	Sec. Fossil Fuel	0	0	10.47	27.91	8.14	39.53	9.30	4.65
	Prim. Biomass	0	0	25	25	0	0	0	50
	Sec. Biomass	0	3.70	18.52	40.74	14.81	0	18.52	3.70
	Dust	14.29	7.14	28.57	7.14	7.14	0	14.29	21.43

Table 6.4 Contingency matrix constructed from the aircraft measurements representing the percentage of aerosol sources from the ATOMFS classified into the different Ångström matrix classes.

Finally, we apply the Ångström matrix to the in situ optical properties, obtaining an estimate of the aerosol composition using optical properties that can be compared with the actual chemical composition. Table 6.4 shows a contingency table where the rows are the chemical composition detected with the A-ATOFMS and columns are the different estimated aerosol types from the Ångström matrix. Values presented are percentages of measurements classified in one type or another and they sum 100 across rows. Primary fossil fuel sources, i.e. elemental carbon, were classified mainly as organic carbon or a mixture of organic carbon and elemental carbon or dust. Secondary fossil fuel sources, i.e. secondary organic aerosols, fall mainly into the dust/EC mix (almost 40%) indicating that those were particles with absorption properties similar to organic carbon, but larger in size. On the other hand, primary biomass burning sources were classified as organic carbon, organic mixed with dust, or well-mixed types. Secondary fossil fuel sources are classified in almost 60% into the organic carbon or organic carbon mixed with dust categories. Finally, dust sources were only significant during CalWater. However, the Ångström matrix does not classify them correctly as dust-dominated type mainly because of the limitation of measurements.

6.6 The California case study

The estimates of aerosol types applying the Ångström matrix to the California AERONET stations (Fig. 6.3) show similar aerosol contribution in both seasons in northern California. Over 40% of the contribution is due to a mixture of EC and

OC, about 10% due to EC, and 11% due to OC or OC/dust mixture. For southern California, during the summer/autumn season almost 40% of the aerosol contribution corresponds to a mixture of EC and OC, 27% corresponds to OC or OC/dust types and 5% corresponds to EC. During the winter/spring season, the aerosol mixture is dominated by dust (over 45%) and coated large particles (almost 30%), and no pure EC type is present.

The EC/OC mixture type seems to dominate in the Ångström matrix classification and indicates the difficulty of separating the sources from column-integrated measurements. More fossil fuel sources (primary and secondary) were expected in southern California since it is a more populated, urban area, and the chemical composition detected during the aircraft campaigns for southern California (Fig. 6.5a) shows about 33% of the aerosol contribution due to primary fossil fuel sources, 47% due to secondary fossil fuel sources, and about 15% due to biomass burning sources. Figure 6.6(d) shows that the chemistry component of the Ångström matrix (the AAE) has a mean value of 1.1 for primary fossil fuel sources, 1.5 for secondary fossil fuel sources and 1.8 for biomass burning. All those sources would fall into the EC/OC mixture type or the OC type, with some overlapping on the different sources, and leaving the EC type misclassified. On the other hand, northern California was expected to have more biomass burning sources respect to the south because of the less populated and more rural environment, and the aircraft data in northern California (Fig. 6.5(b) and 6.5(c)) indicates about 40% of the contribution due to secondary fossil fuel sources and about 30% due to biomass burning sources with a small contribution due to primary fossil fuel sources (about 7 to 10%). Again, the overlapping of the optical properties makes the classification to be dominated by the EC/OC mixture type.

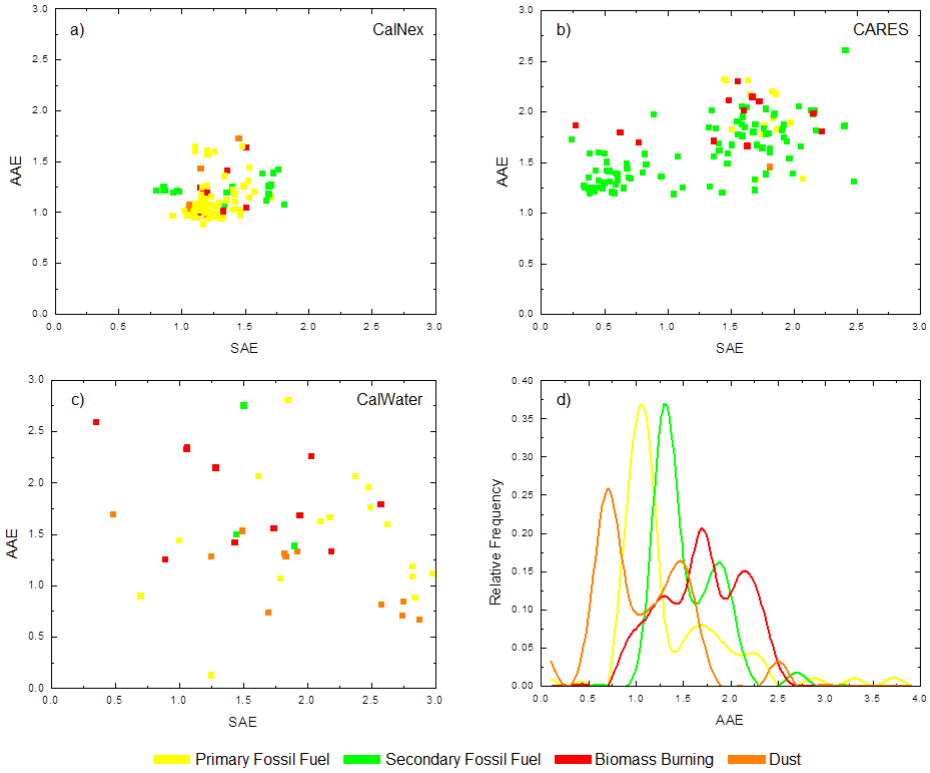

Figure 6.6 (a-c) Absorption Ångström Exponent vs. Scattering Ångström Exponent scatter plot of in situ aircraft measurements in California; the color code represents the dominant aerosol source detected with the ATOFMS for each measurement. Also shown is (d) frequency histogram of the Absorption Ångström Exponent for each aerosol source.

Pure dust-type measurements that appear to dominate the winter and spring seasons were concentrated in the UCLA and MISR-JPL AERONET stations, both in the Los Angeles metropolitan area, and dust is not expected to make such large contributions in urban areas. This suggests that those dust cases were instead larger hygroscopic organic carbon particles that had undergone aqueous phase processing. The aerosol species producing strong absorption at short wavelengths and primarily in the coarse mode are most likely humic-like substances (HULIS) species formed by fog or cloud processing. These aerosols have been detected in California in previous studies (e.g. [*Qin et al.*, 2006]) and represent organic carbon particles, but larger than 1µm due to their water content, therefore they might have spectral properties similar to dust, i.e. they are large particles and absorb more radiation at shorter wavelengths (AAE>1) which can fall in the Dust dominant or Dust/EC mixture types in the Ångström matrix. On the other hand, the in-situ chemical composition from the aircraft campaigns indicates the larger contribution due to dust from northern California during the winter (14% vs. 5%). During the CalWater flights, dust particles were detected mainly at higher altitudes in layers. Long-range transported dust crossing the

Pacific has been detected during the winter in northern California and it is known to have an impact on the precipitation in California [*Ault et al.*, 2011].

The differences in sources leading to absorption in different regions of California, as shown in Fig. 6.5, can be explained not only by the different sources of aerosols in the different regions, but by the different objectives of the flights during each of the campaigns. During CalNex, the flights were comprised of mainly low level passes within the boundary layer in the Los Angeles area, very close to the sources of pollution. On the other hand, CARES had flights mainly over the Sierra foothills (away from urban sources in the Sacramento area), at higher altitude, and intercepting plumes from fires if they were present.

The overall in-situ spectral properties agree with the detected chemical composition. By looking at Fig. 6.6, we can see that the chemical component of the Ångström matrix, the AAE, is smaller on average during CalNex than during CARES, consistent with the type of dominant aerosol detected, more primary fossil fuel during CalNex, in contrast with the secondary fossil fuel and biomass that dominate during CARES. The number of samples for CalWater is small, as the flights focused on clouds and thus not many data samples were acquired from outside of clouds. Also, Fig. 6.6(d) shows that the AAE has a mean value of 1.1±0.6 for primary fossil fuel sources, secondary fossil fuel sources can be associated with an AAE = 1.5±0.3, and biomass burning to AAE = 1.8±0.4. These values agree with the values expected for BC (AAE = 1) and OC (AAE > 1). More dust data would be necessary to establish a good statistics for this source. On the other hand, the size component of the Ångström matrix, the SAE, shows less variability during CARES than during CalNex, but we need to take into account that the cut size of the aircraft sampling inlet does not allow us to detect the larger aerosol particles.

Finally, the application of the Ångström matrix to the in-situ aircraft measurements and comparison with the chemical composition of the aerosol (Table 6.4) shows some of the limitations of the Ångström matrix. Particles detected as a primary fossil fuel source, i.e. elemental carbon, were classified mainly as organic carbon or a mixture of organic carbon and elemental carbon or dust. This reinforces the conclusions extracted from the comparison of the overall chemistry composition for the different regions and seasons in California. The external mixing of aerosol on a column integrated value like the AOD, or its absorption and scattering components, would yield a higher AAE value and, therefore misclassifies the EC type (primary fossil fuel source). Particles detected as secondary fossil fuel, i.e. secondary organic aerosols, fall mainly into the dust/EC mix (almost 40%) indicating that those were particles with absorption properties similar to organic carbon (AAE > 1), but larger in size. This could be biased by the size detection limit of the sampling inlet onboard the aircrafts. Primary biomass burning measurements were limited: 5.7, 2.3 and 0.6% of the overall particles detected in CalNex, CARES and CalWater respectively (Fig. 6.5), but when detected as dominant, the Ångström matrix classified them as organic carbon or organic mixed with dust (50%), or well-mixed types (the other

50%). The amount of data from this source is very limited and more values are necessary for accurate statistics. Secondary biomass burning dominant sources are the ones that the Ångström matrix classifies the best, with almost 60% falling into the organic carbon or organic carbon mixed with dust. Finally, the dust sources are only significant during CalWater with a 14%, and more data are necessary for accurate statistics.

6.7 Conclusions

In-situ chemical composition results reveal a higher contribution from fossil fuel sources in southern California in contrast with more biomass burning sources in northern California. This agrees with the spectral optical measurements. The estimation of aerosol types with spectral optical properties shows a dominance of mixed types. Pure EC is underestimated since it is being classified as a mixture of EC and OC. This is expected from column integrated aerosol optical properties, and the overlapping of sources and optical properties is also revealed in the in-situ measurements. Comparison of detailed chemical measurements and spectral properties reveals a new class of absorbing aerosols - i.e. secondary organic aerosols processed in aqueous phase that might be a significant contributor in urban areas with a predominance of smog events, such as the Los Angeles basin.

On the other hand, separating aerosol sources based only on spectral optical measurements (using the Ångström matrix) also shows limitations compared to the in-situ chemical measurements of the chemical composition. Primary sources are difficult to classify, since the external mixing of aerosols would make them to be classified as a mixture. Secondary species are well classified, but the separation between fossil fuel and biomass burning sources has limitation because of the overlapping of the optical properties. In general, OC is better identified as a biomass-burning source than a secondary fossil fuel source. Despite these limitations, the detailed comparison reveals the significance of aerosol absorption due to Brown (OC) carbon in addition to BC, which is currently underestimated in climate models. A significant number of absorption events are related to BrC from both biomass and secondary sources indicating that it must be a primary consideration while developing future climate mitigation policies.

In conclusion, the availability of long-term global optical properties makes them a great candidate for the estimation of chemistry composition, but studies with actual chemical composition measurements are necessary in order to constrain the applicability of the technique to specific regions. This is necessary if we want to accurately address the contribution of different aerosol sources to the radiative forcing.

7.0 Woodsmoke as a source of absorbing BrC

7.1 Introduction

As established in Chapter 5 and Chapter 6, organic carbon emitted from biomass burning is a strong absorber of light at short wavelengths. This study examines if residential wood burning in California may be a significant contributor to aerosol forcing, in addition to fossil fuel combustion emissions. With an AAE of approximately 1, freshly emitted BC from fossil fuel sources absorbs solar radiation without much wavelength selectivity [*Kirchstetter et al.*, 2004]. The observation that particulate matter, and especially biomass combustion-generated particulate matter, can exhibit AAEs much greater than 1 is the basis for concluding that species other than BC contribute to absorption of solar radiation, namely biomass smoke OC [*Hoffer et al.*, 2006; *Kirchstetter et al.*, 2004]. For this study, we consider that OC is the collection of hundreds or more particle-phase organic compounds, only some of which absorb solar radiation. Biomass smoke particles often look brown rather than black because, compared to BC, they absorb solar radiation with stronger wavelength selectivity in the blue and ultraviolet spectral regions, which has led to use of the term brown carbon to refer to biomass smoke particulate matter [*Andreae and Gelencser*, 2006]. AAE values for biomass smoke (or brown carbon) generally range from greater than 1 to about 3 [*Bergstrom et al.*, 2007; *Kirchstetter et al.*, 2004; *Rizzo et al.*, 2011; *Sandradewi et al.*, 2008]. The range reflects variation in combustion conditions and the chemical composition of the observed particles. A few studies have estimated the mass specific absorption of wood smoke OC (in units of m^2/g), which tends to be at least an order of magnitude smaller than that of BC at visible wavelengths [*Barnard et al.*, 2008; *Kirchstetter et al.*, 2004; *Sun et al.*, 2007b]. The fact that OC is often much more abundant than BC in wood smoke [*Piazzalunga et al.*, 2011] suggests that the contribution of OC to wood smoke absorption of solar radiation can, however, be significant.

7.2 Field measurements

We consider the spectral absorption selectivity of 115 particulate matter samples that were collected outside of 12 houses in the residential community of Cambria, California. Cambria is located in a rural portion of San Luis Obispo County midway between San Francisco and Los Angeles. In Cambria, wood burning is prevalent and the only significant source of nighttime particulate matter generation [*Thatcher et al.*, 2011]. It is likely that many residents burn *Pinus radiata*, also known as Monterey Pine, as it is the native species in region. Particulate matter samples were collected during evening and nighttime hours (from 1800h to 0600h) in the winter (of 2010) to maximize the collection of wood smoke particles and minimize the collection of particles from other anthropogenic or natural sources, such as restaurants along the single main street in downtown Cambria. Elevated chimney temperatures, measured using an infrared camera,

verified that residents were operating their fireplaces. Little vehicle activity was observed in the area during the evening and nighttime. Particulate matter samples were collected on quartz filters using a sampling device equipped with a single stage impactor to select particles smaller than 2.5 μm in aerodynamic diameter (SKC Inc. PEM model 200).

Samples were analyzed using a spectrometer in transmission mode in a manner similar to that described by [*Kirchstetter et al.*, 2004]. Light transmission through (dry) particulate matter on quartz filters is predominantly due to particle light absorption rather than particle light scattering when the particulate matter is even weakly absorbing [*Arnott et al.*, 2005]:[*Bergstrom et al.*, 2007; *Kirchstetter et al.*, 2004; *Rizzo et al.*, 2011; *Sandradewi et al.*, 2008]

$$\text{absorption}(\lambda) = k' \text{ATN}(\lambda) \tag{7.1}$$

where k´ is nominally constant and ATN(λ) is the optical attenuation computed from measured transmission,T(λ):

$$\text{ATN}(\lambda) = -100 \ln[T(\lambda)] \tag{7.2}$$

Further, [*Bond*, 2001] reported that particle light scattering does not significantly affect spectral absorption selectivity. Thus, we compute the AAE for each particulate matter sample by performing a linear regression of ln(ATN) against ln(λ) over the visible and near ultraviolet spectral range $360 < \lambda < 700$ nm.

7.3 Contribution of BC to absorption

We estimate the contribution of BC to each sample's spectral attenuation, $\text{ATN}_{BC}(\lambda)$, by (a) attributing all attenuation at 880 nm to BC, an assumption consistent with prior work [*Kirchstetter et al.*, 2004; *Sun et al.*, 2007b], and (b) extrapolating to other wavelengths assuming that the AAE of BC is 0.86. This is the minimum AAE value exhibited by the wood smoke particulate matter samples in this analysis and it is close to the nominal value of 1.0 that theory predicts for small BC particles [*Bohren and Huffman*, 1998]. The contribution of OC to each sample's spectral attenuation, $\text{ATN}_{OC}(\lambda)$, is determined by subtracting the BC attenuation from the total attenuation:

$$\text{ATN}_{OC}(\lambda) = \text{ATN}(\lambda) - \text{ATN}_{BC}(\lambda) \tag{7.3}$$

Based on the apportionment of spectral attenuation to BC and OC, we compute for every wood smoke sample the fraction of radiation at each wavelength in the solar spectrum that would be absorbed by OC:

$$f_{OC}(\lambda) = \text{ATN}_{OC}(\lambda) / \text{ATN}(\lambda) \tag{7.4}$$

Last, we compute the fraction of solar radiation that OC in the wood smoke would absorb in the atmosphere:

$$Foc = \int foc(\lambda) i(\lambda) d\lambda / \int i(\lambda) d\lambda \quad (7.5)$$

where *i*(λ) is the clear sky air mass one global horizontal solar spectrum at the earth's surface [*Levinson et al.*, 2010].

[*Gyawali et al.*, 2009] noted that coatings of non-absorbing species may collapse the fractal aggregate structure of BC particles and, consequently, increase spectral absorption selectivity. Therefore, it is conceivable that in applying Eq. 7.4, we may attribute a portion of the optical attenuation of particulate matter samples to light-absorbing OC rather than non-absorbing OC that increases BC absorption selectivity.

7.4 Sources of error

Finally, a few measurement artifacts warrant mention. A filter-loading artifact that causes k´ (Eq. 7.1) to increase as the collection filter becomes increasingly loaded with particles may be important for determining spectral absorption selectivity. Studies acknowledging the filter-loading artifact provide mixed evidence – on one hand indicating that the filter-based light transmission method accurately measures the spectral dependence of particulate matter light absorption [*Weingartner et al.*, 2003] and, on the other hand, indicating that this artifact is wavelength dependent [*Schmid et al.*, 2006]. Generally speaking, this artifact is most pronounced for highly absorbing particulate matter, such as black soot from diesel engines or kerosene flames [*Arnott et al.*, 2005; *Kirchstetter and Novakov*, 2007], which the particulate matter in this analysis is not. For the samples in the current analysis, there is no correlation between filter loading expressed in terms of ATN at 880 nm, which ranged between 3 and 23 for 98% of samples, and AAE (linear correlation coefficient, R^2 = 0.003). Thus, we don't expect this artifact to have a large influence on our results.

7.5 Results from field study

Figure 7.1 shows the spectral attenuation of a particulate matter sample, which is similar to the spectral attenuation of many other samples in this analysis. The AAE value for this sample is 2.36. As noted above, we estimate the contribution of BC to this sample's spectral attenuation, $ATN_{BC}(\lambda)$. As shown, BC accounts for the overwhelming majority of this sample's attenuation at wavelengths above 700 nm. At shorter wavelengths, the sample absorbs more radiation than is attributed to BC. The difference is attributed to attenuation by OC, $ATN_{OC}(\lambda)$, as illustrated in Figure 1. OC attenuation rises sharply with decreasing wavelength and is well described by a power law over the wavelength region shown. The AAE of OC is 4.89 for this sample.

We perform this analysis for all samples and generate the AAE histograms shown in Figure 7.2. The AAE of all wood smoke particulate matter samples ranged from 0.86 to 3.48 and averaged 1.89 (n = 115). These AAE values are consistent with the predominance of wood smoke during sample collection. The AAE of OC in the wood smoke samples ranged from 3.02 to 7.39 and averaged 5.00 (n = 87, AAE values cannot be computed for a minority of samples because application of Eq. 7.3 yields some slightly negative values of OC attenuation). These AAE values for OC are consistent with those recommended by Sun et al. (2007), who used band-gap and Urbach relationships to describe the absorption spectra of water-soluble humic-like OC (AAE = 6) and more polymerized OC (AAE = 4).

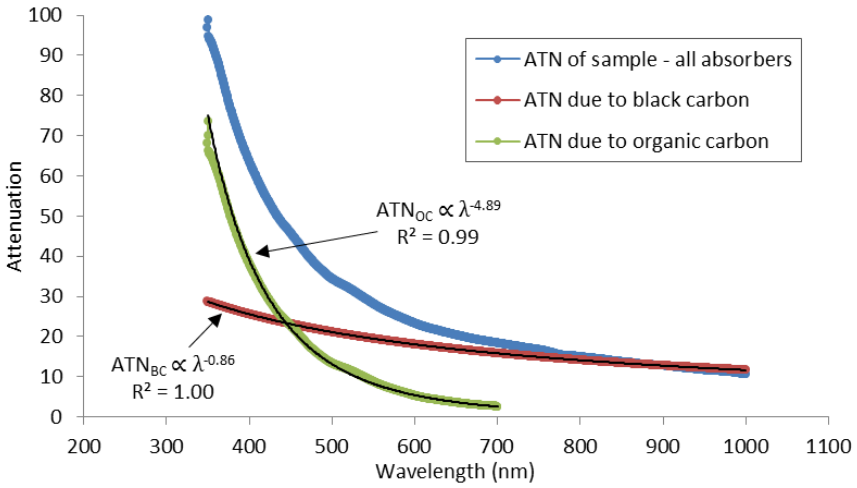

Figure 7.1 Estimated contributions of black and organic carbon to the spectral attenuation of a residential wood smoke particulate matter sample. The exponents of the power law trend lines, 0.86 and 4.89, are the absorption Ångström exponents of the black and organic carbon, respectively, for this sample.

Based on the apportionment of spectral attenuation to BC and OC (as illustrated in Fig. 7.1), we compute (Eq. 7.4) for every wood smoke sample the fraction of spectral radiation that would be absorbed by OC rather than BC, $f_{OC}(\lambda)$. The averages and standard deviations are shown in Figure 7.3. The red line in Figure 7.3 is a model of $f_{OC}(\lambda)$ based on a 5^{th} order polynomial fit of our measurements (our spectrometer operated between 350 and 990 nm), a prescribed value of zero above 880 nm (rather than unrealistic negative values), and a linear extrapolation of the data below 350 nm. The fraction of light absorbed by the wood smoke particulate matter that we attribute to OC decreases approximately linearly from 0.43 at 400 nm to 0.26 at 500 nm to 0.11 at 600 nm (Table 7.1).

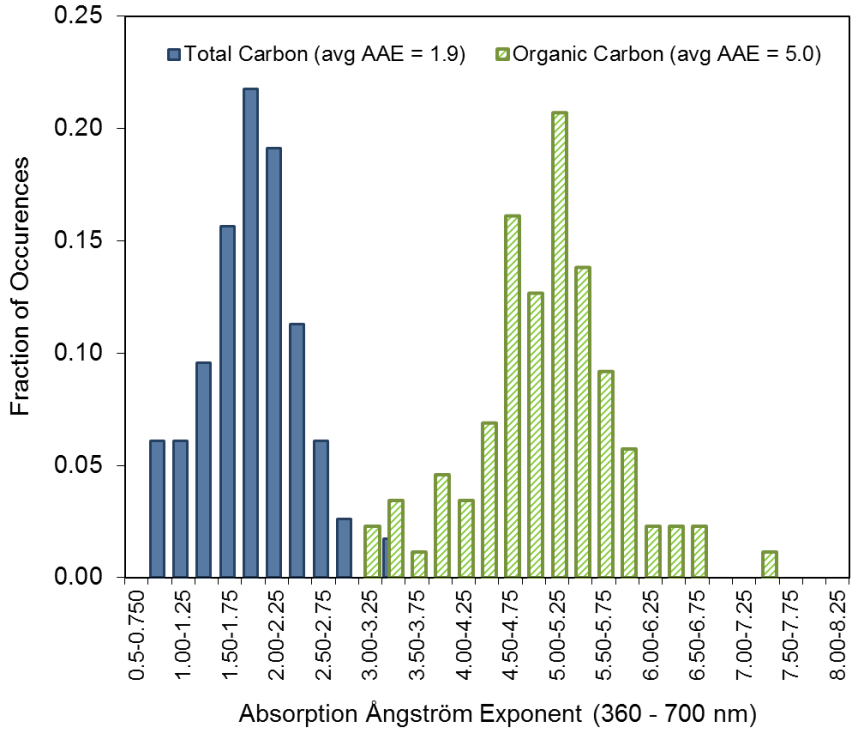

Figure 7.2 Histograms of absorption Ångström exponents computed over the 360 to 700 nm spectral range: (blue bars) 115 residential wood smoke samples considered in this analysis and (green bars) the light-absorbing organic carbon portion in 87 of the wood smoke samples.

		fraction of solar radiation absorbed by OC rather than BC in wood smoke at the wavelength or spectral region indicated				
BC AAE	OC AAE	400 nm	500 nm	600 nm	full solar spectrum[1]	UV[2]
0.86	5.00	0.43	0.26	0.11	0.14	0.49
1.00	5.48	0.36	0.20	0.06	0.10	0.42
1.15	6.19	0.28	0.13	0.00	0.07	0.34

[1]integrated over the solar spectrum, $300 < \lambda < 2500$ nm

[2]integrated over the ultraviolet region of the solar spectrum, $300 < \lambda < 400$ nm

Table 7.1 Derived values of OC AAE and OC contribution to wood smoke absorption of solar radiation as they depend on the chosen value of BC AAE.

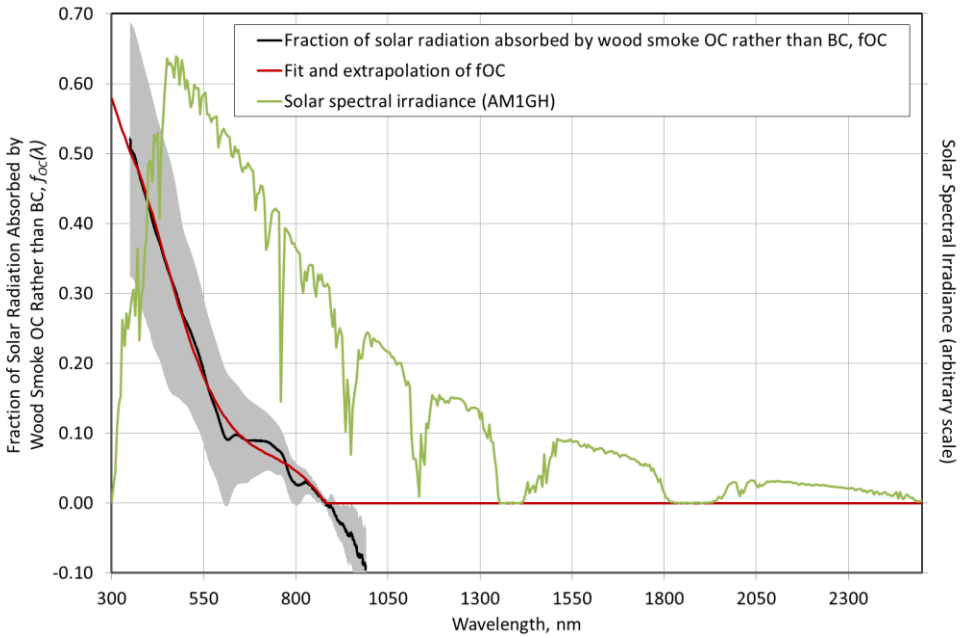

Figure 7.3. Fraction of solar radiation absorbed by organic carbon rather than black carbon in residential wood smoke particulate matter, $f_{OC}(\lambda)$: (black line and gray region) average values for 115 samples ± 1 standard deviation and (red line) a model fit and extrapolation of the data. Also shown (green line) is the clear sky air mass one global horizontal (AM1GH) solar spectrum at the earth's surface [*Levinson et al.*, 2010].

The results of this analysis depend on the value of the AAE of BC assumed in the apportionment of light attenuation (Fig. 7.1). To illustrate this sensitivity, we recalculated most results assuming values for BC AAE of 1.00 and 1.15 rather than 0.86 (Table 7.1). The larger the value of BC AAE, the smaller is the contribution of OC to wood smoke absorption: for BC AAE values of 1.00 and 1.15, OC accounts for 10% and 7%, respectively, of the solar radiation absorbed by the wood smoke particulate matter.

7.6 Significance of results

The AAE of OC in wood smoke has potential application for apportionment of solar radiation absorption to different particulate matter species and of atmospheric particulate matter to different sources [*Favez et al.*, 2010; *Praveen et al.*, 2012; *Russell et al.*, 2010; *Sandradewi et al.*, 2008]. The AAE values we report for a large number of wood smoke particulate matter samples (AAE = 1.9, n = 115) and especially for the light-absorbing OC fraction (AAE = 5.0, n = 87) may be useful in this regard.

The fraction of solar radiation that would be absorbed by OC rather than BC in wood smoke particulate matter (14%) indicates that BC is the dominant light-absorbing species in atmospheres burdened with residential wood smoke and OC absorption is secondary but not insignificant. Since the relative amounts of OC and BC emitted from fires have been shown to depend on combustion

conditions and wood type [*Mazzoleni et al.*, 2007; *McMeeking et al.*, 2009] and have been reported to vary widely [*Piazzalunga et al.*, 2011], the results of this investigation apply strictly to the residential wood smoke samples collected in Cambria, California. The contribution of OC to solar radiation absorption may be more or less in other situations than we find here.

7.7 Conclusions

A broad comparison can be made with other studies that have characterized particulate matter in regions with open burning (e.g., wildfires in Africa and South America) and residential biofuel combustion (e.g., wood and crop residues used for cooking and heating in Asia). On a global scale, these others sources are the dominant emitters of carbonaceous particulate matter [*Bond et al.*, 2004]. Our results, which show that wood smoke OC and BC absorb a comparable amount of solar radiation at wavelengths below 400 nm, are consistent with those of [*Hoffer et al.*, 2006], who found that OC in Amazonian biomass smoke particles contributed up to 50% of light absorption at 300 nm and significantly to absorption of broadband solar radiation, and those of [*Flowers et al.*, 2010], who found that OC accounted for up to 50% of the 400 nm light absorption of particulate matter transported over mainland Asia. These results suggest that OC absorption may influence tropospheric photochemistry [*Li et al.*, 2011; *Vuilleumier et al.*, 2001]. Also, the fraction of light absorbed by OC rather than BC in the wood smoke particulate matter in this investigation is similar to that which we previously reported for samples collected over southern Africa during the dry biomass burning season [*Kirchstetter et al.*, 2004].

The similarities across studies, despite different analytical methods and differences in fuels, combustion processes, and atmospheric processing, indicates that light-absorbing OC is ubiquitous in atmospheres influenced by biomass and biofuel burning. Since biomass and biofuel combustion generates a major portion of atmospheric carbonaceous particulate matter globally, and since carbonaceous particulate matter affects climate [*Ramanathan and Carmichael*, 2008], these observations support the notion that light-absorbing OC should be considered when particulate matter effects on the radiative forcing of climate are evaluated [*Chakrabarty et al.*, 2010].

8.0 Direct radiative forcing of carbonaceous aerosols

8.1 Introduction

To quantify the impact of carbonaceous aerosols on the regional climate, recent modeling studies have made great efforts to simulate both their spatial and temporal distribution of and the associated radiative forcing. Rather than relying solely on model predictions, this chapter presents an observationally constrained assessment of the direct radiative forcing at a regional scale over California. To accomplish this task, we follow a three-step approach – first, by exploiting multiple observations (including ground sites and satellites), we construct the distribution of aerosol optical depths and aerosol absorption optical depths over California for the years 2000-2010. The total aerosol solar absorption is then partitioned into elemental carbon (EC), organic carbon (OC), and dust aerosols using the scheme described in Chapter 5. Finally, the direct solar absorption attributable to carbonaceous aerosols (EC and OC) i.e. the forcing is estimated using a radiative transfer model, and validated against regional climate models.

8.2 Observations of aerosol properties

The data sets used in this study originate from multi-platform observation of aerosol optical properties, notably aerosol optical depth (AOD) and aerosol absorption optical depth (AAOD). A larger AOD indicates a greater amount of aerosol existing in the column atmosphere, that in turn reduces the penetration of solar radiation towards the surface by either scattering the light back to space or absorbing the energy. The AAOD is defined as the absorbing component of AOD, which directly relates to the aerosol's warming potential. Both the AOD/AAOD are wavelength dependent, and in this study we focus on the visible band (about 400-700 nm) of sunlight. Further, the AOD/AAOD are explicit properties, so total the AOD/AAOD can be roughly treated as the sum of AODs/AAODs from individual aerosol species (if any non-linearity arising from the mixing state is not taken into account).

We incorporate two continuously operating measurement sources for the AOD in this study. AERONET provides ground-based measurement of aerosol optical properties in the atmosphere column [*Holben et al.*, 2001] and has twelve operational sites located within California and the surrounding states of Oregon, Nevada, and Arizona (Figure 8.1). The AOD data we use is level-2 (after cloud screening and quality control) all-points dataset from 2000 to 2010, downloaded from the AERONET website (Version-2). The data are compiled into seasonal averages over individual sites. While AERONET provides high-accuracy quality-controlled measurement of AOD, it cannot provide full spatial coverage of California due to the limited number of stations.

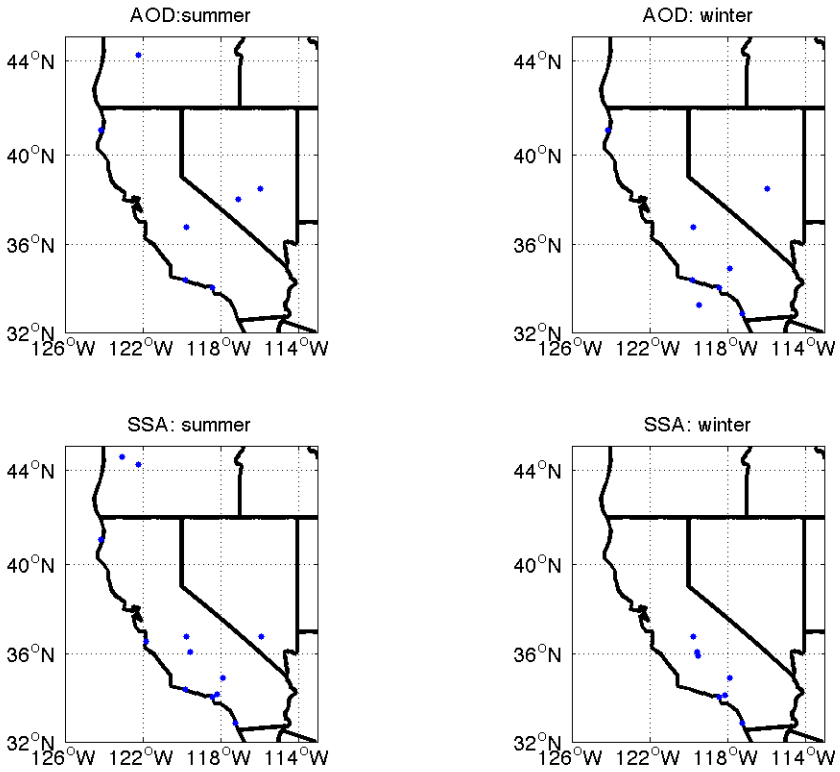

Figure 8.1 Operational AERONET sites in California and neighboring states, indicating availability of valid quality assured measurements.

Due to the somewhat limited coverage provided by AERONET, we need an alternate source of AOD measurements. The Multi-angle Imaging Spectro-Radiometer (MISR) on board NASA Terra satellite has been providing decade-long monitoring of AOD measurement over the globe since 2000 [*Kahn et al.*, 2010], and can fill the gap in spatial coverage. Compared to MISR, the Moderate Resolution Imaging Spectroradiometer (MODIS) also provides AOD measurements that have a greater spatial resolution and shorter revisit time, however the MISR AOD products show a closer agreement to AERONET records, particularly over bright desert surfaces [*Kahn et al.*, 2009] that dominate the southern and eastern part of California. An alternate AOD dataset is provided by the Sea-viewing Wide Field-of-view Sensor (SeaWIFS), however these AOD retrievals are limited to wavelengths shorter than 670 nm over land [*Hsu et al.*, 2012]. As shown in Chapter 5, we require information from multiple wavelengths across the visible bands (e.g 440, 670, 870 nm) to successfully determine the contribution from carbonaceous aerosols and dust. We therefore used the MISR data set to most accurately determine the climatology of absorbing aerosols in California.

We downloaded the 0.5 degree by 0.5 degree monthly-averaged AOD data from NASA website for 2000-2010. Validation of MISR AOD observations with ground-based AERONET and other satellite measurements has been done by numerous studies, and shows reasonably good agreement [*Chen et al.*, 2008; *Kahn et al.*, 2010; *Mishchenko et al.*, 2010]. As an example, Figure 9.2(a) illustrates the AOD at 440 nm obtained from MISR in the fall seasons (June-August), showing the typical climatology of aerosols in this region. The AOD is high along the coast regions and southern California inland, indicating the location of high aerosol concentrations.

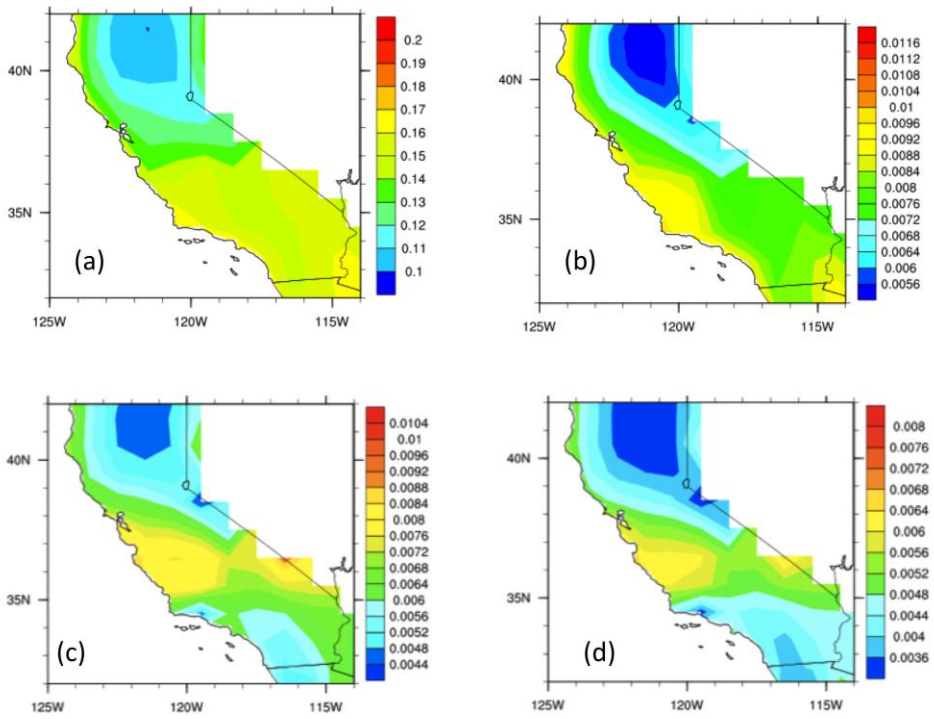

Figure 8.2 Average MISR satellite retrievals of the (a) total AOD, (b) total AAOD, (c) EC AOD, and (d) EC AAOD for the months of June-August in the California domain.

The Single Scattering Albedo (SSA) is defined as 1-AAOD/AOD, and has a range of 0 to 1 (with the limits of 1 corresponding to non-absorbing aerosols and 0 to completely absorbing aerosols). As suggested in Chapter 5, SSA is an intrinsic property that is solely determined by the chemical and physical properties of the aerosol, rather than the amount of mass loading. The total amount of visible light absorbed by BC is highly sensitive to the SSA and it is crucial to accurately estimate it in order to quantify the radiative forcing.

We faced two challenges in obtaining observation-based SSA measurement. First, current SSA observations provided by the satellite (MISR) are not quality-assured. A preliminary analysis suggests significant bias in California and other

parts of the world. Another instrument with capacity to observe SSA, the Ozone Monitoring Instrument (OMI), produces the retrieval only at ultra-violet wavelengths [*Torres et al.*, 2007], which may be useful in distinguishing certain aerosol types such as smoke [*Wilcox et al.*, 2009], but does not provide sufficient information to conduct radiative forcing calculation. Due to these concerns, we did not use any SSA or absorption related information from satellites in this study. It is hoped that future employment of advanced remote sensing techniques such as the planned GLORY project of NASA will provide unprecedented continuous measurement of SSA from space.

The second challenge we faced is that AERONET sites report the AAOD (alternately SSA) value only if the total AOD exceeds a threshold value of 0.4 at 440 nm. This condition must be satisfied to provide a sufficient signal-to-noise ratio for the AERONET retrieval algorithms. Since total AOD over California is typically less than this threshold value (Figure 8.2(a)), most of the time AERONET sites do not resolve the AAOD from the AOD despite the fact that the principle part of the AOD is actually due to absorption. We instead use all available AAOD measurement from AERONET ("all-points"), to calculate the SSA (according to AOD measurements reported at the same time) corresponding to high pollution events. We then apply the same SSA value even to low AOD measurements to calculate AAOD that are not directly reported. The assumption here is that SSA is an intrinsic property determined by chemical composition instead of the total amount of aerosol. Therefore, in the event when the amount of aerosol is not sufficient enough for AERONET instrument to record the SSA, SSA is assumed to be same as the seasonal average as calculated with data reported in large AOD events at the same location. The seasonal mean AERONET SSA measurement from each observational site are then summarized into the average values for six regions in California (North/Central/South, Coastal/Inland region) to account for potential variation in aerosol composition arising out of emission sources differences. Such a division of area is backed up by local air-pollution management agency (e.g. California Air Resource Board's air basin division). The AAOD distribution (Figure 8.2 (b)) suggests stronger aerosol absorption along the coastline, which corresponds to the pattern of human habitation in California.

As discussed, the SSA obtained from AERONET measurements is limited in both location and time. To ensure the credibility of our approach (denoted as SSA_AERONET), we also used simulations from the Goddard Chemistry Aerosol Radiation and Transport [*Chin et al.*, 2002] as the model-based option for SSA (denoted as SSA_GOCART). The seasonal mean SSA_GOCART from 2000 to 2007 is used to validate the SSA_AERONET at various sites (Figure 9.3). Note that SSA_AERONET seasonal observations are not available at all seasons from 2000 to 2007 due to the threshold issue we discussed. We find that SSA_GOCART is smaller than SSA_AERONET at all three-wavelengths, in particular at 440 nm. SSA_AERONET also shows a smaller value in summer and fall, while such a seasonal variation is less obvious from SSA_GOCART.

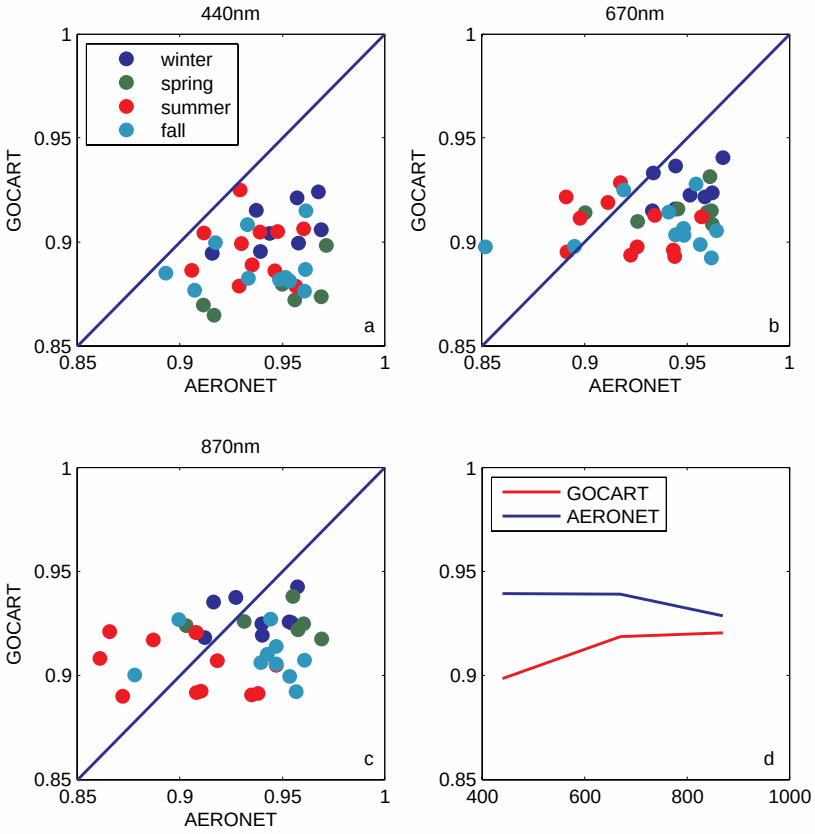

Figure 8.3 Seasonally averaged values of the SSA from GOCART and AERONET at (a) 440 nm, (b) 670 nm, and (c) 870 nm. The wavelength dependence of all available SSA measurements is illustrated in panel (d).

The possible reasons for the discrepancy of SSA values are as follows – first, the dust SSA at 450 nm in GOCART is 0.83 based on refractive index assumptions, which is significantly lower than the value (0.91) we obtained from a purely observation-based approach [*Bahadur et al.*, 2012b]. Therefore the GOCART model may overestimate dust absorption at 440 nm and have a lower SSA value. As dust AOD decrease sharply towards infrared wavelengths (due to large particle size), the discrepancy between the two sources decreases (Figure 8.3(d)). Second, the carbonaceous aerosol emission inventory used by GOCART [*Cooke et al.*, 1999] is based on energy use and combustion technology in early 1990s, and may have larger BC emission. [*Bahadur et al.*, 2011] showed that diesel engine filter installation since 1980s have significantly lower the BC emission in California, almost by half. GOCART may therefore overestimate BC concentrations and have a lower SSA compared to observations. At this stage, we have no further evidence that suggests the 'true' value of SSA and instead posit that SSA inferred from GOCART and AERONET provide limiting values that bracket the SSA, as shown in Figure 8.2(d). We therefore calculate the aerosol properties and radiative forcing in two parallel cases (SSA_AERONET and

SSA_GOCART) to bracket the uncertainty due to the imperfect data sources of SSA measurements.

8.3 Partitioning of aerosol absorption

After obtaining seasonal mean of total AOD and AAOD at multiple wavelengths over California, we partitioned the total among the three different chemical species - EC, dust and, OC that absorb visible solar radiation. The details and verification of the partitioning scheme are discussed in Chapter 5. The values of AAE and SSA used in the partitioning analysis based on AERONET and the GOCART model are summarized in Table 8.1 Our first focus is to separate the AAOD contribution of carbonaceous aerosol (mainly from anthropogenic sources) from natural dust aerosols. On average, the total AAOD over California is about 0.003-0.01, which is about 5% of total AOD as shown in Figure 8.2(b). The overall spatial variations suggest that Southern California has larger AAOD as compared with Northern California, consistent with the greater population density in this region. The breakup of total AAOD into dust and carbonaceous aerosol shows that the loading of dust is larger in the southern region (Figure 8.4(a)), consistent with the drier climate and semi-desert environment. However, using the SSA values from GOCART model (SSA_GOCART), such a north-south difference in dust loading is less significant (Figure 8.8(b)), and the directly simulated AAOD from GOCART (Figure 8.4(c)) does not show any north-south variation at all. The majority of contribution to total AAOD is from carbonaceous aerosols, which is about 4-5 times larger than dust AAOD at 550 nm. As in the case of SSA_GOCART, the carbonaceous aerosol still dominates the AAOD, but dust contribution is significantly increased. The absolute value of AAOD is larger in SSA_GOCART case, due to the lower value of SSA from the GOCART.

AERONET					
Species	AAE1 (440-675 nm)	AAE2 (675-870 nm)	SSA 440 nm	SSA 675 nm	SSA 870 nm
Dust	2.6	1.1	0.91	0.97	0.98
EC	0.55	0.85	0.28	0.10	0.04
OC	4.20	--	0.71	0.92	1.00
GOCART					
Species	AAE1 (450-650 nm)	AAE2 (650-900 nm)	SSA 450 nm	SSA 650 nm	SSA 900 nm
Dust	1.86	1.08	0.83	0.91	0.94
EC	1.18	1.13	0.25	0.18	0.11
OC	0.46	-0.47	0.98	0.96	0.91

Table 8.1 Comparison of spectral properties derived from AERONET observations and the GOCART model.

The difference in partitioning AAOD between SSA_GOCART and SSA_AERONET cases can be understood as the following: The essence of our partitioning method is to use the wavelength dependence of AAOD to find out

how much AAOD contribution is from dust or EC/OC. Pure dust SSA in our calculation is assumed to increase with wavelength (from 0.91 at 440 nm to 0.97 at 670 nm), while the SSA of EC decrease with wavelength (from 0.28 at 440 nm to 0.1 at 670 nm). Since the AERONET observed SSA show a slightly decreased trend of SSA with wavelength (Fig 8.2(d)), the calculation utilizing AERONET SSA tends to attribute more AAOD to carbonaceous aerosol, while the SSA_GOCART case suggests relatively more contribution from dust. The limitation of multiple wavelength measurement of SSA at current stage is the fundamental reason that we cannot further narrow down the difference between two cases.

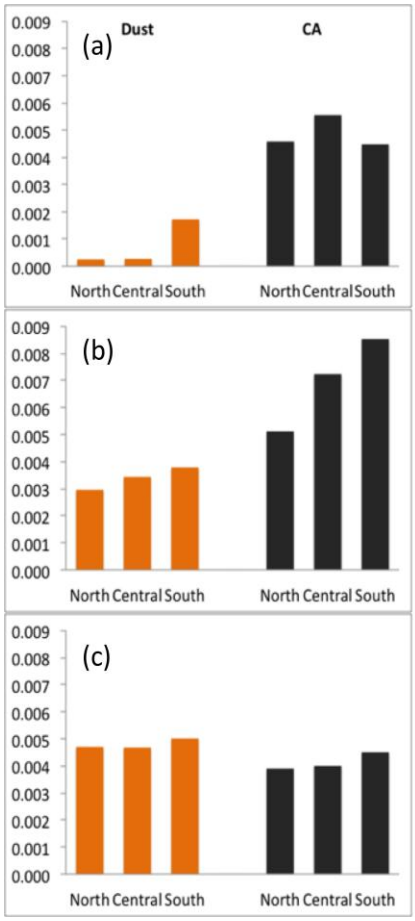

Figure 8.4 Relative contributions to the AAOD (550 nm) from dust (shown in orange) and carbonaceous aerosols (shown in black) calculated using (a) MISR AOD and SSA_AERONET, (b) MISR AOD and SSA_GOCART, (c) GOCART simulations.

We further assess the relative contribution of AAOD from EC and OC based on the difference in the wavelength dependence of absorption [*Bahadur et al.*, 2012b]. The partitioning based on SSA_AERONET suggests that OC AAOD at 440 nm is about half of EC, as shown in Figure 8.5(a), dropping down to only 15% at 550 nm. On the other hand, partitioning based on SSA_GOCART (Figure

8.5(b)) suggests a much smaller OC contribution to AAOD, presumably because the model does not fully take into account of OC absorption (The OC SSA in GOCART is 0.98 at 450 nm, in contrast to 0.71 obtained from empirical approach used in this study). The EC AAOD in SSA_GOCART case is larger than SSA_AERONET because the total AAOD is also larger. This difference in OC absorption clearly indicates further studies from observations and modeling are needed to clarify this issue.

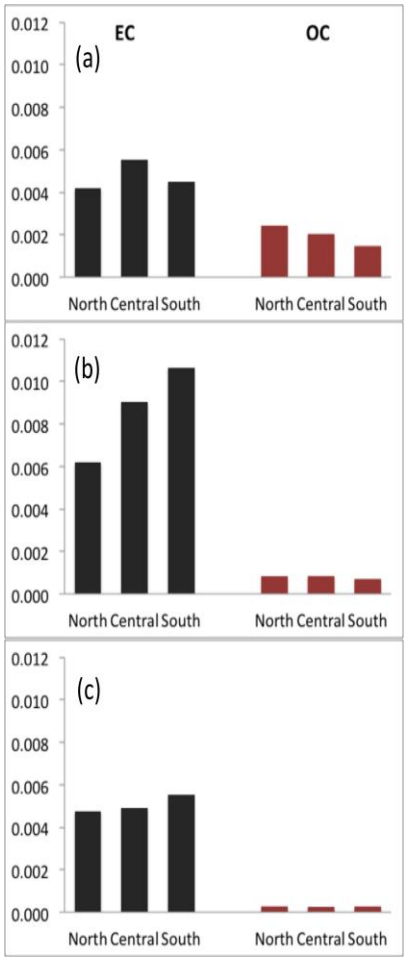

Figure 8.5 Relative contributions to the AAOD (550 nm) from EC (shown in black) and OC (shown in brown) calculated using (a) MISR AOD and SSA_AERONET, (b) MISR AOD and SSA_GOCART, (c) GOCART simulations.

The spatial variability of AOD and AAOD for EC are illustrated in Figure 8.2 (c) and (d). The EC AOD and AAOD so determined is mainly concentrated in population-dense areas including the Bay Area, Central Valley, and Los Angeles metropolitan region, suggesting EC in California is dominated by anthropogenic sources. The EC does not have high AOD value over Southern California inland region (Figure 8.2(c) compared with Figure 8.2(a)), where dust lofted from the Mojave desert eco-regions (extending into Arizona and northern Mexico) appears to be the main absorber.

Finally, we also assessed the seasonal variation of the aerosol properties. The dust in Southern California has the largest seasonal variation, with much higher values during winter and spring, which is possibly due to long-range transport from Asia. The AAOD of BC is larger in summer, which might be caused by wild fire activities. The larger OC AOD value in summer and fall, especially in Central and South California, seems to support this hypothesis. However, most of carbonaceous aerosol emissions in California are due to anthropogenic activities, which do not have obvious seasonal variation, and therefore the seasonal variation of BC and OC is not entirely clear. It should be noted that for the SSA_GOCART case, although the absolute values of the AOD and AAOD are different, the seasonal trends discussed above remains valid, suggesting the model successfully captures the meteorological condition's influence on aerosol transport. The AAOD at 550 nm for dust, EC, and OC resolved by season and region are summarized in Table 8.2.

	Winter (Dec-Feb)	Spring (Mar-May)	Summer (Jun-Aug)	Fall (Sep-Nov)	Annual	
North	0.0003	0.0003	0.0002	0.0002	0.0002	Dust
Central	0.0002	0.0003	0.0000	0.0006	0.0003	
South	0.0027	0.0029	0.0000	0.0012	0.0017	
North	0.0038	0.0041	0.0038	0.0031	0.0037	EC
Central	0.0042	0.0057	0.0058	0.0035	0.0048	
South	0.0021	0.0040	0.0058	0.0038	0.0039	
North	0.0009	0.0009	0.0009	0.0008	0.0009	OC
Central	0.0005	0.0005	0.0012	0.0008	0.0007	
South	0.0001	0.0000	0.0010	0.0010	0.0005	

Table 8.2 Average AAOD for absorbing species at 550 nm in California determined from MISR and SSA_AERONET observations resolved by region and season.

8.4 Comparison with model simulations

As an additional validation of our hybrid approach, we compare the AOD and AAOD values determined in Section 8.3 with climate model simulations. Simulations from GOCART [*Chin et al.*, 2003] from 2000 to 2007 are resolved into North/Central/South California and seasonally averaged to provide a point of comparison. The BC AAOD shows reasonably good agreement as shown in Figures 8.6(a) and 8.6(b) between GOCART and observations, although the OC AAOD is at least underestimated by approximately a factor of 2, despite the fact that OC AOD is overestimated (as the SSA of OC in GOCART is 0.98 at 450 nm).

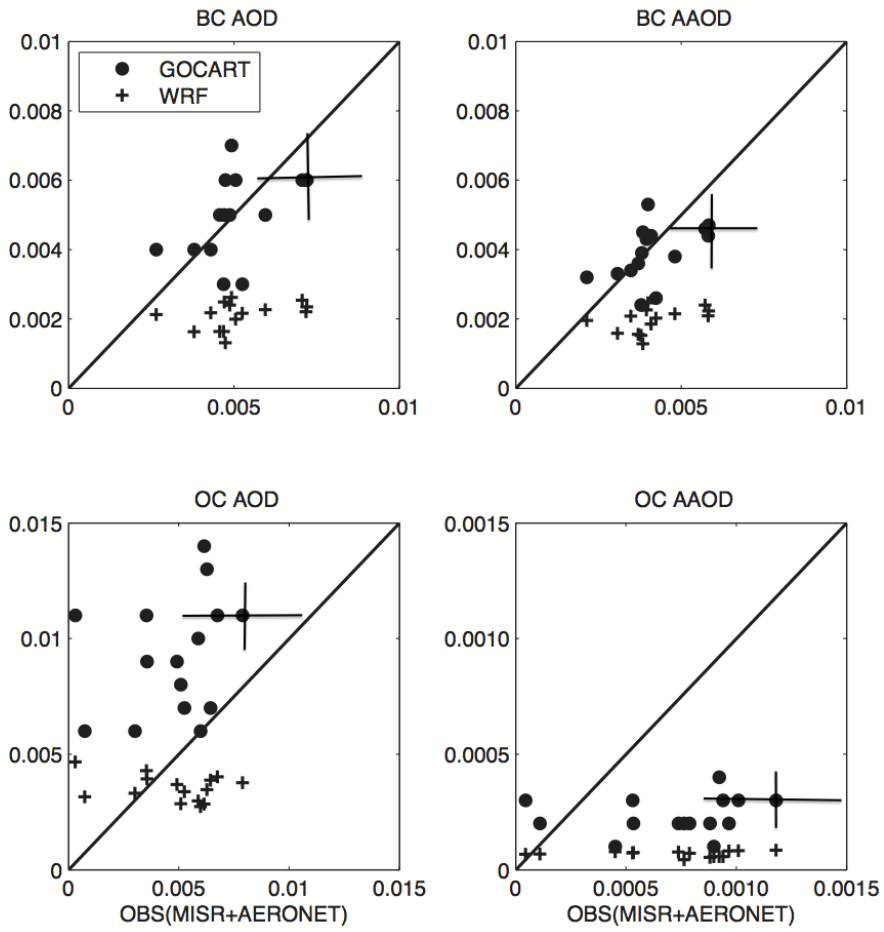

Figure 8.6 (a) AOD of BC (550 nm) at different seasons and regions (Northern, Central and Southern California) from observation-based method (SSA_AERONET), compared with GOCART and WRF simulations (with standard BC emission). The whiskers show standard deviation of AOD average in a given season and region. (b)-(d) same as (a), but for BC AAOD, OC AOD and OC AAOD, respectively.

Another model used in the comparison is Weather Research Forecast (WRF) model specifically configured for the California region at the Pacific Northwest National Laboratory, which includes a more updated emission inventory and finer spatial resolution (Chapter 11 and Chapter 12). We found that the BC AOD and AAOD simulated by WRF are 50% lower than both GOCART and observational estimates. This could be due to a potential underestimation in the BC emission (as discussed in greater detail in Chapter 10). WRF-simulated OC AOD is comparable with observational estimates (Figure 8.6(c)), but the OC AAOD simulated is virtually zero (Figure 8.6(d)), as the model does not take into account any OC absorptions. The small OC AAOD is a result of the enhancement of absorption when OC is internally mixed with EC, rather than direct absorption by the OC itself.

8.5 Aerosol vertical profiles

Since aerosols in the atmosphere are not homogenously mixed, the location of the aerosol layer is important for its radiative impact. If the aerosols are above the cloud layer their absorption tends to get enhanced [*Koch and Del Genio*, 2010] due to a higher albedo. The Cloud-Aerosol Lidar and Infrared Pathfinder Satellite Observation (CALIPSO) satellite [*Young and Vaughan*, 2009] provides the aerosol extinction coefficient profile over the globe since summer of 2006, which corresponds to the vertical distribution of aerosols. CALIPSO profiles have been validated with aircraft measurements and show reasonably good similarity (Cazorla et al., in preparation). However, current satellite observation can only provide limited snap shots of aerosol layers at particular days due to the narrow footprint of laser beam. The profiles in California are similar across the seasons, showing an elevated aerosol layer at about 200 m (Figure 8.7). Winter and spring profiles have additional elevated layers at about 2000 m, especially for Northern California, which probably correspond to the long-range transport from Asia [*Hadley et al.*, 2007].

The use of near-surface observations from CALIPSO can be problematic however, due to the local topography and cloud contamination. To account for this problem, we adopt the surface extinction coefficient directly measured at surface sites maintained by the IMPROVE network for altitudes below 500m. The final vertical structure of the aerosol is then obtained by constructing a hybrid profile combining seasonal mean profiles combining CALIPSO (above 500 m) and IMPROVE (below 500 m) measurements over North/Central/South regions in California.

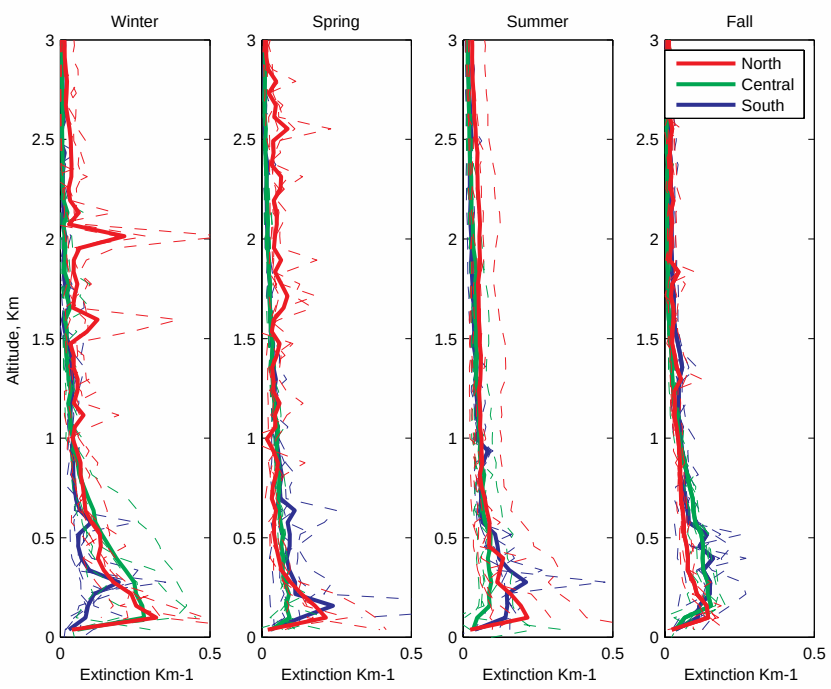

Figure 8.7 Seasonally and spatially resolved vertical profiles of aerosols in California (solid lines) constructed from CALIPSO satellite retrievals (dashed lines). Aerosol extinction is directly correlated to aerosol mass loading.

8.6 The MACR model

The radiative forcing attributed to a certain type of aerosol is defined as the energy flux change when that type of aerosol is removed from the atmosphere. We can therefore estimate the radiative forcing by performing two parallel radiation transfer calculations: one with all types of aerosol optical property included in the grid-by-grid model, and the other with the specific type of aerosol removed from the model. Note that the radiative forcing discussed in this study is the so-called aerosol "direct forcing" and any potential impact of the aerosol on clouds is not considered. In this study, we use the Monte Carlo Aerosol and Cloud Radiation transfer model (MACR) initially designed at UCSD that has been improved over the years and successfully applied in a number of global and regional aerosol studies [*Chung et al.*, 2005; *Podgorny and Ramanathan*, 2001]. The model simulates energy flux from top to bottom of the atmosphere by tracing the movement of photons with random processes. The scattering and absorption of water vapor, ozone, clouds and aerosols are taken into account in the simulation. The radiative transfer model used in this study is a clear-sky Monte Carlo model [*Podgorny et al.*, 2000] that accounts for all multiple scattering by individual aerosol species, air molecules and reflections from the surface. In the case of externally mixed aerosol, the probability of a scattering interaction is determined by relative contribution of the species to the total aerosol extinction coefficient in a layer. Scattering angles are computed by linear interpolation in a table of the inverse cumulative scattering probability, so that the model

assimilates the Mie phase functions without compromising the angular resolution. We also use Henyey–Greenstein approximation to the Mie phase function as a sensitivity study. For a given wavelength, an AOT is computed by least square fitting of the spectral CIMEL optical depths in a log–log scale. The entire broad band solar spectrum (200–4000 nm) divided into 38 spectral bands is integrated for aerosol radiative forcing calculations

The model atmosphere spans altitudes from the surface up to 100 km and has 33 reference levels, which are 1 km thick each below 25 km of altitude. Rayleigh scattering and ozone absorption are tabulated on each of the reference levels and are then linearly interpolated in the process of Monte Carlo computations using the maximum cross-section method. The solar irradiance, cross sections for Rayleigh scattering, ozone absorption, and vertical temperature and pressure profiles follow standards from the World Meteorological Organization. Absorption by oxygen, water vapor, and carbon dioxide is calculated by exponential sum fitting.

The total cloud amount are from Clouds and the Earth's Radiant Energy System [*Wielicki*, 1996] and were subdivided into low, middle and high cloud based on data from International Satellite Cloud Climatology Project [*Jin et al.*, 1996]. The various data sets comprising aerosol inputs to the model are typically available at different spatial and temporal resolutions, but are all reconciled into 1-degree by 1-degree grids and monthly averages before the model is deployed. The assimilated AOD/AAOD measurements at multiple wavelengths along with the hybrid vertical profiles provide the input describing aerosols into the model. The MACR model then simulates the energy flux at 1-degree by 1-degree grids through the atmosphere to the surface, and the difference in flux between two sets of simulations (due to removal of a certain type of aerosol from the second simulation) yields the radiative forcing of that type of aerosol. A similar calculation can be done with absence of cloud to calculate the radiative forcing of aerosol in cloud-free sky.

8.7 Radiative forcing results

To capture the 3-D forcing structure of carbonaceous aerosols, we subdivided California into three regions (North, Central, and South), and calculate the forcing at Top of the Atmosphere (TOA), at the surface level (Sfc), and within the column atmosphere layer (Atm). The atmospheric heating due to the absorption by EC and OC is between 1.7-2.4 W m^{-2} (Table 8.3) according to our observational estimates, as illustrated in Figure 8.8. The GOCART model's simulation yields atmospheric heating at comparable magnitude, which is consistent with the comparison of AAOD (Figure 8.6). However, GOCART, due to its coarser resolution, is not able to capture the finer spatial variation (coast to inland, north to south) seen in our observational estimates. In contrast, the WRF model, due to its finer resolution, is able to capture the high concentration hotspot close to cities and urban agglomerations.

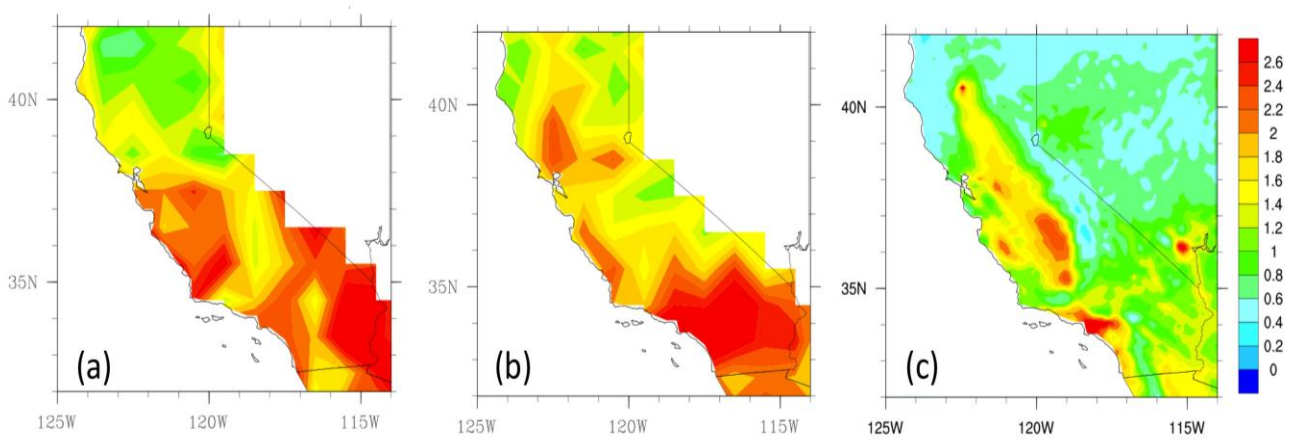

Figure 8.8 Atmospheric heating due to carbonaceous aerosols (EC+OC) in California calculated using (a) observationally constrained data, (b) GOCART simulations, and (c) WRF simulations.

The average TOA forcing due to carbonaceous aerosol is illustrated in Figure 8.9 and is about 0.2-1.9 W m^{-2}. The positive sign indicates carbonaceous aerosol overall is a considerably large warming source (as a reference, the global average CO_2 warming is 1.7 W m^{-2}). In contrast, dust aerosols have cooling effect at TOA especially over the Southern region. The TOA forcing of carbonaceous aerosol also has a north-to-south asymmetry, potentially associated with population and industry activity difference between Northern and Southern California. The carbonaceous aerosol radiative forcing at TOA calculated from GOCART simulation is much smaller (-0.1 to 0.7 W m^{-2}), mainly because OC forcing from the model simulation is more negative (-0.3 W m^{-2}). The large overall positive value of carbonaceous aerosol forcing is in contrast with model simulations that suggest that the OC scattering effect can largely offset the co-emitted BC's heating effect. We can therefore infer from the results here that environmental protection activities in California targeting BC pollutants (and co-emitted OC) have effectively contributed to the mitigation of global warming by cutting down on the direct absorption.

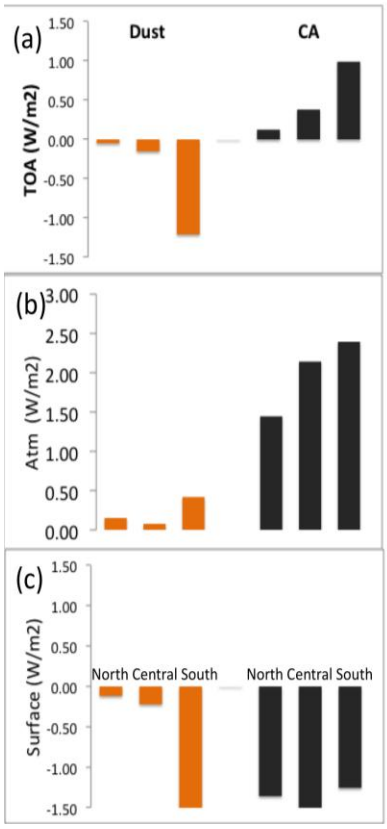

Figure 8.9 Radiative forcing at the (a) Top-of-Atmosphere (TOA), (b) in the Atmosphere (atm), and (c) at the surface (sfc) attributable to dust and carbonaceous aerosols in California determined using observationally constrained aerosol properties.

More importantly for regional climate, the carbonaceous aerosols intercept the heat that would be reaching the ground level and then induce atmospheric heating. According to our calculation, the existence of carbonaceous aerosol reduces the solar radiation reaching the ground by between 0.4 to 1.4 W m^{-2} (Figure 8.9(c)). Such a dimming effect has climatic consequences in water budget as it suppresses the evaporation of water from surface [*Ramanathan et al.*, 2001].

As with the AOD and AAOD, carbonaceous aerosol forcing can be further partitioned into EC and OC. As illustrated in Table 8.3, the heating effect of EC is about 75-85% of the total, with the rest contributed by OC. Although the OC absorption at 440 nm is as large as 30-50% of EC absorption it declines strongly towards the larger wavelength, and EC dominates the overall heating effect. The TOA forcing attributed to carbonaceous aerosols and EC alone in the two bounding SSA_AERONET and SSA_GOCART scenarios is illustrated in Figure 8.10.

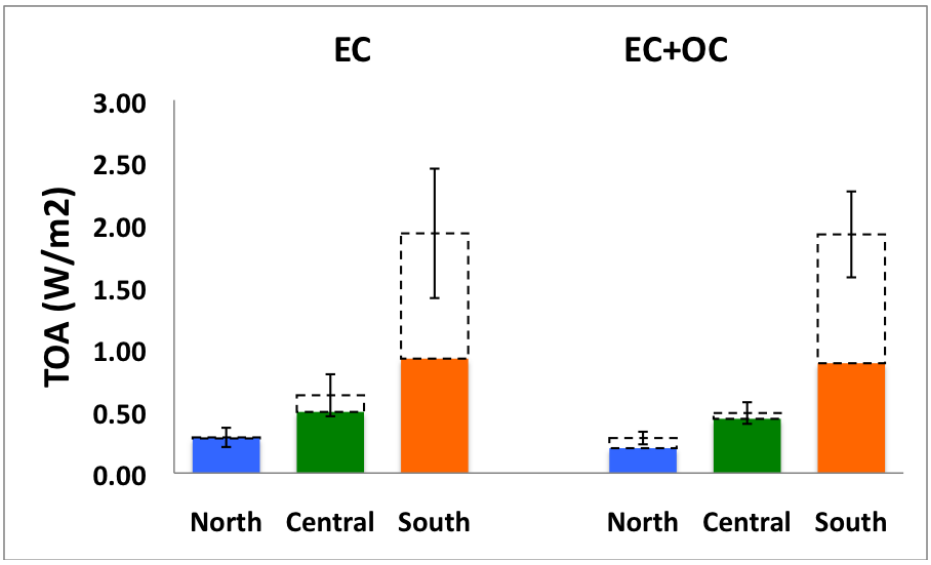

Figure 8.10 Top of the Atmosphere forcing for EC and Carbonaceous aerosols determined in the bounding cases using SSA_AERONET (solid bars) and SSA_GOCART (dashed boxes) in California.

Similar to the regional variation in AAOD, EC atmospheric heating is larger in Southern California, while OC is larger in Northern California, and both this pattern in spatial variation and the magnitude of atmospheric heating are supported by GOCART simulation. The surface dimming effect of EC is between two to four times larger than OC. The estimation of SSA_GOCART show larger dimming contributed from BC with less dimming from OC. Compared with the GOCART model, our radiative transfer calculations underestimate EC surface dimming, and overestimates the OC contribution. GOCART also captures the elevated forcing over Southern California (Fig 8.8(b)), while the observation-based estimate also suggests high aerosol loading over Central California (Fig 8.8(a)), which is supported by WRF simulations. Note that since AOD/AAOD comparisons (Fig 8.3) indicate that the baseline WRF simulation underestimated BC AOD by at least a factor of two, the forcing results shown here are from a simulation in which default emission inventory are doubled. Despite this, the atmospheric forcing simulated by WRF is still smaller than observational estimates by 15-30%. We speculate that the discrepancy is due to a combination of emission inventory bias and neglect of OC absorption in the model. The OC TOA forcing is negative but small according to our estimates (-0.1 W m^{-2}), as the scattering effect of OC is partially offset by its relatively weak absorption. The TOA cooling effect of OC simulated by GOCART in contrast is three times larger than our estimates. However, we point out the uncertainty associated with selection of SSA sources is at least 50% (black bars in Figure 8.10) and this uncertainty covers most of the discrepancy between the models. Compared to SSA_GOCART, calculations using SSA_AERONET have a stronger OC absorption.

	MISR AOD SSA_AERONET	MISR AOD SSA_GOCART	GOCART		
North	1.3	1.7	1.3		
Central	2.0	2.7	1.6		
South	2.1	4.0	2.3	EC	
North	0.5	0.1	0.2		
Central	0.4	0.1	0.1		Atm
South	0.3	0.0	0.0	OC	
North	1.7	1.8	1.5		
Central	2.4	2.8	1.7		
South	2.4	4.0	2.3	EC+OC	
North	0.3	0.3	0.2		
Central	0.5	0.6	0.3		
South	0.9	1.9	1.0	EC	
North	-0.1	0.0	-0.3		
Central	-0.1	-0.1	-0.3		TOA
South	0.0	0.0	-0.3	OC	
North	0.2	0.3	-0.1		
Central	0.4	0.5	0.0		
South	0.9	1.9	0.7	EC+OC	
North	-1.0	-1.3	-1.1		
Central	-1.4	-2.1	-1.1		
South	-1.3	-2.2	-1.3	EC	
North	-0.5	-0.1	-0.5		
Central	-0.5	-0.3	-0.4		Sfc
South	-0.3	-0.2	-0.4	OC	
North	-1.5	-1.5	-1.6		
Central	-1.9	-2.4	-1.5		
South	-1.6	-2.5	-1.7	EC+OC	

Table 8.3 Radiative forcing of EC and carbonaceous aerosols determined at the TOA, surface, and within atmosphere column from the data assimilation scenarios in this work.

The bias in OC absorption simulated by GOCART and WRF suggests that the current model parameterization is not able to fully capture the real OC absorption and that the models need to be further improved to incorporate the new experimental evidence of OC absorption. The future inclusion (and enhancement) of OC absorption in the models has several consequences in our understanding of carbonaceous aerosol's radiative forcing. For example, in areas where aerosol emission is greatly influenced by wildfire events (Africa, Amazonia, South East Asia) or by biofuel burning (India), the overall radiative forcing contributed by carbonaceous aerosol might have been underestimated, as current models generally treat OC as non-absorbing. Therefore, even models

that well simulate the loading of OC will not yield the correct magnitude of radiative effect of OC. If the OC amount is sufficient enough, such an underestimation of OC absorption effect may even reverse the sign of carbonaceous aerosol to change from warming to cooling.

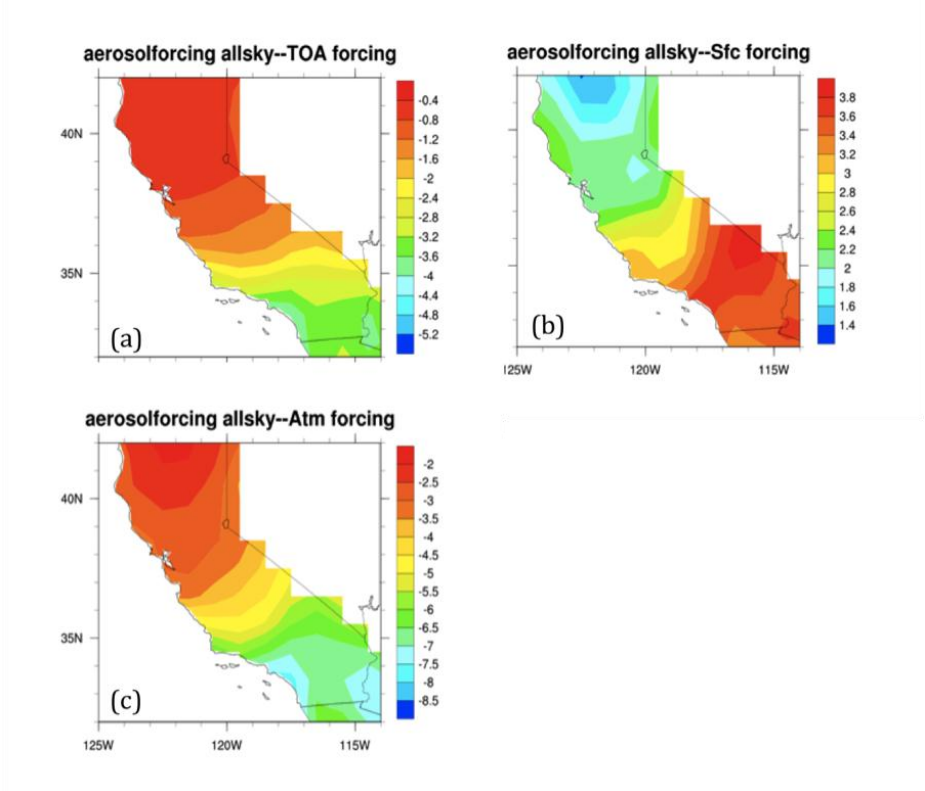

Figure 8.11 Change in the radiative forcing due to carbonaceous aerosols as a consequence of a 50% reduction in EC aerosol loading in California between 1980-2000.

8.8 Comparison with climate models

The radiative forcing associated with BC and BrC calculated using the observationally constrained MACR model is summarized in Table 8.4. The total aerosol optical depth (AOD) is retrieved from the MISR satellite whereas the single scattering albedo (SSA) is based upon observations from the AERONET network, and from the GOCART climate model, as listed in Table 8.3. The BC is found to have a positive (warming) forcing at the top of the atmosphere, and a strong atmosphere heating, leading to a net negative (dimming) forcing at the surface. The BrC is also found to heat the atmosphere, and act as a dimming agent at the surface, however, the net effect is found to be cooling at the TOA. In comparison to the observationally constrained estimates, the WRF-Chem regional climate model underestimates both the TOA and atmospheric heating of the BC. The model also finds the BrC to be strongly cooling, as it does not allow OC to absorb solar radiation. The discrepancy in the forcing, along with

differences in BC concentration (details in Chapter 11) lead us to believe that BC emissions are underrepresented, and the 2xBC simulation is found to agree much better with the observationally constrained estimates of forcing.

	Observationally Constrained SSA from AERONET	Observationally Constrained SSA from GOCART	WRF_PNNL model (1*BC)	WRF_PNNL model (2*BC)	Species
TOA Forcing					
North	0.28	0.29	0.21	0.29	**EC**
Central	0.49	0.63	0.32	0.47	**EC**
South	0.92	1.93	0.38	0.56	**EC**
State	**0.56**	**0.95**	**0.30**	**0.44**	**EC**
North	-0.08	-0.01	-0.12	-0.12	**OC**
Central	-0.06	-0.14	-0.15	-0.15	**OC**
South	-0.04	-0.01	-0.16	-0.16	**OC**
State	**-0.06**	**-0.05**	**-0.14**	**-0.14**	**OC**
Atmospheric Forcing					
North	1.25	1.72	0.57	0.78	**EC**
Central	1.99	2.68	0.81	1.20	**EC**
South	2.11	4.03	0.93	1.37	**EC**
State	**1.78**	**2.81**	**0.77**	**1.12**	**EC**
North	0.47	0.07	0.03	0.03	**OC**
Central	0.41	0.10	0.05	0.05	**OC**
South	0.33	0.02	0.04	0.04	**OC**
State	**0.40**	**0.06**	**0.04**	**0.04**	**OC**
Surface Forcing					
North	-1.01	-1.34	-0.36	-0.50	**EC**
Central	-1.41	-2.08	-0.49	-0.73	**EC**

South	-1.29	-2.24	-0.55	-0.81	**EC**
State	**-1.24**	**-1.89**	**-0.47**	**-0.68**	**EC**
North	-0.53	-0.13	-0.16	-0.16	**OC**
Central	-0.52	-0.30	-0.19	-0.19	**OC**
South	-0.32	-0.22	-0.20	-0.20	**OC**
State	**-0.46**	**-0.22**	**-0.18**	**-0.18**	**OC**

Table 8.4 Species resolved forcing at the TOA, in the atmosphere, and at the surface determined using the MACR model and the WRF-Chem regional climate model

8.9 BC reduction scenario

As recently reported by [*Bahadur et al.*, 2011] using IMPROVE measurement, BC loading in California has declined by 50% between 1980 and 2000, while no trends are seen for other aerosols, an effect attributed to the effectiveness of air pollution control measures that have targeted reductions in PM, specifically from diesel combustion sources that result in reduced BC [*CARB*, 2008; *Kirchstetter et al.*, 2008a]. We have also performed calculations that demonstrate the radiative forcing impact of such a 50% reduction of BC (Figure 8.11). This calculation should be seen as an extreme example of the possible changes in the forcing. Reducing emissions by 50% need not reduce column average BC by 50%; Due to advection by atmospheric transport, some of the BC reductions will happen downwind over rest of N America and even beyond. The life time of BC is of the order of a week and in this time air parcels (particularly the ones above 3 km) can travel across the USA in a week. Given the above caveat, BC emission reduction during the last two decades leads to a cooling of 0.8 to 3 W m^{-2} at TOA, and the atmospheric cooling due to BC reduction is as large as 6 W m^{-2} over Southern California region. Another consequence of preferentially removing BC from the atmosphere is a surface brightening of between 1.5-3.5 W m^{-2}. Such a brightening signal, if detected in observation record, can provide an objective confirmation of the magnitude of forcing estimates and historical trends.

8.10 Conclusions

We found that for California the largest fraction of atmospheric heating is contributed by EC, with OC contribution the remaining 15 to 25%. EC has a larger contribution over Southern California, while OC contribution is larger over Northern California. We validated our calculations against two chemical transport models (GOCART and WRF), and find reasonable agreement of BC absorption with GOCART, but the model underestimates the OC at least by 50%. Models

typically treat OC as purely scattering and therefore significantly underestimate its absorbing ability.

The observation-based estimates serve as an independent result to validate the performance of chemistry transport models in simulating the concentration and radiative effect of aerosols. One major implication from our analysis here is that current models (possibly with biased emission inventory and lack of treatment of OC absorption) overestimate the TOA cooling effects from OC and therefore underestimate the overall warming effect from carbonaceous aerosols (co-emitted BC and OC), in particular over biomass burning regions.

9.0 Surface solar flux in California

9.1 Introduction

The data assimilation studies performed in this work (described in Chapters 3 and 4) have led to a major finding by showing that BC over California's IMPROVE sites have decreased by as much as 50% in the 1980-2000s time period, with an even more significant decrease going back to the 1960s. The analysis of emission inventories [*Bahadur et al.*, 2011] and energy use patterns lead us to believe that the black carbon control policies as implemented by California are responsible for this reduction. Since BC is a strong absorber at all wavelengths, this decrease is expected to translate into an increase in incoming solar radiation at the surface. The MACR radiative-forcing model suggests that the observed BC reduction should have led to an increase of surface solar radiation (surface brightening) by about 1-4 W m^{-2} (about a 0.5% to 2% increase) depending on the optical properties (such as SSA) of BC. Such a large change in BC radiative forcing should be detectable with surface radiation data. A full analysis of measured solar flux has the potential to provide an observational tool for constraining predictions of radiative forcing and surface brightening, and provide a metric for determining the relative significance and magnitudes of the direct, indirect, and semi-direct effects of BC. To date, validation of these model predictions of changes in radiative forcing (or solar flux) has been restricted both by a scarcity in spatially and temporally resolved ground-based measurements (such as those provided by AERONET), and the difficulty in separating the cloud effects from remote sensing measurements (such as those provided by satellites).

9.2 The CIMIS network

The California Irrigation Management Information System (CIMIS), a program of the Office of Water Use Efficiency (OWUE) and California Department of Water Resources (DWR), manages an integrated network of over 120 automated weather stations in the state of California dating back to 1982 and overcomes the limitations in other data sets. Although the primary mission of the CIMIS network is facilitation of irrigation and water use, it provides a valuable resource to research in a wide variety of fields including air quality and climate by providing meteorological measurements with a very high spatial and temporal resolution. Each of the CIMIS monitoring stations is constructed with a standardized design and directly measures solar flux, relative humidity, air temperature, soil temperature, wind speed and direction, and precipitation. Most relevant to the surface brightening are measurements of the surface solar flux, performed by a high stability Li-Cor silicon photovoltaic detector Pyranometer. The instrument has a response time of 10 microseconds and is rated to be accurate within 95%

under natural sunlight. CIMIS stations collect measurements every minute, which are combined and logged as hourly averages in their central database that is available for unlimited and free access for all registered users. Although the public data repository provides measurements from a total of 235 stations, many of these stations have come online (or alternately gone offline) over the years the network has been in place. In order to assure a uniform data coverage, and to access trends dating back to the 80s, we restrict our analysis in this work only to stations that are (a) currently operational, and (b) provide measurements dating back to at least November, 1986. A total of 21 stations in the network, illustrated in Figure 9.1, satisfy these conditions.

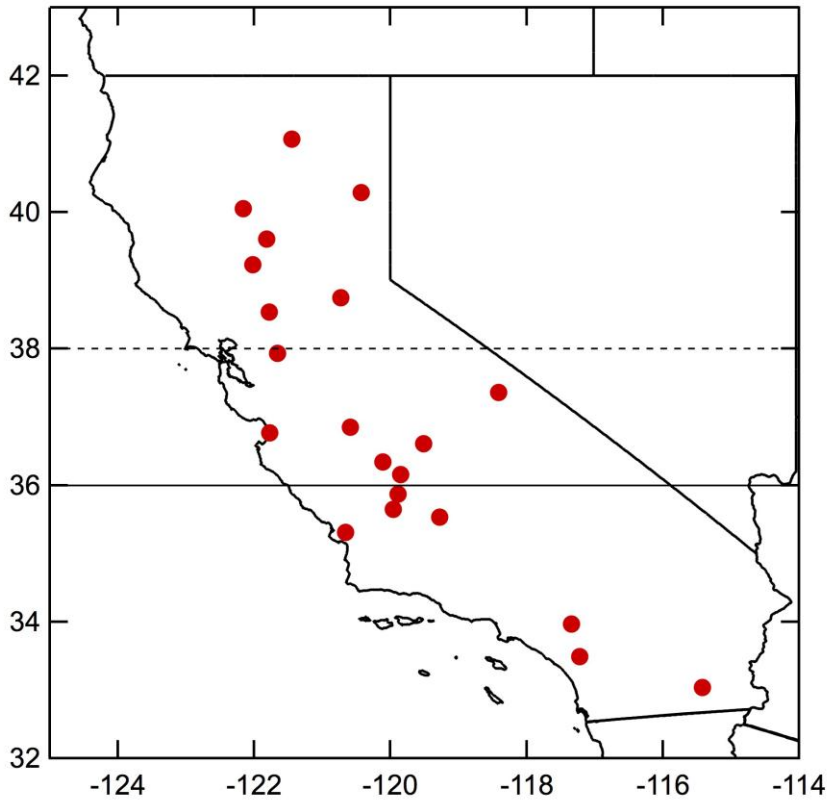

Figure 9.1 Location of sites in the CIMIS network in California that provide solar flux data in the decades between 1980-2010. The 36N and 38N parallels indicate the divisions between North-Central (combined) and Southern California used in this analysis.

Since CIMIS was intended primarily to be an agricultural resource, the majority of these sites lie in the Central Valley region where the bulk of California's crops are cultivated. Despite this however, the selected sites provide an adequate North-South spread, as well as sampling along the coast and further inland allowing us to examine trends that are representational of the entire state. The sites are

separated into North-Central California (Abbreviated as North California, North of 36N) and South California for the purpose of regional analysis. The locations and details for the sites used in this study are summarized in Table 9.1.

Site Name	County	Latitude	Longitude	Operational Since	Designated Region
McArthur	Shasta	41.07	-121.45	1983	North
Buntingville	Lassen	40.29	-120.43	1986	North
Gerber	Tehama	40.05	-122.16	1982	North
Durham	Butte	39.61	-121.82	1982	North
Colusa	Colusa	39.23	-122.02	1983	North
Camino	El Dorado	38.75	-120.73	1982	North
Davis	Yolo	38.54	-121.78	1982	North
Brentwood	Contra Costa	37.93	-121.66	1985	North
Bishop	Inyo	37.36	-118.41	1983	North
Firebaugh/ Telles	Fresno	36.85	-120.59	1982	North
Castroville	Monterey	36.77	-121.77	1982	North
Parlier	Fresno	36.61	-119.51	1983	North
Five Points	Fresno	36.34	-120.11	1982	South
Stratford	Kings	36.16	-119.85	1982	South
Kettleman	Kings	35.87	-119.89	1982	South
Blackwells Corner	Kern	35.65	-119.96	1986	South
Shafter/ USDA	Kern	35.53	-119.28	1982	South
San Luis Obispo	San Luis Obispo	35.31	-120.66	1986	South
UC Riverside	Riverside	33.97	-117.34	1985	South
Temecula	Riverside	33.49	-117.22	1986	South
Calipatria/ Mulberry	Imperial	33.04	-115.42	1983	South

Table 9.1 CIMIS stations included in this analysis. All sites operational from (at least) November, 1986-December, 2011.

9.3 Variability in the CIMIS measurements

Figure 9.2 illustrates the monthly averages for the incident surface solar flux for the entire state of California. Based upon a simple linear regression, the average change in surface flux ranges between -12.3 to 8.3 W m^{-2} in the 1980s, -8.8 to 4.0 W m^{-2}in the 1990s, and -7.3 W m^{-2} to 3.7 W m^{-2} in the 2000-2010 decade. Based upon the observed trends in aerosols (Chapters 3-4) we expect a surface brightening, however this large range spans a negative change as well. A few trends become evident upon examining this data. First, there is a consistent and persistent seasonal variability between the summer and winter months – the surface flux being of the order of 900 W m^{-2} in the summer months (Jun-Aug) compared to about 400 W m^{-2} in the winter months (Nov-Feb). Further there is an additional uncertainty of between 30-50 W m^{-2} (illustrated as error bars) associated with inter-station variability. This range of variability spans and exceeds the expected brightening of 5.0 W m^{-2} (Chapter 4) and explains the large uncertainty in the linear analysis. In order to clarify these trends therefore, we need to refine our analysis and resolve the data by separating out the summer and winter months, and to separate the North and South California measurements.

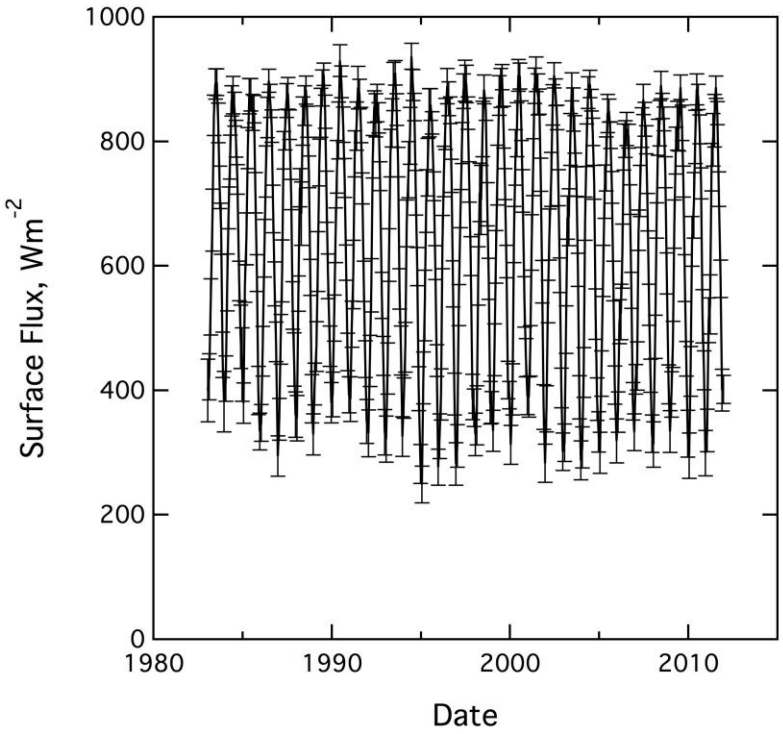

Figure 9.2 Monthly averages of surface solar flux in California obtained from the CIMIS network. A large summer-winter variability is observed.

In addition to any uncertainty introduced due to seasonal and spatial variations, there is another issue with the raw flux measurements. Figure 9.3 illustrates the measurements for the months of June and December at the Davis station. While the upper envelope indicates the diurnal variation in the incident flux, there are several measurements that deviate from this value by as much as 80%. These deviations are caused by the existence of low clouds that block incoming solar radiation. Although there is some evidence that clouds may be influenced by variations in the BC concentration [*Bahadur et al.*, 2012c], any surface brightening caused due to a change in direct absorption can only be detected if the cloudy points are filtered out from the measurements.

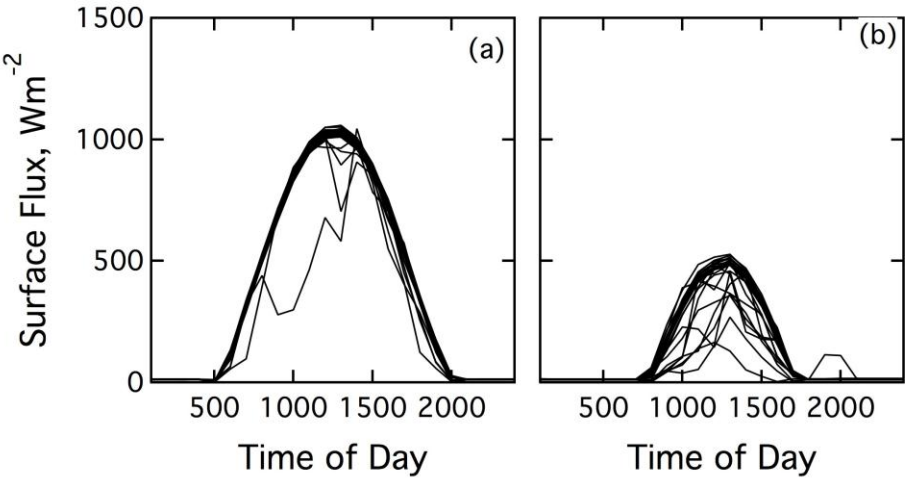

Figure 9.3 Diurnal variations in surface flux measured at the Davis station in (a) June and (b) December. Large deviations from the upper envelope indicate the influence of clouds.

9.4 Filtering the clear-sky signal

In order to refine the CIMIS data set to de-convolute the clear-sky solar flux signal from the total measured we adopt the following approach. The first assumption we make is that the measurements for any given station in any given month (the 30 day period is adopted for convenience of analysis) contains only minimal fluctuations (with no observable variability due to change in aerosol concentrations or seasonal variation etc.) and provides a robust picture of the incident solar flux. As can be seen in Figure 9.3, the solar flux measurements over a period of one month provide an upper envelope that represents the clear sky-flux. Since this envelope likely consists of a composite of measurements that may correspond to different days, we examine the frequency distribution of all daytime measurements, defined as the hours between 0600-1800 PST, as illustrated in Figure 9.4.

We expect that the highest modes represent the clear sky (or alternately, least cloudy sky) signal while short-lived (i.e. of an order of one hour, equivalent to the

resolution of the measurements) deviations from this peak are caused by the presence of clouds. For both the sites in Davis (North) and Riverside (South), this separation is more apparent in December, which is consistent with the winter months being associated with the cloudy/rainy season in California. While the separation between the clear-sky maximum and cloud influence is less apparent in June, we still include only the small peak corresponding to maximum insolation in the final climatological trend analysis.

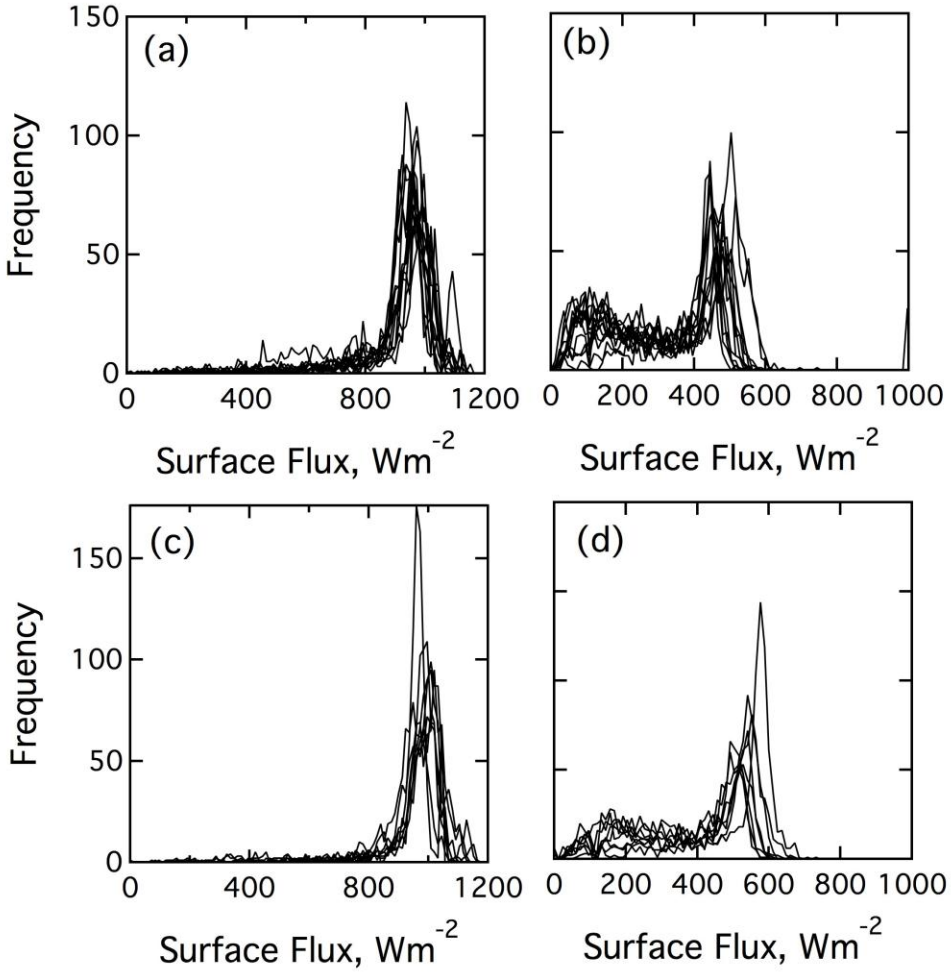

Figure 9.4 Histogram of hourly surface flux measurements at the (a-b) Davis and (c-d) Riverside stations in (a,c) June and (b,d) December. The second (higher) mode represents clear-sky flux. Measurements between 0600-1800 PST are used.

9.5 Climatology of Clear-Sky flux

In order to minimize impact of the diurnal cycle (and localized emission patterns such as rush hour) on the long-term trends, we consider only measurements

during the peak daytime hours (defined here as 1100 – 1500 PST) in determining the monthly mean values of solar flux, following the elimination of the cloud effect as described in section 9.4. Long-term trends in the average summer (defined as June-August) and winter (defined as December-February) clear-sky flux as determined are illustrated in Figure 9.5 for all the sites in this study, along with the North and South California trend lines. Again, two basic trends are apparent that are consistent with expectations. First, the summer time flux is approximately 300-400 W m^{-2} higher than the winter flux. Second, the surface clear sky flux is higher by between 40-50 W m^{-2} for the Southern California sites. We attribute this difference largely to the more southerly latitude, although it is also possible that the more heavily wooded regions in Northern California play a small role in reducing surface flux.

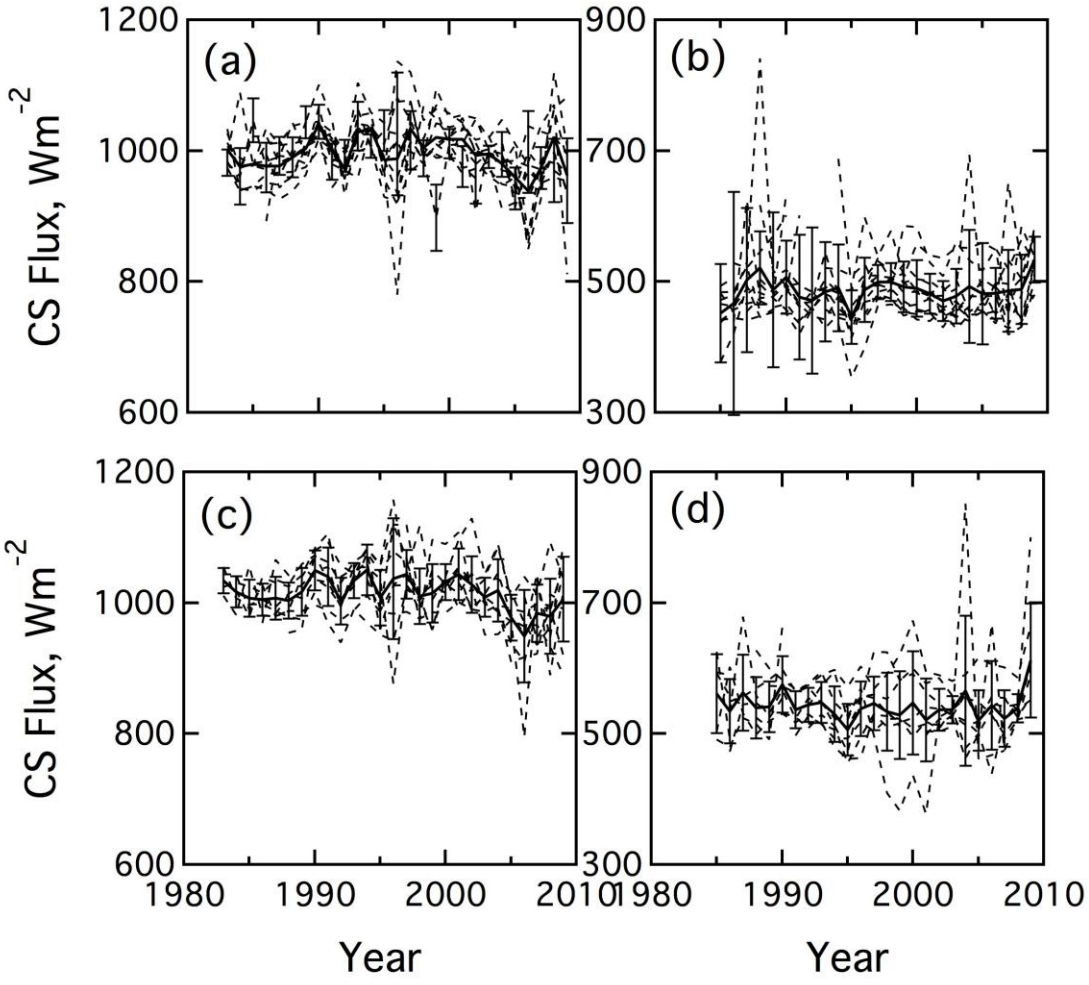

Figure 9.5 Time series in the clear-sky daytime surface flux measured by the CIMIS network sites listed in table 9.1 for (a,c) summer (June-August) months and (b,d) winter (December-February) months, in (a-b) Northern and (c-d) Southern California.

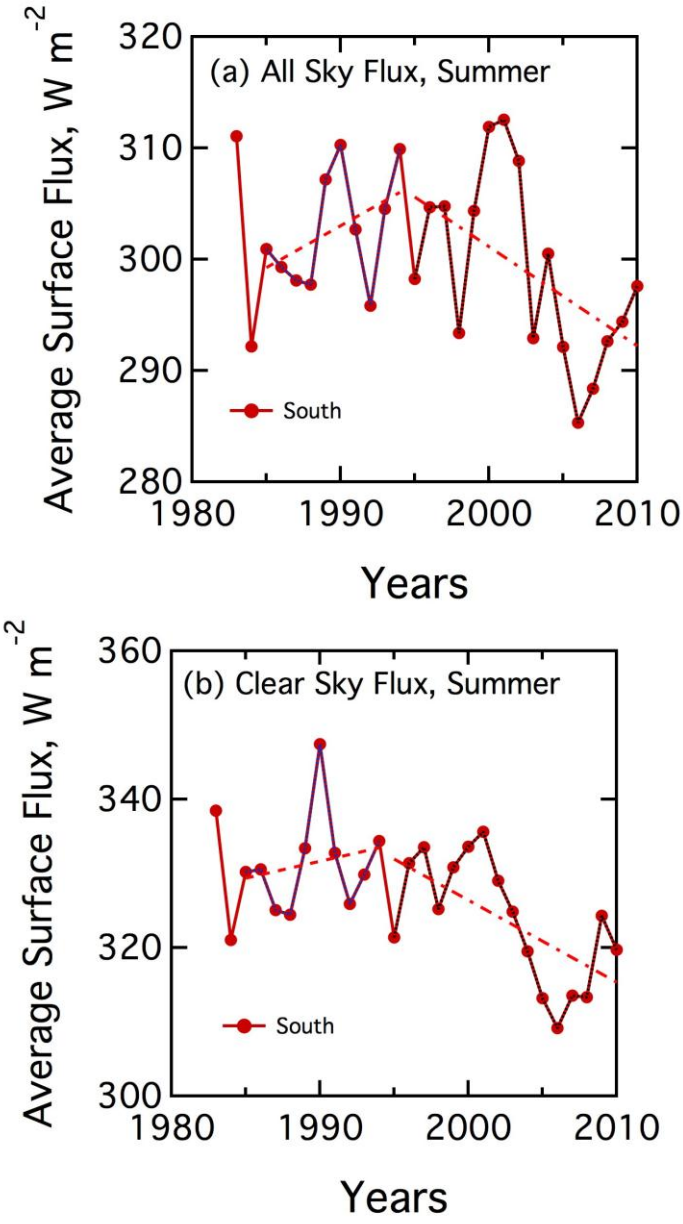

Figure 9.6 Time-space average diurnal-seasonal average summer time-series for Southern California for all-sky (a) and clear-sky fluxes (b).

We examine the trends in the surface flux for the entire 30-year period, and for each decade within separately in order to detect any measureable signal in brightening that may be associated with the observed reduction in BC loading. An example of the trends for southern California during summer time is shown in Figure 9.6. The trend in W m^{-2}/Yr for these time periods and both regions is summarized in Table 9.2 along with the uncertainty in the trends and the correlation coefficients.

		All Sky Flux				Clear Sky Flux			
		1985-1995		1995-2010		1985-1995		1995-2010	
		Rate	R^2	Rate	R^2	Rate	R^2	Rate	R^2
Summer	North	0.54±0.80	0.05	-0.08±0.36	0.09	0.18±1.03	0.01	-0.31±0.41	0.04
	South	0.75±0.54	0.19	-0.89±0.39	0.26	0.45±0.75	0.04	-1.10±0.36	0.39
	Statewide	0.66±0.67	0.11	-0.42±0.35	0.01	0.30±0.87	0.01	-0.65±0.37	0.18
Winter	North	-1.70±0.92	0.31	0.59±0.49	0.09	-0.81±1.01	0.06	0.23±0.39	0.02
	South	0.60±1.07	0.04	0.92±0.45	0.23	1.27±0.98	0.17	1.12±0.59	0.20
	Statewide	-0.74±0.91	0.07	0.73±0.41	0.18	0.06±0.79	0.00	0.62±0.28	0.25

Table 9.2 Annual average rate of change in surface solar flux in W m^{-2}/Year in North and South California separated by season as determined by the CIMIS network. Trends in shaded panels are not considered statistically significant.

While the brightening during the 1985-1995 period for summer (Figure 9.6) is consistent both in sign and magnitude with the simulated trends, the uncertainty is as large as the signal and the correlation coefficients are low. Furthermore, emissions in aerosol trends for the 1995-2005 time period cannot account for the dimming trends post-1995. If we invoke natural variability for the post-1995 trends we must invoke the same to explain the brightening trends during the previous decade. In view of the above, we conclude that the fitted trends are not statistically significant to test model predictions.

Trends in the mean AOD and AAOD measured in California by the AERONET network are illustrated in Figure 9.7. Due to the limitations on SSA retrieval, these measurements only cover the time period between 2000 and 2008, and provide a very poor spatial and temporal representation of the state. Since these measurements cover a very small portion of the multi-decadal period over which we expect to see surface brightening, we cannot compare them in any meaningful way to the trends in surface flux.

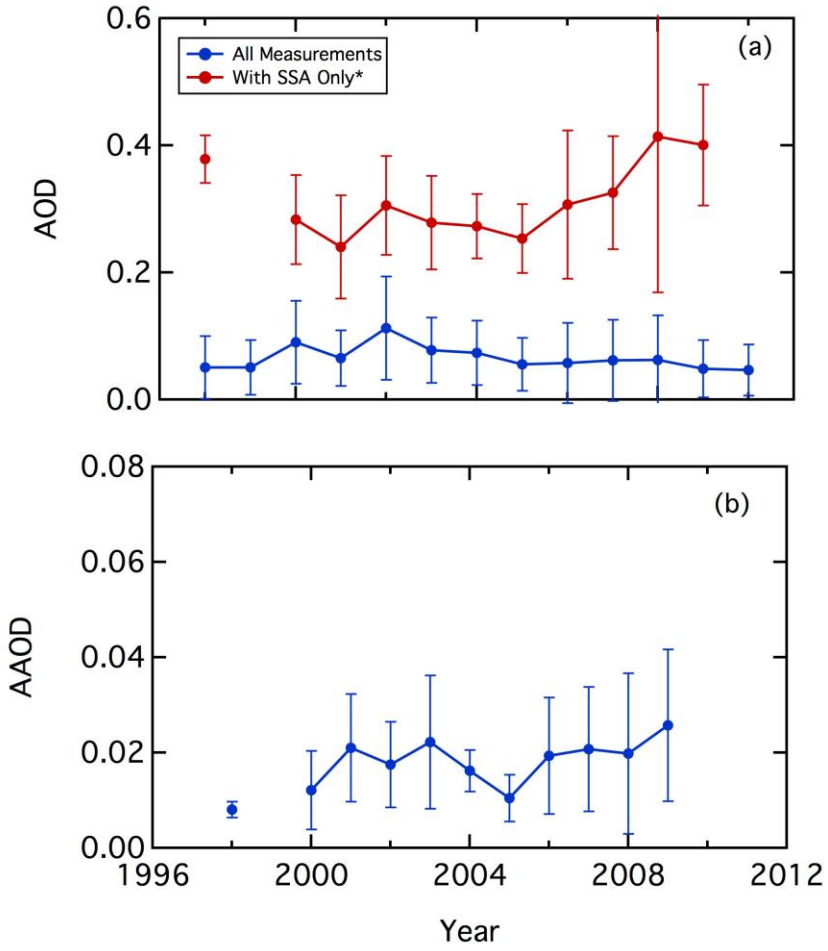

Figure 9.7 Time series of measured (a) AOD and (b) AAOD at 675 nm from the AERONET network in California. Bars represent the standard deviation of the daily variability in the annual mean values.

9.6 Conclusions

We have examined solar flux measurements from the CIMIS networks established in California for the past three decades. A filtering algorithm was developed to separate the clear sky flux from the cloud-influenced measurements based upon established long-term diurnal trends. Although there is some evidence of brightening (i.e. an increase in incident radiation) at the surface at some of the sites, we find that on average in both the summer and winter months the measurable increase in incident radiation is quite small, especially when compared to the change expected based upon changes in BC concentrations, and in fact there appears to be a dimming in some regions. We can offer two explanations – first, the data set itself is too noisy, with an inter-annual and inter-station variability of the order of 10-50 W m^{-2} which far exceeds the expected and observed brightening. Secondly, while there was a decrease in the observed BC loading, we did not find any change in the OC concentrations in

California between 1980-2009. As established, at least some fraction of this OC may also be absorbing solar radiation, thus leading us to over-estimate the expected change in surface brightening. Based upon our analysis, we caution against drawing firm conclusions as, due to this noisy data, we cannot definitively state that the observed trends are statistically significant.

10.0 Implications for mitigation of global warming

The observed trends in BC concentrations and their link with negative trends in diesel emissions have significant implications for California's role in mitigating global warming. It should be noted that BC is one of the four short-lived climate pollutants (SLCPs). The other three are: Methane; tropospheric ozone and HFCs. It has been estimated that, reducing global emissions of these four SLCPs using available technologies by between 30% and 50% can reduce the predicted warming trends from 2010 to 2050 by as much as 50% [*Ramanathan and Xu*, 2010; *Shindell et al.*, 2012a]. *Jacobson*, [2010a] has extensively studied the effectiveness of BC mitigation in reducing global warming and in this section, we adopt Jacobson's model results for the GWP for BC and the present study's results for emission trends to discuss the implications of our findings to climate mitigation. Before we proceed, we will clarify some thorny issues with respect to BC and OC forcing.

BC Forcing: Thus far we had discussed primarily direct forcing by BC, which is the change in the solar radiation absorbed by the atmosphere, and at the surface due to a change in atmospheric BC concentrations. This is often confused with clear sky changes (for example, see [*Bollasina et al.*, 2011]). In fact, the direct radiative forcing includes (should include) changes in clear as well as cloudy skies. The only restriction is that cloud properties (such as cloud fraction, cloud optical depths and single scattering albedo of cloud drops or ice crystals) are held fixed when BC is altered. However, BC also has a greenhouse effect since it absorbs infrared radiation emitted by the surface and the atmosphere. As mentioned earlier, BC also interacts with clouds, which lead to indirect and semi-direct effects. It is beyond the scope of this study to consider all of these effects. Hence we rely on Jacobson's 2010 model studies.

[*Jacobson*, 2010b] used the global-to-regional scale nested GATOR-GCCM model in which cloud microphysical processes (for liquid, ice, and graupel phases) were solved explicitly with size and composition resolution, while cloud thermodynamics were considered to be at quasi-equilibrium. Climate and air pollution processes were explicitly linked, with the universal inclusion of climate feedbacks eliminating the need for the calculation of radiative forcing. To determine the climate impact in the global scenario, two BC mitigation experiments were conducted – in the No Fossil Soot (NFS) scenario, all BC from fossil fuel emissions was eliminated, and in the No Fossil, Biomass Soot, and Biomass Gasses (NFSBSG) scenario all emissions from both fossil fuel and biomass burning were eliminated. The model results were validated using surface measurements from the IMPROVE network, and aerosol concentrations were typically reproduced within a margin of 10-20%.

OC Forcing: OC and other aerosol precursor gases are invariable co-emitted with BC, but the magnitude of these co-emitted species, particularly OC, is much smaller for diesel compared with biomass combustion. The BC trends we find in California are much stronger than the trends in other species including OC. In

fact the ratio of EC to OC as well as the ratio of EC to all Non-BC aerosols has also decreased with the decrease in BC. Further, because of the important warming effects of BrC in OC, any offsetting (cooling) effect of OC is likely to be small.

The diesel emissions decreased from 0.013 Tg/Yr in 1989 to 0.006 Tg/Yr in 2008 [*CARB*, 2008]. Jacobson estimated a value between 2900 and 4600 for the 100-year global warming potential of fossil fuel BC (which includes the effects of co-emitted OC. As a conservative estimate, we choose a value of 3000 that reflects the lower estimate. The reduction from 0.013 Tg/Yr to 0.006 Tg/yr is the equivalent to: (0.013-0.006)*3000=21 Tg/yr or 21 million metric tons of CO_2/yr. In comparison, California's greenhouse gas emissions as of 2009 are 457 million metric tons of CO_2, of which 86%, or 393 million metric tons/Yr is direct CO_2 emissions. We are led to the conclusion that the reductions in BC concentrations witnessed in California between 1989 and 2008 have had a measurable mitigation effect on the warming potential to the atmosphere, equivalent to 5% of the total CO_2 emissions.

11.0 Current BC emission Inventories

11.1 Introduction

As a part of this work, the research teams at the Scripps Institution of Oceanography (SIO) and the Pacific Northwest National Laboratory (PNNL) undertook a comprehensive study to determine the forcing impact of total aerosols and BC in California. The SIO team followed a hybrid approach constrained by field observations by using MISR satellite data in conjunction with column measurements from AERONET to generate the total absorption optical depths and to attribute a relative fraction to BC and organic matter (OM), while the PNNL team followed a bottom-up modeling approach, starting with emission inventory as input and using the WRF-Chem model to simulate BC and OM concentrations, optical depths, and forcing to compare with the observed BC and other aerosol concentrations, as well as the observationally derived radiative forcing by the Scripps team. The simulations were performed using meteorology boundary conditions representing year 2005. A comparison between the SIO and PNNL studies revealed a few unexpected discrepancies.

The total surface PM2.5 and sulfates were reasonably close to filter based measurements from the IMPROVE and EPA–STN networks; however the surface BC and OC concentrations were significantly lower (details provided later in Chapter 12), on occasion by as much as a factor of 2 to 2.5. Since PM2.5 simulations were close to observed values, the hypothesis was that the underestimation of BC was due to the uncertainty in the emission inventory.

The simulated BC column integrated AAOD was also significantly lower when compared to measurements from MISR/AERONET. Furthermore, the WRF-Chem BC-AAOD was lower by about a factor of between 2 to 2.5, depending on the location. This difference is very close to the factor of 2 to 2.5 underestimation detected in the surface BC comparison with IMPROVE and EPA measurements. These two sets of observations, i.e., the surface BC concentration (IMPROVE/EPA) and the column integrated AERONET-AAOD, are totally independent data.

Finally, we compared various available estimates for the BC emission inventory. The WRF-Chem simulations used the ARCTAS-CA scenario, corresponding to BC emissions of 17.8 Gg/Yr. We compared it with the ARB “original” ARB web-based PM2.5 emission inventory of 42.2 Gg/Yr, and again find they differ by a factor of 2.5. Note that ARB has updated their emission estimates (as indicated in ARB communications to Scripps, dated 6/14/12) to approximately 25 Gg/Yr, this is still higher than the ARCTAS-CA scenario by 29%. In addition to the Leung/Zhao work at PNNL, we also have an independent set of simulations done at LBL (by Hadley/Kirchstetter) using a different configuration of WRF-Chem that produces in essence the same trends - i.e. the BC surface concentrations agree

much better with surface BC observations and the column AAODs, when the ARCTAS emission inventory value of 17.8 Gg/yr is doubled. The combination of these comparisons motivated us to suspect that uncertainties in the emission inventory might be the primary cause of the BC discrepancy.

11.2 Emission Scenarios

There are three principle technology-based emission inventories that were compared in this work. The details of these scenarios and total BC emissions in the state of California are summarized in Table 11.1.

Table 11.1 BC emissions in California based on various available sources.

Scenario	Year	BC Gg/yr	Source	Notes	Application
ARCTAS-CA	2008	17.8	http://www.cgrer.uiowa.edu/arctas/	This is based on a two week campaign in June 2008	Used as baseline emissions in modeling studies reported in Ensberg et al. (CMAQ) and Zhao et al. (WRF-Chem)
ARCTAS	2006	22.6	http://www.cgrer.uiowa.edu/arctas/	This "pre-campaign" number represents annual measurements	Used to compare with baseline emissions scenarios to establish range of uncertainty, not applied in modeling studies
Ensberg et al. JGR 2012	2008	17.8	ARB communication to Seinfeld.	The modeling study used the ARCTAS-CA scenario with the assumption that 2008~2010 emissions did not appreciably change	Community Multiscale Air Quality (CMAQ version 4.7.1) model was employed to simulate May 2010 over Southern California with 4 km by 4 km horizontal grid cells
Zhao et al. submitted to JGR 2012	2008	17.8	Daily average of the day-specific ARCTAS-CA hourly emission gridded at 4km resolution provided by ARB	The ARCTAS-CA emission is used with meteorological conditions for 2005 and evaluated using IMPROVE (~40 rural sites) and EPA (~100 urban sites) measurements from 2005	WRF-Chem was used to simulate one year (2005) over California and the surrounding area at 12 km horizontal grid spacing
Original BC Emission Estimates,	2005	42.2	ARB communication to Ramanathan, Dated 6/4/12	This is based on "original" ARB web-based PM2.5 emission inventory	Used to establish the upper bounding case of 2.5 x Baseline emissions (compared to ARCTAS-CA) currently being investigated using WRF-Chem
Revised BC Estimate	2005	**25.4**	ARB communication to Ramanathan, Dated 6/4/12	This is based on "revised' ARB-PM2.5 data using SIP inventory which accounts for diesel rules	Used to compare with baseline emissions scenarios to establish range of uncertainty, not applied in modeling studies
BC estimates	2008	44.7	http://www.arb.ca.gov/app/emsinv/	This is based on published PM2.5 data with an emissions factor of 0.7 for diesel	Used to establish the upper bounding case of 2.5 x Baseline emissions (compared to ARCTAS-CA) currently being investigated using WRF-Chem
Original BC Emission Estimates	2010	39.1	ARB communication to Ramanathan, Dated 6/4/12	This is based on "original" ARB web-based PM2.5 emission inventory	Used to establish the upper bounding case of 2x Baseline emissions (compared to ARCTAS-CA) currently being investigated using WRF-Chem
Revised BC Estimate	2010	**24.2**	ARB communication to Ramanathan, Dated 6/4/12	This is based on "revised' ARB-PM2.5 data using SIP inventory which accounts for diesel rules	Used to compare with baseline emissions scenarios to establish range of uncertainty, not applied in modeling studies
Revised BC Estimate	2000	**27.5**	ARB communication to Ramanathan, Dated 6/4/12	This is based on "revised' ARB-PM2.5 data using SIP inventory which accounts for diesel rules.	Used to compare with baseline emissions scenarios to establish range of uncertainty, not applied in modeling studies

The ARCTAS [*Streets et al.*, 2003] emissions inventory is a composite gridded data set of global emissions developed at Argonne National Laboratory. The emissions are separated into anthropogenic and biomass-burning sources, and provided for both gas-phase and particle-phase species. The gas-phase inventory includes SO_2, NO_x (as NO_2), CO_2, CO, CH_4, and NMVOC as full MW of constituent compounds, while the particle phase-inventory includes BC, OC, and NH_3. This inventory only includes combustion-based emissions (i.e., no volcanic SO_2, biogenic VOC, or wetlands CH_4). CO_2 emissions are from direct releases only; they do not include C uptake by growing vegetation. Biomass burning values presented are annual average emissions typical of the mid-1990s. Further information on this inventory, including access to gridded emissions data is available at http://www.cgrer.uiowa.edu/EMISSION_DATA/index_16.htm.

The baseline ARCTAS inventories have been updated based upon several small-scale measurement campaigns. The ARCTAS-CA [*Jacob et al.*, 2010] mission consisted of a series of flights in California in the summer of 2008, sponsored by CARB. The objectives of the California deployment were to: (1) improve the California emission inventories for greenhouse gases and aerosols; (2) characterize offshore emissions of sulfur and other pollutants from shipping and natural sources; and (3) characterize upwind boundary conditions for modeling local surface ozone and PM2.5. The flights took advantage of the fully loaded DC-8 and P-3 aircraft based in California. In addition to the local air quality objectives, these flights provided contrasting data, expanding the ranges of the instruments, and characterizing emissions from California wildfires that were then sampled as aged plumes from the aircraft based in Canada. The flights were based in Palmdale, and primarily sampled the air above the Los Angeles metropolitan area.

Finally, CARB itself maintains an emission inventory of total particulates that can be used to estimate BC by applying prescribed sector-based emission factors [*CARB*, 2008]. The inventory is based on information periodically compiled by State and local air pollution control agencies, which includes information on the emissions of reactive organic gases (ROG), oxides of nitrogen (NOx), oxides of sulfur (SOx), carbon monoxide (CO), and particulate matter (PM10). Data are gathered on an ongoing basis and stored in the California Emission Inventory Development and Reporting System (CEIDARS). The California emission inventory contains information on stationary sources (such as electric power plants and refineries), area-wide sources (such as regional architectural coatings), and most importantly mobile sources (including all on-road and off-road vehicles).

11.3 The CalNex study

A recent modeling study of BC in California [*Metcalf et al.*, 2012] suggested that BC emissions might be significantly over-estimated in California, in apparent contradiction of the finding reported above. We clarify our findings in the context of this study (referred here as Cal_SNFLD).

The CMAQ model used in Cal-SNFLD and the WRF-Chem model used in the PNNL study used a different resolution for their simulations over the California domain. In order to eliminate model configuration as a contributing factor, the PNNL group performed an additional simulation at 4 km resolution (same as that used by the model in Cal-SNFLD) to compare with their previous 12km simulation. The new simulation uses the same domain as the 12km simulation, and the emissions were generated from the original ARTAS-CA data for the 4km run. The results comparing the two simulations with IMPROVE and EPA data averaged over all the stations in CA at daily and monthly resolution are provided in Chapter 12. Based on the results, we can conclude that the resolution does not make a significant difference in the simulated BC or the AAOD. By eliminating model resolution as the cause for the difference between the two studies we can support the conclusion that whether the models over- or under-predict BC depends on the measurements used to evaluate the simulations (i.e., measured BC is noticeably lower in 2010 than previous years, but the 2010 emission inventory is not significantly lower than the 2008 scenario).

As per Table 11.1, the Cal_SNFLD and the PNNL study used the lowest value of emission. It should also be noted that according to *Chen et al.*, [2012], the emission inventory has a 6-fold error bar for the global mean, and regional values are certain to be comparable if not more uncertain. Finally, we acknowledge that although the emission inventory for the LA basin (fine tuned during ARCTAS-CA) may be accurate, there is no guarantee that the inventory is equally accurate for other locations in California.

11.4 Conclusions

Besides comparing observed and simulated BC averaged over CA, a comparison was also made over southern CA (south of 36 N, as suggested) where it was found that the model underestimated BC compared to observations by a factor of ~two regardless of the regions used. In addition, the ratio of day time average vs. 24 hour average was calculated and was found to be close to 1 (varies between 0.97 and 1.02 depending on the season), which suggests that our conclusion is not biased by the use of 24 hour averages. Lastly, annual amounts of BC from IMPROVE and EPA have been calculated for 2005 to 2009 and the results show that the year-to-year variability of the observed BC mass concentration is much smaller than the model bias. However, BC is noticeably lower in 2010 compared to previous years. This partly explains why Cal_SNFLD concluded that their simulation (using the ARCTAS emission for 2008 but with meteorology for 2010)

over-predicted BC compared to observed BC in 2010, while the PNNL study concluded that their WRF-Chem simulation (using the ARCTAS emission for 2008) but with meteorology for 2005) under-predicted BC compared to observed BC for 2005. This points to the importance of matching meteorology, emission, and BC evaluation data for the same time period when assessing model skill, as inter-annual variability for any or all of them could be large.

12.0 Radiative Forcing Estimates from Regional Models

12.1 Introduction

To more fully understand the potential impact of emission controls on aerosol forcing and the resulting effects on regional climate of California, accurate calculation of aerosol direct radiative forcing is important. This study investigates the aerosol direct radiative forcing over California, including its variations by composition, geographically, and seasonally, using two configurations of a coupled meteorology-chemistry regional model (WRF-Chem). The first set of simulations (denoted WRF_PNNL) use the WRF updated as described in section 11.2, while the second set of simulations (denoted WRF_LBL) use the standard form of the climate model. The model results are evaluated by comparing the simulations with observations of meteorological conditions from the California Irrigation Management Information System (CIMIS), aerosol mass from the rural Interagency Monitoring for Protected Visual Environments (IMPROVE) program and the urban US EPA Chemical Speciation Network (CSN), and aerosol optical depth from the ground-based Aerosol Robotic NETwork (AERONET), and the satellite-based Moderate Resolution Imaging Spectroradiometer (MODIS) and Multi-angle Imaging SpectroRadiometer (MISR) instruments. The WRF-Chem model is then used to estimate the seasonality and spatial distribution of major aerosol species in California using a new method for diagnosing the individual aerosol optical depth and direct radiative forcing associated with each species.

12.2 WRF_PNNL model description

This study used the WRF-Chem model v3.2.1, with updates by Pacific Northwest National Lab including GOCART dust emission coupled with MADE/SORGAM and MOSAIC [*Zhao et al.*, 2010] and aerosol direct and indirect radiative feedbacks to RRTMG radiation and Morrison microphysics schemes [*Yang et al.*, 2011; *Zhao et al.*, 2011]. One of the chemistry options in WRF-Chem, the RADM2 (Regional Acid Deposition Model 2) photochemical mechanism [*Stockwell et al.*, 1990] and the MADE/SORGAM (Modal Aerosol Dynamics Model for Europe (MADE) and Secondary Organic Aerosol Model (SORGAM)) aerosol model [*Ackerman et al.*, 1998; *Schell et al.*, 2001] is selected. Aerosol optical properties such as extinction, single-scattering albedo, and the asymmetry factor for scattering are computed as a function of wavelength and three-dimensional position. Aerosols in this study are assumed internally mixed in each mode, i.e., a complex refractive index is calculated by volume averaging for each mode for each chemical constituent of aerosols. Further details of the model configuration are provided by *Zhao et al.*, [2012].

Since aerosols in the model are assumed internally mixed, a methodology needs to be developed to diagnose the optical depth and direct radiative forcing of individual aerosol species. In this study, calculation of aerosol optical properties

and radiative transfer is performed multiple times with the mass of one or more aerosol species (i.e., the mass of an individual or a group of aerosol species) and also its associated water aerosol mass removed from the calculation each time. Following this diagnostic iteration procedure, the optical properties (e.g., optical depth) and direct radiative forcing for an individual or a group of aerosol species are estimated by subtracting the optical properties and direct radiative forcing from the diagnostic iterations from those estimated following the standard procedure for all the aerosol species. That is

$$AOD_{[species\ i]} = AOD_{[all\text{-}species]} - AOD_{[without\ species\ i]} \quad (12.1)$$

$$Forcing_{[species\ i]} = Forcing_{[all\text{-}species]} - Forcing_{[without\ species\ i]} \quad (12.2)$$

For example, the optical depth and direct radiative forcing for EC is calculated by subtracting the values from the calculation with aerosol species other than EC from the values calculated with all aerosol species. In this study, we estimate the optical properties and direct radiative forcing for OM, EC, dust, sulfate, and all other aerosol species lumped in a single group.

The WRF-Chem simulation was performed on a domain at 12-km horizontal resolution covering California and its surrounding areas with 106×140 grid cells (112°W-126°W, 29°N-44°N) with meteorological initial and lateral boundary conditions derived from the North American Regional Reanalysis (NARR). The chemical initial and boundary conditions are from a WRF-Chem simulation with a larger domain at 36-km horizontal resolution covering the western U.S. (98^oW-136^oW, 24^oN-53^oN) driven by NARR meteorological boundary conditions and chemical boundary conditions derived from the Model for Ozone and Related chemical Tracers (MOZART) for the same time period. The simulation is conducted from December 15th 2004 to December 31st 2005. Only the results for the year of 2005 (referred to as the simulation period hereafter) are analyzed to minimize the impact from initial condition.

Anthropogenic and biogenic emissions over California used in this study are based on the 2008 inventory produced by California Air Resources Board (CARB) from the ARCTAS-CA (Arctic Research of the Composition of the Troposphere from Aircraft and Satellites - California Air Resources Board) campaign. The emissions were available as a gridded inventory with a 4-km horizontal resolution and chemical speciation based on the SAPRC99 chemical mechanism. The SAPRC99 species were mapped to the WRF-Chem species, which include CO, NO_x, SO_2, NH_3, volatile organic compounds (VOCs), sulfate, nitrate, EC, OM, and unspeciated $PM_{2.5}$ and PM_{10} mass and interpolated to the WRF-Chem 12-km grid. Anthropogenic emissions not covered by ARCTAS-CA inventory are derived from US EPA NEI-2005 inventory. Biomass burning emissions in 2005 are obtained from the Global Fire Emissions Database, Version 3 (GFEDv3) with monthly temporal resolution [*van der Werf et al.*, 2010]. Dust emission is calculated following the GOCART scheme [*Ginoux et al.*, 2001], coupled with MADE/SORGAM within the WRF-Chem framework implemented by

[*Zhao et al.*, 2010]. The size distribution of emitted dust and other details on the coupling of GOCART dust emission scheme with WRF-Chem follows [*Zhao et al.*, 2010]. In this study, the sea salt emission scheme is updated to include correction for particles with radius less than 0.2 μm [*Gong*, 2003] and to include the sea salt emission dependence on sea surface temperature [*Jaegle et al.*, 2011].

12.3 WRF_PNNL model evaluation

To determine how well WRF-Chem simulated aerosols, Figure 12.1 shows the seasonal cycle of statewide averaged surface mass concentrations of speciated $PM_{2.5}$ (sulfate, nitrate, ammonium, OM, EC, dust, sea salt, and unspeciated $PM_{2.5}$) from the IMPROVE (rural) and EPA (urban) measurements and the corresponding WRF-Chem simulations over California in 2005. In general, the seasonality of aerosol surface concentrations is determined by the seasonality of emissions (anthropogenic emissions are assumed constant throughout the year in this study), meteorological conditions (e.g., vertical turbulent mixing and ventilation), chemical production, and removal processes. Aerosol can either be emitted into the atmosphere or generated by physical and chemical processes within the atmosphere (called primary and secondary aerosols, respectively).

One example of primary aerosols is EC in WRF-Chem. Although total emission of EC is not constant through the year due to biomass burning emission with a summer maximum and a winter minimum (not shown), both observation and simulation show the seasonality of EC surface concentration in urban areas with a winter maximum and a spring minimum. This is likely due to stronger vertical turbulent mixing in spring compared to winter, which is reflected in the seasonality of the planetary boundary layer height that is the highest in spring and lowest in winter (not shown). The surface winds are also stronger in spring, indicating more efficient ventilation. It is evident that the vertical turbulent mixing and ventilation determines the seasonal variation in EC surface concentration in urban areas. In rural areas, the seasonality of EC is not obvious. Although the boundary layer depth follows the same seasonality in the urban and rural areas, EC in rural areas is mainly transported into the region rather than being mixed vertically from local emissions. Therefore vertical mixing and ventilation should have much less effects on the seasonality of aerosols in the rural areas, hence the much smaller seasonal variation. Unspeciated $PM_{2.5}$ as another example of primary aerosols has a similar seasonal variation with EC in the model.

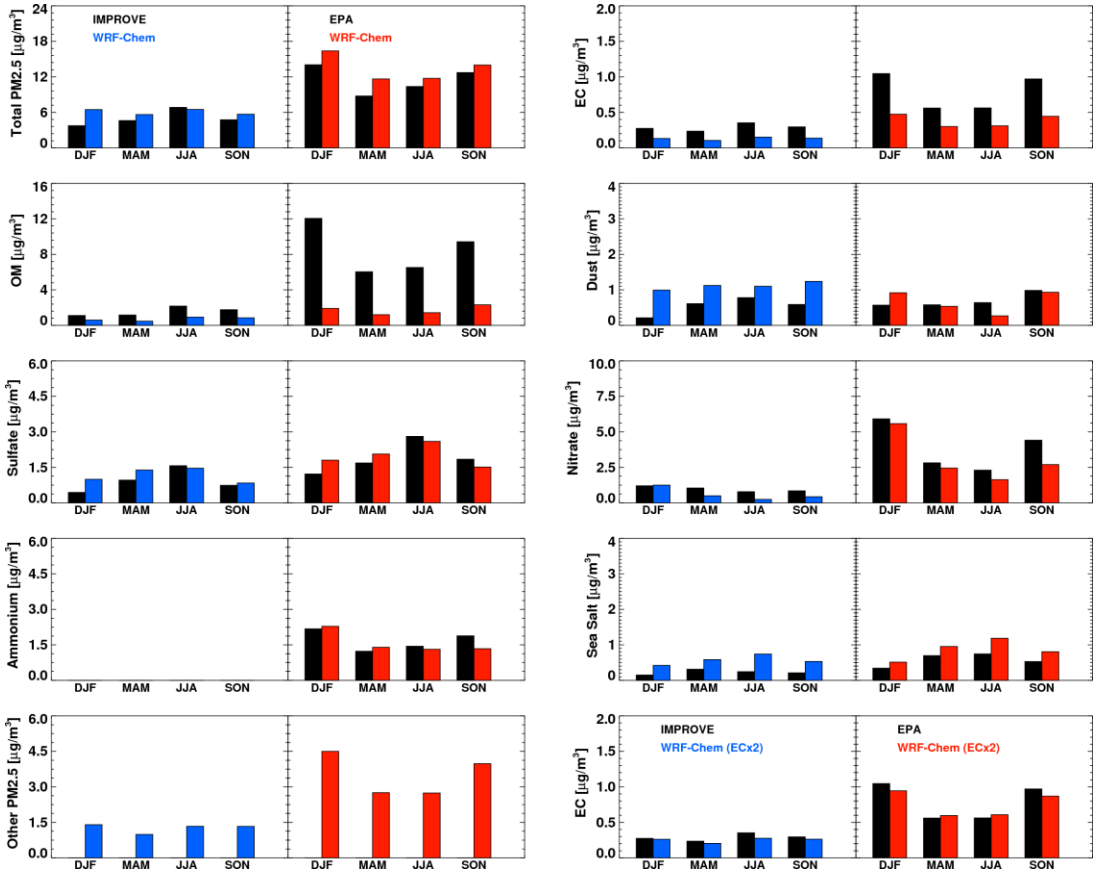

Figure 12.1 Seasonal mean mass concentrations of speciated $PM_{2.5}$ such as EC, OM, dust, sulfate, nitrate, ammonium, sea salt, and unspeciated $PM_{2.5}$ from IMPROVE and EPA measurements and the corresponding WRF-Chem simulations over California in 2005. The right-bottom panel shows the results from WRF-Chem sensitivity simulation with anthropogenic EC emissions doubled.

It is noteworthy that the EC surface concentration is significantly underestimated in the model by a factor of ~2 in both urban and rural areas. The bias may be partly due to the inability of the model to resolve emissions and aerosol/meteorological processes reflected by the measurements at the local scale. Sensitivity experiment with WRF-Chem applied at 4km-resolution shows that the EC surface concentration does not change significantly at higher resolution. Uncertainties and inter-annual variabilities of the anthropogenic EC emission might also contribute to the bias. Since the 2008 emission inventory for a two-week period is used with meteorological boundary conditions of 2005 in this study, our simulation may not be able to capture the measured EC concentration in 2005. Sensitivity simulation with anthropogenic EC emission doubled reproduces the observed EC surface concentration and its seasonal variation in both urban and rural areas very well (right-bottom panel of Figure 12.1).

Figure 12.2 shows the spatial distributions of seasonal mean 550 nm AOD and absorption AOD (AAOD) from the WRF-Chem simulation with anthropogenic EC emissions doubled over California in 2005. In general, the AOD is largely dependent on the aerosol column burden (vertically integrated aerosol mass) and RH. The high AOD simulated over the Central Valley, the Los Angeles metropolitan regions, and the southeast US deserts is consistent with the spatial distribution of total $PM_{2.5}$ surface concentration and column mass burden (not shown).

Figure 12.3 shows the seasonal statewide mean AOD and AAOD and their contributions from individual (OM, EC, dust, and sulfate) and lumped (other aerosol including nitrate, ammonium, sea salt, and unspeciated $PM_{2.5}$) aerosol species from the WRF-Chem simulation with anthropogenic EC emissions doubled over California in 2005. In WRF-Chem, aerosols are assumed internally mixed. Therefore, differences between the sum of AOD and AAOD diagnosed for the individual aerosol species and that of the internally mixed aerosol reflect non-linear interactions among the aerosol species. It is critical to examine the consistency between the diagnosed and simulated total AOD and AAOD to assess the representativeness of the diagnosed AOD and AAOD for individual aerosol species. It is encouraging that the diagnosed values (sum of AOD and AAOD for individual and lumped aerosol species) are generally comparable to the simulated values for the internally mixed aerosols, which suggests that the diagnostic calculation can provide reasonable estimates of the contribution from individual or lumped aerosol species.

Although the sulfate surface concentration is less than the lumped aerosol species, sulfate AOD is larger than the AOD from the lumped aerosols (sum of nitrate, ammonium, sea salt, and unspeciated $PM_{2.5}$) because it has larger column mass burden resulting from aqueous phase production in the free troposphere. The AOD for EC and OM is small, but the OM AOD may be biased by the model underestimation of OM concentration. The seasonality of AOD and AAOD from individual and lumped aerosol species is different. Dust AOD shows a summer maximum and a winter minimum, while sulfate and other aerosols (i.e., anthropogenic aerosols) show a winter/spring maximum and a fall minimum. Anthropogenic aerosols determine the seasonality of total AOD, with a maximum (~0.06) in winter and a minimum (~0.04) in fall. It is not surprising that EC is the main contributor to the AAOD. Dust follows as the second largest contributor.

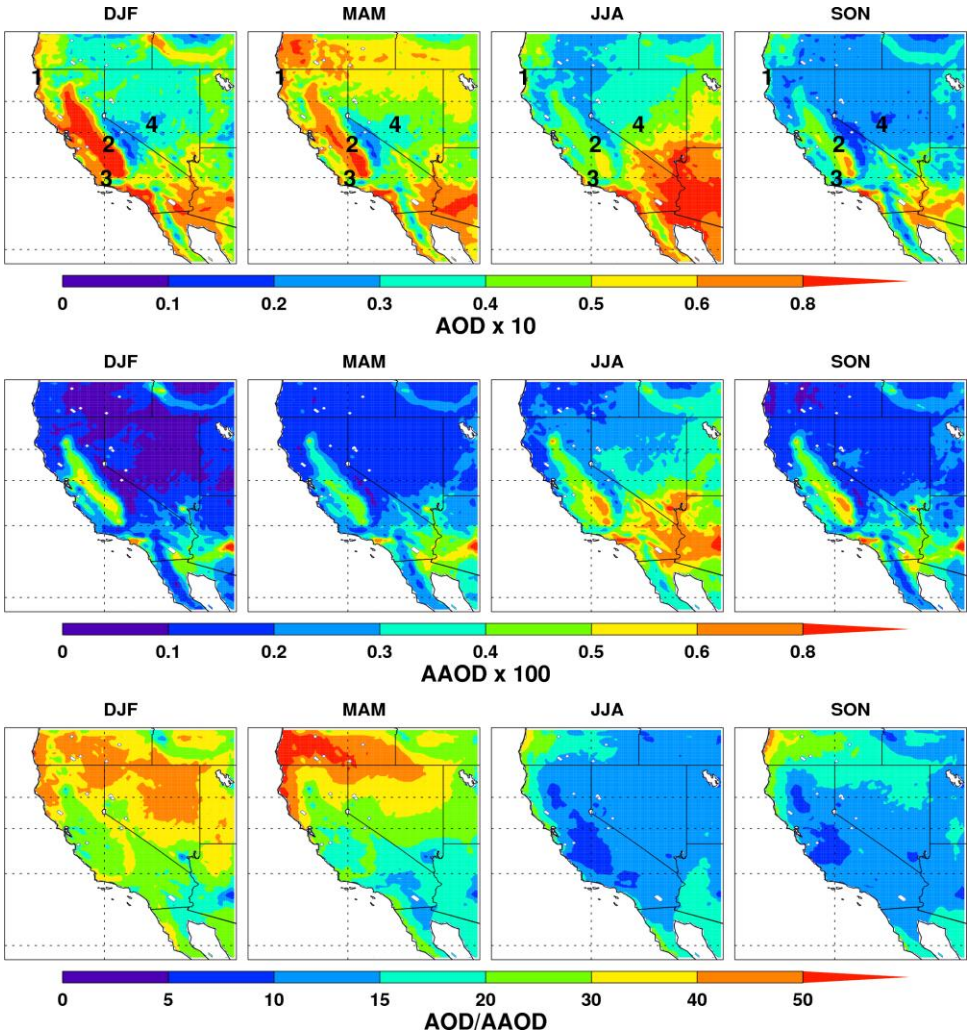

Figure 12.2 Spatial distributions of seasonal mean 550 nm AOD and AAOD from the WRF-Chem simulations with anthropogenic EC emissions doubled over California in 2005. The numbers represent the four AERONET sites: 1-Trinidad Head; 2-Fresno; 3-UCSB; 4-Tonopah Airport.

Although, aerosol species other than EC and dust are assumed non-absorbing in the model, they enhance the absorption by EC and dust and account for 15-20% of the state-wide averaged total AAOD. The seasonality of AAOD (from 0.0023 to 0.0038) is determined by EC, which shows a maximum in summer and a minimum in winter. This is different from the seasonality of EC surface mass concentration, but is consistent with that of the column mass burden of EC with a summer maximum due to biomass burning that peaks in the summer, indicating that biomass burning emission has larger impact on column mass burden than on surface concentrations. In this study, the total AAOD and OM AAOD may be underestimated due to not accounting for the absorption of OM (i.e., brown carbon) that has been found to be an important absorbing agent in the atmosphere [*Bahadur et al.*, 2012b; *Chung et al.*, 2012b; *Jacobson*, 1999].

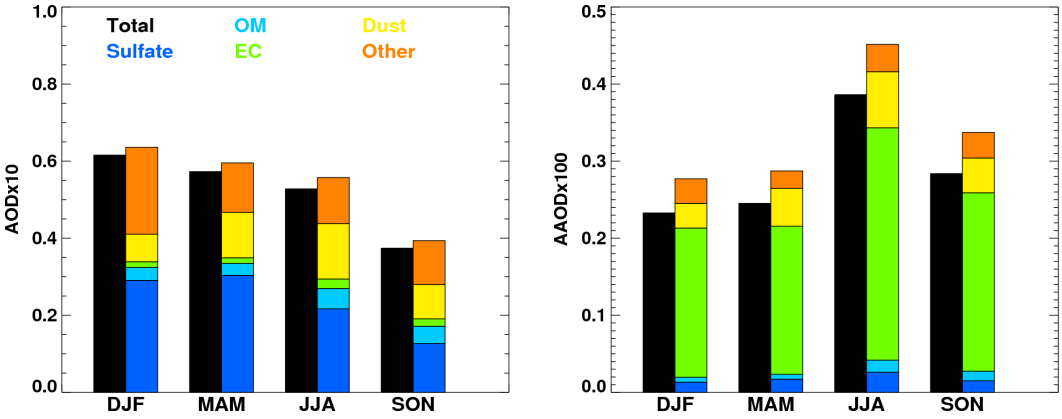

Figure 12.3 Seasonal variations of total 550 nm AOD and AAOD and their contributions from sulfate, OM, EC, dust, and other species from the WRF-Chem simulations with anthropogenic EC emission doubled. Other species include nitrate, ammonium, sea salt, and unspeciated $PM_{2.5}$.

12.4 Estimates of BC radiative forcing

Figure 12.4 shows the spatial distribution of seasonal mean aerosol direct radiative forcing at the top of atmosphere (TOA), in the atmosphere, and at the surface from the WRF-Chem simulation with anthropogenic EC emission doubled over California in 2005. The seasonality of TOA aerosol direct radiative forcing over California is relatively small. Aerosols result in a TOA cooling (i.e., negative forcing) over the entire California with a domain-average of -1.0 Wm^{-2} and a maximum of -3.5 Wm^{-2}. In the atmosphere, aerosols introduce a warming effect. The spatial distribution of atmospheric warming follows that of EC and dust and is consistent with that of AAOD. The maximum atmospheric warming reaches 10 Wm^{-2} over the Central Valley and the Los Angeles metropolitan regions. The atmospheric warming has a distinct seasonality with a summer maximum of 2.0 W m^{-2} and a winter minimum of 0.5 W m^{-2} on domain average, determined by the seasonality of AAOD and solar radiation fluxes, which peak in summer. Aerosols cool the surface over the entire California by up to -10 Wm^{-2}. The aerosol surface cooling shows a winter minimum of -1.5 Wm^{-2} and a summer maximum of -3.0 Wm^{-2} on domain average.

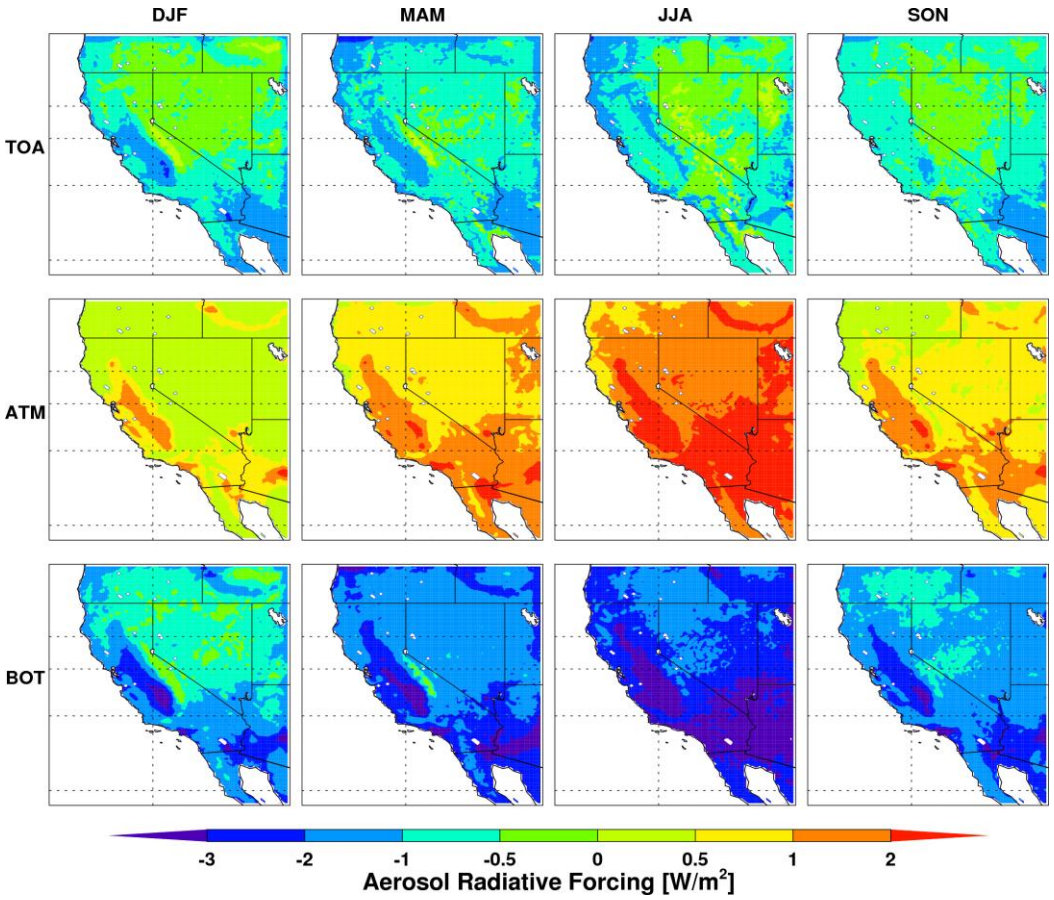

Figure 12.4 Spatial distributions of seasonal mean aerosol direct radiative forcing at the top of atmosphere (TOA), in the atmosphere (ATM), and at the surface (BOT) from the WRF-Chem simulations with anthropogenic EC emissions doubled over California in 2005. At TOA and BOT, positive value represents downward radiation; in ATM, positive value represents warming.

Figure 12.5 shows the seasonal mean aerosol direct radiative forcing and its contribution from individual and lumped aerosol species at the TOA, in the atmosphere, and at the surface from the WRF-Chem simulation with anthropogenic EC emissions doubled over California in 2005. Non-linear interactions can again be inferred from the comparison between the diagnosed (purple) and simulated (black) total aerosol forcing. Similar to the total AOD and AAOD, it is encouraging that the diagnosed total aerosol forcing is generally comparable to the simulated value. At the TOA, most aerosols introduce a negative radiative forcing with the largest contribution coming from sulfate (seasonal variation from -0.4 W m^{-2} in winter to -0.7 W m^{-2} in summer) followed by dust (seasonal variation from -0.2 W m^{-2} in winter to -0.3 W m^{-2} in summer) and other aerosols (seasonal variation from -0.25 W m^{-2} in spring to -0.3 W m^{-2} in winter), except that EC leads to a positive forcing (seasonal variation from 0.2 W m^{-2} in winter to 0.7 W m^{-2} in summer).

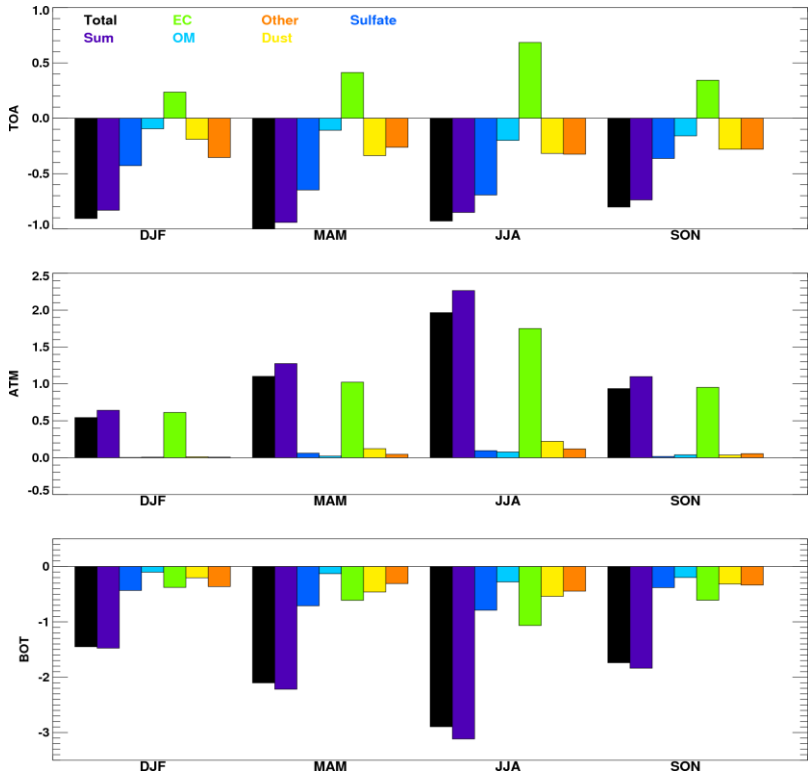

Figure 12.5 Seasonal variations of aerosol direct radiative forcing and its contributions from sulfate, OM, EC, dust, and other species at the TOA, in the atmosphere, and at the surface from the WRF-Chem simulations with anthropogenic EC emission doubled.

In the atmosphere, EC and dust contribute to the majority of total aerosol warming, with a seasonal range of about 75-95% and 1-10%, respectively. The rest of the aerosol warming is the enhancement of EC and dust warming by all other non-absorbing aerosols through internal mixing. Again, the atmospheric warming may be underestimated because of the underestimation of OM concentration and the ignorance of its absorption. At the surface, all aerosols have a cooling effect. In summer, EC is the largest contributor (-1.1 W m^{-2} and ~35%) to the total surface cooling, followed by sulfate (-0.8 W m^{-2} and ~25%), dust (-0.6 W m^{-2} and ~18%), other aerosols (-0.4 W m^{-2} and ~13%), and OM (-0.3 W m^{-2} and ~9%), while in winter, sulfate is the largest contributor (-0.45 W m^{-2} and ~30%), followed by EC (-0.39 W m^{-2} and ~26%), other aerosols (-0.38 W m^{-2} and ~25%), dust (-0.2 W m^{-2} and ~13%), and OM (-0.1 W m^{-2} and ~6%). Again, the forcing from OM is likely underestimated.

12.5 Significance of WRF_PNNL simulations

The model captures the general characteristics of 550 nm AOD observed at the AERONET sites. Aerosols result in a TOA cooling (i.e., negative forcing) over the entire California with a domain average of -1.0 Wm^{-2} and a maximum of -3.5 W m^{-2} with negligible seasonality. Aerosols introduce atmospheric warming with a

maximum reaching 10 Wm^{-2} over the Central Valley and the Los Angeles metropolitan regions, following the spatial distribution of AAOD. The seasonality of atmospheric warming shows, on state-wide average, a summer maximum of 2.0 W m^{-2} and a winter minimum of 0.5 W m^{-2}, determined by that of AAOD and the solar radiation fluxes. Aerosols cool the surface over all of California by up to -10 Wm^{-2}. The state-wide average cooling has a winter minimum of -1.5 W m^{-2} and a summer maximum of -3.0 W m^{-2}, dominated by the seasonality of solar radiation fluxes. *Jacobson et al.*, [2007] reported a total anthropogenic radiative forcing of -7.7 Wm^{-2} at the surface in February and -7.91 W m^{-2} in August for 1999 over California. Their larger radiative forcing estimates at the surface may be because of larger anthropogenic emissions in 1999 and also the inter-annual variability of meteorology. In addition, their radiative forcing, estimated from the baseline and sensitivity simulations, has been defined as a radiative flux perturbation (RFP) that includes the change of radiative fluxes due to aerosol-cloud interaction, while our diagnostic method estimate the "real" aerosol direct radiative forcing [*Lohmann and Ferrachat*, 2010].

The direct radiative forcing of speciated aerosols estimated in this study may be biased by the model uncertainties identified through the comparison with available observations. First, the RH is underestimated and precipitation is overestimated. The underestimation of RH may result in low bias of AOD and AAOD and hence the low bias of aerosol radiative forcing. The overestimation of precipitation may contribute to the low bias of aerosol concentrations due to wet removal and hence the low bias of aerosol radiative forcing. Second, the simulation with doubled anthropogenic EC emission that is used to estimate the aerosol radiative forcing significantly underestimates the surface mass concentrations of OM by a factor of 2-4 (even larger if a factor of 1.8 instead of 1.4 was applied to convert the measured OC to OM). In addition, the brown carbon is not treated in this study so that the absorption due to OM is underestimated. These OM related biases might lead to an underestimation of aerosol-induced atmospheric warming. The TOA OM radiative forcing (negative) may be overestimated because the net effect of OM may be close to zero if accounting for its absorption [Chung et al., 2012]. Third, the radiative forcing of dust and sea salt may have biases near the desert source regions and the coastal areas, respectively. The evaluation of their biases is difficult due to the absence or uncertainties of observations. Finally, the aerosol radiative forcing estimated in this study is based on 2005 meteorological conditions with 2008 anthropogenic and biogenic emissions. Therefore, the inter-annual variability of radiative forcing due to meteorological conditions and emissions should be acknowledged.

12.6 The WRF_LBL study

In addition to the simulations described in Sections 12.2-12.4, the standard model WRF-Chem (v.3.2.1) [*Fast et al.*, 2006; *Grell et al.*, 2005; *Skamarock and Klemp*, 2008], was used to simulate meteorology and atmospheric chemistry, including gas and particle phase pollutants in a parallel study denoted WRF_LBL.

Each scenario was comprised of a continuous 14-month simulation period, November 2004 through December 2005, with the output during 2004 discarded as spin-up time. A small modification was made to the model code to ensure proper initialization of aerosol and chemistry species during model restart, which was performed each model day at midnight. Hourly model output, averaged by month and then season was used as the basis for the analysis.

The model was comprised of two domains: The parent domain contained 90 by 90 cells with horizontal dimensions of 36 km. The child domain, centered on California contained 96 (east-west) by 120 (south-north) cells with horizontal dimensions of 12 km. Feedback, with 1-2-1 smoothing, between the domains was included. Both domains have telescoping vertical dimensions with 35 total layers and with the lowest layer extending to ~30 meters above the surface. Meteorological initial and boundary conditions in the parent domain, and initial conditions for the child domain, were based on North American Regional Reanalysis (NARR) data[*Mesinger et al.*, 2006]. Sea surface temperatures were updated daily also using NARR. The ARCTAS-CA 2008 emissions inventory was used in this study. Use of this emission inventory in WRF-Chem produced surface concentrations of BC that were too low by a factor of two when compared to measured concentrations at 37 sites across CA. Therefore, the ARCTAS-CA BC emissions were doubled for the control simulations. All other emissions were left unchanged. Comparisons between model simulations and measurements are discussed in the following section.

12.7 Comparing WRF_LBL with observations

The WRF-Chem output for cloud optical thickness (COT) and surface solar flux were gridded to the same spatial resolution as the MERRA data, which was lower at 50 km than the WRF-Chem output at 12 km. The seasonally resolved, percent difference and total difference between the WRF-Chem and MERRA predicted shortwave solar flux at the surface and COT is shown in Table 11.1, along with the difference between WRF-Chem AOD and the AOD retrievals from MISR, for all seasons. The model indicates a small positive bias for surface SW flux in all seasons except for fall, where the agreement between model and satellite is nearly perfect. The two primary variables affecting the surface shortwave flux are the COT and the AOD. WRF-chem under-predicts COT relative to MERRA by 50 to 60% at all seasons and subsequently allows more solar radiation to reach the surface. Most likely due to reduced cloud cover in summer and fall, WRF-Chem also more accurately reproduces the surface solar flux for these two seasons.

WRF-Chem over-predicts atmospheric AOD relative to the MISR retrievals. This is most likely due to simulated PM2.5 concentrations exceeding observed values and will be discussed in greater detail below. At all seasons the simulated AOD is higher than predicted AOD by a factor of 2 (Table 11.1). WRF-Chem's negative bias in COT and positive bias in AOD have opposing effects on the surface SW flux. Reduced clouds let more radiation through, while higher AOD blocks

radiation. The magnitude of these discrepancies will be used to determine the uncertainties associated with the calculated BC forcing over California, as well as those associated with reducing BC emissions.

Season	diff SW	% diff SW	diff COT	%diff COT	diff in AOD	% diff in AOD
winter	9.7 (+/-3.4)	7.4 (+/-2.9)	-10.5 (+2.0)	-56 (+/-8.9)	0.05 (+0.03)	131 (+/-104)
spring	3.8 (+/-7.3)	0.94 (+/- 2.65)	-12.0 (+/-2.0	-66 (+/-12.7)	0.09 (+0.05)	113 (+/-101)
summer	7.2 (+/- 11.2)	1.7 (+/- 3.7)	-4.3(+/-1.7)	-71 (+/- 14.6)	0.04 (+/-0.04)	73 (+/- 85)
fall	-0.06(+/-4)	-0.5 (+/-2.3)	-5.6(+/-1.3)	-65 (+/- 8.9)	0.05 (+/-0.02)	118 (+/- 74)

Table 12.1 Average seasonal difference between WRF output and MERRA retrievals for short-wave solar flux at the surface and cloud optical thickness over California. WRF AOD was compared to MISR retrievals of AOD.

WRF-Chem predictions of the 2005 seasonal temperatures were compared with available measurements covering the same period. Figure 11.6 demonstrates that both field measurements and WRF-Chem agree on the spatial and seasonal variability in surface temperatures across CA. Seasonal precipitation totals were also compared to WRF-Chem's predicted precipitation (Figure 11.7) and generally agree well in both summer and winter (Figure 11.7). In summer both model and observations indicate very low rain totals (between 0 and 200 mm) with the highest precipitation totals in the Olympic and Sierra Nevada mountain ranges. The spatial pattern of precipitation in the winter is similar to that of summer and captured well by the model. Total accumulation over the winter months is almost an order of magnitude larger, and WRF-Chem generally agrees with the measurements although under-predicts winter precipitation in the mountains by about 20-30%.

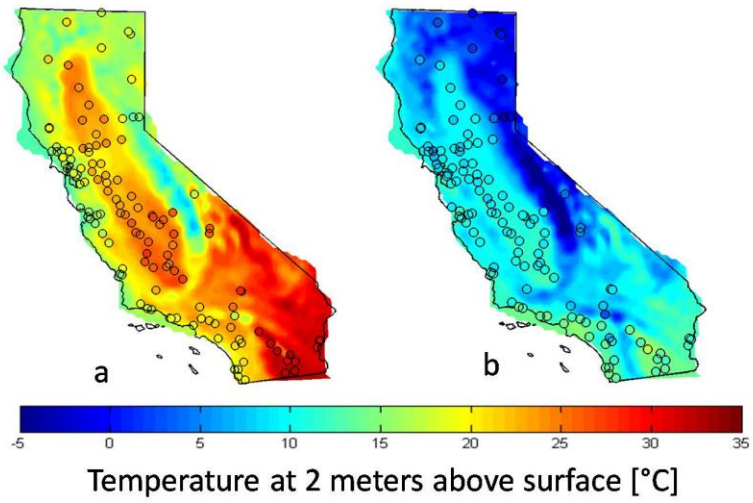

Figure 12.6 WRF surface temperature (contour map) compared to CIMAS measurements (circles) for (a) summer and (b) winter.

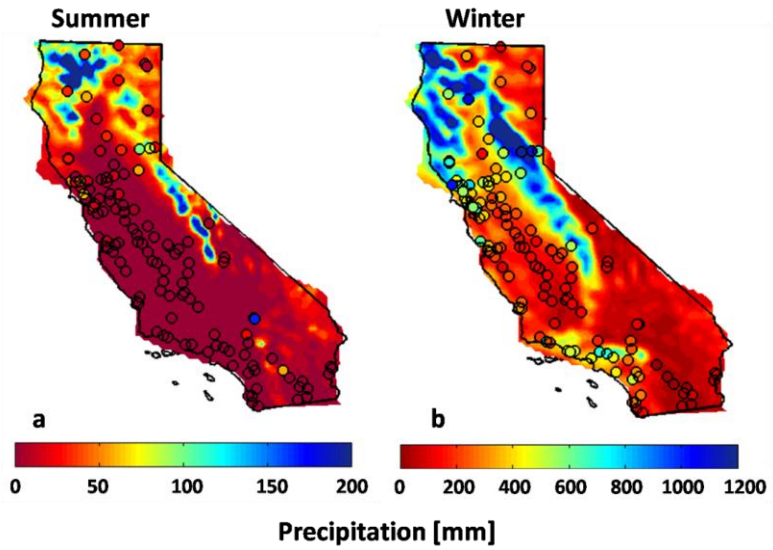

Figure 12.7 WRF precipitation (contour map) compared to CIMAS measurements (circles) for (a) summer and (b) winter.

As previously mentioned, BC is unique among atmospheric aerosols for its absorptive properties. Therefore it is most important for the purposes of this study to ensure that the WRF-Chem model is able to capture the spatial and temporal patterns of both PM2.5 and BC. After doubling the BC emissions in the chemical inventory file, the magnitude and spatial distribution of BC appear to be generally well simulated by WRF-Chem for both summer and winter months (Figure 11.8). Increased stability in the atmosphere and strong temperature inversions during the winter months, keep the pollution near the source and high concentrations are observed in large urban areas like San Francisco, Sacramento, and Los Angeles, as well as throughout the San Joaquin Valley and other low lying regions. Strong gradients in BC concentration are observed at the borders between urban and rural locations indicating that very little BC is transported to the mountains and other remote locations during the winter months. In the summer, atmospheric transport is much greater and pollutants are more effectively transported to rural and remote areas of CA, thereby dramatically decreasing surface concentrations of BC in the urban and low lying areas and increasing atmospheric aerosol concentrations in remote locations. This sets up opposing seasonal cycles in BC concentrations for urban and rural regions of CA, found in both the observations [*Kirchstetter et al.*, 2008b] as well as in the WRF-Chem predictions. There is almost no annual variability in the observed concentrations of BC, or the seasonal trends, from 2003 to 2007, supporting the robustness of the data and its comparison to the model.

The PM2.5 follows the same pattern as the BC, both in observations and in the WRF-Chem prediction (Figure 12.9). However, agreement between model and observations of PM2.5 is not as good as with the BC. WRF-Chem tends to over-predict PM2.5 in rural locations during the winter months and in urban and low lying regions during the summer months. This is not unexpected, given that the

predicted AOD was nearly twice the observed AOD. A comparison of major contributors to PM2.5 – BC, dust, sulfate, nitrate, organic carbon, and sea salt – revealed that, for surface measurements, WRF-Chem typically over-predicts sulfate by a factor of 2, while all other species are generally well represented. WRF-Chem generates more sulfate over the ocean than is typically observed at coastal sites and transports it inland. Despite the discrepancy the predicted PM2.5 is close enough to the observations that the simulated aerosol is a reasonable representation of California for both summer and winter and may be used to simulate general conditions across the state. A sensitivity test of the effects of changing PM2.5, in addition to BC, on climate should also be conducted, but is beyond the scope of this work.

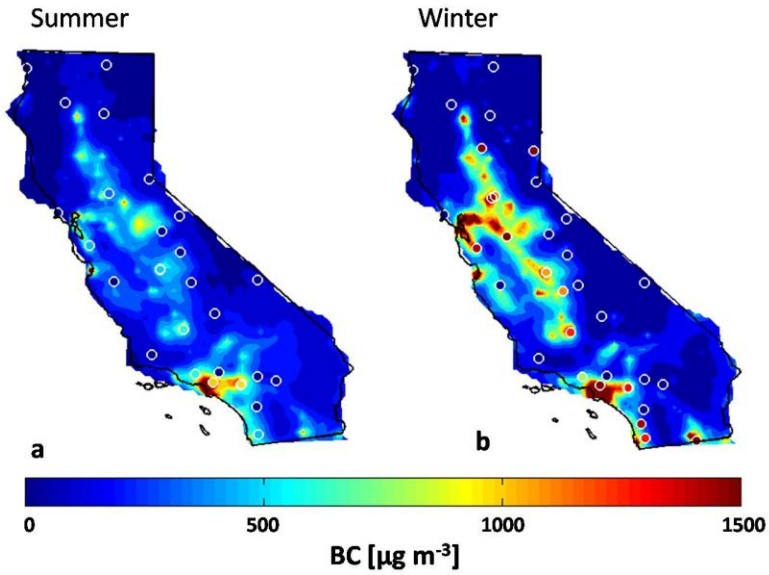

Figure 12.8 Comparison of WRF-Chem-predicted surface concentrations (contour map) of EC with measured EC concentrations (circles) from the IMPROVE and EPA networks for (a) summer and (b) winter.

12.8 Radiative forcing from WRF_LBL

Seasonal and annual atmospheric heating and surface forcing from both the WRF-Chem simulated BC and absorbing aerosol optical depth (AAOD), which includes both dust and BC were calculated off-line using the WRF-Chem, seasonally-averaged, output of: AOD, SSA, COT, and BC concentrations for each grid point and atmospheric layer. WRF-Chem provides AOD and SSA at four wavelengths, 300, 400, 600, and 1000 nm. Using the four wavelengths as references, spectral AOD and AAOD were interpolated for the full solar spectrum (200 – 2500 nm) and then cross multiplied with the fraction of solar radiation [*Levinson et al.*, 2010] at each wavelength to obtain the broadband values of AOD(z) and AAOD(z) in each atmospheric layer. A mass absorption cross section (MAC) of 7.5 m^2 g^{-1} was assigned to BC [*Bond and Bergstrom*, 2006]

and 0.1 m^2 g^{-1} to dust [*Linke et al.*, 2006]. The BC and dust concentrations in each layer were multiplied by their respective MAC as well as each layer height to obtain absorption.

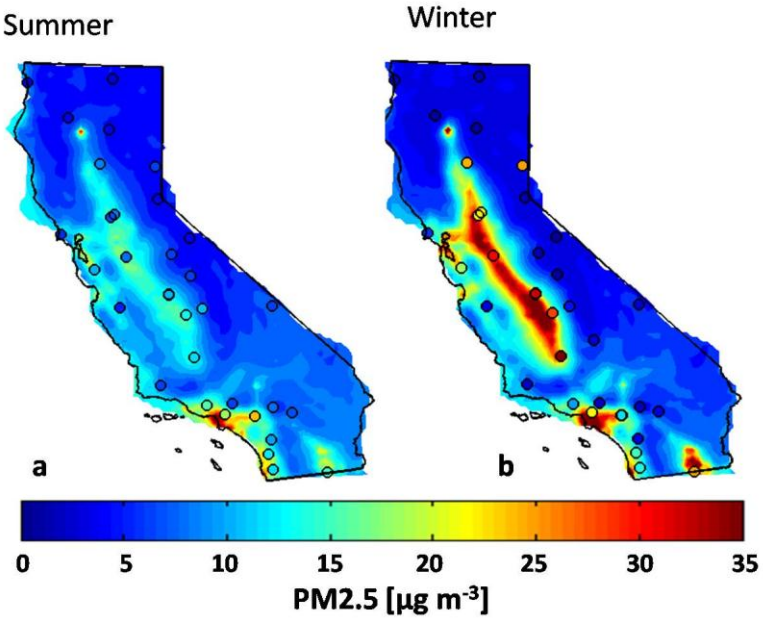

Figure 12.9 Comparison of WRF-Chem-predicted surface concentrations (contour map) of PM2.5 with measured PM2.5 concentrations (circles) from IMPROVE and EPA data for (a) summer and (b) winter.

The average simulated SW flux at TOA ranged from 447 W m^{-2} at 29º latitude to 450 W m^{-2} at 43º latitude in the summer and from 240 W m^{-2} to 145 W m^{-2}over the same span in the winter. SW radiation transfer was calculated through each layer of the atmosphere

$$I(z) = Io(z)*(\exp(AOD(z) + \exp(Rayleigh(z)))*Cl\_Trans(z). \quad (12.3)$$

Io(z) is the downward flux of shortwave radiation transmitted through the atmospheric layer immediately above. Io(0) is the initial SW flux calculated at TOA. Rayleigh(z) is the optical depth of a clean atmosphere, and was found using a parameterization published by [*Bodhaine et al.*, 1999]. Cl_Trans is the percent of light transmitted through each cloud layer and was evaluated using the method developed by [*Fitzpatrick et al.*, 2004] for calculating an effective optical depth for optically thick clouds. The COT used to calculate Cl_Trans was not the averaged COT from WRF-Chem for each season. Not only does averaging COT over many days cause a significant over prediction in light attenuated, but also includes nighttime cloud cover, which does not affect solar radiation. A more representative cloud cover was calculated as the fraction of solar flux at the surface for all-sky relative to a clear-sky scenario and then multiplied by the average COT (from WRF-Chem) in each atmospheric layer. To test the

applicability of these off-line calculations to the model results, the model output of seasonally averaged SW flux at the surface was compared to the calculated I(z = surface layer) and found to be consistent for all seasons (Figure 12.10).

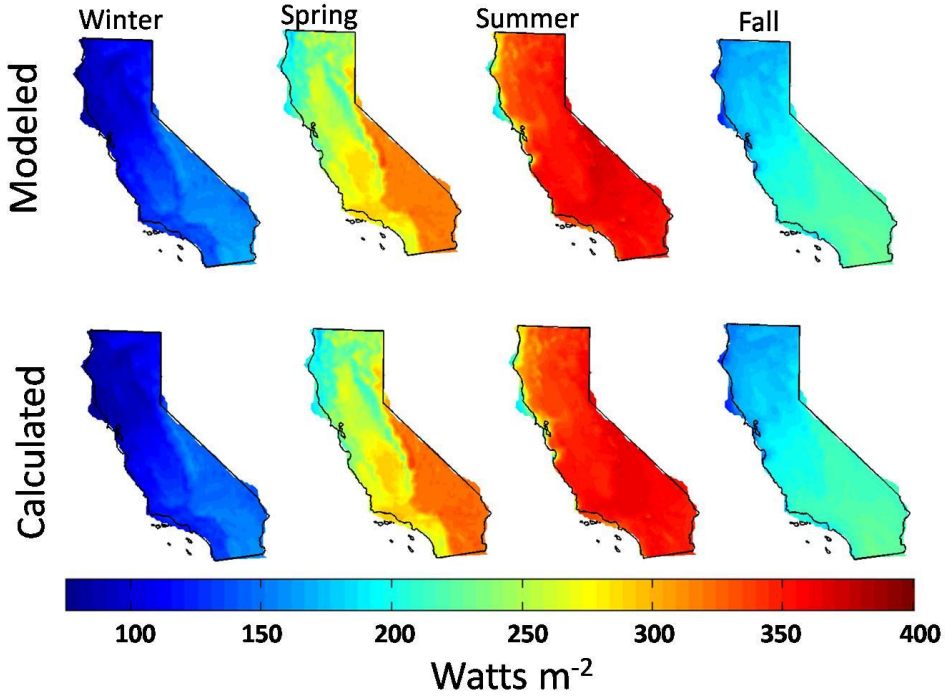

Figure 12.10 Modeled SW surface flux vs. the off-line, calculated SW surface flux.

The forcing estimates for BC in Northern, Central, and Southern California are shown in Table 12.2. The uncertainties in the forcing are derived from WRF-Chem's ability to accurately reproduce either COT or AOD relative to the MERRA and MISR data products respectively. As previously shown (Table 11.1), WRF-Chem under-predicts COT by a factor of 1.4 to 2 and over-predicts AOD by a factor of 2. Therefore the atmospheric and surface forcing due to BC were also calculated for 2 times the simulated COT and at half the simulated AOD while keeping AAOD constant.

Figure 12.11 shows the vertical profile of the fraction of atmospheric heating from BC. At the surface nearly all (> 90%) of the atmospheric heating is from BC, which is expected and consistent with previous studies[*Yang M. et al.*, 2009]. At higher altitudes however, WRF-Chem predicts that dust is contributing to 50 to 60% of the atmospheric heating, which is inconsistent with what has been previously observed[*Yang M. et al.*, 2009]. Given the relative mass absorption efficiencies of BC and dust, the mass concentration of dust in the model would need to be about 75 times greater than that of BC. It is our conclusion that WRF-Chem is generating and transporting too much dust at altitude and that, along

with the excess sulfate, explains why the modeled AOD values are so much higher than the MISR AOD retrievals.

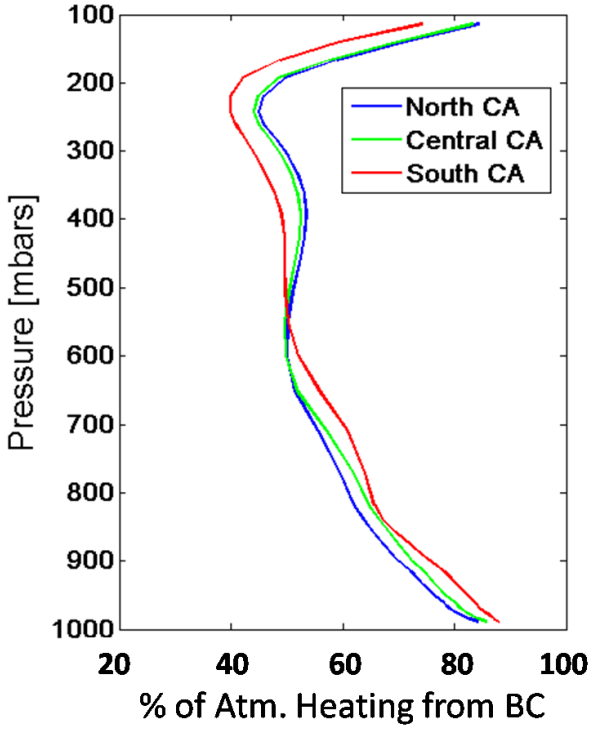

Figure 12.11 Contribution of BC to total atmospheric heating due to aerosol absorption as a function of altitude.

Atmospheric heating (BC only) W m^{-2}				
	winter	spring	summer	fall
North	0.40 (0.36 0.47)	0.94 (0.83 0.99)	1.79 (1.73 1.84)	0.91 (0.94 1.06)
Central	0.59 (0.53 0.74)	1.33 (1.22 1.41)	1.87 (1.8 1.92)	1.22 (1.19 1.37)
South	0.73 (0.66 0.94)	1.62 (1.5 1.71)	2.14 (2.01 2.23)	1.34 (1.34 1.57)
Surface forcing (BC only) W m^{-2}				
	winter	spring	summer	fall
North	-0.29 (-0.3 -0.21)	-0.80 (-0.9 -0.8)	-1.37 (-1.15 -1.46)	-0.62 (-0.45 -0.65)
Central	-0.48(-0.51 -0.39)	-1.28 (-1.42 -1.25)	-1.48 (-1.27 -1.57)	-0.96(-0.76 -1.02)
South	-0.6 (-0.64 -0.5)	-1.53(-1.7 -1.5)	-1.84 (-1.63 -1.97)	-1.12 (-0.9 -1.17)

Table 12.2 Atmospheric heating and surface forcing from BC in Northern, Central, and Southern CA calculated off-line from WRF-Chem simulation. Upper and lower limits on uncertainty are given in parentheses.

12.9 Conclusions

A fully coupled meteorology-chemistry model (WRF-Chem) is used to study the spatial and seasonal distribution of speciated aerosols and their direct radiative forcings over California in two configurations. Model simulations are evaluated with various datasets including the meteorological fields, the surface aerosol mass concentrations from EPA and IMPROVE, and the aerosol optical depth from AERONET and satellites. In general, the model well captures the observed seasonal and spatial distributions of meteorological fields. The simulations reproduce the observed spatial distributions of aerosol surface mass concentrations, showing high mass concentrations of total $PM_{2.5}$ over the Central Valley and the Los Angeles metropolitan regions due to anthropogenic aerosols. In addition, the simulations also show high $PM_{2.5}$ concentrations over southeastern California due to natural dust aerosol. The spatial gradients of natural aerosol mass concentrations are well simulated and the impact of natural aerosols is confined to limited regions (coastal areas for sea-salt and southeastern California for dust).

Aerosol direct radiative forcing is presented along with the contribution from each aerosol species over California for the first time. At the TOA, most aerosols introduce a negative radiative forcing with sulfate as the biggest contributor of minimum -0.4 W m^{-2} in winter and maximum -0.7 W m^{-2} in summer, except that EC leads to a positive forcing from minimum 0.2 W m^{-2} in winter to maximum 0.7 W m^{-2} in summer. In the atmosphere, EC and dust contribute about 75-95% and 1-10% of the total aerosol warming (about 0.5-2.0 W m^{-2}), respectively. The rest of the aerosol warming comes from non-absorbing aerosols due to non-linear interactions of internal mixing. All aerosols cool the surface with EC being the largest contributor in summer (-1.1 W m^{-2} and ~35%) and sulfate (-0.45 W m^{-2} and ~30%) in winter. The TOA radiative forcing of EC over California is comparable with that of total carbonaceous aerosols on global average (0.75±0.25 W m^{-2}, mainly from EC, since the net effect of OM is close to zero if accounting for the OM absorption effect) as estimated by Chung et al. [2012] with observational constraints.

13.0 Regional Climate impacts of BC

13.1 Introduction

The previous chapters of this report have discussed estimates of the radiative forcing of BC in California using measurements and modeling. Overall, the reduction of BC over the last few decades (as a result of pollution control through stringent emission standards for diesel engines and reformulated low-sulfur diesel fuel) could have induced detectable changes in the regional climate of CA by reducing the amount of absorbed sunlight, and increasing the solar radiation reaching the surface. Over this time scale, the climate of CA has experienced decadal changes including a warming trend of about 0.2^{o}C per decade from 1979 – 2005 (e.g., Trenberth et al. 2007), which is consistent with the observed earlier snowmelt and reduced snowpack in the mountains (e.g., Stewart et al. 2005). This chapter describes numerical experiments and analyses that have been performed to study the potential impacts of BC reduction on California's climate. Such estimates are needed to understand, attribute, and predict regional climate changes in the context of regional-to-global changes in response to the greenhouse gas and aerosol forcing.

13.2 Numerical experiments

Following a similar modeling approach described in Chapter 11, the coupled meteorology-aerosol-chemistry model WRF-Chem is used to simulate regional climate changes associated with reduction of BC. Again, several parallel sets of simulations were conducted using the model configurations described in Chapter 11 with a domain that covers the western U.S. at 12 km grid resolution, and are denoted WRF_PNNL and WRF_LBL here. The main differences between these model configurations are the choices of physics parameterizations, particularly for cloud microphysics and radiative transfer, which are important for simulating aerosol direct and indirect effects. Since the inter-annual climate variability in CA is large, simulations of multiple years are needed to discern the signal from noise. Due to the large computational requirements of WRF-Chem, we estimate the BC effects by comparing two five-year simulations covering the time period from 2005 – 2009. In the control simulation, the EC emissions from the ARCTAS-CA are doubled. As discussed in Chapters 10 and 11, this 2xEC configuration has been shown to simulate aerosol concentrations and AOD more comparable to observations for 2005. This simulation is therefore used to represent the conditions of the 2000s. In the perturbed simulation, the EC emissions from the ARCTAS-CA are multiplied by a factor of 10. Compared to the control simulation, the factor of 5 increases in EC emissions from the 2000s is used to represent the EC emissions of the 1960s, as suggested by the analysis of COH described in Chapter 3 (Figures 3.3 and 3.4 show historical trends in reconstructed BC concentration). Hence this simulation is used to represent the conditions of the 1960s. Comparison of the mean conditions from the two simulations is used to

investigate the potential impacts of BC reduction from the 1960s to the 2000s on the regional climate of CA. These results obtained by WRF-PNNL are discussed below in Section 13.3. Due to limited computing resources, WRF_LBL was used to perform two simulations, each for one year, with the ARTAS-CARB EC emission and half of that to simulate the effects of reduced BC emission on CA climate, and these results are described in Section 13.4.

13.3 WRF_PNNL: Effects of BC on California climate

Figure 13.1 shows the change in the all-sky net solar radiation at the surface and the TOA solar radiation comparing the simulations for the 2000s (2xEC) with that for the 1960s (10xEC). Reduction of BC leads to increases in the surface solar radiation by 5 W m^{-2} in the summer. The patterns of change are similar for all seasons, reflecting the larger reductions of BC in the Central Valley and Southern CA, as well as in specific city locations such as Las Vegas, NV and Phoenix, AZ. At TOA, the changes are opposite showing reduction by up to 3 W m^{-2}. The changes are larger in the summer due to the stronger solar fluxes.

Based on the Student t-test, changes in summer and fall are statistically significant at the 90% confidence level, except for coastal southern CA in summer where large inter-annual variability in solar radiation due to cloudiness is masking the changes in solar radiation due to BC reduction. This suggests that controlling BC emissions has important effects on solar radiation at TOA and reaching the surface during summer and fall. While non-parametric tests are more powerful than the Student t-test because they made no assumption of normality or homogeneity of variance, these analyses were performed using only 5 years of simulation each for the 2xEC and 10xEC concentrations. The usefulness of the statistical tests is primarily limited by the sample size rather than by the statistical methods used. Hence this report does not include other statistical tests that complicate the interpretations of the results.

Due to solar absorption, BC warms the atmosphere. As a result of BC reduction, Figure 13.2 shows negative changes in diabatic heating in the 2000s compared to the 1960s by up to 0.06 K/day, with a maximum in the atmosphere at about 2 km above the surface. The vertical profile of diabatic heating changes is influenced by the vertical profile of BC and clouds, as well as changes in latent heating and radiation from feedbacks through clouds and other processes. During summer when cloudiness is low, changes in diabatic heating due to BC reduction are mainly influenced by turbulence that mixes BC vertically within the boundary layer. Negative changes in diabatic heating are found from about 1 km upward, with larger changes found at altitudes between 1.5 km and 4.5 km above the surface. The diabatic heating changes are strongest during summer and weakest during winter. In addition, the altitudes of maximum changes decrease from about 2km in summer to 1 km in winter, reflecting the higher boundary layer depth in summer than in winter due to stronger turbulence mixing. Below 1 km, the diabatic heating changes become positive due to mixing of surface air that warmed in response to the changes in solar forcing shown in Figure 13.1. We

note, however, that the changes in diabatic heating are only significant at the 70% confidence level, as inter-annual variability of diabatic heating is large.

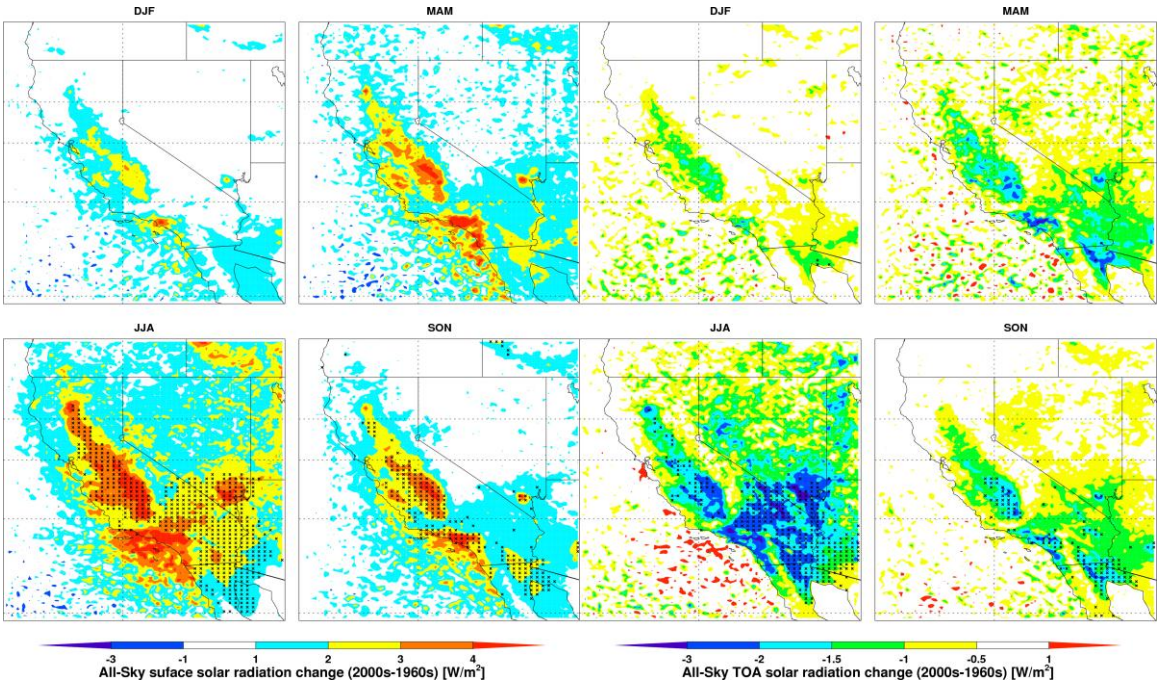

Figure 13.1 Changes in all-sky net solar radiation at the surface (left) and TOA solar radation (right) (in W m^{-2}) comparing simulations for the 2000s (2xEC) to the 1960s (10xEC). Areas with changes that are statistically significant at the 90% confidence level are stippled. Panels in the figure represent seasonal averages and are labeled using the corresponding months.

In response to the diabatic heating changes, Figure 13.2 also shows the changes in atmospheric temperature profile for each season. The dominant response to BC reduction is cooling in the lower atmosphere due to reductions in BC absorption. The cooling peaks around 1 km during winter and 2 km during summer, corresponding to the peaks in the diabatic heating changes. Temperature changes are confined to below 5 km. Overall, the atmosphere cools as a result of BC reduction, with a maximum of about 0.02^{o}C.

Figure 13.3 shows the changes in atmospheric temperature at 2m and 2km, respectively. Due to diabatic cooling, temperature at 2km is reduced by up to 0.03^{o}C. Near the surface, however, the atmosphere and the land surface respond primarily to changes in the surface solar radiation. Due to the enhanced surface solar radiation, the 2m surface temperature increases as a result of BC reduction by up to 0.08^{o}C regionally over the Central Valley and along the southern CA coast during summer (Figure 13.3). The surface temperature changes during winter and spring are generally negligible. Larger temperature changes are also found in the northeastern part of the domain despite only small

changes in solar radiation (Figure 13.1). Since mountains dominate the area, the temperature response may be larger due to lower surface pressure. Figure 13.4 shows a comparison of the observed and simulated temperature profiles at three sounding locations in CA. The model realistically simulated the vertical distribution and seasonality of temperature. During summer, CA is under the influence of the subtropical high-pressure system so a temperature inversion occurs in the boundary layer. Therefore, surface temperature responds primarily to radiative forcing at the surface rather than TOA, hence surface warming due to BC reduction. Based on the Student t-test, however, none of the changes in temperature at 2m or 2km is statistically significant at 90% confidence level due to the large inter-annual variability.

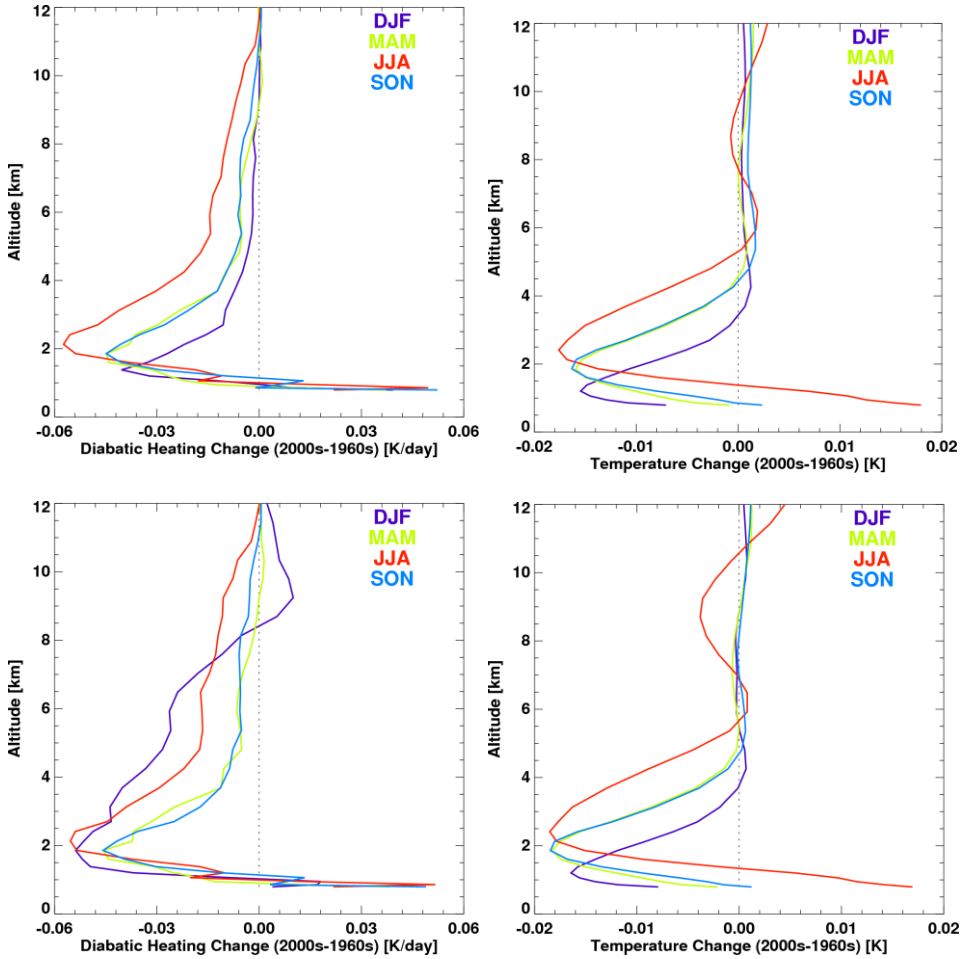

Figure 13.2 Left: Changes in diabatic heating comparing the simulation for the2000s with the 1960s (in K/day). Right: Similar to the left but for changes in atmospheric temperature (^{o}C).

The climate of CA has a distinct seasonal cycle with surface hydrology dominated by cold season precipitation, snow accumulation and melt, and runoff.

As changes in the surface energy budgets are small in the cold season, changes in the surface hydrology are generally small with little change in runoff and snowpack. During summer, changes in the surface solar radiation are larger (Figure 13.1), but the changes are mainly balanced by changes in sensible heat fluxes because latent heat fluxes are limited by the relatively dry land surface in CA (not shown). The small increase in evaporation associated with the increased latent heat fluxes leads small reductions in soil moisture. The boundary layer height increases by up to 10 m in the summer in response to the enhanced surface sensible heat fluxes.

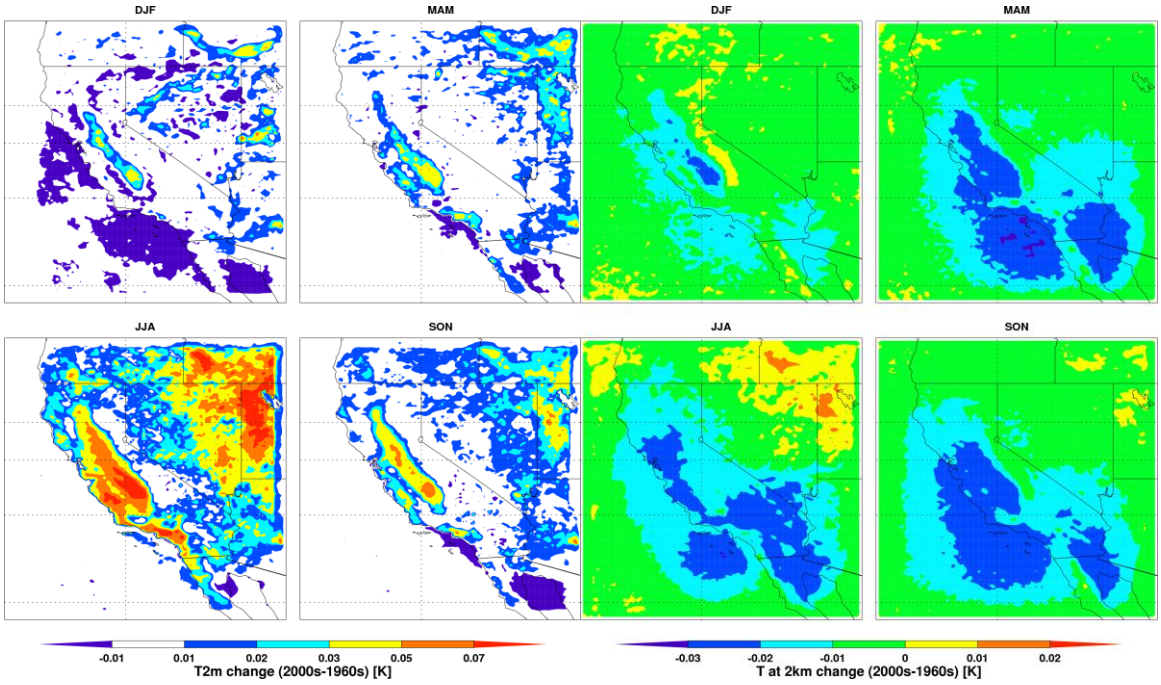

Figure 13.3 Changes in atmospheric temperature at 2 meter (left) and 2 km (right) comparing the 2000s to the 1960s in ^{o}C. Panels in the figure represent seasonal averages and are labeled using the corresponding months.

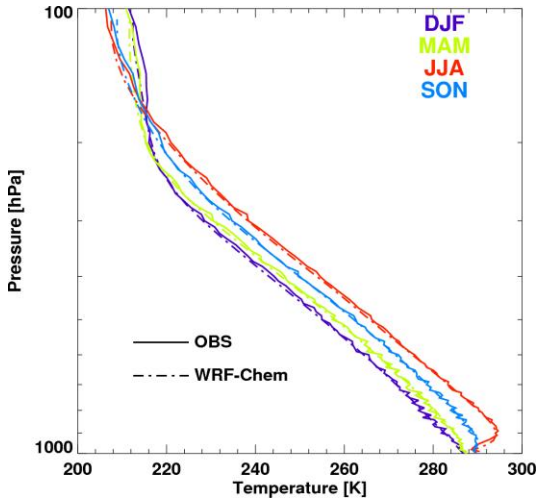

Figure 13.4 Comparison of observed (solid) and simulated (dashed) temperature profiles averaged over three sounding locations in CA (OAK, VGB, NKX) for four seasons for 2005.

13.4 WRF_LBL: Effects of BC on California climate

In contrast with the PNNL study, the LBL study examines the impact of BC by cutting the baseline emissions in half (as opposed to the 2xEC and 10xEC scenarios). The modeled reduction in atmospheric heating as a result of this reduction is shown for each season in Table 13.1 and, vertically resolved for both summer and winter, in Figure 13.4. This was calculated off-line using the previously described method for both the predicted BC in the control case and that obtained after reducing emissions by half. Each run used the modeled AOD and AAOD specific to their respective BC emission scenario; however the same meteorology from the control run was used in both calculations to remove secondary effects from changes in cloud cover and provide an estimate of only the direct effect.

	Winter	Spring	Summer	Fall
Δ Atmospheric Heating, W m^{-2}				
North	-0.07 (-0.13 -0.05)	-0.13 (-0.13 -0.08)	-0.27 (-0.28 -0.25)	-0.13 (-0.15 -0.13)
Central	-0.13 (-0.27 -0.1)	-0.26 (-0.29 -0.23)	-0.33 (-0.48 -0.42)	-0.29 (-0.29 -0.24)
South	-0.16 (-0.35 -0.13)	-0.34 (-0.37 -0.3)	-0.5 (-0.53 -0.46)	-0.33 (-0.35 -0.29)
Δ Surface Forcing, W m^{-2}				
North	0.06 (0.04 0.06)	0.1 (0.09 0.13)	0.23 (0.19 0.25)	0.13 (0.09 0.13)
Central	0.13 (0.09 0.13)	0.26 (0.22 0.26)	0.42 (0.37 0.44)	0.24 (0.19 0.27)
South	0.14 (0.13 0.14)	0.32 (0.29 0.47)	0.44 (0.4 0.48)	0.3 (0.24 0.32)

Table 13.1 Change in atmospheric heating and surface forcing as a result of cutting BC emissions in half (indirect effects not included)

Cutting the BC emissions in half leads to a 20-25% decrease in atmospheric heating. In winter, this amounts to approximately -0.1 W m^{-2}, while the change in BC forcing during the summer is between -0.3 and -0.5 W m^{-2}. Figure 13.4(a) presents the vertically resolved, percent change in seasonal BC concentration for Northern, Central, and Southern California. Cutting BC emissions by half lowers the surface concentration by a similar percentage, but the corresponding change in BC concentration with altitude quickly goes to zero. The BC at higher elevations is likely from long-range transport and thus unaffected by the changes in California emissions. The decrease in BC emissions from 1980 to present was likely to have had a larger effect on regional climate than what might be expected from a further reduction in emitted BC. This is primarily because BC emissions from CA sources were much greater in the eighties relative to the long-range

transport of BC from Asia [*Bey et al.*, 2001; *Hadley et al.*, 2007]. With increased industrial activities in India and China over the last decade [*Ohara et al.*, 2007], transport of BC from these regions has likely increased.

To look at the combined direct and indirect forcing, the respective COT for each simulation was used and the results from the off-line calculation compared to the direct radiative forcing. There was no significant change from the direct forcing calculations in either summer or winter (<0.01), however the average change in BC induced surface forcing obtained directly from the on-line simulations (direct plus indirect) was compared with the off-line forcing calculations and there is a significant difference in the predicted change in surface forcing in winter and summer (Table 13.2). The on-line calculation show that in central and southern CA, reducing BC emissions in the winter appears to cause a negative, rather than positive, surface forcing, likely corresponding to the increased cloud cover in this region (Figure 13.5). A very slight decrease in winter COT (0.04) over Northern CA leads to a positive forcing of 0.18 W m^{-2}. Summer time forcing is all positive and 2 to 4 times larger than that predicted by the off-line calculations. These differences are most likely a result of non-linear affects introduced when averaging cloud cover and changes in instantaneous downward SW flux. They also suggest that the off-line calculations presented may be biased low. On-line and off-line surface forcing calculations for spring and fall are generally consistent with each other.

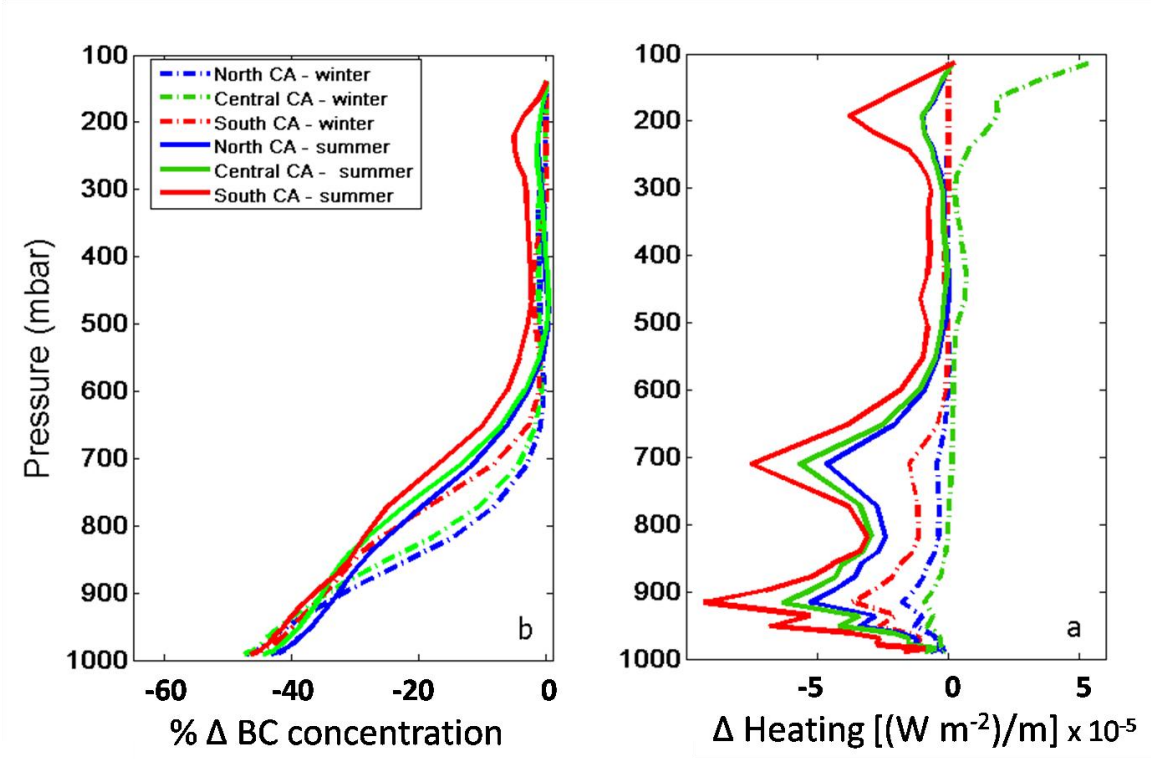

Figure 13.5 (a) Percent reduction in BC concentration as a result of cutting BC emissions in half, and (b) the associated change in atmospheric heating as a function of altitude.

Surface radiative forcing (direct + indirect), W m^{-2}				
	winter	spring	summer	fall
North	0.18	0.08	0.98	0.26
Central	-0.44	0.23	1.71	0.35
South	-0.11	0.51	0.9	0.36

Table 13.2 The change in total downward short-wave flux at the surface as a result of reducing BC emissions by half using the WRF-Chem model.

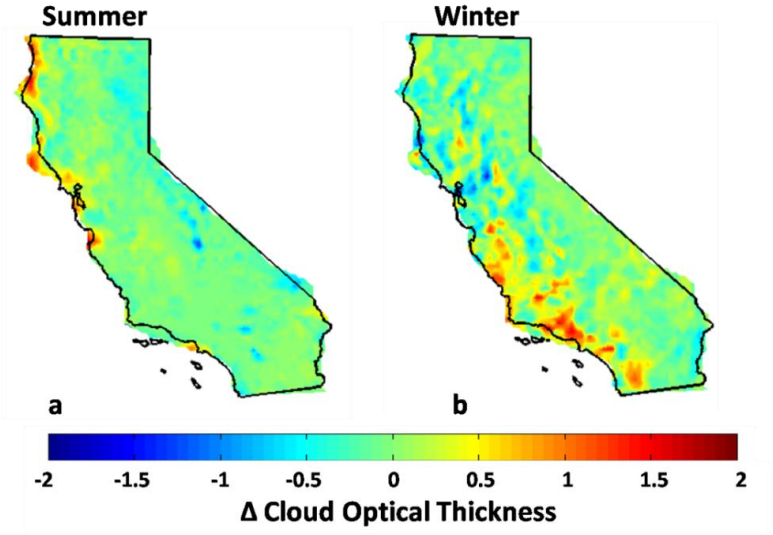

Figure 13.6 The change in cloud optical thickness in (a) Summer and (b) Winter as a result of reducing baseline BC emissions by half.

13.5 Conclusions

Based on numerical experiments using WRF-PNNL with the ARCTAS-CA emissions multiplied by a factor of 10 (10xEC) representing the EC emission of the 1960s and a factor of 2 (2xEC) representing the EC emission of the 2000s, potential impacts of BC reduction since the 1960s are investigated. Our results show that BC reduction leads to increases in the net solar radiation at the surface (up to 5 W m^{-2} in summer), reductions in diabatic heating in the lower atmosphere, and net cooling at the top of the atmosphere, with larger effects during summer than winter because solar radiation is much higher during summer. In response to these changes, the lower atmosphere cools by up to

0.02^{o}C averaged over CA, and surface temperature at 2 m increases by up to 0.08^{o}C locally over the Central Valley and Southern CA in summer. Therefore changes near the surface are decoupled from the cooling at the top of the atmosphere because convective coupling is weak in the relatively dry atmosphere over CA. The warming near the surface as a result of BC reduction could have contributed to the overall warming trend in the last few decades. However, due to the large inter-annual variability, the changes in surface temperature due to BC reduction are not statistically significant at the 90% confidence level. Longer simulations are needed to determine more robust changes associated with EC emission changes.

Changes in the surface hydrology are found to be generally small because changes in the surface energy budgets are small during winter when surface hydrological processes such as snowpack and runoff are more prominent. We note, however, that potential changes in surface energy and water budgets due to BC deposition on mountain snowpack are not represented in our simulations. *Qian et al.*, [2009] showed that changes in surface albedo due to soot deposition in snowpack could lead to warming and the effects could be amplified by snow-albedo feedback. Such effects due to BC reduction could dominate the changes over mountain and counter the warming due to greenhouse and BC radiative forcing locally.

Our estimates of the effects of BC reduction on the climate of CA are based on regional models in which the lateral boundary conditions are identical between the control and perturbed experiments. This approach ignores potential changes in the large-scale circulation that may result from BC reduction in CA, which could influence the simulations through changes in the lateral boundary conditions. How the local surface climate of CA will be influenced by BC reduction depends on both changes in response to the local forcing, as well as the influence from changes in large-scale circulation. Given the decoupling between the surface and the upper atmosphere during summer when CA is under the influence of the subtropical high pressure system, it is likely that the response to local forcing will dominate, but large scale changes may still have some influence on CA climate as well as climate in other regions through remote response to the diabatic heating changes from BC reduction in CA. Cooling in the top of the atmosphere from BC reduction should result in overall cooling of the climate system, based on estimates of BC forcing from both observations and models reported in previous chapters. Our results, however, motivate the need for future study to better characterize the regional response, which could be opposite to the larger scale or global response depending on the climate regimes.

14.0 Conclusions and Findings

14.1 Primary conclusions

This report provides an assessment of the climate impact of black carbon on California's climate. The assessment uses climate models constrained by field measurements. Targeted emission controls adopted by the State of California are shown to be effective in reducing BC concentrations, by a factor of at least two dating back to the 1980s, and by as much as a factor of five dating back to the 1960s. At the regional level this decrease is associated with a TOA cooling of between 0.5-1.5 W m^{-2}, serving as a counterbalance to the warming introduced by greenhouse agents over the same time period. The control of short-lived climate pollutants therefore is shown to be an effective means of combating climate change at the regional level.

An analysis of the spectral dependence of solar absorption indicates that solar absorption due to brown carbon contributes as much as 50% of the BC forcing in the near-UV wavelengths. The brown carbon is primarily related to residential wood burning. However, a new class of particles related to secondary organics and aged large organic particles are also found to contribute to solar absorption. The observationally constrained EC absorption agrees reasonably well with estimates from regional transport models (GOCART and WRF-Chem), but the models underestimate the OC AAOD by at least 50%.

The climate impact of BC was evaluated by changing the emissions by factors of 10x, 5x, and 2x, and 5 years of simulation were performed using the same meteorological fields. The mean signal was calculated as the difference between the mean of the 2x (baseline) and the mean of the 5x and 10x simulations. The uncertainty was estimated as the variance in the difference for each pair simulations for each year. We found significant BC radiative forcing over CA (-0.3 in the winter to -1.8 W m^{-2} in the summer at the surface and 0.4 to 2.1 W m^{-2} of atmospheric heating) from current BC levels. In response to this change, the lower atmosphere was found to cool by up to 0.02^{o}C (between 0.017 and 0.023^{o}C) averaged over CA, and surface temperature at 2 m increased by up to 0.08^{o}C (between 0.08 and 0.12^{o}C) locally over the Central Valley and Southern CA in summer, indicating changes near the surface were decoupled from the cooling at the top of the atmosphere (due to weak convective coupling in the relatively dry atmosphere over CA). The warming near the surface as a result of BC reduction could have contributed to the overall warming trend in the last few decades.

In summary, for regions like California, where mitigation policies have historically targeted primarily fossil fuel sources leading to a large decrease in atmospheric BC, the climate benefits of direct forcing reduction has masked the net warming due to greenhouse gases by a measureable fraction (estimated to be 5% of the

CO_2 warming potential). This climate benefit dates back to at least the 1960s, and is currently ongoing. Brown carbon, emitted from residential wood burning is found to be another attractive target for policy makers seeking to combat anthropogenic climate change.

14.2 Research highlights

1. We refurbished COH instruments provided by CARB and performed extensive field measurements in the Bay Area to calibrate them against aethalometer BC measurements. The refurbished COH instruments were modified to include a mass flow controller and data acquisition hardware.

2. We performed a comparison of two-hour average COH concentrations measured using the two field-bound refurbished monitors subject to soot from a methane-air flame and determined there was no operational bias between the instruments.

3. A correlation between average BC and COH concentrations measured in San Jose (March 2010 thru April 2011) and Vallejo (March 2010 thru March 2012) indicates that COH is a strong proxy for BC, with R^2 values greater than 0.95.

4. We accessed all existing records of COH measurements in the U.S., and determined annual BC trends in nine states having extensive records.

5. We found (based upon COH data) that the statewide average BC concentration declined steadily since the 1960s, by as much as a factor of 5 compared to current levels.

6. We found that the average BC concentrations in California reconstructed from COH records declined comparably in all the major air basins, and the trend is not driven by a localized phenomenon.

7. The weekly cycle of BC concentration in California suggests that emissions from fossil fuel combustion (primarily in the transportation sector) are the predominant source, as they reach a maximum during the standard workweek and drop off over the weekends.

8. The total consumption of on-road diesel steadily increased in California, however this trend is overshadowed by the decrease in the emission factor from diesel combustion, leading to smaller net emissions. This decrease can be attributed to cleaner burning engines, down stream filters, and sulfur-free fuel.

9. Trends in the annual mean measured BC concentration from the IMPROVE network (representing non-urban and remote locations) are consistent with the trends reconstructed from COH (representing urban locations), with a 50% reduction in BC between 1980-2000s. This trend is again found to be consistent in Northern, Central, and Southern California, and between non-urban and urban locations.

10. Fossil fuel emissions (obtained from two independent sources) in California have declined by the same factor over this time period, again suggesting that diesel emission control is the primary driver for decreased BC.

11. The annual mean of measured BC/non-BC Aerosol ratios in California also declined between 1989 and 2008, indicating that the change in BC concentration cannot be attributed to cleaner air in general or a change in boundary layer conditions. We find that the BC been preferentially removed.

12. We found that the spectral properties of absorbing aerosols, expressed as the Scattering Angstrom Exponent and Absorption Angstrom Exponent can be used to segregate aerosols dominated by dust, BC, or OC (brown Carbon). We have performed an extensive analysis of worldwide AERONET measurements in both urban and non-urban areas and found consistent results.

13. We determined the AAE for pure EC and OC based upon an extensive spectral analysis. The AAE values are found to be 0.55 and 4.55 respectively, these bracket the idealized value of 1.00 attributed to BC in the literature.

14. We also calculated SSA values for EC, OC, and Dust using AERONET stations segregated into source regions. This is a significant improvement over current model estimates that treat the OC as being purely scattering, whereas we found an SSA value of 0.85 for the OC.

15. We developed a robust algorithm exploiting the differences in spectral properties that allows for the partitioning of total aerosol absorption and aerosol optical depth into EC, OC, and dust; and applied it to California.

16. We found that the species resolved AOD and AAOD are consistent with emissions in California for EC, OC, and dust. The OC absorption is approximately 40% of the EC absorption near the UV band (at 440 nm) but rapidly drops off, decreasing to 15% at 675 nm, and 0% at 870 nm.

17. We determined a wavelength dependent Single Scattering Albedo (especially for OC), that can be used to incorporate brown carbon absorption into regional climate models by suitably modifying their optical properties.

18. We proposed a relation between the optical properties of observed ambient aerosols (combination of the AAE and SAE) to the dominant absorbing species (fossil fuel, biomass burning or dust).

19. We used detailed chemical measurements (from the ATOFMS) in three aircraft-based field campaigns alongside co-located optical measurements to relate the absorbing species to emission sources.

20. We identified for the first time a new class of particles (large aged secondary particles) that absorb solar radiation, indicating that biomass burning may not be the only source of absorbing organics.

21. We estimated the contributions of black and organic carbon to solar absorption in a field campaign directed at residential wood burning particulates in Northern California.

22. We found again in the targeted field campaign, that Brown Carbon is responsible at short wavelengths (300-500 nm) for approximately one-half of the total aerosol absorption. This offers more evidence that current climate models are masking a potential source of warming in the atmosphere.

23. We used satellite retrievals from MISR to construct seasonally resolved 3-dimensional pictures of the total AOD, total AAOD, EC AOD, and EC AAOD over the California domain.

24. We found in a comparison of simulated AOD and AAOD for carbonaceous aerosols from the GOCART and WRF models with the observationally constrained approach followed in this study that while the models correctly predict the total AOD (indicating a consistent aerosol loading), they under-predict OC AAOD by as much as 50 %.

25. We reconstructed seasonally and spatially resolved vertical profiles of aerosols in California using a hybrid of CALIPSO satellite retrievals for high altitudes (above 500 m) and ground based measurements close to the surface (below 500 m). The aerosol extinction measured by the satellite is directly correlated to aerosol mass loading.

26. We calculated the radiative forcing at the Top-of-Atmosphere (TOA), in the Atmosphere (atm), and at the surface (sfc) attributable to dust and carbonaceous aerosols in California using observationally constrained aerosol properties to initialize a Monte Carlo model. The BC was found to have a large heating effect in the atmosphere (up to 3.5 W m^{-2}) that is larger in Southern California and in the summer. OC was found to have neither a net cooling nor heating effect at the TOA.

27. We used solar flux measurements from the CIMIS network using sites operational form November, 1986-December, 2011 to examine the climatology of surface solar flux and attempted to detect a brightening signal (related to the decreased BC absorption).

28. We found that the inter-annual and inter-site variability in the existing data set is much larger than the brightening trend, and as such any change in surface solar flux cannot be considered statistically significant. We have separated the clear sky flux from the total to eliminate the effect of clouds, but again, a significant trend was not detected.

29. We compared the total BC emissions in California based on various available sources. A comparison between model predictions and surface measurements revealed that current emission inventories (specifically the ARCTAS-CA scenario) may be under reporting the BC by a factor of two.

30. We used the WRF-Chem model operating in two configurations to predict the seasonal mean mass concentrations of speciated $PM_{2.5}$ such as EC, OM, dust, sulfate, nitrate, ammonium, sea salt, and unspeciated $PM_{2.5}$. These predictions were validated against surface measurements from the IMPROVE and EPA sampling networks. While the total aerosol concentration agrees well with observations, the EC is found to be severely underpredicted by the model.

31. WRF-Chem is also used to calculate the seasonal variations of aerosol direct radiative forcing with anthropogenic EC emission doubled to account for this discrepancy in emissions. The estimates for atmospheric warming range between 0.8-2.7 W m^{-2} and agree well with our observationally constrained calculations.

32. The WRF-Chem model was also validated against meteorological data including surface temperature and precipitation from CIMAS for summer and winter seasons. The model is found to agree well with these measurements

33. To determine the climate impact of BC, we have calculated changes in all-sky net solar radiation at the surface (in W m^{-2}) comparing simulations for the 2000s (2xEC) to the 1960s (10xEC). We find a surface brightening of 5 W m^{-2} that is statistically significant at the 90% confidence level, and a net cooling at the top of the atmosphere attributable to this change in the EC concentration.

34. The change in the BC concentrations introduced a cooling in the atmosphere between 1-2 km in altitude, but a warming trend near the surface indicating a decoupling due to poor convection. Overall, the atmosphere is found to have cooled by 0.02 ^{o}C. However, neither the changes in temperature profile nor surface temperature are statistically significant at the 90% confidence level.

References

Ackerman, A. S., O. B. Toon, D. E. Stevens, A. J. Heymsfield, V. Ramanathan, and E. J. Welton (2000), Reduction of tropical cloudiness by soot, *Science*, *288*(5468), 1042-1047.

Ackerman, I. J., H. Hass, M. Memmescheimer, A. Ebel, F. S. Binkowski, and U. Shankar (1998), Modal aerosol dynamics model for Europe : development and first applications, *Atmospheric Environment*, *32*(17), 2981-2999.

Alfaro, S. C., S. Lafon, J. L. Rajot, P. Formenti, A. Gaudichet, and M. Maille (2004), Iron oxides and light absorption by pure desert dust: An experimental study, *J. Geophys. Res.-Atmos.*, *109*(D8), 9.

Allen, G. A., J. Lawrence, and P. Koutrakis (1999), Field validation of a semi-continuous method for aerosol black carbon (aethalometer) and temporal patterns of summertime hourly black carbon measurements in southwestern PA, *Atmospheric Environment*, *33*(5), 817-823.

Anderson, T. L., and J. A. Ogren (1998), Determining aerosol radiative properties using the TSI 3563 integrating nephelometer, *Aerosol Sci Tech*, *29*(1), 57-69.

Andreae, M. O., and P. Merlet (2001), Emission of trace gases and aerosols from biomass burning, *Global Biogeochemical Cycles*, *15*(4), 955-966.

Andreae, M. O., and A. Gelencser (2006), Black carbon or brown carbon? The nature of light-absorbing carbonaceous aerosols, *Atmos. Chem. Phys.*, *6*, 3131-3148.

Andreae, M. O., and D. Rosenfeld (2008), Aerosol-cloud-precipitation interactions. Part 1. The nature and sources of cloud-active aerosols, *Earth-Sci. Rev.*, *89*(1-2), 13-41.

Arnott, W. P., K. Hamasha, H. Moosmuller, P. J. Sheridan, and J. A. Ogren (2005), Towards aerosol light-absorption measurements with a 7-wavelength Aethalometer: Evaluation with a photoacoustic instrument and 3-wavelength nephelometer, *Aerosol Science and Technology*, *39*(1), 17-29.

Arola, A., G. Schuster, G. Myhre, S. Kazadzis, S. Dey, and S. N. Tripathi (2011), Inferring absorbing organic carbon content from AERONET data, *Atmos. Chem. Phys.*, *11*(1), 215-225.

Ault, A. P., C. R. Williams, A. B. White, P. J. Neiman, J. M. Creamean, C. J. Gaston, F. M. Ralph, and K. A. Prather (2011), Detection of Asian dust in

California orographic precipitation, *Journal of Geophysical Research-Atmospheres*, *116*.

BAAQMD (2012), Personal communication regarding COH monitor, edited by P. Martien and D. Fairley.

Bahadur, R., Y. Feng, L. M. Russell, and V. Ramanathan (2011), Impact of California's air pollution laws on black carbon and their implications for direct radiative forcing, *Atmospheric Environment*, *45*(5), 1162-1167.

Bahadur, R., P. S. Praveen, Y. Xu, and V. Ramanathan (2012a), Supplement to Relative solar absorption by Elemental and Organic Carbon determined from unique aerosol optical properties, *Proc. Natl. Acad. Sci. U. S. A.*

Bahadur, R., P. S. Praveen, Y. Xu, and V. Ramanathan (2012b), Solar absorption by elemental and brown carbon determined from spectral observations, *Proceedings of the National Academy of Sciences*, *109*(43), 17366-17371.

Bahadur, R., L. M. Russell, M. Z. Jacobson, K. Prather, A. Nenes, P. Adams, and J. H. Seinfeld (2012c), Importance of composition and hygroscopicity of BC particles to the effect of BC mitigation on cloud properties: Application to California conditions, *J. Geophys. Res.-Atmos.*, *117*, 15.

Bahreini, R., J. L. Jimenez, J. Wang, R. C. Flagan, J. H. Seinfeld, J. T. Jayne, and D. R. Worsnop (2003), Aircraft-based aerosol size and composition measurements during ACE-Asia using an Aerodyne aerosol mass spectrometer, *J Geophys Res-Atmos*, *108*(D23).

Ban-Weiss, G. A., J. P. McLaughlin, R. A. Harley, M. M. Lunden, T. W. Kirchstetter, A. J. Kean, A. W. Strawa, E. D. Stevenson, and G. R. Kendall (2008), Long-term changes in emissions of nitrogen oxides and particulate matter from on-road gasoline and diesel vehicles, *Atmospheric Environment*, *42*(2), 220-232.

Barnaba, F., and G. P. Gobbi (2004), Aerosol seasonal variability over the Mediterranean region and relative impact of maritime, continental and Saharan dust particles over the basin from MODIS data in the year 2001, *Atmos Chem Phys*, *4*, 2367-2391.

Barnard, J. C., R. Volkamer, and E. I. Kassianov (2008), Estimation of the mass absorption cross section of the organic carbon component of aerosols in the Mexico City Metropolitan Area, *Atmos Chem Phys*, *8*(22), 6665-6679.

Bergstrom, R. W., P. Pilewskie, P. B. Russell, J. Redemann, T. C. Bond, P. K. Quinn, and B. Sierau (2007), Spectral absorption properties of atmospheric aerosols, *Atmos. Chem. Phys.*, *7*(23), 5937-5943.

Bey, I., D. J. Jacob, J. A. Logan, and R. M. Yantosca (2001), Asian chemical outflow to the Pacific in spring: Origins, pathways, and budgets, *J. Geophys. Res.-Atmos.*, *106*(D19), 23097-23113.

Bodhaine, B. A., N. B. Wood, E. G. Dutton, and J. R. Slusser (1999), On Rayleigh Optical Depth Calculations, *J. Atmos. Oceanic Technol.*, *16*, 1854-1861.

Bohren, C. F., and D. R. Huffman (1998), *Absorption and Scattering of light by small particles*, Wiley Interscience, New York.

Bollasina, M. A., Y. Ming, and V. Ramaswamy (2011), Anthropogenic Aerosols and the Weakening of the South Asian Summer Monsoon, *Science*, *334*(6055), 502-505.

Bond, T. C. (2001), Spectral dependence of visible light absorption by carbonaceous particles emitted from coal combustion, *Geophys Res Lett*, *28*(21), 4075-4078.

Bond, T. C., D. G. Streets, K. F. Yarber, S. M. Nelson, J. H. Woo, and Z. Klimont (2004), A technology-based global inventory of black and organic carbon emissions from combustion, *J. Geophys. Res.-Atmos.*, *109*(D14).

Bond, T. C., and R. W. Bergstrom (2006), Light absorption by carbonaceous particles: An investigative review, *Aerosol Sci. Technol.*, *40*(1), 27-67.

Bond, T. C., D. S. Covert, and T. Muller (2009), Truncation and Angular-Scattering Corrections for Absorbing Aerosol in the TSI 3563 Nephelometer, *Aerosol Sci Tech*, *43*(9), 866-871.

Bond, T. C., S. J. Doherty, D. W. Fahey, P. M. Forster, T. Berntsen, B. J. DeAngelo, M. G. Flanner, S. Ghan, B. Kärcher, D. Koch, S. Kinne, Y. Kondo, P. K. Quinn, M. C. Sarofim, M. G. Schultz, M. Schulz, C. Venkataraman, H. Zhang, S. Zhang, N. Bellouin, S. K. Guttikunda, P. K. Hopke, M. Z. Jacobson, J. W. Kaiser, Z. Klimont, U. Lohmann, J. P. Schwarz, D. Shindell, T. Storelvmo, S. G. Warren, and C. S. Zender (2013), Bounding the role of black carbon in the climate system: A scientific assessment, *Journal of Geophysical Research: Atmospheres*, n/a-n/a.

Cachier, H., M. P. Bremond, and P. Buatmenard (1989), Carbonaceous Aerosols from Different Tropical Biomass Burning Sources, *Nature*, *340*(6232), 371-373.

CARB (2008), Emission Inventory Data
http://www.arb.ca.gov/ei/emissiondata.htm.

Cass, G. R., M. H. Conklin, J. J. Shah, and J. J. Huntzicker (1984), Elemental Carbon Concentrations - Estimation of an Historical Data-Base, *Atmos Environ*, *18*(1), 153-162.

CCR (2010), California Code of Regulations Title 13
http://www.arb.ca.gov/regs/regs.htm.

Chakrabarty, R. K., H. Moosmuller, L. W. A. Chen, K. Lewis, W. P. Arnott, C. Mazzoleni, M. K. Dubey, C. E. Wold, W. M. Hao, and S. M. Kreidenweis (2010), Brown carbon in tar balls from smoldering biomass combustion, *Atmos Chem Phys*, *10*(13), 6363-6370.

Chen, W. T., A. Nenes, H. Liao, P. J. Adams, J. F. Li, and J. H. Seinfeld (2010), Global Climate Response to Anthropogenic Aerosol Indirect Effects : Present Day and Year 2100, *J Geophys Res-Atmos*, *submitted*.

Chen, Y. J., C. A. Roden, and T. C. Bond (2012), Characterizing Biofuel Combustion with Patterns of Real-Time Emission Data (PaRTED), *Environ Sci Technol*, *46*(11), 6110-6117.

Chen, Y. M., S. Liang, J. Wang, H. Y. Kim, and J. V. Martonchik (2008), Validation of MISR land surface broadband albedo, *Int J Remote Sens*, *29*(23), 6971-6983.

Chin, M., P. Ginoux, S. Kinne, O. Torres, B. N. Holben, B. N. Duncan, R. V. Martin, J. A. Logan, A. Higurashi, and T. Nakajima (2002), Tropospheric aerosol optical thickness from the GOCART model and comparisons with satellite and Sun photometer measurements, *J Atmos Sci*, *59*(3), 461-483.

Chin, M., P. Ginoux, R. Lucchesi, B. Huebert, R. Weber, T. Anderson, S. Masonis, B. Blomquist, A. Bandy, and D. Thornton (2003), A global aerosol model forecast for the ACE-Asia field experiment, *J Geophys Res-Atmos*, *108*(D23).

Chin, M., T. Diehl, O. Dubovik, T. F. Eck, B. N. Holben, A. Sinyuk, and D. G. Streets (2009), Light absorption by pollution, dust, and biomass burning aerosols: a global model study and evaluation with AERONET measurements, *Ann. Geophys.*, *27*(9), 3439-3464.

Chow, J. C., J. G. Watson, D. Crow, D. H. Lowenthal, and T. Merrifield (2001), Comparison of IMPROVE and NIOSH carbon measurements, *Aerosol Sci Tech*, *34*(1), 23-34.

Chow, J. C., J. G. Watson, L. W. A. Chen, W. P. Arnott, and H. Moosmuller (2004), Equivalence of elemental carbon by thermal/optical reflectance and transmittance with different temperature protocols, *Environ Sci Technol*, *38*(16), 4414-4422.

Chow, J. C., J. G. Watson, P. K. K. Louie, L. W. A. Chen, and D. Sin (2005), Comparison of PM2.5 carbon measurement methods in Hong Kong, China, *Environ Pollut*, *137*(2), 334-344.

Chow, J. C., J. G. Watson, P. Doraiswamy, L. W. A. Chen, D. A. Sodeman, D. H. Lowenthal, K. Park, W. P. Arnott, and N. Motallebi (2009), Aerosol light absorption, black carbon, and elemental carbon at the Fresno Supersite, California, *Atmos. Res.*, *93*(4), 874-887.

Chung, C. E., V. Ramanathan, D. Kim, and I. A. Podgorny (2005), Global anthropogenic aerosol direct forcing derived from satellite and ground-based observations, *J. Geophys. Res.-Atmos.*, *110*(D24).

Chung, C. E., K. Lee, and D. Muller (2012a), Effect of internal mixture on black carbon radiative forcing, *Tellus B*, *64*, 1-13.

Chung, C. E., V. Ramanathan, and D. Decremer (2012b), Observationally constrained estimates of carbonaceous aerosol radiative forcing, *Proc. Natl. Acad. Sci. U. S. A.*, *109*(29), 11624-11629.

Clarke, A., C. McNaughton, V. Kapustin, Y. Shinozuka, S. Howell, J. Dibb, J. Zhou, B. Anderson, V. Brekhovskikh, H. Turner, and M. Pinkerton (2007), Biomass burning and pollution aerosol over North America: Organic components and their influence on spectral optical properties and humidification response, *J. Geophys. Res.-Atmos.*, *112*(D12), 13.

Clarke, A. D., and K. J. Noone (1985), Soot in the Arctic Snowpack - a Cause for Perturbations in Radiative-Transfer, *Atmospheric Environment*, *19*(12), 2045-2053.

Clarke, A. D., Y. Shinozuka, V. N. Kapustin, S. Howell, B. Huebert, S. Doherty, T. Anderson, D. Covert, J. Anderson, X. Hua, K. G. Moore, C. McNaughton, G. Carmichael, and R. Weber (2004), Size distributions and mixtures of dust and black carbon aerosol in Asian outflow: Physiochemistry and optical properties, *J. Geophys. Res.-Atmos.*, *109*(D15), 20.

Coe, D. L., C. A. Gorin, L. R. Chinkin, and S. R. Reid (2003), Observations of Weekday-Weekend activity patterns for area sources in the Los Angeles area, Presented at the US Environmental Protection Agency 12th International Emission Inventory conferece - 'Emission Inventories - Applying New Technologies'. Sonoma Technology, Inc. .

Coen, M. C., E. Weingartner, D. Schaub, C. Hueglin, C. Corrigan, S. Henning, M. Schwikowski, and U. Baltensperger (2004), Saharan dust events at the Jungfraujoch: detection by wavelength dependence of the single scattering albedo and first climatology analysis, *Atmos. Chem. Phys.*, *4*, 2465-2480.

Coen, M. C., E. Weingartner, A. Apituley, D. Ceburnis, R. Fierz-Schmidhauser, H. Flentje, J. S. Henzing, S. G. Jennings, M. Moerman, A. Petzold, O. Schmid, and U. Baltensperger (2010), Minimizing light absorption measurement artifacts of the Aethalometer: evaluation of five correction algorithms, *Atmos Meas Tech*, *3*(2), 457-474.

Cooke, W. F., C. Liousse, H. Cachier, and J. Feichter (1999), Construction of a 1 degrees x 1 degrees fossil fuel emission data set for carbonaceous aerosol and implementation and radiative impact in the ECHAM4 model, *J Geophys Res-Atmos*, *104*(D18), 22137-22162.

Countess, R. J. (1990), Interlaboratory Analyses of Carbonaceous Aerosol Samples, *Aerosol Sci Tech*, *12*(1), 114-121.

Dey, S., S. N. Tripathi, R. P. Singh, and B. N. Holben (2006), Retrieval of black carbon and specific absorption over Kanpur city, northern India during 2001-2003 using AERONET data, *Atmos. Environ.*, *40*(3), 445-456.

Dieselnet (2012), http://www.dieselnet.com/standards/us/nonroad.php, edited.

Dreher, D. B., and R. A. Harley (1998), A fuel-based inventory for heavy-duty diesel truck emissions, *J Air Waste Manage*, *48*(4), 352-358.

Dubovik, O., and M. D. King (2000), A flexible inversion algorithm for retrieval of aerosol optical properties from Sun and sky radiance measurements, *J. Geophys. Res.-Atmos.*, *105*(D16), 20673-20696.

Dubovik, O., B. Holben, T. F. Eck, A. Smirnov, Y. J. Kaufman, M. D. King, D. Tanre, and I. Slutsker (2002), Variability of absorption and optical properties of key aerosol types observed in worldwide locations, *J. Atmos. Sci.*, *59*(3), 590-608.

Dusek, U., G. P. Reischl, and R. Hitzenberger (2006), CCN Activation of Pure and Coated Carbon Black Particles, *Environmental Science & Technology*, *40*(4), 1223-1230.

Echalar, F., A. Gaudichet, H. Cachier, and P. Artaxo (1995), Aerosol Emissions by Tropical Forest and Savanna Biomass Burning - Characteristic Trace-Elements and Fluxes, *Geophys Res Lett*, *22*(22), 3039-3042.

Eck, T. F., B. N. Holben, J. S. Reid, O. Dubovik, A. Smirnov, N. T. O'Neill, I. Slutsker, and S. Kinne (1999), Wavelength dependence of the optical depth of biomass burning, urban, and desert dust aerosols, *J. Geophys. Res.-Atmos.*, *104*(D24), 31333-31349.

Eck, T. F., B. N. Holben, A. Sinyuk, R. T. Pinker, P. Goloub, H. Chen, B. Chatenet, Z. Li, R. P. Singh, S. N. Tripathi, J. S. Reid, D. M. Giles, O. Dubovik, N. T. O'Neill, A. Smirnov, P. Wang, and X. Xia (2010), Climatological aspects of the optical properties of fine/coarse mode aerosol mixtures, *J. Geophys. Res.-Atmos.*, *115*, 20.

EIA (2012), Energy Information Administration State Energy Data: Consumption, 1960-2010, California

http://www.eia.gov/beta/state/seds/seds-data-complete.cfm?sid=CA#Consumption, edited.

Fairley, D. (2006), Revised estimates of Wood Burning in the San Francisco Bay Area. Draft Report to the Bay Area Air Quality Management District.

Fast, J. D., W. I. Gustafson, R. C. Easter, R. A. Zaveri, J. C. Barnard, E. G. Chapman, G. A. Grell, and S. E. Peckham (2006), Evolution of ozone, particulates, and aerosol direct radiative forcing in the vicinity of Houston using a fully coupled eteorology-chemistry-aerosol model, *Journal of Geophysical Research-Atmospheres*, *111*(D21).

Favez, O., I. El Haddad, C. Piot, A. Boreave, E. Abidi, N. Marchand, J. L. Jaffrezo, J. L. Besombes, M. B. Personnaz, J. Sciare, H. Wortham, C. George, and B. D'Anna (2010), Inter-comparison of source apportionment models for the estimation of wood burning aerosols during wintertime in an Alpine city (Grenoble, France), *Atmos. Chem. Phys.*, *10*(12), 5295-5314.

Fialho, P., M. C. Freitas, F. Barata, B. Vieira, A. D. A. Hansen, and R. E. Honrath (2006), The Aethalometer calibration and determination of iron concentration in dust aerosols, *J. Aerosol. Sci.*, *37*(11), 1497-1506.

Fisher, J. A., D. J. Jacob, M. T. Purdy, M. Kopacz, P. Le Sager, C. Carouge, C. D. Holmes, R. M. Yantosca, R. L. Batchelor, K. Strong, G. S. Diskin, H. E. Fuelberg, J. S. Holloway, E. J. Hyer, W. W. McMillan, J. Warner, D. G. Streets, Q. Zhang, Y. Wang, and S. Wu (2010), Source attribution and inter-annual variability of Arctic pollution in spring constrained by aircraft (ARCTAS, ARCPAC) and satellite (AIRS) observations of carbon monoxide, *Atmos. Chem. Phys.*, *10*(3), 977-996.

Fitzpatrick, M. F., R. E. Brandt, and S. G. Warren (2004), Transmission of solar radiation by clouds over snow and ice surfaces: A parameterization in terms of optical depth, solar zenith angle, and surface albedo, *J Climate*, *17*(2), 266-275.

Flanner, M. G., K. M. Shell, M. Barlage, D. K. Perovich, and M. A. Tschudi (2011), Radiative forcing and albedo feedback from the Northern Hemisphere cryosphere between 1979 and 2008, *Nature Geoscience*, *4*(3), 151-155.

Flowers, B. A., M. K. Dubey, C. Mazzoleni, E. A. Stone, J. J. Schauer, S. W. Kim, and S. C. Yoon (2010), Optical-chemical-microphysical relationships and closure studies for mixed carbonaceous aerosols observed at Jeju Island; 3-laser photoacoustic spectrometer, particle sizing, and filter analysis, *Atmos. Chem. Phys.*, *10*(21), 10387-10398.

Forster, P., V. Ramaswamy, P. Artaxo, B. T., R. Betts, D. W. Fahey, J. Haywood, J. Lean, D. C. Lowe, G. Myhre, J. Nganga, R. Prinn, G. Raga, M. Schulz, and R. van Dorland (2007), Changes in Atmospheric Constituents and in Radiative Forcing, in *Climate Change 2007 : The physical Science Basis. Contribution of*

Working Group I to the Fourth Assessment Report of the Intergovernmental Panel on Climate Change, edited by S. Solomon, D. Qin, M. Manning, Z. Chen, M. Marquis, K. B. Averyt, M. Tignor and H. L. Miller, Cambridge University Press, Cambridge, UK and New York, USA.

Ginoux, P., M. Chin, I. Tegen, J. M. Prospero, B. Holben, O. Dubovik, and S. J. Lin (2001), Sources and distributions of dust aerosols simulated with the GOCART model, *J Geophys Res-Atmos*, *106*(D17), 20255-20273.

Glen, W. G., M. P. Zelenka, and R. C. Graham (1996), Relating meteorological variables and trends in motor vehicle emissions to monthly urban carbon monoxide concentrations, *Atmos Environ*, *30*(24), 4225-4232.

Gong, S. L. (2003), A parameterization of sea-salt aerosol source function for sub- and super-micron particles, *Global Biogeochemical Cycles*, *17*(4).

Grell, G. A., S. E. Peckham, R. Schmitz, S. A. McKeen, G. Frost, W. C. Skamarock, and B. Eder (2005), Fully coupled "online" chemistry within the WRF model, *Atmospheric Environment*, *39*(37), 6957-6975.

Gyawali, M., W. P. Arnott, K. Lewis, and H. Moosmuller (2009), In situ aerosol optics in Reno, NV, USA during and after the summer 2008 California wildfires and the influence of absorbing and non-absorbing organic coatings on spectral light absorption, *Atmos. Chem. Phys.*, *9*(20), 8007-8015.

Hadley, O. L., V. Ramanathan, G. R. Carmichael, Y. Tang, C. E. Corrigan, G. C. Roberts, and G. S. Mauger (2007), Trans-Pacific transport of black carbon and fine aerosols (D < 2.5 mu m) into North America, *J. Geophys. Res.-Atmos.*, *112*(D5), -.

Hadley, O. L., and T. W. Kirchstetter (2012), Black-carbon reduction of snow albedo, *Nat. Clim. Chang.*, *2*(6), 437-440.

Hansen, A. D. A., H. Rosen, and T. Novakov (1984), The Aethalometer - an Instrument for the Real-Time Measurement of Optical-Absorption by Aerosol-Particles, *Sci Total Environ*, *36*(Jun), 191-196.

Hansen, J., M. Sato, A. Lacis, and R. Ruedy (1997), The missing climate forcing, *Philos. Trans. R. Soc. B-Biol. Sci.*, *352*(1350), 231-240.

Hansen, J., and L. Nazarenko (2004), Soot climate forcing via snow and ice albedos, *Proceedings of the National Academy of Sciences of the United States of America*, *101*(2), 423-428.

Hemeon, W. C. L., G. F. Haines, and H. M. Ide (1953), Determination of haze and smoke concentrations by filter paper samples, *Air Repair*, *3*, 22-28.

Higurashi, A., and T. Nakajima (2002), Detection of aerosol types over the East China Sea near Japan from four-channel satellite data, *Geophys Res Lett*, *29*(17).

Hoelzemann, J. J., K. M. Longo, R. M. Fonseca, N. M. E. do Rosario, H. Elbern, S. R. Freitas, and C. Pires (2009), Regional representativity of AERONET observation sites during the biomass burning season in South America determined by correlation studies with MODIS Aerosol Optical Depth, *J. Geophys. Res.-Atmos.*, *114*, 20.

Hoffer, A., A. Gelencser, P. Guyon, G. Kiss, O. Schmid, G. P. Frank, P. Artaxo, and M. O. Andreae (2006), Optical properties of humic-like substances (HULIS) in biomass-burning aerosols, *Atmos. Chem. Phys.*, *6*, 3563-3570.

Holben, B. N., T. F. Eck, I. Slutsker, D. Tanre, J. P. Buis, A. Setzer, E. Vermote, J. A. Reagan, Y. J. Kaufman, T. Nakajima, F. Lavenu, I. Jankowiak, and A. Smirnov (1998), AERONET - A federated instrument network and data archive for aerosol characterization, *Remote Sensing of Environment*, *66*(1), 1-16.

Holben, B. N., D. Tanre, A. Smirnov, T. F. Eck, I. Slutsker, N. Abuhassan, W. W. Newcomb, J. S. Schafer, B. Chatenet, F. Lavenu, Y. J. Kaufman, J. V. Castle, A. Setzer, B. Markham, D. Clark, R. Frouin, R. Halthore, A. Karneli, N. T. O'Neill, C. Pietras, R. T. Pinker, K. Voss, and G. Zibordi (2001), An emerging ground-based aerosol climatology: Aerosol optical depth from AERONET, *J Geophys Res-Atmos*, *106*(D11), 12067-12097.

Horvath, H., and K. E. Noll (1969), Relationship between Atmospheric Light Scattering Coefficient and Visibility, *Atmos Environ*, *3*(5), 543-&.

Horvath, H. (1993), Atmospheric Light-Absorption - a Review, *Atmos Environ a-Gen*, *27*(3), 293-317.

Hsu, N. C., R. Gautam, A. M. Sayer, C. Bettenhausen, C. Li, M. J. Jeong, S. C. Tsay, and B. N. Holben (2012), Global and regional trends of aerosol optical depth over land and ocean using SeaWiFS measurements from 1997 to 2010, *Atmos. Chem. Phys.*, *12*(17), 8037-8053.

Ito, A., and J. E. Penner (2005), Historical emissions of carbonaceous aerosols from biomass and fossil fuel burning for the period 1870-2000, *Global Biogeochem Cy*, *19*(2), -.

Jacob, D. J., J. H. Crawford, H. Maring, A. D. Clarke, J. E. Dibb, L. K. Emmons, R. A. Ferrare, C. A. Hostetler, P. B. Russell, H. B. Singh, A. M. Thompson, G. E. Shaw, E. McCauley, J. R. Pederson, and J. A. Fisher (2010), The Arctic Research of the Composition of the Troposphere from Aircraft and Satellites (ARCTAS) mission: design, execution, and first results, *Atmos Chem Phys*, *10*(11), 5191-5212.

Jacobson, M. Z. (1999), Isolating nitrated and aromatic aerosols and nitrated aromatic gases as sources of ultraviolet light absorption, *J. Geophys. Res.-Atmos.*, *104*(D3), 3527-3542.

Jacobson, M. Z. (2001), Strong radiative heating due to the mixing state of black carbon in atmospheric aerosols, *Nature*, *409*(6821), 695-697.

Jacobson, M. Z. (2002), Control of fossil-fuel particulate black carbon and organic matter, possibly the most effective method of slowing global warming, *Journal of Geophysical Research-Atmospheres*, *107*(D19), 22.

Jacobson, M. Z. (2006), Effects of externally-through-internally-mixed soot inclusions within clouds and precipitation on global climate, *Journal of Physical Chemistry A*, *110*(21), 6860-6873.

Jacobson, M. Z., Y. J. Kaufman, and Y. Rudich (2007), Examining feedbacks of aerosols to urban climate with a model that treats 3-D clouds with aerosol inclusions, *J Geophys Res-Atmos*, *112*(D24).

Jacobson, M. Z. (2010a), Short-term effects of Controlling Fossil-Fuel Soot, Biofuel Soot and Gases, and Methane on Climate , Arctic Ice, and Air Pollution Health, *J. Geophys. Res.-Atmos.*, *115*(D14), D14209.

Jacobson, M. Z. (2010b), Short-term effects of Controlling Fossil-Fuel Soot, Biofuel Soot and Gases, and Methane on Climate , Arctic Ice, and Air Pollution Health, *Journal of Geophysical Research-Atmospheres*, *115*(D14).

Jacobson, M. Z. (2010c), Short-term effects of Controlling Fossil-Fuel Soot, Biofuel Soot and Gases, and Methane on Climate , Arctic Ice, and Air Pollution Health, *J Geophys Res-Atmos*, *In Press*.

Jaegle, L., P. K. Quinn, T. S. Bates, B. Alexander, and J. T. Lin (2011), Global distribution of sea salt aerosols: new constraints from in situ and remote sensing observations, *Atmos Chem Phys*, *11*(7), 3137-3157.

Jeong, C. H., P. K. Hopke, E. Kim, and D. W. Lee (2004), The comparison between thermal-optical transmittance elemental carbon and Aethalometer black carbon measured at multiple monitoring sites, *Atmospheric Environment*, *38*(31), 5193-5204.

Jeong, M. J., Z. Q. Li, D. A. Chu, and S. C. Tsay (2005), Quality and compatibility analyses of global aerosol products derived from the advanced very high resolution radiometer and Moderate Resolution Imaging Spectroradiometer, *J. Geophys. Res.-Atmos.*, *110*(D10).

Jin, Y., W. B. Rossow, and D. P. Wylie (1996), Comparison of the climatologies of high-level clouds from HIRS and ISCCP, *J Climate*, *9*(11), 2850-2879.

Kahn, R. A., D. L. Nelson, M. J. Garay, R. C. Levy, M. A. Bull, D. J. Diner, J. V. Martonchik, S. R. Paradise, E. G. Hansen, and L. A. Remer (2009), MISR Aerosol Product Attributes and Statistical Comparisons With MODIS, *IEEE Trans. Geosci. Remote Sensing*, *47*(12), 4095-4114.

Kahn, R. A., B. J. Gaitley, M. J. Garay, D. J. Diner, T. F. Eck, A. Smirnov, and B. N. Holben (2010), Multiangle Imaging SpectroRadiometer global aerosol product assessment by comparison with the Aerosol Robotic Network, *J. Geophys. Res.-Atmos.*, *115*.

Kaplan, I. R., and R. J. Gordon (1994), Non-Fossil-Fuel Fine-Particle Organic-Carbon Aerosols in Southern California Determined during the Los-Angeles Aerosol Characterization and Source Apportionment Study, *Aerosol Sci Tech*, *21*(4), 343-359.

Kaufman, Y. J., O. Boucher, D. Tanre, M. Chin, L. A. Remer, and T. Takemura (2005), Aerosol anthropogenic component estimated from satellite data, *Geophys Res Lett*, *32*(17).

Kim, D., M. Chin, H. Yu, T. F. Eck, A. Sinyuk, A. Smirnov, and B. Holben (2011), Dust Optical properties over North Africa and Arabian Peninsula derived from the AERONET dataset, *Atmos. Chem. Phys.*, *11*, 10733-10741.

Kim, D. Y., and V. Ramanathan (2008), Solar radiation budget and radiative forcing due to aerosols and clouds, *J Geophys Res-Atmos*, *113*(D2), -.

Kirchstetter, T. W., R. A. Harley, N. M. Kreisberg, M. R. Stolzenburg, and S. V. Hering (1999), On-road measurement of fine particle and nitrogen oxide emissions from light- and heavy-duty motor vehicles, *Atmospheric Environment*, *33*(18), 2955-2968.

Kirchstetter, T. W., T. Novakov, P. V. Hobbs, and B. Magi (2003), Airborne measurements of carbonaceous aerosols in southern Africa during the dry biomass burning season, *J. Geophys. Res.-Atmos.*, *108*(D13).

Kirchstetter, T. W., T. Novakov, and P. V. Hobbs (2004), Evidence that the spectral dependence of light absorption by aerosols is affected by organic carbon, *J. Geophys. Res.-Atmos.*, *109*(D21), 12.

Kirchstetter, T. W., and T. Novakov (2007), Controlled generation of black carbon particles from a diffusion flame and applications in evaluating black carbon measurements, *Atmospheric Environment*, *41*, 1874-1888.

Kirchstetter, T. W., J. Aguiar, S. Tonse, T. Novakov, and D. Fairley (2008a), Black Carbon concentrations and diesel emission factors derived from coefficient of haze measurements in California, *Atmospheric Environment*, *42*, 480-491.

Kirchstetter, T. W., J. Agular, S. Tonse, D. Fairley, and T. Novakov (2008b), Black carbon concentrations and diesel vehicle emission factors derived from coefficient of haze measurements in California: 1967-2003, *Atmospheric Environment*, *42*(3), 480-491.

Koch, D., T. C. Bond, D. Streets, N. Unger, and G. R. van der Werf (2007), Global impacts of aerosols from particular source regions and sectors, *J. Geophys. Res.-Atmos.*, *112*(D2), 24.

Koch, D., and A. D. Del Genio (2010), Black carbon semi-direct effects on cloud cover: review and synthesis, *Atmospheric Chemistry and Physics*, *10*(16), 7685-7696.

Koehler, K. A., P. J. DeMott, S. M. Kreidenweis, O. B. Popovicheva, M. D. Petters, C. M. Carrico, E. D. Kireeva, T. D. Khokhlova, and N. K. Shonija (2009), Cloud condensation nuclei and ice nucleation activity of hydrophobic and hydrophilic soot particles, *Phys. Chem. Chem. Phys.*, *11*(36), 7906-7920.

Koven, C. D., and I. Fung (2006), Inferring dust composition from wavelength-dependent absorption in Aerosol Robotic Network (AERONET) data, *J. Geophys. Res.-Atmos.*, *111*(D14), 13.

Koylu, U. O., and G. M. Faeth (1994), Optical properties of overfire soot in buoyant turbulent diffusion flames at long residence times, *Trans. ASME, J. Heat Transf.*, *116*(1), 152-159159.

Lammel, G., and T. Novakov (1995), Water nucleation properties of carbon black and diesel soot particles, *Atmospheric Environment*, *29*(7), 813-823.

Laskin, J., A. Laskin, P. J. Roach, G. W. Slysz, G. A. Anderson, S. A. Nizkorodov, D. L. Bones, and L. Q. Nguyen (2010), High-Resolution Desorption Electrospray Ionization Mass Spectrometry for Chemical Characterization of Organic Aerosols, *Anal. Chem.*, *82*(5), 2048-2058.

Levin, E. J. T., G. R. McMeeking, C. M. Carrico, L. E. Mack, S. M. Kreidenweis, C. E. Wold, H. Moosmuller, W. P. Arnott, W. M. Hao, J. L. Collett, and W. C. Malm (2010), Biomass burning smoke aerosol properties measured during Fire Laboratory at Missoula Experiments (FLAME), *J. Geophys. Res.-Atmos.*, *115*, 15.

Levinson, R., H. Akbari, and P. Berdahl (2010), Measuring solar reflectance-Part I: Defining a metric that accurately predicts solar heat gain, *Sol Energy*, *84*(9), 1717-1744.

Li, G., N. Bei, X. Tie, and L. T. Molina (2011), Aerosol effects on the photochemistry in Mexico City during MCMA-2006/MILAGRO campaign, *Atmos Chem Phys*, *11*(11), 5169-5182.

Linke, C., O. Möhler, A. Veres, Á. Mohácsi, Z. Bozóki, G. Szabó, and M. Schnaiter (2006), Optical properties and mineralogical composition of different Saharan mineral dust samples: a laboratory study, *Atmos. Chem. Phys.*, *6*(11), 3315-3323.

Liousse, C., H. Cachier, and S. G. Jennings (1993), Optical and Thermal Measurements of Black Carbon Aerosol Content in Different Environments - Variation of the Specific Attenuation Cross-Section, Sigma (Sigma), *Atmos Environ a-Gen*, *27*(8), 1203-1211.

Lloyd, A. C., and T. A. Cackette (2001), Diesel engines: Environmental impact and control, *J Air Waste Manage*, *51*(6), 809-847.

Lohmann, U., and J. Feichter (2005), Global indirect aerosol effects: a review, *Atmospheric Chemistry and Physics*, *5*, 715-737.

Lohmann, U., and S. Ferrachat (2010), Impact of parametric uncertainties on the present-day climate and on the anthropogenic aerosol effect, *Atmos Chem Phys*, *10*(23), 11373-11383.

Long, C. N., E. G. Dutton, J. A. Augustine, W. Wiscombe, M. Wild, S. A. McFarlane, and C. J. Flynn (2009), Significant decadal brightening of downwelling shortwave in the continental United States, *J Geophys Res-Atmos*, *114*, 20.

Magi, B. I., P. Ginoux, Y. Ming, and V. Ramaswamy (2009), Evaluation of tropical and extratropical Southern Hemisphere African aerosol properties simulated by a climate model, *J. Geophys. Res.-Atmos.*, *114*, 19.

Malm, W. C., and K. A. Gebhart (1996), Source apportionment of organic and light-absorbing carbon using receptor modeling techniques, *Atmos Environ*, *30*(6), 843-855.

Malm, W. C., and M. L. Pitchford (1997), Comparison of calculated sulfate scattering efficiencies as estimated from size-resolved particle measurements at three national locations, *Atmos Environ*, *31*(9), 1315-1325.

Mazzoleni, L. R., B. Zielinska, and H. Moosmuller (2007), Emissions of levoglucosan, methoxy phenols, and organic acids from prescribed burns, laboratory combustion of wildland fuels, and residential wood combustion, *Environ. Sci. Technol.*, *41*(7), 2115-2122.

McMeeking, G. R., S. M. Kreidenweis, S. Baker, C. M. Carrico, J. C. Chow, J. L. Collett, W. M. Hao, A. S. Holden, T. W. Kirchstetter, W. C. Malm, H. Moosmuller, A. P. Sullivan, and C. E. Wold (2009), Emissions of trace gases and aerosols during the open combustion of biomass in the laboratory, *J. Geophys. Res.-Atmos.*, *114*.

Meloni, D., A. di Sarra, G. Pace, and F. Monteleone (2006), Aerosol optical properties at Lampedusa (Central Mediterranean). 2. Determination of single scattering albedo at two wavelengths for different aerosol types, *Atmos. Chem. Phys.*, *6*, 715-727.

Menon, S., D. Koch, G. Beig, S. Sahu, J. Fasullo, and D. Orlikowski (2010), Black carbon aerosols and the third polar ice cap, *Atmos. Chem. Phys.*, *10*(10), 4559-4571.

Mesinger, F., G. DiMego, E. Kalnay, K. Mitchell, P. C. Shafran, W. Ebisuzaki, D. Jovic, J. Woollen, E. Rogers, E. H. Berbery, M. B. Ek, Y. Fan, R. Grumbine, W. Higgins, H. Li, Y. Lin, G. Manikin, D. Parrish, and W. Shi (2006), North American regional reanalysis, *B Am Meteorol Soc*, *87*(3), 343-+.

Metcalf, A. R., J. S. Craven, J. J. Ensberg, J. Brioude, W. Angevine, A. Sorooshian, H. T. Duong, H. H. Jonsson, R. C. Flagan, and J. H. Seinfeld (2012), Black carbon aerosol over the Los Angeles Basin during CalNex, *J Geophys Res-Atmos*, *117*.

Mishchenko, M. I., L. Liu, I. V. Geogdzhayev, L. D. Travis, B. Cairns, and A. A. Lacis (2010), Toward unified satellite climatology of aerosol properties. 3. MODIS versus MISR versus AERONET, *J Quant Spectrosc Ra*, *111*(4), 540-552.

Moffet, R. C., B. de Foy, L. T. Molina, M. J. Molina, and K. A. Prather (2008), Measurement of ambient aerosols in northern Mexico City by single particle mass spectrometry, *Atmospheric Chemistry and Physics*, *8*(16), 4499-4516.

Moosmuller, H., R. K. Chakrabarty, K. M. Ehlers, and W. P. Arnott (2011), Absorption Angstrom coefficient, brown carbon, and aerosols: basic concepts, bulk matter, and spherical particles, *Atmos. Chem. Phys.*, *11*(3), 1217-1225.

Myhre, G., C. R. Hoyle, T. F. Berglen, B. T. Johnson, and J. M. Haywood (2008), Modeling of the solar radiative impact of biomass burning aerosols during the Dust and Biomass-burning Experiment (DABEX), *J. Geophys. Res.-Atmos.*, *113*, 10.

Novakov, T., M. O. Andreae, R. Gabriel, T. W. Kirchstetter, O. L. Mayol-Bracero, and V. Ramanathan (2000), Origin of carbonaceous aerosols over the tropical Indian Ocean: Biomass burning or fossil fuels?, *Geophys Res Lett*, *27*(24), 4061-4064.

Novakov, T., T. W. Kirchstetter, S. Menon, and J. Aguiar (2008a), Response of California temperature to regional anthropogenic aerosol changes, *Geophys Res Lett*, *35*(19), -.

Novakov, T., T. W. Kirchstetter, S. Menon, and J. Aguiar (2008b), Response of California temperature to regional anthropogenic aerosol changes, *Geophys Res Lett*, *35*(19).

Ogren, J. A., and R. J. Charlson (1983), Elemental Carbon in the Atmosphere - Cycle and Lifetime, *Tellus Series B-Chemical and Physical Meteorology*, *35*(4), 241-254.

Ogren, J. A. (2010), Comment on "Calibration and Intercomparison of Filter-Based Measurements of Visible Light Absorption by Aerosols", *Aerosol Sci Tech*, *44*(8), 589-591.

Ohara, T., H. Akimoto, J. Kurokawa, N. Horii, K. Yamaji, X. Yan, and T. Hayasaka (2007), An Asian emission inventory of anthropogenic emission sources for the period 1980-2020, *Atmos. Chem. Phys.*, *7*(16), 4419-4444.

Park, S.-U., and L.-S. Chang (2007), *Direct radiative forcing due to anthropogenic aerosols in East Asia during 21-25 April 2001*, 312-320 pp., Springer, 233 Spring Street, New York, Ny 10013, United States.

Piazzalunga, A., C. Belis, V. Bernardoni, O. Cazzuli, P. Fermo, G. Valli, and R. Vecchi (2011), Estimates of wood burning contribution to PM by the macro-tracer method using tailored emission factors, *Atmospheric Environment*, *45*(37), 6642-6649.

Platnick, S., M. D. King, S. A. Ackerman, W. P. Menzel, B. A. Baum, J. C. Riedi, and R. A. Frey (2003), The MODIS cloud products: Algorithms and examples from Terra, *IEEE Trans. Geosci. Remote Sensing*, *41*(2), 459-473.

Podgorny, I. A., W. Conant, V. Ramanathan, and S. K. Satheesh (2000), Aerosol modulation of atmospheric and surface solar heating over the tropical Indian Ocean, *Tellus B*, *52*(3), 947-958.

Podgorny, I. A., and V. Ramanathan (2001), A modeling study of the direct effect of aerosols over the tropical Indian Ocean, *J. Geophys. Res.-Atmos.*, *106*(D20), 24097-24105.

Pratt, K. A., J. E. Mayer, J. C. Holecek, R. C. Moffet, R. O. Sanchez, T. P. Rebotier, H. Furutani, M. Gonin, K. Fuhrer, Y. X. Su, S. Guazzotti, and K. A. Prather (2009), Development and Characterization of an Aircraft Aerosol Time-of-Flight Mass Spectrometer, *Anal Chem*, *81*(5), 1792-1800.

Praveen, P. S., T. Ahmed, A. Kar, I. H. Rehman, and V. Ramanathan (2012), Link between local scale BC emissions in the Indo-Gangetic Plains and large scale atmospheric solar absorption, *Atmos. Chem. Phys.*, *12*(2), 1173-1187.

Qian, Y., W. I. Gustafson, L. R. Leung, and S. J. Ghan (2009), Effects of soot-induced snow albedo change on snowpack and hydrological cycle in western United States based on Weather Research and Forecasting chemistry and regional climate simulations, *J. Geophys. Res.-Atmos.*, *114*, 19.

Qin, X. Y., P. V. Bhave, and K. A. Prather (2006), Comparison of two methods for obtaining quantitative mass concentrations from aerosol time-of-flight mass spectrometry measurements, *Analytical Chemistry*, *78*(17), 6169-6178.

Ramanathan, V., P. J. Crutzen, J. Lelieveld, A. P. Mitra, D. Althausen, J. Anderson, M. O. Andreae, W. Cantrell, G. R. Cass, C. E. Chung, A. D. Clarke, J. A. Coakley, W. D. Collins, W. C. Conant, F. Dulac, J. Heintzenberg, A. J. Heymsfield, B. Holben, S. Howell, J. Hudson, A. Jayaraman, J. T. Kiehl, T. N. Krishnamurti, D. Lubin, G. McFarquhar, T. Novakov, J. A. Ogren, I. A. Podgorny, K. Prather, K. Priestley, J. M. Prospero, P. K. Quinn, K. Rajeev, P. Rasch, S. Rupert, R. Sadourny, S. K. Satheesh, G. E. Shaw, P. Sheridan, and F. P. J. Valero (2001), Indian Ocean Experiment: An integrated analysis of the climate forcing and effects of the great Indo-Asian haze, *J Geophys Res-Atmos*, *106*(D22), 28371-28398.

Ramanathan, V., M. Ramana, G. Roberts, D. Kim, C. Corrigan, C. Chung, and D. Winker (2007), Warming trends in Asia amplified by brown cloud solar absorption, *Nature*, *448*, 575-578.

Ramanathan, V., and G. Carmichael (2008), Global and regional climate changes due to black carbon, *Nature Geoscience*, *1*(4), 221-227.

Ramanathan, V., and Y. Y. Xu (2010), The Copenhagen Accord for limiting global warming: Criteria, constraints, and available avenues, *P Natl Acad Sci USA*, *107*(18), 8055-8062.

Rizzo, L. V., A. L. Correia, P. Artaxo, A. S. Procopio, and M. O. Andreae (2011), Spectral dependence of aerosol light absorption over the Amazon Basin, *Atmos. Chem. Phys.*, *11*(17), 8899-8912.

Roberts, G. C., A. Nenes, J. H. Seinfeld, and M. O. Andreae (2003), Impact of biomass burning on cloud properties in the Amazon Basin, *Journal of Geophysical Research-Atmospheres*, *108*(D2).

Russell, P. B., R. W. Bergstrom, Y. Shinozuka, A. D. Clarke, P. F. DeCarlo, J. L. Jimenez, J. M. Livingston, J. Redemann, O. Dubovik, and A. Strawa (2010), Absorption Angstrom Exponent in AERONET and related data as an indicator of aerosol composition, *Atmos. Chem. Phys.*, *10*(3), 1155-1169.

Sandradewi, J., A. S. H. Prevot, S. Szidat, N. Perron, M. R. Alfarra, V. A. Lanz, E. Weingartner, and U. Baltensperger (2008), Using aerosol light absorption measurements for the quantitative determination of wood burning and traffic emission contributions to particulate matter, *Environ. Sci. Technol.*, *42*(9), 3316-3323.

Sato, M., J. Hansen, D. Koch, A. Lacis, R. Ruedy, O. Dubovik, B. Holben, M. Chin, and T. Novakov (2003), Global atmospheric black carbon inferred from AERONET, *Proc. Natl. Acad. Sci. U. S. A.*, *100*(11), 6319-6324.

Schauer, J. J., and G. R. Cass (2000), Source apportionment of wintertime gas-phase and particle-phase air pollutants using organic compounds as tracers, *Environ Sci Technol*, *34*(9), 1821-1832.

Schauer, J. J. (2003), Evaluation of elemental carbon as a marker for diesel particulate matter, *J Expo Anal Env Epid*, *13*(6), 443-453.

Schell, B., I. J. Ackermann, H. Hass, F. S. Binkowski, and A. Ebel (2001), Modeling the formation of secondary organic aerosol within a comprehensive air quality model system, *J. Geophys. Res.-Atmos.*, *106*(D22), 28275-28293.

Schmid, H., L. Laskus, H. J. Abraham, U. Baltensperger, V. Lavanchy, M. Bizjak, P. Burba, H. Cachier, D. Crow, J. Chow, T. Gnauk, A. Even, H. M. ten Brink, K. P. Giesen, R. Hitzenberger, C. Hueglin, W. Maenhaut, C. Pio, A. Carvalho, J. P. Putaud, D. Toom-Sauntry, and H. Puxbaum (2001), Results of the "carbon conference" international aerosol carbon round robin test stage I, *Atmos Environ*, *35*(12), 2111-2121.

Schmid, O., P. Artaxo, W. P. Arnott, D. Chand, L. V. Gatti, G. P. Frank, A. Hoffer, M. Schnaiter, and M. O. Andreae (2006), Spectral light absorption by ambient aerosols influenced by biomass burning in the Amazon Basin. I: Comparison and field calibration of absorption measurement techniques, *Atmos Chem Phys*, *6*, 3443-3462.

Schnaiter, M., H. Horvath, O. Mohler, K. H. Naumann, H. Saathoff, and O. W. Schock (2003), UV-VIS-NIR spectral optical properties of soot and soot-containing aerosols, *J. Aerosol. Sci.*, *34*(10), 1421-1444.

Schnaiter, M., O. Schmid, A. Petzold, L. Fritzsche, K. F. Klein, M. O. Andreae, G. Helas, A. Thielmann, M. Gimmler, O. Mohler, C. Linke, and U. Schurath (2005), Measurement of wavelength-resolved light absorption by aerosols utilizing a UV-VIS extinction cell, *Aerosol Sci. Technol.*, *39*(3), 249-260.

Schnaiter, M., M. Gimmler, I. Llamas, C. Linke, C. Jager, and H. Mutschke (2006), Strong spectral dependence of light absorption by organic carbon particles formed by propane combustion, *Atmos. Chem. Phys.*, *6*, 2981-2990.

Shindell, D., and G. Faluvegi (2010), The net climate impact of coal-fired power plant emissions, *Atmos. Chem. Phys.*, *10*(7), 3247-3260.

Shindell, D., J. C. I. Kuylenstierna, E. Vignati, R. van Dingenen, M. Amann, Z. Klimont, S. C. Anenberg, N. Muller, G. Janssens-Maenhout, F. Raes, J. Schwartz, G. Faluvegi, L. Pozzoli, K. Kupiainen, L. Hoglund-Isaksson, L. Emberson, D. Streets, V. Ramanathan, K. Hicks, N. T. K. Oanh, G. Milly, M. Williams, V. Demkine, and D. Fowler (2012a), Simultaneously Mitigating Near-Term Climate Change and Improving Human Health and Food Security, *Science*, *335*(6065), 183-189.

Shindell, D., V. Ramanathan, F. Raes, L. Cifuentes, and N. T. K. Oanh (2012b), Integrated assessment of black carbon and tropospheric ozone: A summary for descision makers, United Nations Environment Programme.

Silva, P. J., D. Y. Liu, C. A. Noble, and K. A. Prather (1999), Size and chemical characterization of individual particles resulting from biomass burning of local Southern California species, *Environmental Science & Technology*, *33*(18), 3068-3076.

Silva, P. J., and K. A. Prather (2000), Interpretation of mass spectra from organic compounds in aerosol time-of-flight mass spectrometry, *Analytical Chemistry*, *72*(15), 3553-3562.

Skamarock, W. C., and J. B. Klemp (2008), A time-split nonhydrostatic atmospheric model for weather research and forecasting applications, *Journal of Computational Physics*, *227*(7), 3465-3485.

Song, X. H., P. K. Hopke, D. P. Fergenson, and K. A. Prather (1999), Classification of single particles analyzed by ATOFMS using an artificial neural network, ART-2A, *Anal Chem*, *71*(4), 860-865.

Stier, P., J. H. Seinfeld, S. Kinne, and O. Boucher (2007), Aerosol absorption and radiative forcing, *Atmospheric Chemistry and Physics*, *7*(19), 5237-5261.

Stockwell, W. R., P. Middleton, J. S. Chang, and X. Y. Tang (1990), The 2nd Generation Regional Acid Deposition Model Chemical Mechanism for Regional Air-Quality Modeling, *J. Geophys. Res.-Atmos.*, *95*(D10), 16343-16367.

Streets, D. G., T. C. Bond, G. R. Carmichael, S. D. Fernandes, Q. Fu, D. He, Z. Klimont, S. M. Nelson, N. Y. Tsai, M. Q. Wang, J. H. Woo, and K. F. Yarber (2003), An inventory of gaseous and primary aerosol emissions in Asia in the year 2000, *J Geophys Res-Atmos*, *108*(D21).

Sun, H. L., L. Biedermann, and T. C. Bond (2007a), Color of brown carbon: A model for ultraviolet and visible light absorption by organic carbon aerosol, *Geophys. Res. Lett.*, *34*(17), 5.

Sun, H. L., L. Biedermann, and T. C. Bond (2007b), Color of brown carbon: A model for ultraviolet and visible light absorption by organic carbon aerosol, *Geophys Res Lett*, *34*(17).

Thatcher, T., S. Tan, C. Malejan, C. Ward, and T. W. Kirchstetter (2011), Assessing near-field exposures from distributed residential wood-smoke combustion sources.
Final report to California Air Resources Board.

Torres, O., A. Tanskanen, B. Veihelmann, C. Ahn, R. Braak, P. K. Bhartia, P. Veefkind, and P. Levelt (2007), Aerosols and surface UV products from Ozone

Monitoring Instrument observations: An overview, *J Geophys Res-Atmos*, *112*(D24).

Turpin, B. J., J. J. Huntzicker, and K. M. Adams (1990), Intercomparison of Photoacoustic and Thermal Optical Methods for the Measurement of Atmospheric Elemental Carbon, *Atmos Environ a-Gen*, *24*(7), 1831-1835.

Turpin, B. J., P. Saxena, and E. Andrews (2000), Measuring and simulating particulate organics in the atmosphere: problems and prospects, *Atmos Environ*, *34*(18), 2983-3013.

van der Werf, G. R., J. T. Randerson, L. Giglio, G. J. Collatz, M. Mu, P. S. Kasibhatla, D. C. Morton, R. S. DeFries, Y. Jin, and T. T. van Leeuwen (2010), Global fire emissions and the contribution of deforestation, savanna, forest, agricultural, and peat fires (1997-2009), *Atmos Chem Phys*, *10*(23), 11707-11735.

VanCuren, R. A., S. S. Cliff, K. D. Perry, and M. Jimenez-Cruz (2005), Asian continental aerosol persistence above the marine boundary layer over the eastern North Pacific: Continuous aerosol measurements from Intercontinental Transport and Chemical Transformation 2002 (ITCT 2K2), *J Geophys Res-Atmos*, *110*(D9), -.

VanCuren, R. A., and T. A. Cahill (2006), Asian aerosols in North America: Frequency and concentration of fine dust (vol 107, pg 4804, 2002), *J Geophys Res-Atmos*, *111*(D20), -.

Virkkula, A., N. C. Ahlquist, D. S. Covert, W. P. Arnott, P. J. Sheridan, P. K. Quinn, and D. J. Coffman (2005), Modification, calibration and a field test of an instrument for measuring light absorption by particles, *Aerosol Sci. Technol.*, *39*(1), 68-83.

Vuilleumier, L., J. T. Bamer, R. A. Harley, and N. J. Brown (2001), Evaluation of nitrogen dioxide photolysis rates in an urban area using data from the 1997 Southern California Ozone Study, *Atmospheric Environment*, *35*(36), 6525-6537.

Watson, J. G., J. C. Chow, L. W. A. Chen, and N. H. Frank (2009), Methods to Assess Carbonaceous Aerosol Sampling Artifacts for IMPROVE and Other Long-Term Networks, *J Air Waste Manage*, *59*(8), 898-911.

Weingartner, E., H. Saathoff, M. Schnaiter, N. Streit, B. Bitnar, and U. Baltensperger (2003), Absorption of light by soot particles: determination of the absorption coefficient by means of aethalometers, *J Aerosol Sci*, *34*(10), 1445-1463.

Weinzierl, B., D. Sauer, M. Esselborn, A. Petzold, A. Veira, M. Rose, S. Mund, M. Wirth, A. Ansmann, M. Tesche, S. Gross, and V. Freudenthaler (2011), Microphysical and optical properties of dust and tropical biomass burning aerosol

layers in the Cape Verde region-an overview of the airborne in situ and lidar measurements during SAMUM-2, *Tellus Ser. B-Chem. Phys. Meteorol.*, *63*(4), 589-618.

Westerling, A. L., H. G. Hidalgo, D. R. Cayan, and T. W. Swetnam (2006), Warming and earlier spring increase western US forest wildfire activity, *Science*, *313*(5789), 940-943.

Wielicki, B. A. (1996), Clouds and the Earth's radiant energy system (CERES): An earth observing system experiment (vol 77, pg 860, 1996), *B Am Meteorol Soc*, *77*(7), 1590-1590.

Wilcox, E. M., Harshvardhan, and S. Platnick (2009), Estimate of the impact of absorbing aerosol over cloud on the MODIS retrievals of cloud optical thickness and effective radius using two independent retrievals of liquid water path, *J Geophys Res-Atmos*, *114*.

Wolff, G. T., C. M. Stroup, and D. P. Stroup (1983), The Coefficient of Haze as a Measure of Particulate Elemental Carbon, *Japca J Air Waste Ma*, *33*(8), 746-750.

Wolff, M. J., M. D. Smith, R. T. Clancy, R. Arvidson, M. Kahre, F. Seelos, S. Murchie, and H. Savijarvi (2009), Wavelength dependence of dust aerosol single scattering albedo as observed by the Compact Reconnaissance Imaging Spectrometer, *Journal of Geophysical Research-Planets*, *114*.

Xia, X. G., T. F. Eck, B. N. Holben, G. Phillippe, and H. B. Chen (2008), Analysis of the weekly cycle of aerosol optical depth using AERONET and MODIS data, *J. Geophys. Res.-Atmos.*, *113*(D14), 11.

Yan, F., E. Winijkul, S. Jung, T. C. Bond, and D. G. Streets (2011), Global emission projections of particulate matter (PM): I. Exhaust emissions from on-road vehicles, *Atmos Environ*, *45*(28), 4830-4844.

Yang, M., S. G. Howell, J. Zhuang, and B. J. Huebert (2009), Attribution of aerosol light absorption to black carbon, brown carbon, and dust in China - interpretations of atmospheric measurements during EAST-AIRE, *Atmos. Chem. Phys.*, *9*(6), 2035-2050.

Yang M., S. G. Howell, J. Zhuang, and B. J. Huebert (2009), Attribution of aerosol light absorption to black carbon, brown carbon, and dust in China – interpretations of atmospheric measurements during EAST-AIRE, *Atmospheric Chemistry and Physics*, *9*, 2035–2050.

Yang, Q., W. I. Gustafson, J. D. Fast, H. Wang, R. C. Easter, H. Morrison, Y. N. Lee, E. G. Chapman, S. N. Spak, and M. A. Mena-Carrasco (2011), Assessing regional scale predictions of aerosols, marine stratocumulus, and their interactions during VOCALS-REx using WRF-Chem, *Atmos Chem Phys*, *11*(23), 11951-11975.

Young, S. A., and M. A. Vaughan (2009), The Retrieval of Profiles of Particulate Extinction from Cloud-Aerosol Lidar Infrared Pathfinder Satellite Observations (CALIPSO) Data: Algorithm Description, *J Atmos Ocean Tech*, *26*(6), 1105-1119.

Zhao, C., X. Liu, L. R. Leung, B. Johnson, S. A. McFarlane, W. I. Gustafson, J. D. Fast, and R. Easter (2010), The spatial distribution of mineral dust and its shortwave radiative forcing over North Africa: modeling sensitivities to dust emissions and aerosol size treatments, *Atmos Chem Phys*, *10*(18), 8821-8838.

Zhao, C., X. Liu, L. R. Leung, and S. Hagos (2011), Radiative impact of mineral dust on monsoon precipitation variability over West Africa, *Atmos Chem Phys*, *11*(5), 1879-1893.

Zhao, C., L. R. Leung, R. Easter, J. Hand, and J. Avise (2012), Characterization of speciated aerosol forcing over California, *J. Geophys. Res.-Atmos.*, *submitted*.